Neutron Scattering Studies on Complex Magnetic Structures in Magnetoelectric Materials

Inaugural-Dissertation

zur

Erlangung des Doktorgrades

der Mathematisch-Naturwissenschaftlichen Fakultät

der Universität zu Köln

vorgelegt von

Simon Holbein

aus Leinefelde

Köln, 2016

Berichterstatter:	Prof. Dr. Markus Braden Prof. Dr. Joachim Hemberger
Vorsitzender der Prüfungskommission:	Prof. Dr. Simon Trebst
Tag der mündlichen Prüfung:	25.01.2016

"La frustration fait bouger le monde."

Fred Vargas [1, p. 17]

Contents

Chapter 1

Motivation

In order to increase the functionality of technical devices, there is ongoing research for materials with sophisticated properties. Especially the coupling between electric and magnetic properties in a material, known as the magnetoelectric effect, has the potential to improve today's technology [3]. The effect was predicted already in the 19th century [2] but its application was hindered in the last century by the low number of available materials and the weakness of the effect [4]. The recent discovery of spin-induced ferroelectricity in $TbMnO_3$ showed that frustrated magnets are ideal systems to develop a giant coupling between magnetic and electric order [5].
In magnetic oxides, frustration can arise due to competing magnetic exchanges and anisotropies. Common examples are systems with geometric frustration or competing nearest- and next-nearest neighbor exchanges [6, p. 173ff]. The frustration destabilizes the magnetic order which can subsequently be modulated even by the intrinsically weak magnetoelectric effect [7]. As a result, these systems show spectacular cross-coupling effects, such as magnetically induced polarization flops [8] and giant magneto-capacitance [9].
Systems in which a complex magnetic structure directly induces a ferroelectric polarization generated great interest [10]. These multiferroic systems with coexisting antiferromagnetic and electric order develop per definition a strong coupling of both orders. Neutron scattering is an experimental technique which is perfectly adapted to study antiferromagnetic materials. It has been a valuable tool to understand the microscopic properties of these interesting materials [11, 12, 13]. The aim of current research is to find novel multiferroic and magnetoelectric materials and to understand the various underlying microscopic origins that can lead to such effects [14].
In this thesis, experimental data on four different transition-metal oxides was gathered and evaluated. Their magnetic properties were investigated by neutron

scattering on single crystalline samples. In order to study the magnetic structure, the critical behaviour and the dynamics of the systems, several different scattering techniques were applied. The observations contributed to a better understanding of the underlying physics. This work contains two introductory and four experimental chapters which are organized as follows:

Chapter 2 introduces the recent developments concerning the magnetoelectric effect and multiferroic materials. The focus is on multiferroics whose ferroelectric polarization is induced by a spin-spiral structure via the inverse Dzyaloshinskii-Moriya effect [15, 16], and on the first observations of electromagnons: hybridized phonon-magnon excitations.
The experimental technique of neutron scattering is presented in **Chapter 3**. The basics of nuclear and magnetic scattering are briefly summarized, followed by an overview of the use of neutron polarization analysis. The different experimental techniques applied in this work are introduced.
$TbMnO_3$, which is discussed in **Chapter 4**, is a prototype material for spin-induced multiferroics. In this material, the spiral order of Mn-moments accounts for the induced ferroelectricity [5]. The sequence of magnetic phase transitions and the correlation of the magnetic moments were investigated. The spin dynamics in the multiferroic phase were studied in detail and a spin-wave model was developed which can describe the full magnon dispersion. In addition, the magnetic excitation spectrum in the multiferroic high-field phase is analyzed and the influence of the rare-earth ion on the excitation spectrum is discussed.
Another prototype multiferroic is $MnWO_4$, which is presented in **Chapter 5**. A complex spin-spiral of Mn-moments induces an electric polarization in this system [17]. The properties of the sequence of magnetic phase transitions were investigated in detail. The use of polarized neutrons in combination with applied magnetic fields allowed to observe ferroelectric fluctuations in the dielectric phase. Furthermore, the excitation spectrum in the multiferroic phase is presented.
Chapter 6 presents a comprehensive study of the magnetic phase diagram of $NaFe(WO_4)_2$. The double tungstate is isostructural to $MnWO_4$ and it could be demonstrated in this work that the system develops a similar spin-spiral structure. In a magnetic field applied along $\vec{b}$, the structure transforms into a collinear antiferromagnetic structure.
Finally, **Chapter 7** presents studies on the ilmenite $Ni_{0.42}Mn_{0.58}TiO_3$. In this material, the linear magnetoelectric effect was observed in the absence of a long-range magnetic order [18]. It could be shown, that two competing orders are coexistent in the spin-glass phase and that the antiferromagnetic domains can be controlled by the application of crossed magnetic and electric fields. Furthermore, the magnetic excitations in the spin-glass phase were investigated and compared to spin-wave simulations.

Chapter 2

Magnetoelectric and multiferroic materials

The fundamentals of electricity and magnetism, and in particular their interaction, are stated in Maxwell's equations from 1865 [20]. In condensed matter, these two phenomena are separated due to their distinct origin: electric charges on one hand, and spins on the other hand. While there are many materials in which one of these effects can be observed, materials with coexisting or coupled order are rare.

Figure 2.1 sketches the distribution of electric (red) and magnetic (green) properties in the material class of insulating oxides, indicating regions of polarizability and ferroic order. Multiferroic materials are materials at the intersection of ferromagnetism and ferroelectricity. Materials showing a coupling of magnetism and electric properties, i.e. the magnetoelectric effect, which is indicated by a white region, span over four different intersections.

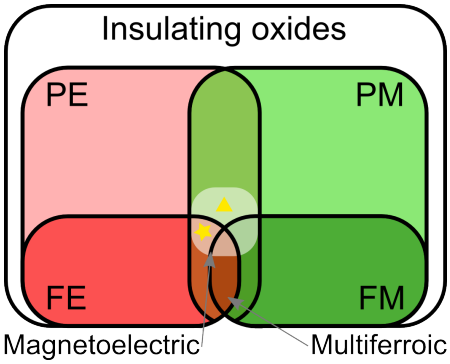

Figure 2.1.: Classification of magnetic and electric properties in insulating oxides. Rounded squares correspond to materials being electrically polarizable (PE), magnetically polarizable (PM), ferroelectric (FE) and ferromagnetic (FM). Inspired from Ref. [19].

In this chapter, an overview is given of the magnetoelectric effect and the class of multiferroic materials. The focus is on the materials investigated in this work, which positions are indicated in Fig. 2.1 as a star ($TbMnO_3$ and $MnWO_4$) and a triangle ($Ni_{0.42}Mn_{0.58}TiO_3$).

2.1. The magnetoelectric effect

The term "*magnetoelectric* (ME) effect" denotes in general the coupling between magnetic and electric properties in matter. In times of a booming digital industry with increasing demand for electronic storage and computing capacity, this effect opens possibilities for novel applications [21]. The interest in this field of research increased enormously since the beginning of the new century [7], revitalized, among others, by the observation of a giant ME effect in $TbMnO_3$ in 2003 by Kimura *et al.* [5]. A detailed overview of the recent revival of the ME effect is given in Ref. [7].
The first reference of the ME effect can be traced back to Pierre Curie in 1894, who pointed out the possibility of such an effect on the basis of symmetry considerations [2]. But the effect was not experimentally observed before 1960, when Astrov reported a linear ME coupling in Cr_2O_3 [22], which has been theoretically predicted by Dzyaloshinskii [23]. Since then, a variety of materials has been discovered, spanning over the complete region denoted in Fig. 2.1.
Following the phenomenological approach by Landau, the ME effect can be described by the free energy $F(\vec{E}, \vec{H})$ of a material [24]. Differentiation of F with respect to $\vec{E}$ or $\vec{H}$ leads to the polarization and magnetization:

$$P_i(\vec{E}, \vec{H}) = -\frac{\partial F}{\partial E_i} = P_i^{\mathrm{s}} + \epsilon_0 \epsilon_{ij} E_j + \alpha_{ij} H_j + \frac{1}{2}\beta_{ijk} H_j H_k + \gamma_{ijk} H_i E_j + ... \quad (2.1)$$

$$M_i(\vec{E}, \vec{H}) = -\frac{\partial F}{\partial H_i} = M_i^{\mathrm{s}} + \mu_0 \mu_{ij} H_j + \alpha_{ij} E_i + \beta_{ijk} E_i H_j + \frac{1}{2}\gamma_{ijk} E_j E_k + ... \quad (2.2)$$

$\vec{P}^{\mathrm{s}}$ and $\vec{M}^{\mathrm{s}}$ are the spontaneous polarization and magnetization, ϵ_{ij} is the electric and μ_{ij} the magnetic susceptibility and ϵ_0 and μ_0 are the electric and magnetic constants. The tensor susceptibility α_{ij} describes the linear magnetoelectric effect, i.e. the induction of an electric polarization by a magnetic field and of a magnetization by an electric field. The linear effect is accompanied by higher order terms, characterized by the tensors β_{ijk} (bilinear ME effect) and γ_{ijk} (quadratic ME effect). In the following, we will focus on the linear effect, omitting higher order terms.
The linear ME effect is only observed in few materials, and its limitation can be understood by a symmetry analysis. Electric and magnetic polarization behave differently on time reversal and spatial inversion operations. The electric polarization, given by an electric dipole, is invariant under time reversal and changes its sign under spatial inversion. The case for the magnetization can be visualized when expressing the magnetic moment by small current loops. These are invariant under spacial inversion, but change their current direction under time reversal.

This implies, that the linear ME tensor α_{ij} can only be non-zero for a material which simultaneously breaks both time reversal and spacial inversion.
The symmetry constraints given above limit the number of magnetic groups in which the linear ME effect is possible. One can deduce, that the effect is excluded for all dia- and paramagnets, as their magnetic space groups contain the time reversal operator $1'$. Furthermore, the magnetic space group cannot posses a center of symmetry $\bar{1}$. Overall there are 58 magnetic points groups, which allow for the linear magnetoelectric effect, summarized in Ref. [25, p. 138]. The magnetic point group of the system determines the shape of the ME tensor, e.g. the existence of diagonal and off-diagonal terms.
A detailed study of the microscopic origin of the magnetoelectric effect in ordered magnetic compounds was published in Ref. [26]. These are crucial in order to understand the strength of the effect and to be able to design materials suiting technical applications. In general, the effect can be described as a perturbation of an external field, modulating a microscopic exchange or anisotropy parameter. As an example, the electric field can move ions relative to its ligands, modulating the ions anisotropy or exchange path. The relevant interactions discussed to induce the ME effect are (in order of strength): the single-ion anisotropy, the symmetric superexchange, the antisymmetric superexchange, dipolar interactions and the Zeeman effect [26]. Technical applications based on the ME effect strongly depend on the strength of the effect. In the compounds that are known until now, the effect is relatively weak. It could be shown that an important limitation exists for the size of the ME tensor [27]:

$$\alpha_{ij}^2 < \epsilon_{ii}\mu_{jj} \ . \tag{2.3}$$

This upper boundary of α_{ij} is given by the geometric mean of the materials magnetic and electric susceptibilities. The chances to observe a strong ME coupling are thus increased for materials which develop strong ferroelectric and magnetic order.

2.2. Multiferroic materials

The limitation of the linear magnetoelectric effect, given by Eq. 2.3, shows that materials with simultaneous ferroelectric and magnetic order are best suited to exhibit strong ME effects. The term *multiferroic* used by Schmid in Ref. [28] is now widely recognized for this group of materials (*ferroelectromagnets* was also used in earlier publications [29]). In its initial formulation, this term is used to state the coexistence of at least two types of ferroic ordering, i.e. ferroelectricity,

ferromagnetism and ferroelasticity. In a broader context, also ferri- and antiferromagnetic order along with ferrotoroidal order are included in the term. The multiferroic materials investigated in this work, $TbMnO_3$ and $MnWO_4$, show the coexistence of ferroelectric polarization and antiferromagnetic order.
It is indicated in Figure 2.1 that the magnetoelectric effect is not necessary a property of a multiferroic material. This is for example the case for the widely studied room-temperature multiferroics $BiFeO_3$ and $BiMnO_3$. It can be explained by the distinct microscopic origin of both ordering types in these materials [10].
The first multiferroic material, in which both ferroic orderings were observed simultaneously in the absence of magnetic and electric field, was $Ni_3B_7O_{13}I$ in 1966 [30]. There are two aspects that explain the difficulty of having magnetism and ferroelectricity together in the same phase. On one hand, the system has to obey specific symmetry restrictions, similar to the ME effect. The space group of the system must simultaneously break time reversal and spacial inversion symmetry, in order to allow for both ordering types (see Ref. [31] for a comprehensive discussion of symmetry aspects for multiferroic materials).
On the other hand, magnetic order and ferroelectricity have a distinct microscopic origin. Most ferroelectric materials are transition-metal oxides with perovskite structure, where the metal ion is in the center of an oxygen octahedron. For metals with an empty *d*-shell, a covalent bonding with an oxygen atom is often favored in order to reduce binding energy [32]. The metal ion then shifts toward an oxygen atom which induces an electric dipole moment. In materials with such an electron configuration, it is not possible to develop a magnetization because all electron shells are either full or empty and the electron spins cancel out each other .
Magnetic ordering is a common feature of perovskite transition-metal oxides and arises in general from the intrinsic spin of localized electrons. In contrast to ferroelectricity, it requires metal ions with partially filled shells. The outcome of this incompatibility of ferroelectricity and ferromagnetism is often referred to as d^0-rule [4].
In the following, we will describe different types of multiferroic materials, with a strong focus on systems in which a spiral magnetic structure directly induces ferroelectric polarization. Two chapters in this work are dedicated to materials belonging to this group, namely $TbMnO_3$ and $MnWO_4$. A more detailed distribution of multiferroic materials of all types can be found in References [33] and [6, p. 288ff].

2.2.1. Classification of multiferroics

The multiferroic materials can generally be classified into two groups, following the approach by Khomskii [34][a]. The first group, called *type-I* multiferroics, contains materials in which magnetism and ferroelectricity have a distinct origin. $BiFeO_3$ is a famous example of this group, with a multiferroic phase at room temperature. In this case, the two ordering types can be attributed to different ions, yielding a weak ME interaction [36].
The second group, *type-II* multiferroics, covers materials in which one type of ordering directly induces the other, leading to an intrinsically strong ME coupling. $TbMnO_3$ was the first type-II material to be found in 2003 in the group of Kimura [5]. Magnetic and electric order are coexistent *and* their origins are coupled. The magnetically ordered state induces an electric polarization and thus causes ferroelectricity.
These multiferroics of spin origin are known to exhibit strong magnetoelectric effects. This renders this class of materials interesting to study for the reason of both fundamental physics and technical applications in spin-related electronics [37]. There exist many comprehensive reviews about the spin-induced ferroelectrics, among them References [14] and [38].
Common for all multiferroics of spin origin is the fact that the magnetic structure breaks the inversion symmetry, which is a necessary condition for the development of a spontaneous ferroelectric polarization. The major underlying microscopic mechanism for this effect, which were study up to today, can be classified belonging to one of three models: (a) exchange striction model, (b) inverse Dzyaloshinskii-Moriya (DM) model and (c) spin-dependent p-d hybridization model [14]. We will shortly present the main idea of the models (a) and (c) and focus in the next section on the inverse DM model (b).
The ferroelectricity in model (a) can be attributed to the symmetric spin exchange interaction $\hat{J}_{ij}$ between neighboring spins, $\vec{S}_i$ and $\vec{S}_j$, and is of the form

$$\text{(a) } \vec{P}_{ij} \propto \hat{J}_{ij}(\vec{S}_i \cdot \vec{S}_j) \ . \tag{2.4}$$

The interaction can induce striction along a specific crystallographic direction, yielding a net ferroelectric displacement of ions. A famous example is the commensurate spin chain $\uparrow\uparrow\downarrow\downarrow$ along an alternating lattice with A and B-sites. This structure breaks the inversion symmetry. A modulation of the strength of antiferromagnetic (AFM) and ferromagnetic (FM) exchange leads to a variation of bond-lengths, inducting oriented electric dipoles [6, p. 297]. This can occur in systems with magnetic chains of alternating valences, which is the case for Ca_3CoMnO_6 [39].

[a] Artificial multi-layer compounds are excluded from this consideration. The interested reader is referred to a dedicated review article such as Ref. [35].

There are also single-valence systems, where the FM and AFM interactions are modulated by the bond-angle of the superexchange. An example is the E-type magnetic phase of the $R\mathrm{MnO}_3$ series, where R stands for a rare-earth ion [40]. The exchange-striction model is independent of the spin-orbit coupling (SOC) and consequently exceeds in most systems the magnitude of the other models.
The spin-dependent p-d hybridization model is based on the SOC, similar to the inverse DM model. The connecting vector $\vec{r}_{ik}$ between a spin at site i and its ligand at site k can be modulated by the spin-dependent hybridization [41, 42]. The resulting polarization points along the direction of the bond and is of the form:

$$\text{(c) } \vec{P}_{ik} \propto (\vec{S}_i \cdot \vec{r}_{ik})^2 \vec{r}_{ik} \ . \tag{2.5}$$

2.2.2. Ferroelectricity in spiral magnets

The inverse DM model (b) explains the appearance of spin-induced electric polarization in systems of spiral order. According to Khomskii, most type-II multiferroic materials known by date show this effect [6, p. 293]. A spiral spin order is formed in frustrated magnets, materials in which the magnetic ground state is highly degenerated and thus has a complex magnetic structure. The degeneracy can be due to competing FM and AFM exchange interaction or geometrical properties that forbid simultaneous minimization of the interaction or anisotropy energies. The competition of interactions leads to the development of a complex long-range ordering of magnetic spins, which can be commensurate or incommensurate relative to the crystallographic unit cell.
The induced ferroic displacement in spin-spirals can be related to the relativistic spin-orbit coupling, and is of the form:

$$\text{(b) } \vec{P}_{ij} \propto \vec{r}_{ij} \times (\vec{S}_i \times \vec{S}_j) \ . \tag{2.6}$$

Microscopically this effect was explained in terms of the spin-current [15], which implies a purely electronic displacement, and in terms of the inverse DM interaction [16], yielding a displacement of ions. This expression was also derived phenomenological from the thermodynamic potential of spiral magnets by Mostovoy [43]. The DM interaction (also referred to as antisymmetric or anisotropic exchange) results from a relativistic correction of the superexchange interaction and is of the form $\vec{D}_{ij}(\vec{S}_i \times \vec{S}_j)$ [23, 44]. The situation is sketched in Figure 2.2. Two spins $\vec{S}$ at sites i and i interact via an oxygen ion. When the bridging ion is displaced from the equilibrium position, the system can reduce its energy by a canting of spins. If the neighboring spins are already canted, which is generally

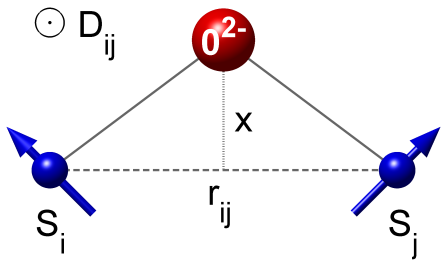

Figure 2.2: Sketch of antisymmetric superexchange between two spins $\vec{S}_i$ and $\vec{S}_j$ with connecting vector $\vec{r}_{ij}$ via a bridging oxygen ion. The Dzyaloshinskii-Moriya-vector follows the condition $\vec{D}_{ij} = \vec{r}_{ij} \times \vec{x}$.

the case for spin-spirals, then the inverse effect can arise, namely a displacement of oxygen ions away from the equilibrium position [16].
The development of a net ferroelectric polarization strongly depends on the form of the spin spiral. While in a helical spiral, where the spins rotate in a plane perpendicular to the propagation vector, the displacements macroscopically cancel out to zero, in a cycloid spiral, with spins rotating in a plane parallel to the propagation direction, the displacements occur along the same direction resulting in a net electric polarization [34].
Prominent examples which belong to this subgroup of type-II multiferroics, are $TbMnO_3$ [5], $Ni_2V_3O_8$ [45] and $MnWO_4$ [17, 46, 47]. In all these compounds, the development of a spin-spiral of cycloid type coincides directly with the onset of a ferroelectric polarization. The close coupling leads to colossal magnetoelectric effects, e.g. it was shown that the electric polarization can be suppressed or flopped by applied magnetic fields. For example in $TbMnO_3$, the induced ferroelectric polarization flops from P_c to P_a in magnetic fields parallel to $\vec{a}$ and $\vec{b}$ [8]. The flop coincides with a flop of the spin spiral [48]. Polarized neutron analysis turned out to be a valuable tool to prove the coupling of spin-spiral and polarization. For example it could be demonstrated, that an applied electric field can align and flip the spiral domains [49, 50] and the hysteresis and switching behaviour of the spin-spiral could be investigated [51, 52].
It was mentioned before, that the induced ferroelectricity in this type of multiferroics is based on the spin-orbit coupling. It can be written as $H_{SO} = \lambda \vec{L} \cdot \vec{S}$ in the LS scheme, which applies for most transition-metal oxides [53, p. 35], with $\vec{L}$ being the orbital momentum. The spin-orbit constant is proportional to the atomic number[b]. In transition-metals with $3d$ electrons, SOC is generally weak and enters the Hamiltonian of the systems only as perturbation. Nevertheless, it can play a significant role in frustrated system leading to the fascinating multiferroic phases, as discussed above.

[b] For hydrogen-like atoms $\lambda \propto Z^4$ is valid. The dependency is more complex for solids and is closer to $\lambda \propto Z^2$ [53, p. 35].

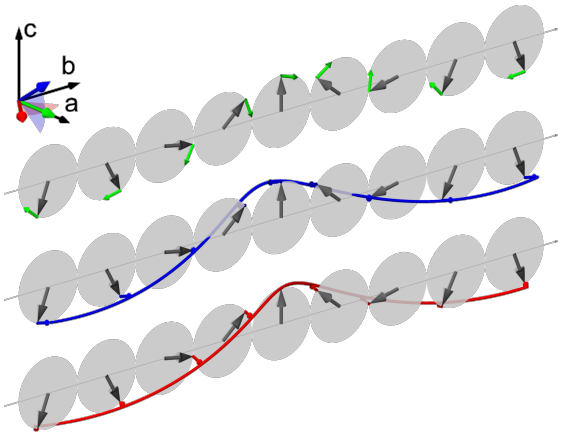

Figure 2.3: Sketch of zone center magnon modes of a cycloid spin spiral propagating along $\vec{b}$. The static spin structure is marked by gray, and the local fluctuations by colored arrows. The modes can be separated in a rotation around the normal vector of the cycloid $\vec{a}$ (top, phason mode), around the propagation direction $\vec{b}$ direction (middle, cycloid mode) and around $\vec{c}$, the vector in the cycloid plane perpendicular to $\vec{b}$ (bottom, helical mode). The axis vectors show the oscillation of the spin vector products $\vec{S}_i \times \vec{S}_j$.

2.2.3. Electromagnons: hybridized excitations

The close coupling of magnetic and electric properties in the spin-induced multiferroics also results in a new type of hybridized magnon-phonon modes, often referred to as electromagnons. Katsura *et al.* developed a theoretical model for the excitation spectrum in the case of a cycloid spin-spiral [54]. Following the interpretation by Senff *et al.* [12], Figure 2.3 sketches the different expected collective spin excitations at the zone center for a *bc* spin spiral propagating along $\vec{b}$. From top to bottom, we can distinguish three different excitations, corresponding to (i) a rotation of spins around the normal vector of the cycloid $\vec{a}$, the phason mode, (ii) a rotation around the propagation vector $\vec{b}$, of the cycloid, the cycloid mode, and (iii) along the vector $\vec{c}$, which is perpendicular to the normal vector and the propagation vector of the cycloid, the helical mode. The same expressions are used to distinguish the different modes as in Ref. [55].
Based on the DM mechanism, represented by Eq. 2.6, it is possible to attribute an electric character to the zone center modes. The direction of induced electric polarization is dependent on the cross product of neighboring spins, the vector chirality:

$$\vec{v}_{\text{chiral}} = \vec{S}_i \times \vec{S}_j \ . \tag{2.7}$$

The modulation of $\vec{v}_{\text{chiral}}$ for the three modes is presented in Fig. 2.3 by colored vectors in the coordinate system. While the phason mode has no influence on $\vec{v}_{\text{chiral}}$, the cycloid mode (middle) rotates $\vec{v}_{\text{chiral}}$ along $\vec{b}$ and the helical mode (bottom) rotates $\vec{v}_{\text{chiral}}$ around $\vec{c}$. From Equation 2.6, we can deduce that only the cycloid mode modulates the direction of the ferroelectric polarization, which results in an oscillation of $\vec{P}$ along $\vec{a}$. The magnetic cycloid mode should thus be excited

by an applied electric field. This mode is the Goldstone mode of the ferroelectric transition and should possess zero energy [54, 56].
The first experimental observations of electromagnon modes in a multiferroic material was reported by Pimenov *et al.* [57]. By using infrared (IR) spectroscopy they observed two modes in $TbMnO_3$, which were magnetically active and could be excited by an electric field. Later IR studies revealed two additional modes at higher energies in the same compound [58]. The lower mode could be identified by inelastic neutron scattering (INS) with polarization analysis to correspond to an out-of-plane excitation at the magnetic zone center [12]. The assumption, that this mode corresponds to the electromagnon of the DM mechanism could be manifested by successive IR [59, 60] and INS experiments [56, 61], showing that the electromagnon follows the orientation flop induced by magnetic fields. Another electromagnon of DM-origin has been observed in $Eu_{0.55}Y_{0.45}MnO_3$ [62].
The electromagnon with the strongest spectral weight, which is observed in $TbMnO_3$ at higher energies, has to arise from a different effect. Several experimental observations in applied field excluded an DM-origin for this mode [59, 63, 64, 65]. In multiferroic $R\mathrm{MnO}_3$, the strongest magnetoelectric mode is always found along $\vec{a}$, independently of the orientation of the cycloid plane. Valdés Aguilar *et al.* were able to explain this mode based on a modulation of the symmetric exchange [66]. The electric field induces a structural distortion, which is associated with the rotation of the $[MnO_6]$-octahedra around $\vec{c}$ in $R\mathrm{MnO}_3$. The distortion modulates the FM nearest-neighbor exchanges along $\vec{b}$, resulting in a rotation of spins. Instead of the DM-electromagnon, which is a zone center mode, the Heisenberg-electromagnon is at a finite momentum transfer $\vec{k} = 1 - \vec{k}_{inc}$ near the zone boundary [55]. The electromagnon based on Heisenberg exchange can be much stronger than the one of the DM mechanism [66].

Electromagnetic excitations have been observed in a series of spin-induced multiferroics (see Ref. [14] for a review) and were recently observed also in the absence of spin-driven ferroelectricity, e.g. in $CuFeO_2$ [67]. They enlarge the spectrum of fascinating effects correlated to the strong magnetoelectric coupling in this group of materials. Possible applications of this type of excitation, especially in the field of spintronics, are discussed for example in References [68] and [69]. It was also suggested to use the multiferroic Goldstone mode in order to deliver electricity without energy loss and to manipulate domain walls [70].

Chapter 3

Neutron scattering techniques

The principal experimental technique applied in this work was coherent neutron scattering on single crystals. There are several advantages of using neutron as projectile, in comparison to X-rays, rendering them most suitable for the study of magnetic structures and excitations. Their weak interaction with matter allows for complex experimental setups, the variation of scattering lengths enables the investigation of light elements and different isotopes, their de-Broglie wavelength can be modulated to be in the range of lattice parameters and most of all, their intrinsic magnetic moment can interact with unpaired electron spins in matter.
The experiments presented in this work were performed at the neutron reactor sources *Institut Laue-Langevin* (ILL) in Grenoble (France), *Laboratoire Léon Brillouin* (LLB) in Saclay (France) and *Forschungsreaktor München II* (FRM II) in Garching (Germany). Different instrumental techniques were applied including magnetic diffraction, inelastic magnetic scattering, neutron spin-echo spectroscopy and neutron polarimetry.
In this chapter, the principal formulas for elastic and inelastic scattering on the crystal and magnetic structure are presented, along with a brief description of the instrumental approaches applied in this work. The focus is on techniques using polarized neutrons, which allows to increase the information obtained from scattering experiments.
For a comprehensive documentation of experimental neutron scattering, the interested reader is referred to dedicated literature, e.g. by Wills and Carlile [71] or by Furrer *et al.* [72].

3.1. Principal neutron scattering formulas

The first observation of antiferromagnetism was achieved by neutron diffraction by Shull and Smart in 1949 [73], shortly after the discovery of the neutron by Chadwick in 1932 [74]. The idea of magnetic neutron scattering originated from Bloch, who pointed out, that the intrinsic magnetic moment of neutron and proton are similar [75]. The scattering technique was extended by Brockhouse and Steward in 1955 in order to also detect inelastic processes on crystal excitations [76]. In the 70 years since then, the flux at the neutron sources was increased and the experimental techniques were perfectionized. The theory of nuclear and magnetic neutron scattering is presented for example in References [77] or [78], from which the formula were taken.
The neutron is a subatomic particle of spin $S_\mathrm{n} = 1/2$ ($\mu_\mathrm{n} \approx -1.91\ \mu_\mathrm{N}$, with μ_N being the nuclear magneton), with an average vanishing electronic charge and a rest mass of $m_\mathrm{n} \approx 1.67 \cdot 10^{-27}\,\mathrm{kg}$. The energy of propagating neutrons is given by $E = \frac{1}{2}mv^2$. It is common to give different equivalent dimensions to describe the energy of neutrons: Energy in meV, Temperature $T = E/k_\mathrm{B}$ in K, wavelength $\lambda = h/mv$ in Å and wave vector $k = 2\pi/\lambda$ in $\mathrm{Å}^{-1}$. Neutrons with wavelengths in the order of lattice parameters of crystals correspond to a temperature of about 300 K and are denoted as thermal neutrons. A conversion table for several neutron energies is given in Appendix A.
Neutrons are scattered by the nuclei and by the unpaired electrons in the material. The result is a superposition of nuclear and magnetic contributions, and both have to be taken into account in order to understand the observed data.
The ratio of total scattered neutrons per time I_s and incident neutron flux I_tot is denoted as cross section $\sigma_\mathrm{tot} = I_\mathrm{s}/I_\mathrm{tot}$. In an experiment, only a part is covered by the detector, given by the double differential cross-section $d^2\sigma/d\omega dE$, within a given solid angle $d\Omega$ and an energy interval E to $E + dE$. In a scattering process, we differ between initial state i and final state f. When the state of the scattering system changes from $\lambda_i \to \lambda_f$ and the neutron wave vector and spin state change from $(\vec{k}_i, \sigma_i) \to (\vec{k}_f, \sigma_f)$, the differential cross section is given by Fermi's golden rule:

$$\left(\frac{d^2\sigma}{d\Omega dE}\right)_{\vec{k}_i \to \vec{k}_f}$$

$$= \frac{1}{N}\frac{k_f}{k_i}\left(\frac{m}{2\pi\hbar^2}\right)^2 \sum_{\lambda_i\sigma_i} p_{\lambda_i} p_{\sigma_i} \sum_{\lambda_f\sigma_f} \left|\langle \vec{k}_f \sigma_f \lambda_f | V | \vec{k}_i \sigma_i \lambda_0 \rangle\right|^2 \delta(E + E_{\lambda_i} - E_{\lambda_f})\ . \quad (3.1)$$

In the equation, p_j is the probability to find neutron or the system in the initial state and V is the interaction potential. This is the master formula for neutron scattering and it is valid even without the knowledge of the exact interaction between sample and neutron [78]. It is the basis for all neutron scattering experiments.

3.1.1. Nuclear scattering

Neutrons interact with the nucleus via the strong-force interaction. The efficiency of neutron scattering by a single nucleus is expressed by its scattering length b: $b^2 = \sigma_{\text{tot}}/4\pi$. The strength of the nucleus-neutron interaction depends on the details of the nuclear structure, which cannot be related to the atomic number in a simple way. The value of b can vary greatly between elements of similar atomic number and even between isotopes of the same element.
The wavelength of thermal neutrons is of orders of magnitude higher than the dimension of the nucleus, and the interaction potential of a system of N atoms at positions $\vec{R}_l$ can be approximated by a delta function:

$$V_{nuc}(\vec{r}) = \frac{2\pi\hbar^2}{m} \sum_l b\delta(\vec{r} - \vec{R}_l) \ . \tag{3.2}$$

The proportionality factor b is called neutron scattering length and varies for different elements and isotopes. In a material which is a composition of isotopes, this gives rise to coherent scattering and incoherent scattering. The coherent part shows interference effects and enables to deduce informations about the nuclear structure. The non-interfering incoherent part arises from deviations fo the scattering length relative to the mean value. In the following, we will focus only on coherent scattering.
By inserting V_{nuc} in Equation 3.1, the differential cross section for elastic coherent nuclear scattering can be derived:

$$\left(\frac{d\sigma}{d\Omega}\right)_{\text{N,coh}} = \frac{8\pi^3}{v_0} \sum_{\vec{\tau}} |F_{\text{N}}(\vec{Q})|^2 \cdot \delta(\vec{Q} - \vec{\tau}) \ , \tag{3.3}$$

with the scattering vector $\vec{Q} = \vec{k}_f - \vec{k}_i$ and the volume of the unit cell v_0. The positions of atoms in a periodic crystal can be expressed as:

$$\vec{R}_i(t) = \vec{R}_l + \vec{r}_j + \vec{u}_i(t) \ . \tag{3.4}$$

The vector $\vec{R}_l$ denotes the coordinate of the unit cell, $\vec{r}_j$ is the equilibrium position of the atom in the unit cell and $\vec{u}_i(t)$ is the displacement from the equilibrium

position due to thermal motion. The *nuclear structure factor* is given by:

$$F_{\mathrm{N}}(\vec{Q}) = \sum_j b_j \mathrm{e}^{\mathrm{i}\vec{Q}\cdot\vec{r}_j} \mathrm{e}^{-W_d(\vec{Q})} \ . \tag{3.5}$$

The term $\mathrm{e}^{-W_d(\vec{Q})}$ is the Debye-Waller factor, which takes into account the effect of thermal motion of atoms on the interference pattern. The coherent nuclear Bragg scattering can thus be derived from the calculation of the nuclear structure, which takes into account the lattice symmetry, the position of atoms in the unit cell and the different scattering length.

Instrumentation

With the help of Equation 3.3, it is possible to compare experimental observed intensities at nuclear Bragg positions with calculations of $F_{\mathrm{N}}(\vec{Q})$ for a given structure. Such experiments are generally performed on powder diffractometers or, when investigating single crystals, on four-circle diffractometers such as the D10 at the ILL [79, p. 38f]. The correct integration of intensity, which is broadened in $\vec{Q}$-space due to a Q-dependent instrument resolution and a finite mosaicity of the crystal is a crucial part of the experiment. In addition, extinction effects and absorption can temper the observed intensities and have to be taken into account [80].
The analysis of nuclear scattering intensities determined on D10 has been done using the program *FullProf* [81]. In addition, a program for *MATLAB* [82] was written to calculate $F_{\mathbf{N}}(\vec{Q})$ for the materials investigated in this work.

3.1.2. Magnetic scattering

Magnetic neutron scattering arises from the dipole-dipole interaction between the magnetic moment of neutron and unpaired electrons in matter. The interaction potential of a neutron in spin state $\vec{\sigma}_{\mathrm{N}}$ and propagating electron with momentum $\vec{p}$ and spin $\vec{s}$ can be written as follows:

$$V_{\mathrm{mag}}(\vec{r}) = -\gamma\mu_N 2\mu_B \vec{\sigma}_N \cdot \left[\nabla \times \left(\frac{\vec{s}\times\vec{R}}{R^3}\right) + \frac{\vec{p}\times\vec{R}}{\hbar R^3}\right] \ . \tag{3.6}$$

The gyromagnetic ratio $\gamma = 1.9132$ and the nuclear and Bohr magneton, μ_N and μ_B, enter the equation. The two terms of V_mag in brackets are due to the intrinsic electron spin and the orbital motion of the electron, respectively. V_mag is, in contrast to V_{nuc}, anisotropic due to the axial symmetry of the dipole field. By integrating V_mag in the master equation, Eq. 3.1, the elastic and purely magnetic cross-section for an unpolarized neutron beam can be written as follows:

$$\left(\frac{d\sigma}{d\Omega}\right)_\mathrm{M,coh} = \frac{1}{N_m}\frac{8\pi^3}{v_0}\sum_{\vec{\tau}_\mathrm{M}} |\vec{F}_{\mathrm{M}\perp}(\vec{\tau}_\mathrm{M})|^2 \cdot \delta(\vec{Q} - \vec{\tau}_\mathrm{M}) \ , \tag{3.7}$$

with N_m being the number of magnetic ions and $\vec{\tau}_\mathrm{M} = \vec{\tau} \pm \vec{k}$ being the reciprocal vector of the magnetic structure. $\vec{k}$ is the propagation vector of the magnetic structure and denotes its periodicity relative to the crystal structure. Finally, the magnetic interacting vector $\vec{F}_{\mathrm{M}\perp}$ is connected to the magnetic structure factor $\vec{F}_\mathrm{M}$ as $\vec{F}_{\mathrm{M}\perp} = \hat{\vec{Q}} \times \vec{F}_\mathrm{M} \times \hat{\vec{Q}}$. Only scattering from electron spins perpendicular to $\vec{Q}$ contribute to the magnetic cross section. The *magnetic structure factor* is given by:

$$\vec{F}_\mathrm{M}(\vec{Q}) = \sum_j f_j^\mathrm{M}(Q)\vec{m}_j \mathrm{e}^{\mathrm{i}\vec{Q}\cdot\vec{r}_j}\mathrm{e}^{-W_d(\vec{Q})} \ . \tag{3.8}$$

f_j^M is the magnetic form factor which describes, similarly to the atom form factor, the distribution of magnetic moments in an atom. This leads to a decrease of magnetic intensity at larger Q, whereas the nuclear scattering length is independent of Q. Furthermore, the magnetic cross section is strongly dependent on the direction of the magnetic moments relative to $\vec{Q}$, as only the components of the magnetization perpendicular to the scattering vector account for the magnetic cross section.
When the magnetic unit cell has the same size as the lattice unite cell, magnetic reflections are at the same position as the nuclear reflections. In this case, the coherence between neutrons scattered by the nucleus and the magnetic moment is of importance. Only in case of scattering from an unpolarized neutrons beam, where the direction of neutron spins is distributed randomly, interference terms cancel out and the absolute intensities of nuclear and magnetic scattering simply sum up to the total intensity:

$$I \propto |F_\mathrm{total}|^2 = |F_\mathrm{N}|^2 + |F_{\mathrm{M}\perp}|^2 \ . \tag{3.9}$$

Instrumentation

Elastic magnetic scattering can be investigated at powder diffractometers and four-circle diffractometers, similar to nuclear Bragg scattering. The data analysis is done by comparing experimental intensities with calculated intensities. In this work, the program *FullProf* has been used to analyze nuclear and magnetic Bragg scattering [81]. In addition, a code for *MATLAB* was written in order to calculate nuclear and magnetic structure factors for the materials investigated in this work.

3.1.3. Inelastic neutron scattering

Until now, only elastic scattering processes were considered, in which no energy is transfered, i.e. $|\vec{k}_i| = |\vec{k}_f|$. In inelastic scattering processes, two transfers can be associated: moment transfer $\vec{Q} = \vec{k}_f - \vec{k}_i = \vec{q} + \vec{\tau}$ and energy transfer $\hbar\omega = E_i - E_f = \frac{\hbar^2}{2m_n}(k_f^2 - k_i^2)$, which occur for both nuclear and magnetic scattering. In this section, only the cross section for inelastic magnetic scattering we be derived. The starting point is again the master equation for neutron scattering, Eq. 3.1. This time, we allow also an energy transfer during the scattering process. The double magnetic cross section for unpolarized neutrons and spin-only scattering can be obtained as:

$$\left(\frac{d^2\sigma}{d\Omega dE}\right)_{M,coh} = (\gamma r_0)^2 \frac{k_f}{k_i} f^2(\vec{Q}) \cdot \mathrm{e}^{-W_d(\vec{Q})} \sum_{\alpha,\beta} \left(\delta_{\alpha,\beta} - \frac{Q_\alpha Q_\beta}{Q^2}\right) S^{\alpha,\beta}(\vec{Q},\omega) \ , \tag{3.10}$$

where α, β denote positions (x, y, z) and r_0 is the classic radius of the electron. The magnetic form factor and the Debye-Waller factor were already discussed. The term $\delta_{\alpha,\beta} - \frac{Q_\alpha Q_\beta}{Q^2}$ is the polarization factor, which determines that neutrons can only couple to a magnetization perpendicular to $\vec{Q}$. The *magnetic scattering function* $S^{\alpha,\beta}$ is given as:

$$S^{\alpha,\beta}(\vec{Q},\omega) = \frac{1}{2\pi\hbar} \sum_{j,j'} \int_{\infty}^{\infty} \mathrm{e}^{i\vec{Q}\cdot(\vec{R}_j - \vec{R}_{j'})} \langle \hat{S}_j^\alpha(0) \hat{S}_{j'}^\beta(t) \rangle \mathrm{e}^{-i\omega t} dt, \tag{3.11}$$

with $\hat{S}_j^\alpha$ being the spin operator of the jth ion at site $\vec{R}_j$. This result for $S^{\alpha,\beta}(\vec{Q},\omega)$ is an approximation, which is valid for modest values of $\vec{Q}$ [72, p. 18]. The term $\langle \hat{S}_j^\alpha(0) \hat{S}_{j'}^\beta(t) \rangle$ is the spin-spin pair correlation function, stating the thermal average of the time-dependent spin operators.

Instrumentation

Inelastic neutron scattering can be measured using a triple-axis spectrometer (TAS). The name originates from the rotation axes of monochromator, sample and analyzer. By a nuclear Bragg reflection at the monochromator, a specific neutron wave vector $\vec{k}_i$ is defined. The neutrons are scattered at the single crystalline sample, which can be rotated within a defined scattering plane. Finally, the energy of the scattered neutrons is analyzed by another nuclear Bragg reflection at the analyzer. The functionality is described in detail by Shirane *et al.* in Ref. [83].
This technique allows to individually select positions in $(\vec{Q}, \omega)$-space and investigate elastic and inelastic scattering processes. Using a large monochromator and analyzer crystals, horizontal and vertical focusing, as well as curved neutron guides, it is possible to increase the neutron flux at the sample, enabling the detection of even small inelastic signals. Furthermore, the setup allows the investigation under extreme sample conditions, such as high magnetic field and high pressure, and can be equipped to allow for polarization analysis. The different polarization techniques will be described in Section 3.2. Another interesting option is the use of multi-analyzer systems, such as *FlatCone* at the ILL [84], which covers a large solid angle. This allows for the simultaneous investigation of multiple positions in $(\vec{Q}, \omega)$-space.
The majority of experiments presented in this work were obtained at TAS instruments. A complete list is given in the appendix. The analysis of TAS data was carried out using *MATLAB*, in combination with a library of programs developed by P. Steffens [85].
Another technique used to measure inelastic neutron scattering, is time-of-flight (TOF) spectroscopy. In direct mode, the incident neutron wavelength λ_i is selected by a velocity selector. A disc-chopper separates the monochromatic beam in short pulses, which arrive separately at the sample stage, after a delay of Δt. The scattered neutrons are position- and energy-dependent analyzed in a detector bank, which covers a large horizontal and vertical solid angle. The position detection is achieved by position-sensitive detectors, while the energy is determined by the varying flight time of neutrons of varying energy. Within this work, an experiment has been performed at the IN5 spectrometer at the ILL [86]. The data analysis was done using the *Horace* suite for *MATLAB* [87].

Simulation of inelastic magnetic scattering

The dispersion of magnetic excitations obtained at INS experiments can be compared to calculations which allow for the determination of magnetic exchange interaction and anisotropy parameters. A commonly applied model is the *linear*

spin wave theory, developed by Bloch and Slater [88,89]. It treats the excitations as perturbations of the static structure and was initially applied to collinear magnetic structures [90].
Recently, Toth and Lake extended the linear spin wave theory for incommensurate structures [91]. Their approach is based on work by Haraldsen and Fishman [92] and Petit [93]. Common in all models is a generalized technique for determining the static and dynamic properties of magnetic structures with canted spins. A local coordinate transformation is introduced for every magnetic atom in the unit cell. By doing so, the ground state is transformed into a state with collinear spins, in which the spin wave spectrum can be calculated [93]. Toth and Lake extended this model to incommensurate structures by adding an additional rotation which takes into account the incommensurability [91].
The algorithm developed by Toth and Lake is implemented in an open source toolbox for *MATLAB*, called *SpinW* [94]. The formalism uses the following Hamiltonian:

$$H = \sum_{mi,nj} \vec{S}_{mi} \hat{J}_{mi,nj} \vec{S}_{nj} + \sum_{mi} \vec{S}_{mi} \hat{A}_{mi} \vec{S}_{mi} + \vec{B} \sum_{mi} \vec{g}_i \vec{S}_{mi} \ . \tag{3.12}$$

The crystallographic unit cell is indexed by $m, n \in [1, .., L]$ and the magnetic atoms are indexed by $i, j \in [1, .., N]$. Furthermore, $\vec{S}_{mi}$ are spin vector operators, $\hat{J}_{mi,mj}$ are 3×3 matrices describing the pair coupling between spins, $\hat{A}_{mi,mi}$ are diagonal 3×3 anisotropy matrices, $\vec{B}$ is an external magnetic field and $\vec{g}_i$ is the g-tensor. This matrix formalism can be used to describe isotropic exchange (diagonal matrix), Dzyaloshinskii-Moriya exchange (antisymmetric matrix) and different anisotropy terms. The single-ion anisotropy can be expressed as easy-axis or easy-plane with any arbitrary orientation.
In order to solve the Hamiltonian by linear spin wave theory, one has to assume that the fluctuations only weakly reduce the expectation value of the spin operators. This is in general the case at low temperatures and with systems with an ordered spin of $S \geq 3/2$ [91]. The spins are expanded in terms of bosonic creation and annihilation operators, using the Holstein-Primakoff approximation [95]. These operators are then expressed in a rotating frame, taking into account the specific magnetic structure. The reformulated Hamiltonian has to be diagonalized, in order to find the eigenstates and eigenvalues, which is done by the formalism proposed by Colpa [96]. Finally, it is possible to calculate the dynamic correlation function $S(\vec{Q}, \omega)$, cf. 3.11. The differential neutron cross section can be derived from $S(\vec{Q}, \omega)$ which enables to directly compare the calculation with inelastic neutron data.
An exemplary calculation will be presented in the following. We start with the *Pbnm* crystal structure of $LaMnO_3$. We assume only a contribution of the Mn moment, which carries a spin of $S = 4/2$. There are four Mn ions in the crys-

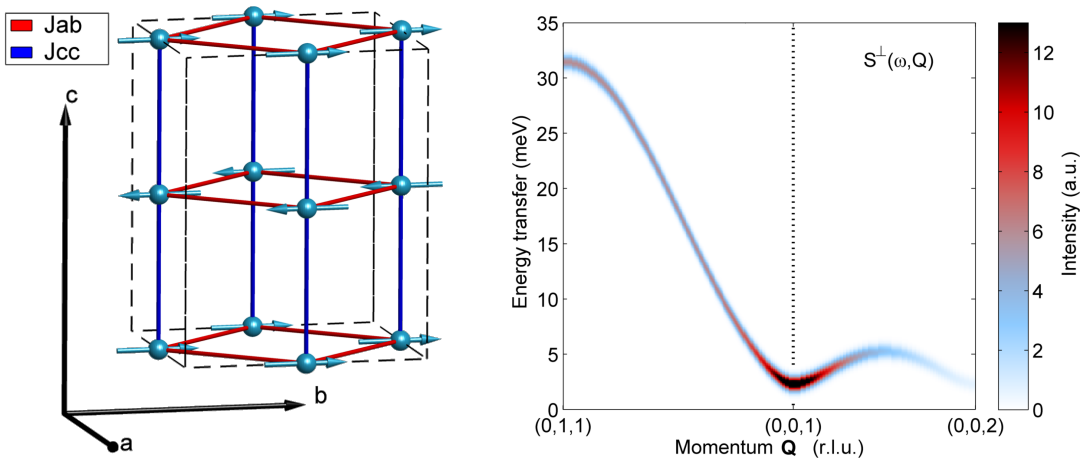

Figure 3.1.: Linear spin wave calculation with *SpinW* [94]. (a) Sketch of a the A-type antiferromagnetic structure with $\vec{k} = (0,\ 0,\ 0)$ and moments along $\vec{b}$. The exchange constants are ferromagnetic in the *ab*-plane, $J_{ab} = -0.4\,\text{meV}$ and antiferromagnetic along $\vec{c}$, $J_c = 0.8\,\text{meV}$. (b) Calculated magnon dispersion between the Bragg positions $\vec{Q}_1 = (0,\ 1,\ 1)$, $\vec{Q}_2 = (0,\ 0,\ 1)$ and $\vec{Q}_3 = (0,\ 0,\ 2)$.

tallographic unit cell, occupying the 4*b* Wyckoff site at $(0, 0, 1/2)$. The model of the magnetic structure is shown in Figure 3.1(a). The moments are aligned in an A-type antiferromagnetic structure with ferromagnetic *ab*-planes which are antiferromagnetically coupled along $\vec{c}$. The propagation vector of this structure is $\vec{k} = (0,\ 0,\ 0)$ [97]. The moments are chosen to be oriented along $\vec{b}$, and two exchange interactions are assumed, which are compatible with the magnetic ground state: a ferromagnetic interaction in the *ab*-plane, $J_{ab} = -1.68\,\text{meV}$ and an antiferromagnetic interaction along $\vec{c}$, $J_c = 1.22\,\text{meV}$. The easy-axis anisotropy is $SIA_b = 0.15\,\text{meV}$. These values were determined by Moussa *et al.* by INS data [97][a].
The calculated magnon dispersion using the *SpinW* model between the Bragg positions $\vec{Q}_1 = (0,\ 1,\ 1)$, $\vec{Q}_2 = (0,\ 0,\ 1)$ and $\vec{Q}_3 = (0,\ 0,\ 2)$ is shown in Figure 3.1(b). The result corresponds perfectly to the model from Moussa *et al.* [97].

[a]The interaction parameters in the *SpinW* model are increased by a factor of two, relative to the values by Moussa *et al.* due to a different formalism.

3.2. Neutron polarimetry

Neutron polarimetry, or neutron polarization analysis, denotes in general the investigation of cross sections in dependence of incident and final neutron polarization. In the previous section, two circumstances were mentioned in which the polarization of neutrons is crucial: (i) the interaction of the neutron spin with the magnetic moment of the nucleus and (ii) the polarization factor which limits the magnetic scattering to components parallel to the scattering vector $\vec{Q}$. The use of a polarized neutron beam, i.e. a well defined quantization axis of the intrinsic spin of the neutron, enables one to observe additional information about the scattering system.
In the first part of this section, we will present the basic formula and concepts which are important to follow the data analysis. More comprehensive descriptions can be found for example in References [98] and [77]. In the second part, different experimental techniques will be presented which are based on polarized neutrons and, which have been used throughout this work.

3.2.1. Basic formulas

In a neutron scattering experiment with analysis of the polarization of neutrons, one has to define a quantization axis of the incident neutron beam. The polarization of the incident beam along this direction is defined by:

$$P_i = \frac{N_{+i} - N_{-i}}{N_{+i} + N_{-i}} = \frac{FR_i - 1}{FR_i + 1} \ , \tag{3.13}$$

with $N_{\pm i}$ being the neutron intensities parallel and antiparallel relative to the quantization axis i. The value of P_i ranges from 0, for an unpolarized beam, to ± 1, for a fully polarized beam. The value $FR_i = N_{+i}/N_{-i}$ is called the flipping ratio. Experimentally, this is an important value, as it describes the quality of beam polarization. Common values for FR on nowadays instruments range between 15 and 35, corresponding to a beam polarization of 88 to 94 %.
The first experimental implementation of neutron polarization analysis was achieved by Moon, Riste and Koehler on a TAS instrument [99]. By looking at the master equation for neutron scattering, Eq. 3.1, one can derive the behaviour of nuclear and magnetic scattering processes along given quantization axis. For this, we look at the correlation function, which can be expressed as $\langle \vec{S}_f | V | \vec{S}_i \rangle$. We define the spin states $\vec{S}$ as $|\uparrow\rangle = (1, 0)$ and $|\downarrow\rangle = (0, 1)$. For nuclear scattering on a single nucleus, the interacting potential can be reduced to $V_{\mathrm{nuc}} = b$, with b being the

scattering length. We can deduce the following scattering processes:

$$\begin{aligned}\langle \vec{S}_f | V_{nuc} | \vec{S}_i \rangle = b \langle \vec{S}_f \vec{S}_i \rangle &= b \text{ , for } |\uparrow\rangle \rightarrow |\uparrow\rangle \text{ and } |\downarrow\rangle \rightarrow |\downarrow\rangle \\ &= 0 \text{ , for } |\uparrow\rangle \rightarrow |\downarrow\rangle \text{ and } |\downarrow\rangle \rightarrow |\uparrow\rangle \text{ .}\end{aligned} \tag{3.14}$$

We can differentiate two scattering processes: *non-spin-flip* $|\uparrow\rangle \rightarrow |\uparrow\rangle$ and $|\downarrow\rangle \rightarrow |\downarrow\rangle$, and *spin-flip* $|\uparrow\rangle \rightarrow |\downarrow\rangle$ and $|\downarrow\rangle \rightarrow |\uparrow\rangle$. According to Equation 3.14, purely nuclear scattering does not affect the polarization direction of the neutron spin and thus it occurs only in non-spin-flip processes.
The potential of the dipole-dipole interaction between neutron and electron spin is more complex. The exact expression, given in Eq. 3.6, can be simplified to $V_{\text{mag}} \propto \hat{\sigma}_k \vec{F}_{\text{M}\perp}$, with the Pauli spin matrices $\hat{\sigma}$, the index $k = x, y, z$ and the magnetic interaction vector $\vec{F}_{\text{M}\perp} = (M_x, M_y, M_z)$. The scattering processes for magnetic scattering at a given propagation vector and a quantization axis of the neutrons along z are:

$$\begin{aligned}\langle \vec{S}_f | V_{mag} | \vec{S}_i \rangle &= M_z && \text{, for } |\uparrow\rangle \rightarrow |\uparrow\rangle \\ &= -M_z && \text{, for } |\downarrow\rangle \rightarrow |\downarrow\rangle \\ &= M_x - iM_y && \text{, for } |\uparrow\rangle \rightarrow |\downarrow\rangle \\ &= M_x + iM_y && \text{, for } |\downarrow\rangle \rightarrow |\uparrow\rangle\end{aligned} \tag{3.15}$$

Two important rules can be derived from this simple consideration, which are valid for magnetic scattering in general:

(i) non-spin-flip processes are sensitive only to components of the magnetization parallel to the neutron spin,

(ii) spin-flip processes are sensitive only to components of the magnetization perpendicular to the neutron spin.

The use of polarized neutrons thus allows for the separation of magnetic scattering from nuclear scattering. In real systems, one has to look also at nuclear-spin dependent processes. These processes, together with Equations 3.14 and 3.15, are summarized in the Moon-Riste-Koehler equations [99]. They also allow for the separation of coherent and incoherent scattering processes.
The upper description is called longitudinal polarization analysis, as incident and final neutron polarization are along the same direction. The general case, when incident and final polarization direction can be arbitrarily chosen, is referred to as spherical polarization analysis. The corresponding theoretical ground work was reported independently by Blume and Maleev [100, 101]. A detailed derivation

was presented by Brown in Ref. [102]. It is common to define three orthogonal polarization directions:

→ x is parallel $\vec{Q}$,

→ z is vertical to the scattering plane,

→ y is perpendicular to x and z.

The advantage of this choice is the resulting form of the magnetic interacting vector: $\vec{F}_{\mathrm{M}\perp} = (0,\ M_y,\ Mz)$. As only magnetic scattering perpendicular to the scattering vector $\vec{Q}$ occurs, this coordination system allows the separation of magnetization along two orthogonal directions. The components of the 36 possible cross sections are given in Table 3.1. The different contributions to the cross sections σ_{ij}, with $i, j \in x, y, z, \bar{x}, \bar{y}, \bar{z}$ are listed. Often, one distinguishes only between spin-flip and non-spin-flip scattering, and the notations 'iSF' and 'iNSF' are used to describe the diagonal cross sections $\sigma_{-i,i}$ and $\sigma_{i,i}$, respectively.
The contributions to the polarization cross sections were separated into four parts in Table 3.1. Nuclear scattering NN^* is independent of the polarization direction of the neutron and it appears for non-spin-flip processes. The magnetic scattering can be separated along y and z with $\vec{M}_\perp \cdot \vec{M}^*_\perp = M_y M^*_y + M_z M^*_z$. In addition, there is a chiral magnetic term, which will be discussed below. The last column contains the terms that arise from nuclear and magnetic interaction. These are in particularly interesting to investigate antiferromagnetic domains [102]. For example, a reversal of a 180°-domain changes the sign of $\vec{M}_\perp$. This is not visible in the quadratic terms MM^* but can be measured for the interactions terms of the form NM, when nuclear and magnetic scattering appear at the same position in reciprocal space.
One of the magnetic terms that can be measured directly by neutron polarization analysis is the chiral magnetic term $-i(\vec{M}_\perp \times \vec{M}^*_\perp)_x$. This term can be determined for example by the subtraction of the cross sections $\sigma_{\bar{x}x}$ and $\sigma_{x\bar{x}}$. For a suitable scattering geometry, this term allows the observation of the vector chirality v_{chiral}, cf. Eq. 2.7. In the case of a monodomain spin-spiral, with non-zero v_{chiral}, the chiral magnetic term will produce a difference in both spin-flip cross sections along x. It was mentioned in Section 2.2.2 that such spiral structures are present in specific multiferroic materials and account for the ferroelectric polarization. The reversal of electric polarization P_{el} is accompanied by a reversal of the spiral, finally resulting in a sign-switch of v_{chiral}. Providing a suitable scattering geometry, neutron polarization analysis can detect the sign of v_{chiral} and thus directly link the states of P_{el} and v_{chiral}. This has been demonstrated for example by Yamasaki *et al.* in $TbMnO_3$ [49].

Table 3.1.: Scattering cross sections for spherical neutron polarization analysis. The coordinate system is chosen in a way that $x||\vec{Q}$, z vertical to the scattering plane and $y = z \times x$ [103].

	nuclear	magnetic	chiral magn.	nuclear magn.
xx =	NN^*			
x$\bar{\text{x}}$ =		$\vec{M}_\perp \cdot \vec{M}_\perp^*$	$-\text{i}(\vec{M}_\perp \times \vec{M}_\perp^*)_x$	
$\bar{\text{x}}$x =		$\vec{M}_\perp \cdot \vec{M}_\perp^*$	$+\text{i}(\vec{M}_\perp \times \vec{M}_\perp^*)_x$	
$\bar{\text{x}}\bar{\text{x}}$ =	NN^*			
yy =	NN^*	$+M_yM_y^*$		$+2\text{Re}(M_y^*N)$
y$\bar{\text{y}}$ =		$M_zM_z^*$		
$\bar{\text{y}}$y =		$M_zM_z^*$		
$\bar{\text{y}}\bar{\text{y}}$ =	NN^*	$+M_yM_y^*$		$-2\text{Re}(M_y^*N)$
zz =	NN^*	$+M_zM_z^*$		$+2\text{Re}(M_z^*N)$
z$\bar{\text{z}}$ =		$M_yM_y^*$		
$\bar{\text{z}}$z =		$M_yM_y^*$		
$\bar{\text{z}}\bar{\text{z}}$ =	NN^*	$+M_zM_z^*$		$-2\text{Re}(M_z^*N)$
2xy = 2y$\bar{\text{x}}$ =	NN^*	$+\vec{M}_\perp \cdot \vec{M}_\perp^*$	$-\text{i}(\vec{M}_\perp \times \vec{M}_\perp^*)_x$	$+2\text{Re}(M_y^*N)$ $+2\text{Im}(M_z^*N)$
2x$\bar{\text{y}}$ = 2$\bar{\text{y}}\bar{\text{x}}$ =	NN^*	$+\vec{M}_\perp \cdot \vec{M}_\perp^*$	$-\text{i}(\vec{M}_\perp \times \vec{M}_\perp^*)_x$	$-2\text{Re}(M_y^*N)$ $-2\text{Im}(M_z^*N)$
2$\bar{\text{x}}$y = 2yx =	NN^*	$+\vec{M}_\perp \cdot \vec{M}_\perp^*$	$+\text{i}(\vec{M}_\perp \times \vec{M}_\perp^*)_x$	$+2\text{Re}(M_y^*N)$ $-2\text{Im}(M_z^*N)$
2$\bar{\text{x}}\bar{\text{y}}$ = 2$\bar{\text{y}}$x =	NN^*	$+\vec{M}_\perp \cdot \vec{M}_\perp^*$	$+\text{i}(\vec{M}_\perp \times \vec{M}_\perp^*)_x$	$-2\text{Re}(M_y^*N)$ $+2\text{Im}(M_z^*N)$
2xz = 2z$\bar{\text{x}}$ =	NN^*	$+\vec{M}_\perp \cdot \vec{M}_\perp^*$	$-\text{i}(\vec{M}_\perp \times \vec{M}_\perp^*)_x$	$+2\text{Re}(M_z^*N)$ $-2\text{Im}(M_y^*N)$
2x$\bar{\text{z}}$ = 2$\bar{\text{z}}\bar{\text{x}}$ =	NN^*	$+\vec{M}_\perp \cdot \vec{M}_\perp^*$	$-\text{i}(\vec{M}_\perp \times \vec{M}_\perp^*)_x$	$-2\text{Re}(M_z^*N)$ $+2\text{Im}(M_y^*N)$
2$\bar{\text{x}}$z = 2zx =	NN^*	$+\vec{M}_\perp \cdot \vec{M}_\perp^*$	$+\text{i}(\vec{M}_\perp \times \vec{M}_\perp^*)_x$	$+2\text{Re}(M_z^*N)$ $+2\text{Im}(M_y^*N)$
2$\bar{\text{x}}\bar{\text{z}}$ = 2$\bar{\text{z}}$x =	NN^*	$+\vec{M}_\perp \cdot \vec{M}_\perp^*$	$+\text{i}(\vec{M}_\perp \times \vec{M}_\perp^*)_x$	$-2\text{Re}(M_z^*N)$ $-2\text{Im}(M_y^*N)$
2yz = 2zy =	NN^*	$+\vec{M}_\perp \cdot \vec{M}_\perp^*$ $+2\text{Re}(M_yM_z^*)$		$+2\text{Re}(M_y^*N)$ $+2\text{Im}(M_z^*N)$
2y$\bar{\text{z}}$ = 2$\bar{\text{z}}$y =	NN^*	$+\vec{M}_\perp \cdot \vec{M}_\perp^*$ $-2\text{Re}(M_yM_z^*)$		$+2\text{Re}(M_y^*N)$ $-2\text{Im}(M_z^*N)$
2$\bar{\text{y}}$z = 2z$\bar{\text{y}}$ =	NN^*	$+\vec{M}_\perp \cdot \vec{M}_\perp^*$ $-2\text{Re}(M_yM_z^*)$		$-2\text{Re}(M_y^*N)$ $+2\text{Im}(M_z^*N)$
2$\bar{\text{y}}\bar{\text{z}}$ = 2$\bar{\text{z}}\bar{\text{y}}$ =	NN^*	$+\vec{M}_\perp \cdot \vec{M}_\perp^*$ $+2\text{Re}(M_yM_z^*)$		$-2\text{Re}(M_y^*N)$ $-2\text{Im}(M_z^*N)$

3.2.2. Experimental techniques

Since the first experiments with polarized neutrons in the 1960's [99], several different instrumental techniques were developed which make use of the unique nature of the neutron. The difficultly of such instruments is the creation of a strongly polarized beam. The strict component separation, as shown in Table 3.1 is only valid for a fully polarized neutron beam. Experimentally, this cannot be achieved due to the limited efficiency of neutron polarizers, polarized guides and spin flippers. This imperfection always results in the superposition of spin-flip and non-spin-flip channels, which is moderated by the instrument- and experiment-specific flipping ratio, cf. Eq. 3.13. As an example, the experimentally observed spin-flip cross section along x will be composed as $\sigma_{\bar{x}x,\mathrm{edxp}} = (1-\frac{1}{FR_x})\sigma_{\bar{x}x} + \frac{1}{FR_x}\cdot\sigma_{xx,\mathrm{exp}}$. The success of a neutron polarimetry experiment thus crucially depends on an optimal setup. A clear overview of the technological progress in neutron polarization is presented in Reference [71].
A large part of the experimental studies presented in this work was performed on instruments using polarized neutrons. The different approaches will be briefly discussed in order to facilitate the understanding of the data analysis.

Longitudinal polarization analysis

This technique allows for the determination of the diagonal polarization cross sections. The initial and final polarization of the neutrons are collinear. Experimentally, this is achieved by a set of three Helmholtz coils, which are oriented around the sample position [104]. The neutron polarization at the polarizer and analyzer is in general along the vertical direction. By a correct tuning of the coils, the direction of the (small) magnetic field at the sample stage can be set along the polarization axes x, y and z. The quantization axis of the propagating neutron spin adiabatically follows the direction of the magnetic field. The Helmholtz setup was used in this work in combination with the TAS instruments IN14 at the ILL and 4F1 at the LLB.
Furthermore, this technique is initially integrated in the multi-detector spectrometer D7 at the ILL [105]. At this instrument, only the polarization of the scattered neutrons is analyzed and thus all energies k_f are integrated in the scattered intensity. The polarization geometry slightly differs from a TAS instrument: The Helmholtz coils, which define the polarization axes x, y and z are fixed and do not depend on $\vec{Q}$. The angle between x and the incident neutron beam is called *Schärpf-angle* [106]. By the application of the x, y, z-polarization, it is possible to separate incoherent and coherent nuclear scattering as well as in-plane and out-of-plane magnetic scattering [105].

Spherical polarization analysis

The experimental determination of all polarization cross sections shown in Table 3.1 requires the independent control of initial and final neutron polarization. This was achieved for the first time at the ILL by the development of the *Cryopad* [107,108]. We will briefly describe the functionality of the third-generation device, which is presented in detail in Reference [109]. The incident and final neutron guide fields are separated by a zero-field sample chamber. The neutron polarization is defined outside of the chamber, enters it by conservation of its polarization state and finally, the polarization of the scattered neutrons is analyzed outside of the chamber. The zero-field condition is accomplished by a μ-metal shielding and two superconducting Nb-Meissner shields, which furthermore account for the conservation of the neutron spin state when entering the chamber. The initial and final polarization state are set by an adiabatic change of the quantization axis in the nutators before and after the zero-field chamber.

Neutron spin-echo spectroscopy

The complex neutron spin-echo technique is discussed in short. For a detailed description we refer to the work edited by Mezei *et al.* [110]. The instrumental approach is based on the Larmor precession of neutrons in a magnetic field, which is perpendicular to the quantization axis of the beam. The Larmor frequency of the precession $\omega_L = -\gamma|\vec{H}|$ can be tuned by the applied magnetic field. A beam of polarized neutrons, which not necessarily have to be monochromatic, enters a path of constant magnetic field H in which each neutron precesses at a constant ω_L. This causes a polarization of the beam due to the variation of neutron velocities. At the sample stage, the polarization of each neutron is reversed either by a π-flipper or by a magnetic spin-flip process. Finally, the scattered neutrons propagate along a path of same length and of opposite magnetic field $-H$. This leads to a recovery of the polarization of the beam at the end of the path.
For elastic processes, which do not effect the neutron velocity, the full polarization is recovered at the detector, which is called the *spin-echo effect*. Energy transfers during scattering lead to a change in k_f (and in v_f) which decreases the final polarization. By scanning the magnetic fields along the paths, one can directly measure the intermediate scattering function $I(\vec{Q},t) = S(\vec{Q},t)/S(\vec{Q},0)$. This technique allows for experiments with a very high energy resolution. Within this work, experiments have been performed at the spin echo spectrometer IN11 at the ILL [111].

Chapter 4

Electromagons in $TbMnO_3$

The observation of ferroelectricity in $TbMnO_3$ was the discovery of a new group of multiferroic materials, in which a complex magnetic structure directly induces macroscopic electric polarization [5]. $TbMnO_3$ has become a reference system for this class of materials due to its sizable ferroelectric polarization and its large magnetoelectric coupling [9] and is well suited for elucidating the magnetic excitations and the coupling mechanism for such multiferroic materials. Since 2003 more than 250 relevant publications [113] are listed proving the high interest in this compound.

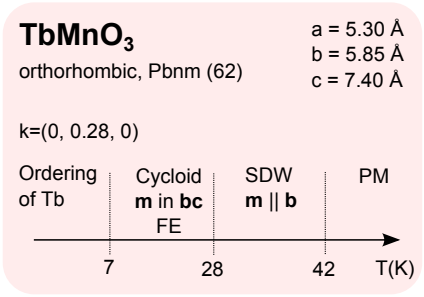

Figure 4.1.: Crystal parameters and magnetic phase transitions in $TbMnO_3$ [11, 112].

One of the strongly discussed topics are hybridized magnon-phonon excitations in multiferroic materials. These were experimentally observed in $TbMnO_3$ by infrared spectroscopy [57] and inelastic neutron scattering [12]. The microscopic origin of these electromagnons is still under debate and several different approaches were postulated [54, 66, 114].

In this chapter, different neutron scattering techniques were used in order to investigate the phase transition towards the multiferroic phase and the magnetic excitations in the multiferroic low-field and high-field phases. Polarized neutrons were a crucial tool to probe specific properties of the magnetic system, such as its chirality.

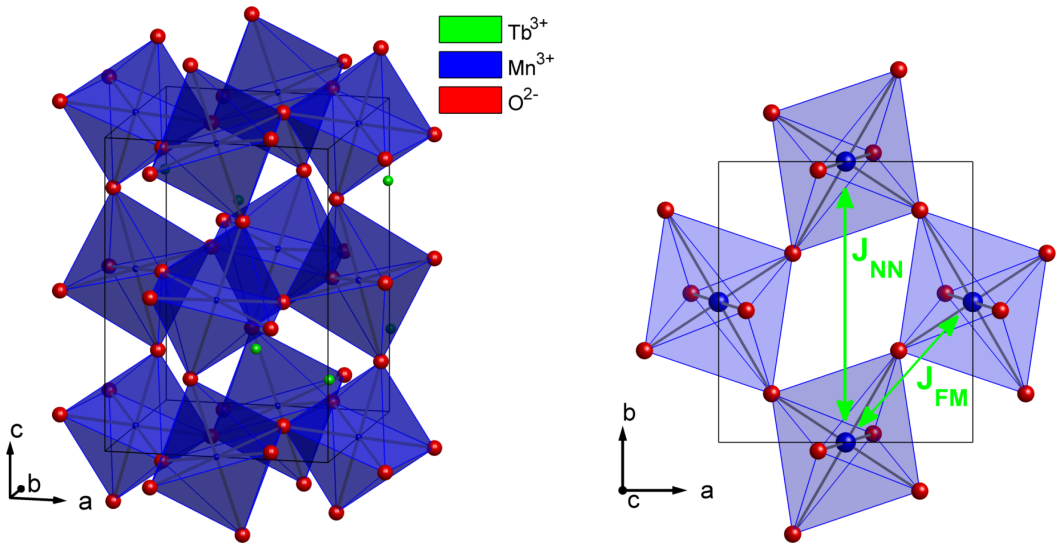

Figure 4.2.: (a) Crystal structure of $TbMnO_3$. The orthorhombic perovskite structure is distorted due to a tilted staggering of $[MnO_6]$-octahedra along $\vec{c}$. (b) The distortion of octahedra leads to a competition of ferromagnetic nearest-neighbor interaction J_{FM} and antiferromagnetic next-nearest-neighbor interaction J_{NN} in the ab-plane.

4.1. Introduction

4.1.1. Crystal and magnetic structure

$TbMnO_3$ belongs to the series of rare-earth manganates[a] $R MnO_3$ and its structure can be described in the orthorhombic space group $Pbnm$. The lattice parameters are given in Figure 4.1. The main characteristics of $TbMnO_3$ will be discussed in this section. For a detailed description of the crystal and magnetic structure of the $R MnO_3$ series, we refer to previous work [116, 117].
Figure 4.2(a) shows the structural unit cell of $TbMnO_3$. $R MnO_3$ compounds crystallize in a distorted $GdFeO_3$ perovskite structure with tilted $[MnO_6]$-octahedra [118]. The distortion of the octahedra is induced by the reduced size of the rare-earth ion. As a consequence, the symmetry of the crystal is reduced from cubic to orthorhombic and the Mn-O-Mn bond angle changes from the linear value of 180° in $GdFeO_3$ to about 145° in $TbMnO_3$ [119].
The Mn^{3+} has four electrons in the 3d orbitals, which loose their degeneracy in the orthorhombic environment in the $R MnO_3$ series and transform to $t_{2g}^3 e_g^1$ [120]. The Jahn-Teller effect in $R MnO_3$ leads to a staggered ordering of single-occupied $d_{3x^2-r^2}$ and $d_{3y^2-r^2}$ orbitals in the ab-plane [120]. This results in a ferromagnetic

[a] The rare-earth lanthanides in order of ionic radius are (from large to small): La, Ce, Pr, Nd, Pm, Sm, Eu, Gd, Tb, Dy, Ho, Er, Tm, Yb, Lu [115].

nearest-neighbor exchange in the *ab*-plane [119]. The coupling between the planes along the *c*-axis is antiferromagnetic [119]. The exchange interactions perfectly explain the A-type antiferromagnetic order in $LaMnO_3$.
The tilting of the octahedra enhances for smaller rare-earth ions. This distortion modulates the exchanges paths in the *ab*-plane, which is the origin of the multitude of different magnetic structures in this series [119, 121, 122]. Figure 4.2(b) shows the arrangement of MnO_6 octahedra in the *ab*-plane. The bond-angle of the nearest-neighbor exchange J_{FM} in the undistorted system is 180°, which renders it ferromagnetic, following the Goodenough-Kanamori-Andersen rules [123, 124]. The reduction of this Mn-O-Mn bond angle weakens the ferromagnetic superexchange coupling J_{FM} between next neighbors. In addition, the reduction of the distance of the inner oxygen ions leads to the enhancement of the antiferromagnetic next-nearest neighbor interaction J_{NN} in the *ab*-plane. This exchange is possible along $\vec{a}$ and along $\vec{b}$ but J_{NN} is stronger along $\vec{b}$ due to the different staggering of oxygen ions along both paths [119].
In $LaMnO_3$, the octahedra distortion is small and the moments in the *ab*-plane order ferromagnetically ($J_{FM} > J_{NN}$, A-type ordering with $\vec{k}_A = (0,\ 0,\ 0)$). In $HoMnO_3$, the distortion is large and the moments order in antiferromagnetic stripes ($J_{NN} > J_{FM}$, E-type ordering with $\vec{k}_E = (0,\ 0.5,\ 0)$) [119]. In the region of intermediate rare-earth ion size, the system is strongly frustrated between both ground states when $J_{FM} \lesssim J_{NN}$ which is the case for R = Tb, Dy. As a result, the Mn-moments order in an incommensurate structure with propagation vector $\vec{k} = (0,\ q_k,\ 0)$ and $0 < q_k < 1/2$ [119].
In $TbMnO_3$, the Mn-moments order at T_N =42 K in an A-type longitudinal spin-density wave (SDW) with a propagation vector of $\vec{k}_{ic} = (0,\ q_k,\ 0)$ [125]. Applying Bertaut's representation theory for the space group *Pbnm* and $\vec{k}_{ic}$, one can derive that the magnetic structure can be described by four irreducible representations, which correspond to four modes A, C, F and G [126]. These modes lead to different superstructure Bragg reflections. The reflections $\vec{Q} = (h,\ k,\ l)$ follow the extinction conditions [127]:

A-mode:	$h+k$ =even,	l =odd,	F-mode:	$h+k$ =even,	l =even,
C-mode:	$h+k$ =odd,	l =even,	G-mode:	$h+k$ =odd,	l =odd.

In the SDW-phase, the value of the incommensurability is $q_k \approx 0.28$ and the structure can be described by a single irreducible representation $\Gamma^3 = (Gx,\ A_y,\ F_z)$ [127]. Neutron diffraction data in this phase could be refined using only the A-mode along $\vec{b}$, and ordered moment is of the form $\vec{M}^{SDW} = (0,\ M_b \cos(\vec{k}_{ic} \cdot \vec{r}),\ 0)$ with $M_b = 2.9\,\mu_B$ [11]. Upon further cooling, the incommensurability decreases slightly until about 31 K where a quasi-lock-in at a value of $q_K \approx 0.276$ sets in [128]. A model of the magnetic structure is shown in Figure 4.3(a).
At $T_{FE} = 28$ K, a second magnetic transition occurs. In this phase the magnetic

order corresponds to an elliptic cycloid still modulated along the *b*-direction. The spiral can be described using a coupling of two irreducible representations $\Gamma^2 \times \Gamma^3$, with $\Gamma^2 = (C_x,\ F_y,\ A_z)$ [127]. Kenzelmann *et al.* could describe their data by $\vec{M}^{FE} = (0,\ M_b \cos(\vec{k}_{ic} \cdot \vec{r}),\ M_c \sin(\vec{k}_{ic} \cdot \vec{r} + \delta))$ with $M_b = 3.9\,\mu_B$ and $M_c = 2.8\,\mu_B$. The phase between both components could not be resolved in the experiment but from the size of the moments, Kenzelmann *et al.* deduce that the Mn-moments form an elliptical spiral in the *bc*-plane, described by two A-modes [11].
In addition, detailed neutron diffraction experiments revealed a smaller Mn-spin component to be along the *a*-axis, which corresponds to a G-mode [127]. A model of the dominating A-mode magnetic structure is shown in Figure 4.3(b). This SDW to spiral transition is accompanied by the appearance of a spontaneous ferroelectric polarization P_{FE} parallel to the *c*-axis. The underlying mechanism will be described in the next section.
The terbium moments order separately below $T_{Tb} = 7\,\mathrm{K}$ and form an incommensurate SDW with moments mainly oriented parallel to $\vec{a}$ and a propagation vector of $\vec{k}_{Tb} = (0,\ 0.415,\ 0)$ [125]. The transition is visible in the magnetic susceptibility, the dielectric constant, the thermal expansion, the ferroelectric polarization and diffraction experiments [8, 9, 125, 129]. The magnetic Bragg peaks are reported to be significantly broadened which emphasizes a short-range order.
Although the Tb-moments order at a lower temperature as the Mn-subsystem, it was shown that the two magnetic ions couple. Already at 15 K, the Tb-moments contribute to the spiral ordering of Mn-moments and had to be taken into account for the structure refinement of the Mn-order [11]. At this temperature, the Tb-moments order weakly primarily along $\vec{a}$, and can be described by C-, F- and G-modes [48, 130]. It was proposed that the Mn- and Tb-order remain coupled even below T_{Tb} through their wave vectors, $3k_{Tb} - k_{Mn} = 1$ [131]. The coupling of the rare-earth ions with the Mn ion J_{Mn-R} has also been reported for $DyMnO_3$ [48]. In $TbMnO_3$, the rare-earth ion significantly contributes to the magnetic properties of the Mn-order and even to the ferroelectric polarization [131, 132].

4.1.2. Multiferroic phase

$TbMnO_3$ was the first compound in which it was observed that a ferroelectric polarization is directly related to an antiferromagnetic spin-spiral ordering [5, 11]. That the spiral magnetic structure [11] directly induces ferroelectricity was later on explained microscopically by the mechanism of the spin current [15], the mechanism of the inverse Dzyaloshinskii-Moriya (DM) interaction [16] and in a phenomenological approach [43]. In all cases the induced polarization is of the form $\vec{P} \propto \vec{r}_{ij} \times (\vec{S}_i \times \vec{S}_j)$, with the neighboring spins $\vec{S}_i, \vec{S}_j$ and their distance vector $\vec{r}_{i,j}$.

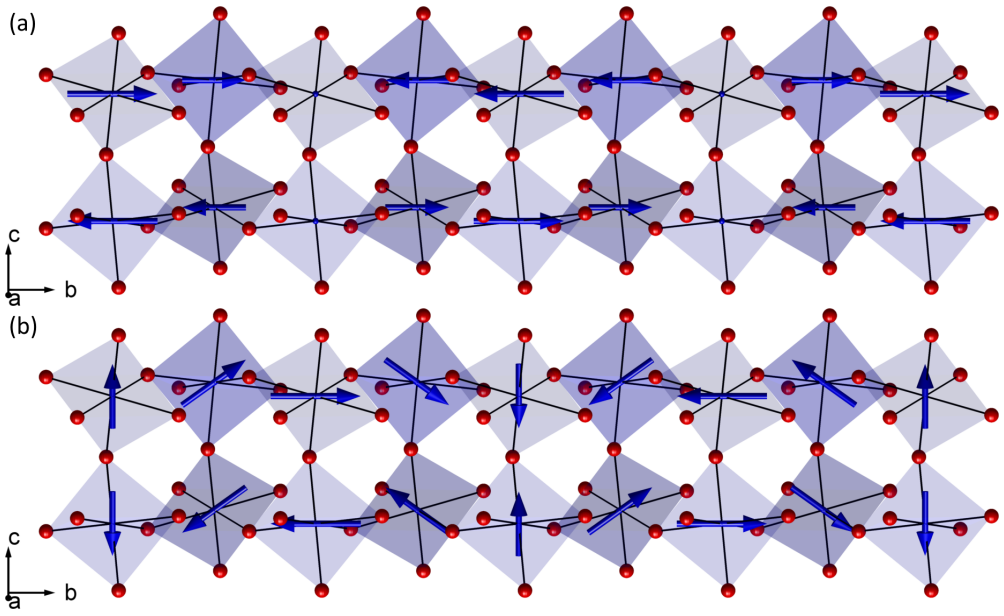

Figure 4.3.: Magnetic structure of manganese moments in $TbMnO_3$. The zig-zag chains of $[MnO_6]$ octahedra are shown along the direction of the propagation vector, with darker oxygen octahedra in the back and brighter in the front. The propagation vector was chosen to be $\vec{k} = (0,\ 0.25,\ 0)$ for a better visibility. The Mn-moments order below T_N (a) in a spin-density-wave with moments modulated parallel $\vec{b}$, and below T_{FE} (b) in an elliptical spiral in the *bc*-plane.

In the $RMnO_3$ series, the compounds with R =Tb, Dy, Gd and $Eu_{1-x}Y_x$ develop a spin-induced ferroelectric polarization at low temperatures [5, 9, 133, 134, 135]. In $TbMnO_3$, the onset of a spontaneous electric polarization P_c parallel to the orthorhombic *c*-axis is observed at $T_{FE} \approx 28\,\mathrm{K}$. The ferroelectric order appears as a secondary effect which is visible in the small value of polarization ($P_c = 0.08\,\mu\mathrm{C\,cm^{-2}}$ at 10 K in comparison to $P = 26\,\mu\mathrm{C\,cm^{-2}}$ in $BaTiO_3$ 300 K [136]). The direction of polarization can be deduced from the magnetic structure of the Mn-subsystem in the incommensurate spiral phase. The accuracy of the model in $TbMnO_3$ could be demonstrated by the application of magnetic and electric fields to the system [8, 49]. The application of magnetic fields will be reviewed in the next section.
The direction of the ferroelectric polarization is connected via the DM mechanism with the cycloid structure of Mn-moments. Clockwise and anticlockwise rotation have an opposite sign of vector chirality $v_{\mathrm{chiral}} = \vec{S}_i \times \vec{S}_j$ which determines the sign of the ferroelectric polarization. This relation was demonstrated using polarized neutron diffraction in combination with the application of an electric field to the sample [49]. Using longitudinal polarized neutrons, it is possible to distinguish different contributions to the total scattering. One of the magnetic term is of the

form $\pm i(\vec{M} \times \vec{M}^*)_x$, cf. Tab. 3.1. Depending on the choice of scattering geometry, it is thus possible to directly measure the sign of the vector chirality $\vec{v}_{\text{chiral}}$ of a magnetic structure. The reversal of the electric field applied to the sample along the direction of polarization thus leads to a modulation of scattered intensity in the spin-flip channels parallel to $\vec{Q}$ ($\sigma_{x\bar{x}}$ and $\sigma_{\bar{x}x}$). With this technique, it is possible to determine the absolute polarization state of the sample. In following neutron studies, polarized neutrons with an applied electric field have been used to investigate the hysteresis behaviour of the magnetic structure in the multiferroic state [52, 137], the relation of the quasi-lock-in with the spin cycloid and the time-resolved switching of the cycloid [128].

4.1.3. Application of magnetic fields

As a result of the strong coupling of magnetism and ferroelectric order in spiral multiferroic materials, the application of external magnetic fields leads to giant magnetoelectric effects [38]. It has been shown in $TbMnO_3$ that the direction of the ferroelectric polarization flops from the c to the a-axis above critical fields $\vec{H} \parallel \vec{a}$ and $\vec{H} \parallel \vec{b}$ [8]. Contrarily, in fields $\vec{H} \parallel \vec{c}$ the polarization is completely suppressed [8]. The flop of the ferroelectric polarization coincides with a first-order transition of the spin cycloid plane from bc to ab, which is fully consistent with the proposed DM mechanism [48]. The propagation vector of the magnetic structure changes from a slightly incommensurate to a commensurate value of $\vec{k}_{com} = (0,\ 0.25,\ 0)$ for both field transitions $\vec{H} \parallel \vec{a}$ and $\vec{H} \parallel \vec{b}$ [138, 139] as the incommensurate spiral becomes instable above those fields [140]. In this chapter, we will distinguish the low field incommensurate phase (LF-IC) from the high field commensurate phases (HF-C) which are similar for magnetic fields $\vec{H} \parallel \vec{a}$ and $\vec{H} \parallel \vec{b}$.

The flop of the spiral plane in magnetic fields applied along $\vec{a}$ and $\vec{b}$ could be reproduced phenomenological as an influence of the strong anisotropy evolving from the rare-earth spins which are coupled to the Mn moments [43]. Contrarily, Mochizuki and Furukawa developed a model where the field flop arises due to a competition of Mn easy-axis anisotropy and a field-dependent antisymmetric exchange interaction [141]. We will discuss their model in detail in Section 4.3.

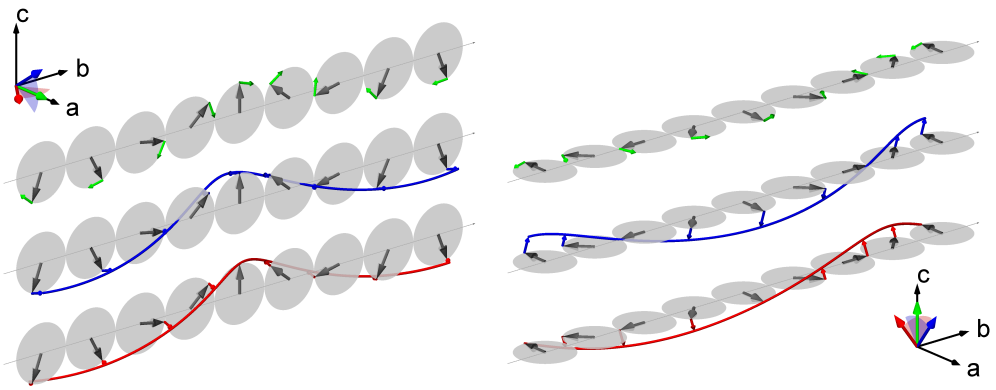

Figure 4.4.: Sketch of the magnetic excitations at the zone center of the cycloid structure in the LF-IC phase (left) and in the HF-C phase (right) of $TbMnO_3$. The static spin structure is marked by thick gray, and the local fluctuations by smaller colored arrows. In each of the two phases there are a phason mode (top) and rotation modes around the b-direction (middle, cycloid mode) and around the vector in the cycloid plane perpendicular to $\vec{b}$ (bottom, helical mode). The axis vectors show the oscillation of the vector chirality $\vec{S}_i \times \vec{S}_j$.

4.1.4. Magnetic and magnetoelectric excitations

The strong magnetoelectric coupling in spiral multiferroics should also influence the character of the magnetic excitations, and the existence hybridized magnon-phonon modes was predicted in 1982 [29]. Katsura *et al.* developed a theory for helical magnets and proposed the existence of these modes in such systems [54]. In addition, the authors predict two electrically inactive low-lying magnon modes. A sketch of the magnetic polarization of these excitations in both multiferroic phases, LF-IC (bc cycloid) and HF-C (ab cycloid), is shown in Figure 4.4. The three expected zone-center modes correspond to the rotation of the spins around one of the principal directions: the rotation around the normal vector of the cycloid (phason or in-plane mode) and two modes associated with the rotation of the cycloid plane around either the propagation vector direction $\vec{b}$ (cycloid out-of-plane mode) or the vector in the cycloid plane but perpendicular to $\vec{b}$ (helical out-of-plane mode). The rotation around the b-direction keeps the cycloid character, whereas the helical rotation changes the character introducing a helical component. When we apply the inverse Dzyaloshinskii-Moriya mechanism, which explains the static multiferroic phases, to the magnon modes, we find that only the cycloid out-of-plane mode affects the direction of the induced electric polarization. This cycloid mode should thus possess a strong dielectric component. Furthermore this component should follow the flop of the cycloid plane from the LF-IC to the HF-C phase.

The magnon dispersion in $TbMnO_3$ was analyzed using inelastic neutron scattering (INS) by Senff *et al.* [12, 142]. Three low-energy modes were found at the magnetic zone center and their polarization could be investigated by the use of linear neutron polarization analysis. The authors identify an in-plane mode at $\omega_1 \approx 0.1\,\mathrm{meV}$ and two out-of-plane modes at $\omega_2 \approx 1.1\,\mathrm{meV}$ and $\omega_3 \approx 2.5\,\mathrm{meV}$, respectively, at 17 K. The exchange interactions could be estimated by applying a Heisenberg model to the different magnon branches, but without reflecting the incommensurate character of the order [12]. Recently Milstein and Sushkov described the magnon dispersion in $TbMnO_3$ and $DyMnO_3$ using the σ-model-like effective-field theory [143]. We will discuss this model in Section 4.3. In a subsequent neutron scattering experiment, the excitation spectrum in the HF-C in magnetic fields $\vec{H} \parallel \vec{a}$ was investigated [56]. Three branches were found and their polarizations perfectly fit to a flop of the cycloid plane.
Complementary studies of the dynamics in the multiferroic phase in $TbMnO_3$ were done using infrared (IR) spectroscopy. Pimenov *et al.* [57] discovered a signal, which is suppressed by a magnetic field; they interpreted this as a mixed excitation and called it electromagnon. Two such electromagnon modes are present at low frequencies and perfectly match the energy of the out-of-plane modes found in INS [59]. This and the matching temperature dependence of IR and INS mode frequencies [61, 144] strongly support the electromagnon interpretation given in Ref. [54]. In the HF-C phase, only fields $\vec{H} \parallel \vec{b}$ were accessible for IR experiments due to instrument limitations. There, Shuvaev *et al.* claimed the existence of a weak *c*-polarized mode in the HF-C phase above the H_b transition [60], which would correspond to the electromagnon activated by the DM mechanism.
However, the various IR and optical measurements performed on the $RMnO_3$ series yield a much more complex picture [66, 145, 146] recently resumed in Reference [55]. There are at least three different optical electromagnon contributions. In particular the strong IR signal is always found along the *a*-direction [59], even for materials in the HF-C phase associated with an *ab* cycloid. A distinct electromagnon origin was proposed to explain this strong *a*-polarized signal based on a magnetostrictive mechanism where the Heisenberg interaction is modulated by a variation of the Mn-O-Mn bond angles [66, 145].

4.2. Diffuse scattering above the magnetic and multiferroic phase transitions

The cycloid ground state ordering of the Mn-moments in $TbMnO_3$ results from the strong magnetic frustration in the *ab*-plane, namely between the ferromagnetic

nearest-neighbor interaction J_{FM} and the antiferromagnetic next-nearest neighbor interaction J_{NN}, see Fig. 4.2(b). One thus expects sizable diffuse magnetic scattering well above the transition temperature T_N. Its characterization and temperature dependence will help to understand the complex system and to evaluate the interaction parameters determined from the magnon dispersion (cf. Ref. [12] and Section 4.3).
Subsequently, we will focus on the ferroelectric transition from SDW to spiral at T_{FE}. Precursors of this second-order transition are present even in the SDW phase. These precursors will be discussed in context of chiral diffuse scattering as observed by Finger *et al.* [137].
The single crystals of $TbMnO_3$ used in this section have been grown by A. C. Komarek in a mirror furnace [147].

4.2.1. Antiferromagnetic transition at T_N

In order to investigate the diffuse magnetic scattering in the paramagnetic phase, a single crystal of $TbMnO_3$ has been mounted in the $[0,1,0]/[0,0,1]$ scattering plane in a closed-cycle cryostat at the cold neutron triple-axis spectrometer 4F1 installed at the LLB, with longitudinal polarization analysis. The neutrons were polarized by a supermirror bender and analyzed using a Heusler monochromator. At the sample stage, a set of Helmholtz coils was used to guide the neutrons. Throughout the experiment, we worked with a fixed neutron energy of $E = 13.6\,\mathrm{meV}$ ($\vec{k} = 2.57\,\mathrm{\AA}^{-1}$) which corresponds to an energy resolution of about $\Delta E \approx 0.5\,\mathrm{meV}$. The polarization of the neutron beam has been verified at the nuclear Bragg reflection $\vec{Q} = (0,\ 0,\ 4)$ and a flipping ratio of $FR \approx 27$ has been observed.
In polarized neutron experiment, a dedicated coordinate system is used, where x is parallel to the scattering vector $\vec{Q}$, z is vertical to the scattering plane and y is perpendicular to z and $\vec{Q}$. A sketch of the scattering geometry at $\vec{Q} = (0,\ 0.28,\ 1)$ is shown in the inset of Figure 4.5(a). The scattered intensity is measured along the principal directions x, y and z for spin-flip and non spin-flip processes. With the help of the selection rules for neutron scattering, the polarization of the magnetic moment can be deduced from these cross sections, cf Tab. 3.1. We find that for the chosen scattering plane z is always parallel to $\vec{a}$. For spin-flip processes, we get the contribution of magnetic moments parallel $\vec{a}$ ($M_z = M_{\|\vec{a}}$). x and y are in the scattering plane and thus depend on the scattering vector $\vec{Q}$. The scattered intensity depends on the angle α. In the spin-flip channels we find a combination of magnetic scattering along $\vec{b}$ and $\vec{c}$. The scattered intensity depends on the angle α between $\vec{Q}$ and the axes, as $I \propto \sin^2(\alpha)$. In the case of the magnetic Bragg peak $\vec{Q} = (0,\ 0.28,\ 1)$, the scattering comes mainly from the b-component, as $\sin^2(\alpha) = 0.88$ for $\vec{b}$ and $\sin^2(\alpha) = 0.12$ for $\vec{c}$.

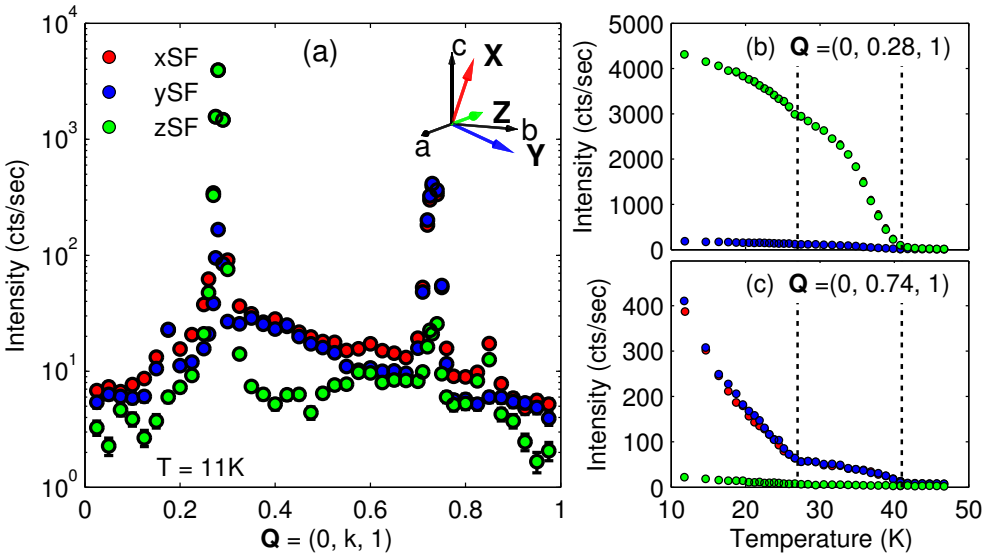

Figure 4.5.: Neutron polarization analysis of elastic scattering in $TbMnO_3$ at 4F1. (a) Elastic scan along $\vec{Q} = (0,\ k,\ 1)$ at 11 K. The directions of the polarized neutron scattering cross sections are shown in the inset. (b) and (c) Temperature dependence at $\vec{Q} = (0,\ 0.28,\ 1)$ and $\vec{Q} = (0,\ 0.74,\ 1)$ of all three cross sections. The dashed lines indicate the phase transitions at T_N and T_{FE}.

The spin-flip scattering in all three channels along $[0, k, 1]$ at 11 K in the cycloid phase is shown in Figure 4.5(a). 11 K was the base temperature of the mounted displex cryostat. Three observations can be deduced from this scan. At $k \approx 0.28$ we find the A-type Bragg peak ($\vec{Q} = (0,\ k_{Mn},\ 1)$) of the *bc*-cycloid which results in a scattered intensity concentrated in the zSF channel. The sharp peak at $k \approx 0.73$ can be identified as G-type Bragg peak ($\vec{Q} = (0,\ 1 - k_{Mn},\ 1)$). These reflections have been reported previously and were assigned to an induced ordering of Tb-moments by the Mn-structure because of their relative weakness and their temperature dependence (concave curvature upon cooling) [125, 130, 131]. The polarization analysis reveals the main contribution of magnetic moments parallel to $\vec{a}$ which is the easy axis of the Ising-like Tb-moments [125]. As third feature, we note the broad scattering around $k \approx 0.4$ which again arises mainly from moments along $\vec{a}$. At 11 K, we are close to the transition temperature of the distinct Tb-order at $T_{Tb} \approx 7$ K with a propagation vector of $\vec{k}_{Tb} = (0,\ 0.42,\ 0)$. The broad signal hence can be attributed to the diffuse magnetic scattering of Tb-moments.
The temperature dependence of scattered intensity at $k = 0.28$ and $k = 0.74$ is shown in Figure 4.5(b) and (c). The polarization of the Bragg reflections, given by the ratio ySF/zSF is stable with temperature at both positions. At $k = 0.28$ the signal comes almost purely from M_y and at $k = 0.74$ the signal comes from M_z. Note that the xSF channel (red points) is hidden behind the ySF channel.

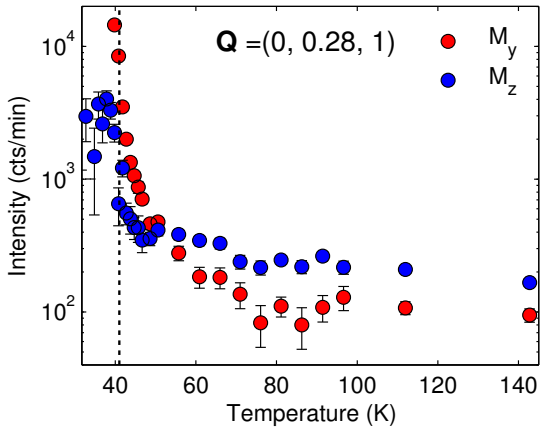

Figure 4.6: Temperature dependence of diffuse magnetic scattering in $TbMnO_3$ at $\vec{Q} = (0,\ 0.28,\ 1)$ at 4F1. The intensities are calculated from spin-flip cross sections as $M_y = xSF - ySF$ and $M_z = xSF - ySF$. The dashed line indicates the phase transitions at $T_N \approx 41\,\mathrm{K}$.

The finite flipping ratio of $FR \approx 27$ leads to a superposition of approximately 5 % non-spin-flip process in the spin-flip channels. As an example, at 11 K and $k = 0.28$ about 170 cts/sec in ySF are due to scattering from yNSF. The intensity in channel yNSF is strong because it is sensible to M_y (similar to zSF, cf. Tab.3.1). From both curves in Figure 4.5 we can identify the transition temperatures towards the SDW at $T_N \approx 41.0\,\mathrm{K}$ and from SDW to spiral phase at $T_{FE} \approx 27.5\,\mathrm{K}$ which are indicated with dashed lines. The deviations of the observed transition temperatures to values from the literature can be attributed to the experimental setup. The sample was placed in an helium-filled aluminum container and the temperature controller was glued outside of the container. The heat conductance to the sample was primarily provided by helium gas which lead to a temperature gradient between the sensor and the sample.
Once the polarization analysis is established and the static signal understood, we can turn our attention to the paramagnetic phase. Figure 4.6 shows the temperature dependence of scattered neutron intensity at the A-type Mn-order position $\vec{Q} = (0,\ 0.28,\ 1)$ along y and z. The contributions of the two directions were determined as $M_y = xSF - ySF$ and $M_z = xSF - zSF$. This analysis not only allows to determine the direction of the moments that contribute to the scattering but also eliminates the instrument background. We find significant diffuse scattering at this position up to 140 K. The polarization analysis in the chosen scattering geometry allows us to separate the contribution from moments along the a-axis (M_z) and b-axis (M_y). The strong Ising-type anisotropy of the Tb-moments along $\vec{a}$ and the large magnetic moment of Tb^{3+} ions ($\mu_{eff} = 9.5\,\mu_B$ [112]) most probably lead to the scattering along $\vec{a}$ at all temperatures. The magnetic susceptibility of $TbMnO_3$ is reported to be anisotropic up to room temperature with the largest contribution along $\vec{a}$ [148]. At lower temperatures, the intensity in M_z increases at T_N and decreases soon after. This behaviour can arise from Tb-moments which first follow the ordering of the Mn-moments (A-type) and finally order separately with the

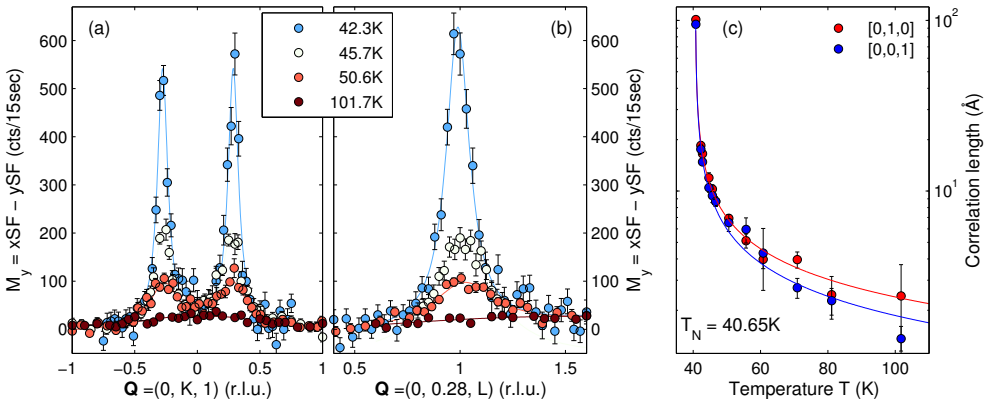

Figure 4.7.: Diffuse magnetic scattering of $TbMnO_3$ in the paramagnetic phase. (a) and (b) show scans along $\vec{Q} = (0,\ K,\ 1)$ and $\vec{Q} = (0,\ 0.28,\ L)$ at selected temperatures above T_N at 4F1. The intensities are calculated from spin-flip cross sections as $M_y = xSF - ySF$ and can be attributed to the Mn-order. Lorentzian functions were fitted to the curves. (c) Temperature dependence of the correlation length as determined from Lorentzian fits, $\xi_{K(L)} = \frac{b(c)}{2\pi \cdot HWHM}$. A power law was fitted to the curves.

same propagation vector (G-type) and moments along $\vec{a}$. The intensity along $\vec{b}$ is less pronounced at higher temperatures and only overcomes the a-component at about 50 K. At lower temperatures, the intensity in M_y increases continuously towards the transition temperature.

We are primarily interested in the scattering of the manganese moments along the $\vec{b}$ direction. The chosen scattering plane $[0,1,0]/[0,0,1]$ allows us to investigate the direction dependency of the diffuse signal. $\vec{Q}$-scans at the magnetic Bragg peak position of the SDW at $\vec{Q} = (0,\ 0.281,\ 1)$ along the main symmetry directions are presented in Figure 4.7(a) for selected temperatures in the paramagnetic phase. The intensity was calculated as $M_y = xSF - ySF$ in order to separate the contribution along $\vec{b}$. Lorentzian functions were fitted to the data. Diffuse magnetic scattering arises from fluctuations which form temporarily ordered regions in the sample. From the width of the diffuse contribution we can derive the average length of correlated regions.

The temperature dependence of the correlation length along $[0,1,0]$ and $[0,0,1]$ is shown in Fig. 4.9(b) in a logarithmic scale. We find significant diffuse magnetic scattering up to 80 K, which is almost twice T_N. Only minor differences between the correlation along $\vec{b}$ and $\vec{c}$ are visible documenting the three-dimensional correlation of the Mn-system.

The fitting of a power law function of the form $\xi(T) = c \cdot (T - T_N)^{-\nu}$ yields: $\nu = 0.58(2)$ along $\vec{b}$ and $\nu = 0.63(3)$ along $\vec{c}$. The transition temperature was fixed to $T_N = 40.65$ K for both directions (the deviation from values in the literature

is again due to the temperature gradient of the cryostat). The critical parameters are similar for both directions and are closer to the theoretical value of a three-dimensional Ising system ($D = 1$, $d = 3$, $\nu = 0.631$ [149]) than to the three dimensional XY model ($D = 1$, $d = 3$, $\nu = 0.669$ [149]). $TbMnO_3$ undergoes a magnetic transition into a SDW with moments aligned along $\vec{b}$ at this temperature. The Mn-moments are confined by an alternating easy-axis anisotropy in the ab due to staggered $d_{3x^2-r^2}/d_{3y^2-r^2}$-type orbital ordering [145].
The critical phenomena in $R\mathrm{MnO}_3$ multiferroics were investigated by Harris *et al.* applying Landau theory [150]. The authors come to the conclusion that the upper transition belongs to universality class of the XY-model, while the lower ferroelectric transition is of Ising-type. The critical behaviour is only valid in a small temperature region. The behaviour at higher temperatures approaches the mean-field value which may lead to deviations from the extracted experimental values the expected values. A slightly different observation was made by calorimetry measurements from Oleaga *et al.* [151]. From the specific heat they deduce a critical exponent of $\alpha = -0.09$ which would suggest a Heisenberg system ($D = 3$ and $d = 3$). The corresponding exponent of this model for the correlation length is $\nu = 0.707$ [149].

Mean-field simulation

The behaviour of the diffuse magnetic scattering in the paramagnetic phase can be simulated using a mean-field approach. Hohlwein *et al.* were able to describe diffuse scattering in MnO with this method [152]. The principal idea of the mean-field approximation is to treat the magnetic system as independent spins in an effective field, which is created by the interactions. The spin-only Hamiltonian can then be expressed as $H \propto \sum_{\vec{q}} J(-\vec{q})\vec{S}(\vec{q}) \cdot \vec{S}(-\vec{q})$, where $\vec{S}(\vec{q})$ is the Fourier transform of the spin $\vec{S}$ and $\vec{q}$ is a reciprocal vector in the first Brillouin zone [153, p. 91ff]. The Fourier transform of the interaction parameters is defined as:

$$J(-\vec{Q}) = \frac{1}{N} \sum_{0,j} J(\vec{R}_0 - \vec{R}_j) \mathrm{e}^{i\vec{Q}\cdot(\vec{R}_0 - \vec{R}_j)} \ , \tag{4.1}$$

with $\vec{R}_i$ being the position of the i-spin and N being the number of spins in the unit cell. For high temperatures, well above the transition to the long-range magnetic order, the Q-dependent magnetic susceptibility can be derived from $J(\vec{Q})$. Furthermore, the susceptibility can be used to directly derive the differential

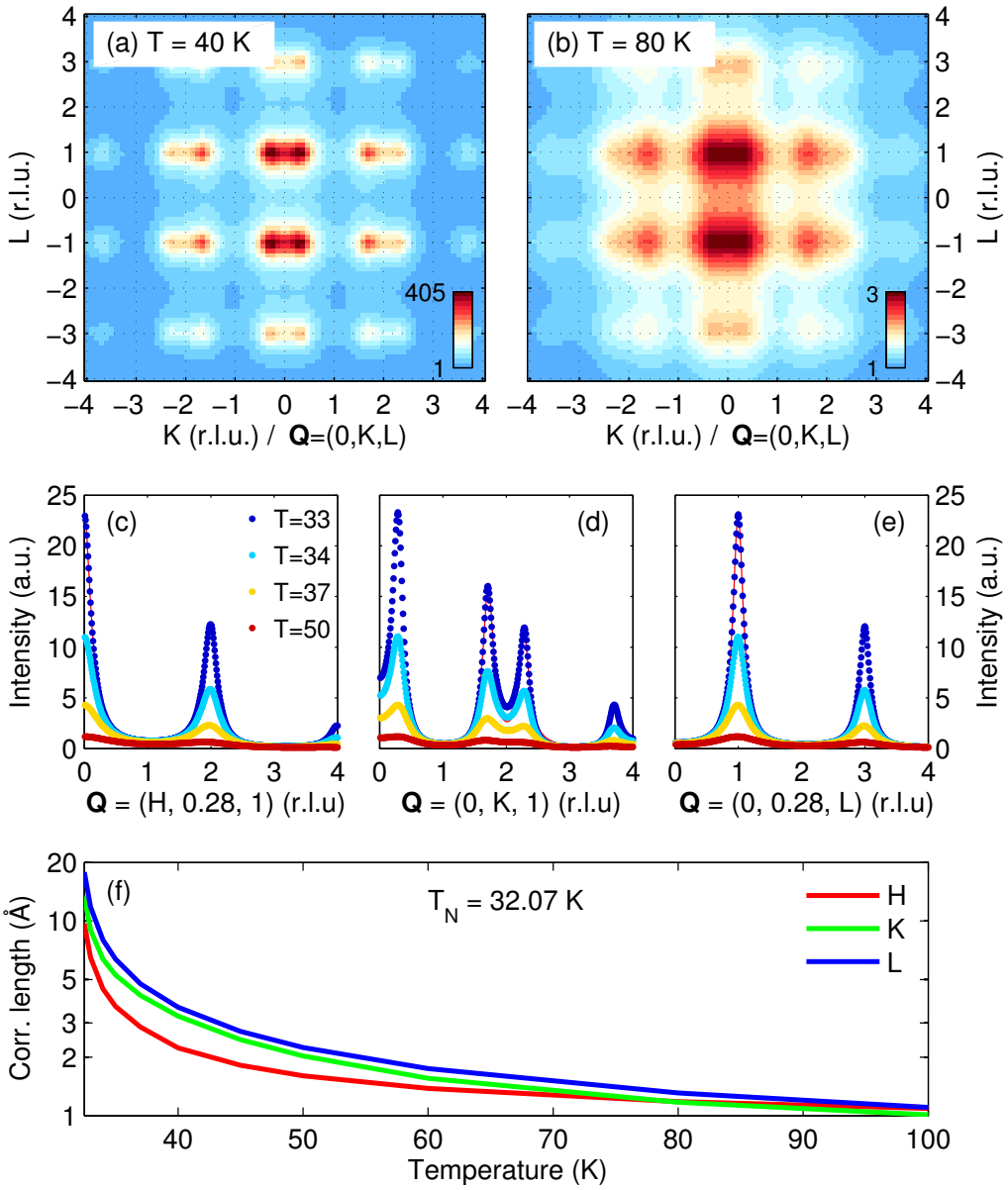

Figure 4.8.: Simulated magnetic scattering in the paramagnetic phase of $TbMnO_3$ calculated using a mean-field model as described in the text. (a, b) Simulated neutron scattering intensities in the $[0, K, L]$ plane at 40 K and 80 K. (c, d, e) Cuts along the three symmetry directions at different temperatures. Lorentzian functions were fitted to the curves. (f) Temperature dependence of correlation lengths derived from the Lorentzian fits along the three symmetry directions.

neutron cross section [153, p. 221ff]:

$$\frac{d\sigma}{d\omega} \propto f_M^2(\vec{Q})\Xi(\vec{Q}) \propto f_M^2(\vec{Q})\frac{S(S+1)}{3k_BT - S(S+1)J(\vec{Q})} \tag{4.2}$$

This calculation was performed for the paramagnetic phase of $TbMnO_3$. To describe the system, we used the *Pbnm* structure parameters given in Fig. 4.1. The Mn-moments carry a spin $S = 4/2$ and occupy the Wyckoff site 4*b*. The exchange interactions were chosen to be antiferromagnetic $J_{AFM} = -0.84\,\text{meV}$ along $\vec{c}$, ferromagnetic $J_{FM} = 0.38\,\text{meV}$ in the *ab*-plane and antiferromagnetic $J_{NN} = -0.31\,\text{meV}$ along $\vec{b}$, after Ref. [142]. A model of the exchange interactions in $TbMnO_3$ is shown in Figure 4.12. J_{FM} and J_{NN} are in the *ab*-plane and lead to a frustration of exchange parameters. The result is a spiral spin ordering and in this case the transition temperature can be calculated from $J(\vec{Q})$ as follows [154]: $T_N = 2S(S+1)J_{max}(\vec{Q})/3k_B = 32.07\,\text{K}$.
The result of the simulation using Eq.4.2 is shown in Figure 4.8. The intensity maps in Fig. 4.8(a-b) simulate the diffuse magnetic scattering in the $[0, K, L]$ plane. This is the same plane in which the experiment in the previous section was performed. The model correctly describes the positions of the magnetic Bragg reflections of the Mn-order in $TbMnO_3$. In particular it is able to get an accurate value of the incommensurability of the propagation vector along $\vec{b}$, $\vec{k}_{ic} \approx (0,\ 0.28,\ 0)$.
Line scans along the three orthorhombic symmetry directions are shown in Fig. 4.8(c-e) at four temperatures in the paramagnetic phase. The scans along $\vec{Q} = (0,\ K,\ 1)$ and $\vec{Q} = (0,\ 0.28,\ L)$ can directly be compared to the experimental data, shown in Fig. 4.7. The intensity curves were fitted by a Lorentzian function in order to obtain the correlation length along the three directions.
The temperature dependence of the correlation lengths obtained by simulation is shown in Fig. 4.8(f). The correlation length diverges along all directions at $T_N = 32.07\,\text{K}$. The absolute value of the transition temperature is slightly underestimated by the mean-field model. The Mn-moments in $TbMnO_3$ order at $T_N \approx 42\,\text{K}$ in a SDW and at $T_{FE} \approx 28\,\text{K}$ in a *bc*-spin spiral [11]. The simple mode does not take into account anisotropy effects and the coupling with the Tb-subsystem, and thus the agreement between simulation and experiment is satisfying. The mean-field approach often fails to describe the critical behaviour close to the phase transition [149, p. 11].
The simulated correlation length in Fig. 4.8(f) can be compared to experimental data in Fig. 4.7. In the experiment, we found that the fluctuations are almost isotropic in the *bc*-plane, which agrees well to the simulation. The correlation is reduced along $\vec{a}$ due to the symmetry of the exchange interactions.
The good agreement between experiment and mean-field model shows, that the magnetic order in $TbMnO_3$ can be reasonably well approximated by a simple

A-type order. This order has only one magnon mode which is the case for $LaMnO_3$. The spin-wave calculation for $LaMnO_3$ is presented in Chapter 3.1.3.

Resonant spin-echo

The dynamic scattering of $TbMnO_3$ has been investigated at the triple-axis spin echo spectrometer TRISP at the FRM II. The instrument combines the technique of TAS and neutron resonant spin echo spectroscopy (NRSE). A large piece ($25 \times 6 \times 6$ mm^3) cut from the same sample has been mounted in a closed-cycle cryostat in [010]/[001] scattering geometry. The incoming neutron energy was fixed to $E_i = 13.9\,\text{meV}$ ($\vec{k}_i = 2.51\,\text{Å}^{-1}$).
Figure 4.9(a) shows spin echo spectra for spin-flip processes at zero energy transfer above and below the magnetic phase transition T_N at the elastic Bragg peak position $\vec{Q} = (0,\ 0.283,\ 1)$. At a NRSE instrument the Fourier time τ is varied using radio frequency spin flippers. The polarization gives the ratio of the polarized beam to the unpolarized beam. Diffuse magnetic scattering transforms to Lorentzian line shapes in reciprocal space and the spin echo polarization follows an exponential decay: $P = \exp(-\Gamma \cdot \tau)$ [155]. The extracted fit values from the spectra are given in Figure 4.9(b) and (c) against the temperature. The polarization P_0 steadily increases when approaching the transition temperature and is constant below the transition were the magnetic structure is static. This demonstrated nicely the *critical slowing down* of magnetic fluctuations in the system.
The relaxation time appears to be stable at temperatures above 43 K and converges close to the transition temperature. The expected power law behaviour is only valid in a small temperature regime. The plateau at higher temperatures is not intrinsic to the sample but a limitation of the instrument. At higher temperatures, fluctuations become faster. There is an instrumental upper limit of the accessible frequency range, determined by the high-frequency spin-flippers. This explains the cut-off close to the transition temperature. The accessible range is furthermore limited by the energy selection of the analyzer. The TAS option at TRISP defines an energy width due to its finite energy resolution. The resolution was determined to be $\Delta E \approx 0.5\,\text{meV}$ which corresponds to a frequency in the order of 10^{12} Hz.
The TRISP instrument is designed to determine linewidths of excitations with a extremely high resolution. This comes with the crucial coast of neutron intensity. The initial aim of this experiment was the investigation of magnon linewidths in the multiferroic phase which could not be achieved within the experiment time. The investigation of phase transitions requires a wide coverage in Fourier time and high neutron flux, to which standard spin-echo instruments are better suited such as the IN11 at the ILL.

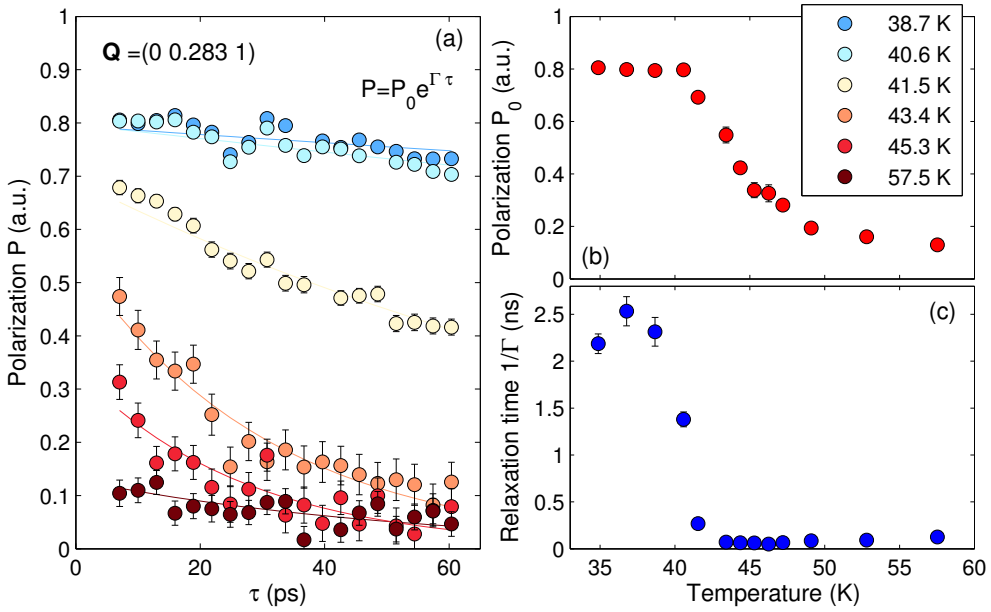

Figure 4.9.: Neutron resonant spin echo signal of $TbMnO_3$ at the magnetic Bragg peak $\vec{Q} = (0,\ 0.283,\ 1)$ around the magnetic phase transition T_N at zero energy transfer at TRISP. (a) Spin echo spectra for selected temperatures. An exponential function $P = \exp(-\Gamma \cdot \tau)$ was used to describe the data. (b) and (c) show the temperature dependence of the extracted polarization P_0 and the relaxation time $1/\Gamma$.

4.2.2. Multiferroic transition at T_{FE}

The subsequent magnetic transition at T_{FE} is defined by a SDW to spiral formation of the Mn-moments and coincides with the development of a spin-induced ferroelectric polarization. Elastic neutron scattering was used to investigate the behaviour at the phase transition. A single crystal of $TbMnO_3$ was mounted at the cold neutron TAS instrument IN3 at the ILL in [201]/[010] scattering geometry. The neutron energy was fixed to $E = 14.7\,\text{meV}$ ($\vec{k} = 2.66\,\text{Å}^{-1}$) and in addition, beam collimation (30′ on $\vec{k}_i$ and 40′ on $\vec{k}_f$) and a PG filter were used in order to reduce the background and to achieve a high angular resolution.
At the transition temperature of $T_{FE} \approx 28\,\text{K}$, the system is already magnetically ordered and the propagation vector does not change at the transition. This makes it difficult to investigate the behaviour at the transition as the signal is dominated by a strong static scattering at the Bragg peak positions. The color map shown in Figure 4.10(a) illustrates the situation. The scattered neutron intensity of

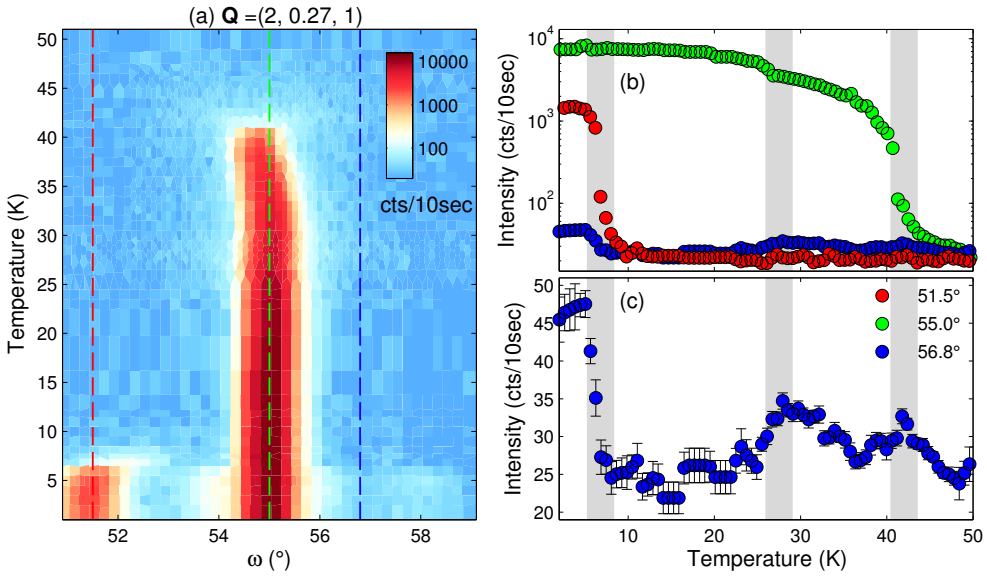

Figure 4.10.: Temperature dependence of rocking scans along the magnetic Bragg peak $\vec{Q} = (2,\ 0.27,\ 1)$ of $TbMnO_3$ at IN3. (a) Logarithmic color mapping of scattered intensity. The dashes lines indicate scan directions in (b). (b) Temperature dependence of line scans extracted from the color map. The intensity in the region of $\Delta\omega = \pm 0.5°$ around the dashed lines was taken into account. (c) Close-up of the temperature dependence. The gray bars indicate the phase transitions at $T_N \approx 42\,\mathrm{K}$, $T_{FE} \approx 28\,\mathrm{K}$ and $T_{Tb} \approx 7\,\mathrm{K}$.

rocking-scans (scan of the sample rotation) through the magnetic Bragg peak at $\vec{Q} = (2,\ 0.27,\ 1)$ is logarithmically plotted for temperatures below 50 K. The Bragg peak at the center develops at $T_N \approx 42\,\mathrm{K}$ and the position locks-in slightly above T_{FE}, which has been investigated in detail in a previous thesis [128]. At $T_{Tb} \approx 7\,\mathrm{K}$, we find the formation of an additional peak which can be attributed to the Tb-order [130]. Its intensity is weakened because the center of this reflection is at $\vec{Q} = (2,\ 0.415,\ 1)$, which is at a slightly different scattering angle 2θ.
The temperature dependencies at three positions (see dashed lines in Fig. 4.10(a), red: Tb-order, green: Mn-order, blue: diffuse signal) are shown in Figure 4.10(b). The intensity was integrated in a range of 1° around the dashed scan lines. We recognize the green curve as temperature dependence of the Mn-order. The two successive phase transitions and the transition of the Tb-order are indicated with gray bars. The diffuse scattering which arises at the phase transition at T_{FE} is not visible at the Bragg peak due to the strong static signal. However, as the diffuse signal is broadened in $\vec{Q}$-space, we can study it even away from the Bragg peak position. The blue curves show the intensity at a rotation of $\Delta\omega = +1.8°$.
Fig. 4.10(c) shows the scan with an enlarged linear scale. By comparison with the temperature dependence at the Bragg position, we can confirm that the signal

Table 4.1.: Comparison of geometry factors and magnetic form factor $f_m(Q)$ for $\vec{Q} = (2,\ 0.27,\ L)$ in $TbMnO_3$ with intensities extracted from diffuse neutron scattering by Lorentzian fits at T_N and T_{FE} (cf. Fig. 4.11).

L	$\angle(\vec{Q},\vec{a})$	$\angle(\vec{Q},\vec{b})$	$\angle(\vec{Q},\vec{c})$	$f_m(Q)$	I_{FE} ($\frac{\text{cts}}{\text{10sec}}$)	I_N ($\frac{\text{cts}}{\text{10sec}}$)
1	22.7°	83.4°	69.2°	0.48	55.7(7)	42.8(6)
3	47.2°	85.2°	48.5°	0.26	18.9(6)	9.8(5)

purely arises from diffuse scattering. When going to lower temperature, the intensity increases towards the upper transition and decreases when the structure becomes static at T_N. At about 35 K, the signal increases again towards the second transition and decreases subsequently after T_{FE}. The increase of intensity at lower temperatures can be attributed to the Tb-order at T_{Tb}.
It has been shown in the previous section that the magnetic fluctuations in the paramagnetic phase are mainly polarized along $\vec{b}$, the directions of moments in the SDW phase. Below T_{FE}, the Mn moments order in a *bc*-spiral and fluctuations attributed to this transitions should thus be polarized along $\vec{c}$. The polarization of modes can be determined either by applied neutron polarization analysis, or by the analysis of the Q-dependence of diffuse scattering. Results from the latter approach will be presented below.
The diffuse signal around the ferroelectric phase transition at T_{FE} emphasized the picture of an almost continuous transition from SDW to spiral phase. It has been reported that in a polarized neutron experiment, the chiral magnetic cross section $-i(\vec{M}_\perp \times \vec{M}^*_\perp)_x$ has been observed up to 2 K above T_{FE} [137]. This term is non-zero for the spiral structure and zero for the spin density wave and hence allows one to distinguish both magnetic orders. These chiral fluctuations could be poled in an electric field of several $100\,\text{V}\,\text{mm}^{-1}$. Our experiment documents diffuse scattering up to 6 K above the phase transition. It is an open question whether the fluctuations only carry chirality at lower temperatures or are chiral at all time. In the latter case it is possible that the chirality of the fluctuations could not be detected at higher temperatures because of a decrease of intensity or the limited strength of the applied electric field.
In an additional experiment on IN3 at the ILL, a single crystal of $TbMnO_3$ was mounted in the $[2, 0.27, 0]/[0, 0, 1]$ scattering plane in order to investigate the polarization of the diffuse scattering around T_{FE}. As magnetic neutron scattering is only present for perpendicular components of the magnetic moments ($\vec{M}_{\perp\vec{Q}}$), the comparison of intensities at different Bragg positions reveals information about the alignment of the moments. For an angle α between $\vec{Q}$ and the magnetic moment

the intensity is given as:

$$I(\vec{Q}) \propto f_M(Q)^2 \sin(\alpha)^2 \ , \tag{4.3}$$

with the magnetic form factor $f_M(Q)$. Table 4.1 lists the angles of the scattering vectors with the principal axis and their corresponding magnetic form factor for Mn^{3+}. The angle with $\vec{b}$ is close to 90° for both $\vec{Q}$ positions, which implies that they are sensitive to magnetic moments along this direction. In contrast, moments along $\vec{c}$ are more visible at $\vec{Q}_1$ and moments along $\vec{a}$ are almost suppressed along at this position.
The temperature dependence of scattered intensity was measured at two magnetic Bragg peak positions $\vec{Q}_1 = (2,\ 0.27,\ 1)$ and $\vec{Q}_3 = (2,\ 0.27,\ 3)$. The detector position was rotated by $2\theta = +1.5°$ relative to the Bragg peak position in order to observe the diffuse scattering close to the peak. Figure 4.11 shows the intensities for both positions. The overall behaviour is similar as the one described in the previous section: Enhanced diffuse scattering is visible around the phase transitions at T_N, T_{FE} and T_{Tb}. The scattering was described by fitting Lorentzian functions to the data. At the upper transition T_N, the moments order in a spin density wave with moments along $\vec{b}$ and we expect the diffuse scattering to be along the same direction. The lower transition T_{FE} is defined by the development of the c-component of the spiral, which implies diffuse scattering along $\vec{c}$. With the given geometry factor, we expect a ratio of $I_1/I_3 = 1.24$ between two positions. The different structure factors between both positions can be taken into account by comparing the intensities of the upper transition. Both $\vec{Q}$-positions have a similar angle to $\vec{b}$ and the difference in intensity thus only depends on the magnetic form factor $f_m(Q)$. In conclusion, we find an experimental ratio of $(I_{FE,1}/I_{FE,2}) \cdot (I_{N,2}/I_{N,1}) = 1.4(1)$. The definition of the background and the description of the scattering from the Tb-moments can influence the exact result. Nevertheless this analysis allows us to state that a large amount of diffuse scattering around T_{FE} comes from fluctuations along $\vec{c}$. This is consistent with fluctuations of a bc-spiral in the SDW phase with moments parallel $\vec{b}$ [142].

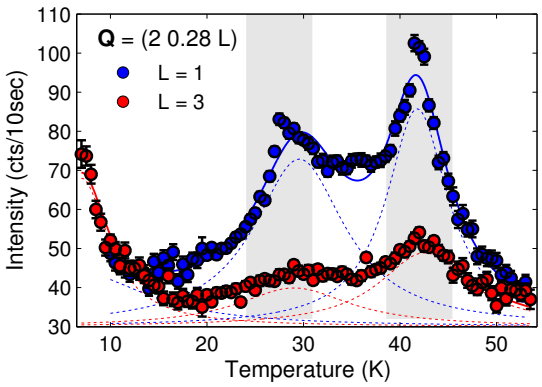

Figure 4.11: Temperature dependence of diffuse scattering around the Bragg peaks $\vec{Q} = (2,\ 0.27,\ 1)$ and $\vec{Q} = (2,\ 0.27,\ 3)$ of $TbMnO_3$ at IN3. The scattered neutron intensity was measured slightly away (1.5° in 2θ) from the Bragg peak in order to avoid elastic signal. Lorentzian functions were used to describe the data. The gray bars indicate the phase transitions at $T_N \approx 42\,\mathrm{K}$ and $T_{FE} \approx 28\,\mathrm{K}$.

4.3. Model for magnetic excitations

The magnon dispersion of $TbMnO_3$ in the multiferroic phase has been investigated intensively using inelastic neutron scattering [12,142]. The dispersion was described based on a model for $LaMnO_3$ by Moussa *et al.* and Hirota *et al.* [97,156]. The spin-wave relations derived for a circular spin-only Hamiltonian with ferromagnetic (FM) exchange J_{FM} in the *ab*-plane and antiferromagnetic (AFM) exchange J_{AFM} along $\vec{c}$ and a single-ion anisotropy could reasonably well described the dispersion along $\vec{a}$ and $\vec{c}$ [142]. In $TbMnO_3$, J_{FM} is weakened and competes with an antiferromagnetic next-nearest neighbor exchange along $\vec{b}$. This frustration leads to the development of a spin spiral with a propagation vector which is incommensurate to the crystal structure. Senff *et al.* argue that this frustration mainly affects the *b*-direction [142]. As a limitation of this approach, the different branches cannot be described with the same set of parameters. In addition, the branches along the propagation direction of the spiral $\vec{b}$ have to be treated separately. The described model works well to estimate the exchange parameters and anisotropies but a complete model of the excitation spectrum is missing.
In a first attempt to model the full magnon dispersion, a linear spin wave theory calculation was performed with Holstein-Primakoff transformation as described by Sáenz [90]. This mechanism is restricted to collinear magnetic structures with a commensurate propagation vector. The *bc*-spiral of $TbMnO_3$ had to be approximated by a sinusoidal modulated $\uparrow\uparrow\downarrow\downarrow$ spin density wave. Apparently the estimations oversimplified the situation and the results determined with this model could not reproduce the experimentally observed dispersion.
The following attempt was done using the program *SpinW* [94]. The program is based on linear spin wave theory, which was extended to account for canted and incommensurate spin structures by Toth and Lake [91]. The formalism is presented in Section 3.1.3.

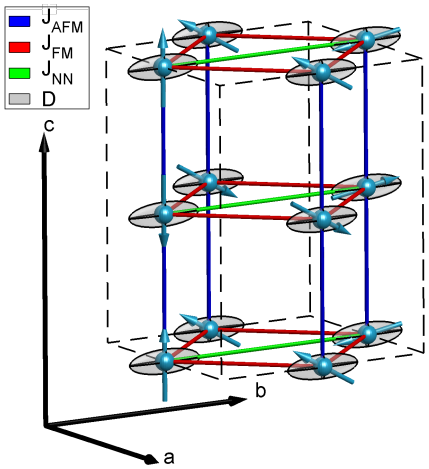

Figure 4.12: Model of the crystallographic unit cell of $TbMnO_3$, showing Mn moments in the spin-spiral phase with exchange interactions: ferromagnetic J_{FM} (red), antiferromagnetic J_{AFM} (blue) and J_{NN} (green). The elliptic easy-plane anisotropy along $\vec{b}$ and $\vec{c}$ is indicated by gray ellipses.

Model calculated with *SpinW* code

We start with the crystal structure of $TbMnO_3$, as reported by Blasco *et al.* [112] with magnetic Mn-moments of spin $S = 4/2$ and non-magnetic Tb-moments. A model of the magnetic moments and interactions is shown in Fig. 4.12. It includes the aforementioned antiferromagnetic exchange along $\vec{c}$ (blue), ferromagnetic exchange J_{FM} (red) in the *ab*-plane and the antiferromagnetic nearest-neighbor interaction J_{NN} (green) along $\vec{b}$. The single-ion anisotropy *SIA* is indicated as gray ellipsoid along $\vec{b}$.
In a first step we model the excitations along $\vec{Q} = (0,\ K,\ 1)$ for a spin-spiral with moments in the *bc*-plane and a propagation vector of $\vec{k} = (0,\ 2/7,\ 0)$ (Model M-I). The value $2/7 \approx 0.2857$ is close to the value which has been found experimentally in $TbMnO_3$ [11]. Furthermore, it allows the calculation of a commensurate structure with a magnetic unit cell extended seven times along $\vec{b}$ with respect to the crystallographic cell. The following parameters were used for the calculation: $J_{AFM} = 0.82\,\text{meV}$, $J_{FM} = -0.34\,\text{meV}$, $J_{NN} = 0.24\,\text{meV}$ and $SIA = 0\,\text{meV}$. The calculated intensities are shown in Fig. 4.13(a). The total cross section $S^{\perp}(\omega, Q)$ (left), and the components $M^{yy}(\omega, Q)$ (center) and $M^{zz}(\omega, Q)$ (right) for a [010]/[001] scattering geometry are given. This setting allows us to distinguish fluctuations of moments in the *bc* (in-plane, $M^{yy}(\omega, Q)$) from fluctuations along $\vec{a}$ (out-of-plane, $M^{zz}(\omega, Q)$).
For a ground state spiral of simple spin chain with FM nearest-neighbor and AFM next-nearest-neighbor interaction ($J_1 - J_2$ model), J_{FM} and J_{NN} are constrained as $cos(k_{inc} \cdot \pi) = J_{FM}/(2 \cdot J_{NN})$, where k_{inc} is the incommensurability along $\vec{b}$. The magnetic zone center splits into two satellites at $\vec{Q} = (0, -2/7,\ 1)$ and $\vec{Q} = (0,\ 2/7,\ 1)$. In addition, we get a clear separation of an in-plane mode (in M^{yy}), which is the phason or sliding mode of the spiral, and an out-of-plane mode

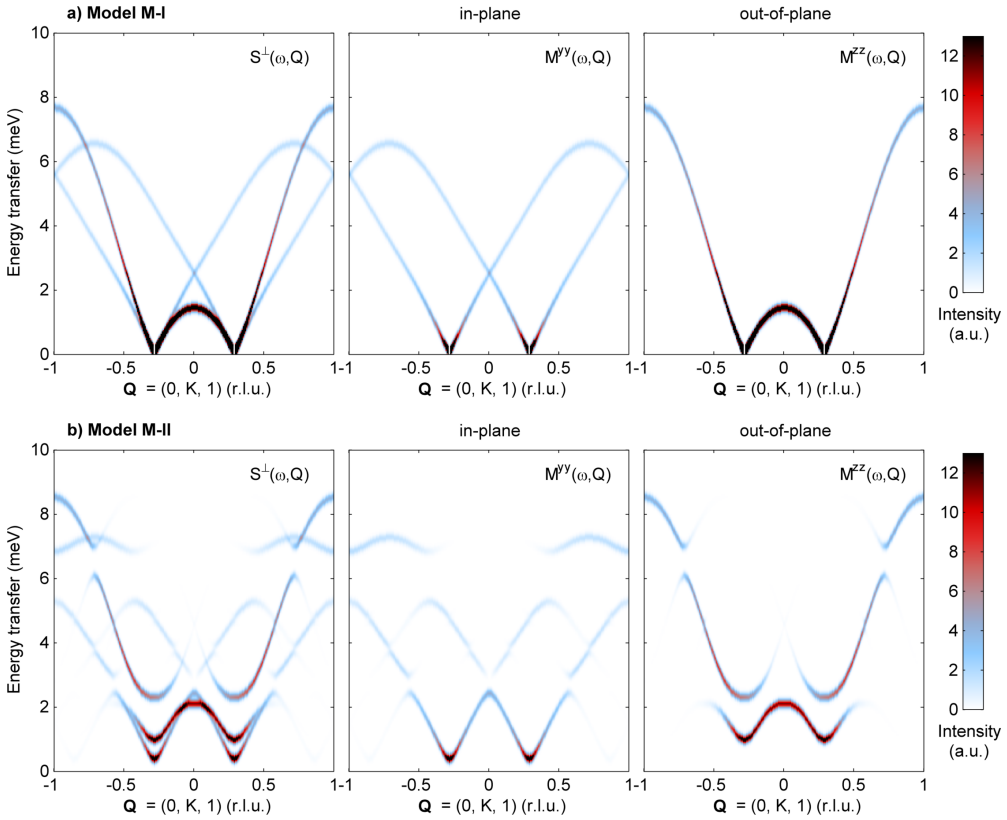

Figure 4.13.: Calculated neutron intensity for $TbMnO_3$ at $\vec{Q} = (0,\ K,\ 1)$ of the total cross section $S^{\perp}(\omega, Q)$ (left) and the components, $M^{yy}(\omega, Q)$ (center) and $M^{zz}(\omega, Q)$ (right). The scattering geometry was chosen in a way that y is in the bc-plane and z is parallel to $\vec{a}$. Different magnetic models were used for the calculation: (a) Model M-I: spiral magnetic structure with moments in the bc-plane and $\vec{k} = (0,\ 2/7,\ 0)$ and (b) model M-II: elliptic spiral with moments in the bc-plane, $\vec{k} = (0,\ 2/7,\ 0)$ and an elliptic easy-plane anisotropy.

(in M^{zz}) with moments oscillating along $\vec{a}$. At the zone center, both modes go down to zero because no anisotropy was inserted and thus there is no preferred directions for the magnetic moments. The phason mode is folded back at the zone center due to the commensurate propagation vector. The dispersion of the out-of-plane mode can be understood by looking again at the $J_1 - J_2$ model with spiral ground state $\uparrow\rightarrow\downarrow\leftarrow$. At the zone boundary $\vec{Q} = (0,\ 1,\ 1)$, the oscillations are out of phase and the alignment $\uparrow\downarrow\uparrow\downarrow$ with the highest cost in energy $E = 4J_{FM} + 2J_{NN}$ is present. The $k = 0$ zone boundary at $\vec{Q} = (0,\ 0,\ 1)$ is preferably in energy $\uparrow\uparrow\uparrow\uparrow$ with $E = -4J_{FM} + 2J_{NN}$. Finally at $\vec{Q} = (0,\ 0.5,\ 1)$, we have an intermediate state with $\uparrow\uparrow\downarrow\downarrow$ and $E = -2J_{NN}$.
The situation in $TbMnO_3$ can described more accurately by introducing an elliptic bc-spiral with moments $M_b = 3.9\,\mu_B$ and $M_c = 2.8\,\mu_B$ and $\vec{k} = (0,\ 2/7,\ 0)$,

$J_{AFM} = 0.82\,\text{meV}$, $J_{FM} = -0.38\,\text{meV}$, $J_{NN} = 0.31\,\text{meV}$, $SIA_b = -0.12\,\text{meV}$ and $SIA_c = -0.09\,\text{meV}$, shown in Fig. 4.13(b) (Model M-II). The values of the ordered magnetic moment along $\vec{b}$ and $\vec{c}$ were determined in a neutron diffraction study [11]. The elliptic spin spiral is stabilized by a distorted *bc* easy-axis, where the ratio of the major and minor axis is equal to M_b/M_c. The magnetic unit cell was extended seven times along the *b*-axis. The calculation shows an anti-crossing of modes at the zone at $\vec{Q} = (0,\ 2k,\ 1)$ and $\vec{Q} = (0,\ 1-2k,\ 1)$ (in-plane) and at $\vec{Q} = (0,\ k,\ 1)$ and $\vec{Q} = (0,\ 1-k,\ 1)$ (out-of-plane), with $k = 2/7$. The phason mode at the zone center is shifted to finite energies which is due to a pinning effect due the commensurate propagation vector. This effect appears to be rather small. The out-of-plane mode splits up into two modes at the zone center which results from the distortion of the easy-plane anisotropy. Modes polarized along $\vec{a}$ with a static *b*-component are energetically preferred to *a*-modes with a static *c*-component[b].
The developed spin-wave model produces a collection of three zone-center modes: a low energy phason mode, an intermediate energy out-of-plane mode with static *b*-component and a high-energy out-of-plane mode with static *c*-component. This corresponds perfectly to the prediction by Katsura *et al.* in spiral magnets, shown in Fig. 4.4. Only the intermediate out-of-plane mode with static *b*-component should be electrically active by the DM mechanism: This mode rotates the spiral plane around $\vec{b}$ which leads to an oscillation of the ferroelectric polarization along $\vec{a}$ via $\vec{P}_{el} \propto \vec{r}_{i,j} \times (\vec{S}_i \times \vec{S}_j)$. This mode is the DM-electromagnon.
In the following we will compare the model described in this section with results reported in the literature. In Section 4.4 we will compare the simulated dispersion with data from inelastic neutron scattering and infrared spectroscopy.

Comparison to the literature

Our results of the elliptic cycloid dispersion along the direction of the propagation vector perfectly match a recently reported calculation by Milstein and Sushkov [143]. Instead of linear spin wave theory they use the σ-model-like effective-field theory to model the magnon branches in $TbMnO_3$. They work with an incommensurate propagation vector of $\vec{k} = (0,\ 0.28,\ 0)$ a deformed elliptic spin spiral and introduce an additional nearest-neighbor exchange J_{3a} along $\vec{a}$. Their anisotropy-terms consists of an easy-axis along $\vec{b}$ and a DM-like anisotropic exchange along $\vec{a}$, which is equivalent to an easy-plane crystal field anisotropy in our model [143]. They attribute this feature to the dipolar displacement of the ferromagnetic polarization

[b] It should be mentioned that the same model with an incommensurate propagation vector did not show the splitting of out-of-plane modes. We attribute this discrepancy to problems of the implementation of incommensurate structures.

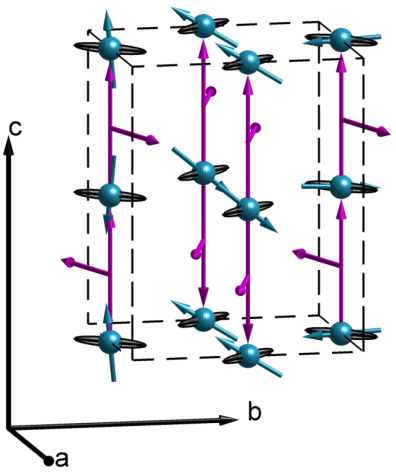

Figure 4.14: Model of the crystallographic unit cell of $TbMnO_3$, showing Mn moments in the spin spiral phase with antisymmetric exchange interactions along $\vec{c}$ (purple vectors) and staggered singe ion anisotropies along $\vec{b}$ (gray ellipsoids).

in the multiferroic phase. In their model, this DM interaction is $D = 0.2\,\text{meV}$ which appears to be too strong for the relatively weak ion-displacement. First-principle calculations estimated very small displacements of the order of 10^{-4} [157, 158], the same order was found in an X-ray study [159]. We verified the influence of the additional exchange J_{3a} and the deformation of the ellipse to our model. The small deformation proposed by Milstein and Sushkov only leads to minor variation and J_{3a} did not affect the dispersion along $\vec{b}$.
A separate calculation of the spin dynamics has been done by Mochizuki *et al.* [114]. The underlying Hamiltonian consists of five terms: $H = H_{ex} + H^D_{sia} + H^E_{sia} + H_{DM} + H_{biq}$. The isotropic exchanges in H_{ex} are identical to our model. The introduced anisotropies include a hard axis H^D_{sia} along $\vec{c}$ and alternating local hard and easy axes H^E_{sia} in the *ab*-plane due to staggering of orbitals. The DM terms along $\vec{c}$ (DM_c) and in the *ab*-plane (DM_{ab}) are taken from local spin density approximation calculations [160] and experiments on $LaMnO_3$ [161]. They arise from the $[MnO_6]$-octahedra tilting and rotation in $TbMnO_3$ (due to Jahn-Teller and $GdFeO_3$ distortion), which moves the oxygen ions away from the symmetry position between two manganese ions [160, 162]. The DM_c is reported to be four times stronger [161] and plays a crucial role in this model. It is able to stabilize the spin spiral in the *bc*-plane and, in competition with H^D_{sia}, it can explain the spiral plane flop in HF-C phases [141, 163, 164]. Finally, the biquadratic interaction term H_{biq} in the *ab*-plane originates from the spin-phonon coupling [165]. It helped to reproduce optical spectra of $DyMnO_3$ [114]. The calculated magnon dispersion shows strong anti-crossing and folding of modes. It does not properly reproduce the magnon dispersion in $TbMnO_3$ [116, 142] or $DyMnO_3$ [55] measured by INS.
The essential differences between the model developed in this section and the model by Mochizuki *et al.* is the handling of the anisotropies. Our model stabilizes the *bc*-cycloid by a distorted easy-plane anisotropy while the other model uses an accurate description of easy-axis anisotropies and DM interactions. We modified

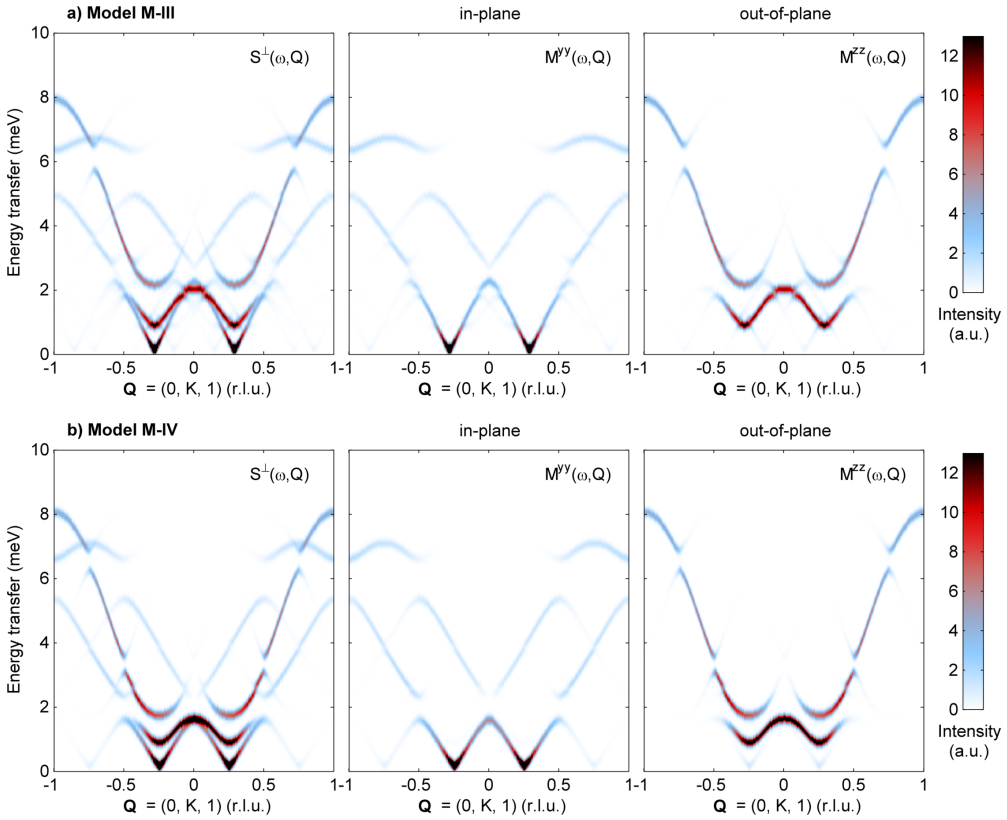

Figure 4.15.: Calculated neutron intensity for $TbMnO_3$along $[0K1]$ of the total cross section $S^{\perp}(\omega, Q)$ and the components $M^{yy}(\omega, Q)$ and $M^{zz}(\omega, Q)$. The scattering geometry was chosen so that y is in the bc-plane and z is parallel $\vec{a}$. Different magnetic models were used for the calculation: (a) Model M-III: elliptic spiral with moments in the bc-plane, $\vec{k} = (0,\ 2/7,\ 0)$ and a staggered elliptic easy-plane anisotropy and (b) model M-IV: elliptic spiral with moments in the bc-plane, $\vec{k} = (0,\ 1/4,\ 0)$, easy-axis anisotropy along $\vec{b}$ and anisotropic exchange (DM).

our model step-by-step in order to analyze the implications on the dispersion. Figure 4.14 shows crystallographic cell of $TbMnO_3$ including the Mn-moments, a staggered easy-plane anisotropy in the ab-plane and a DM_c anisotropy along $\vec{c}$. The vectors point towards the displacement of oxygen ions from the symmetric position between two Mn-ions. The DM interaction in the ab-plane was neglected because of its reported weakness ($DM_c/DM_{ab} \approx 4$ in $LaMnO_3$) [161].
First, we insert the staggering of the anisotropy direction in the ab-plane. The model consists of an elliptic bc-spiral with moments $M_b = 3.9\,\mu_B$ and $M_c = 2.8\,\mu_B$ and $\vec{k} = (0,\ 2/7,\ 0)$, $J_{AFM} = 0.82\,\text{meV}$, $J_{FM} = -0.38\,\text{meV}$, $J_{NN} = 0.31\,\text{meV}$, $SIA_b = -0.18\,\text{meV}$ and $SIA_c = -0.09\,\text{meV}$, shown in Fig. 4.15(a) (Model M-III). The overall dispersion is unchanged from the staggering of the anisotropy. Minor additional features are visible which may arise due to computational problems. To

introduce the staggered anisotropy, the symmetry of the structure had to be set to $P1$, which strongly increases the number of parameters for the calculation.
In a second step, the anisotropy along $\vec{c}$ has been removed and the DM interaction activated. The model has the following parameters: elliptic *bc*-spiral with moments $M_b = 3.9\,\mu_B$ and $M_c = 2.8\,\mu_B$ and $\vec{k} = (0,\ 2/7,\ 0)$, $J_{AFM} = 0.82\,\text{meV}$, $J_{FM} = -0.38\,\text{meV}$, $J_{NN} = 0.31\,\text{meV}$, $SIA_b = -0.10\,\text{meV}$, $SIA_c = 0\,\text{meV}$, $DM_c = (0.64, -0.2,\ 0)\text{meV}$. In the presence of the DM_c interaction, the moments become alternately modulated [164]. To account for this effect, the moments were tilted $\pm 4°$ around the *a*-axis (cf. Fig. 4.14). The calculated intensity is shown in Fig. 4.15(b) (model M-IV).
The result again nicely reproduces the main features of the previous calculations. This calculation of model M-IV verifies the assumption that the *bc* spin cycloid can be stabilized by the combination of an easy-axis anisotropy and a DM interaction. In the presented calculation, a strong antisymmetric exchange of $DM_c = (0.64, -0.2,\ 0)\,\text{meV}$ is required to reproduce the experimental dispersion. The strength of the DM interaction seems to be exaggerated for a relativistic effect induced by spin-orbit coupling [6, p. 144]. In transition-metal ions, the orbital momentum is quenched in the crystal field and spin-orbit coupling can be neglected for most observed systems [53, p. 48]. The values are eight times stronger than the values experimentally determined for $LaMnO_3$ ($DM_c \approx (0.08, -0.025,\ 0)\,\text{meV}$) [161].

The spin waves in the spiral phase of $TbMnO_3$ have been calculated assuming three different approaches. Their main difference with each other lays in the stabilization of the spiral along the *c*-axis: Model M-II assumes a *bc* easy-plane anisotropy, model M-III assumes that the ferroelectric displacement results in an anisotropy along $\vec{c}$, and in model M-IV the spiral is stabilized by an antisymmetric exchange along $\vec{c}$. The comparison of the models M-II, M-III and M-IV shows, that the principal features of the dispersion can be reproduced equally well by all models. In the following section we will compare the spin-wave models with the magnon dispersion obtained by INS and discuss the different sets of exchange parameters.

4.4. Magnetic excitations in the incommensurate phase

In the previous section, we developed a simple spin model with easy-plane anisotropy which nicely reproduces the main features of the magnon dispersion of $TbMnO_3$ in the multiferroic phase. The origin of the easy axis along $\vec{c}$, which stabilizes the spin spiral in the *bc*-plane is still matter of debate. Mochizuki *et al.*

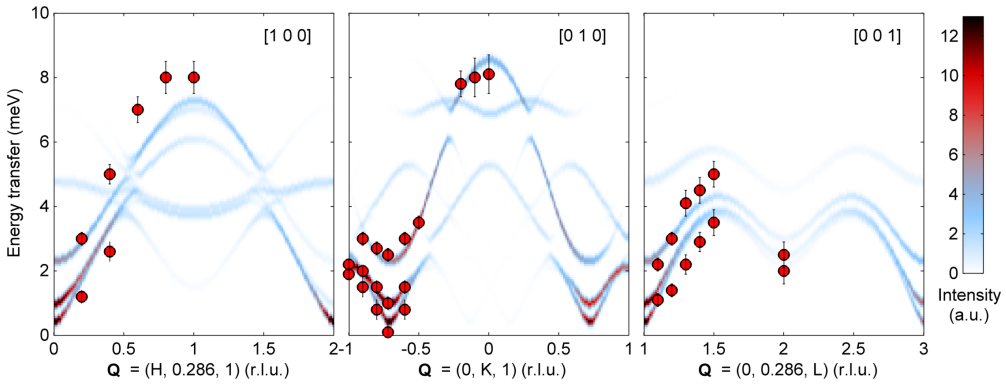

Figure 4.16.: Calculated neutron intensity for $TbMnO_3$ along (a) $[H, 0.28, 1]$, (b) $[0, K, 1]$ and (c) $[0, 0.28, L]$ using model M-II. The calculation is based on an elliptic spiral with moments in the bc-plane, $\vec{k} = (0,\ 2/7,\ 0)$ and an elliptic easy-plane anisotropy. The dispersion was fitted to values obtained from inelastic neutron scattering (red points) taken from Ref. [142].

suggest the influence of the intrinsic DM interaction along $\vec{c}$ [114], whereas Milstein and Sushkov propose the induced ferroelectric displacement in the multiferroic phase to account for it [143]. When we reproduce both models, M-III and M-IV, using *SpinW* [94], strong values of these effects are necessary to stabilize the spiral which seems to overestimate the strength in the real system.
In a phenomenological approach by Mostovoy, the strong influence of Tb-anisotropies was discussed [43] which have not been taken into account by any of these models. The introduction of Tb moments into the calculations presents a considerable enhancement of complexity, since interactions between Tb and Mn moments also have to be considered. Therefore, we will continue to describe our data with the distorted easy-plane anisotropy model M-II and leave the origin of the anisotropy along $\vec{c}$ open for discussion. The *MATLAB* code for model M-II is given in appendix B.

4.4.1. Fitting of the magnon dispersion

The magnon dispersion in the incommensurate multiferroic phase of $TbMnO_3$ has been investigated in detail using inelastic neutron scattering by Senff *et al.* [12, 116, 142]. We will use the positions of the different modes extracted from this data to fit the parameters of our model M-II, which was calculated using the *SpinW* code [94]. Figure 4.16 shows the calculated magnon intensity along the principal directions $[H, 0.28, 1]$, $[0, K, 1]$ and $[0, 0.28, L]$. The mode energies determined by INS at 17 K taken from Ref. [12] are indicated with red points.

Table 4.2.: Comparison of interaction exchanges and anisotropies in the multiferroic phase of $TbMnO_3$ by Senff *et al.* [12], Milstein and Sushkov [143] and this work (M-II, M-III, M-IV). The next-nearest neighbor exchange is fixed to the propagation vector $\vec{k} = (0,\ k_{inc},\ 0)$ as $J_{NN} = J_{FM}/2\cos(k_{inc}\pi)$.

Model	J_{FM} (meV)	J_{AFM} (meV)	*SIA* (meV)	DM (meV)
Senff *et al.*, $\omega_{\perp 1}$	-0.10(1)	0.37(3)	-0.02(1)	
Senff *et al.*, $\omega_{\perp 2}$	-0.15(1)	0.60(3)	-0.11(2)	
Milstein *et al.*	-0.3	0.9	-0.125	-0.2 (DM_{FE})
Model M-II	-0.38	0.82	-(0,0.12,0.09)	
Model M-III	-0.38	0.82	-(0,0.18,0.09)	
Model M-IV	-0.38	0.82	-(0,0.1,0)	(0.64,-0.2,0) (DM_c)

The exchange parameters and the anisotropies of our model have been fitted to the experimental data. The presented calculation was done assuming an elliptic *bc*-spiral with moments $M_b = 3.9\,\mu_B$ and $M_c = 2.8\,\mu_B$ and $\vec{k} = (0,\ 2/7,\ 0)$, $J_{AFM} = 0.82\,\text{meV}$, $J_{FM} = -0.38\,\text{meV}$, $J_{NN} = 0.31\,\text{meV}$, $SIA_b = -0.12\,\text{meV}$ and $SIA_c = -0.09\,\text{meV}$. The points extracted from INS data are very well described by the simulation along the direction $\vec{b}$ of the propagation vector. The commensurate approximation $k = 2/7 \approx 0.286$ of the incommensurate propagation vector seems to be accurate. The dispersion along $\vec{a}$ and $\vec{c}$ can qualitatively be described but there are deviations from the experimentally observed positions.
At this point, we would like to recall the simplicity of the model, which only consists of three exchange interactions and two single-ion anisotropies. In the real system, several other effects may influence the spin dynamics of the Mn-moments, such as (a) the DM interactions both along $\vec{c}$ and in the *ab*-plane [163], (b) the ferroelectric displacements [166], (c) biquadratic [114] and ring exchange interaction [167] and (d) the influence of the strong Tb-moments via direct exchange or crystal field [131]. The complexity of this system highlights the fact that the dispersion can be described by a relatively simple model.
The determined interaction exchanges and anisotropies are compared with values previously reported in Table 4.2. The values from Senff *et al.* differ by a factor of two due to a different definition of the parameters. Bonds between moments are counted either once or twice in different models, producing a factor of two.
The accuracy of the estimated exchange values can be verified by calculating the Néel temperature T_N and the Weiss temperature using the Weiss mean-field

equations [162]:

$$T_{N,MF} = (4/3)S(S+1)(2 \cdot J_{FM} - J_{AFM} - J_{NN})/k_b \approx 30\,\mathrm{K} \tag{4.4}$$

$$\theta_{N,MF} = (4/3)S(S+1)(2 \cdot J_{FM} + J_{AFM} + J_{NN})/k_b \approx -171\,\mathrm{K} \tag{4.5}$$

These theoretical values can be compared to experimental observations. The antiferromagnetic ordering temperature of $TbMnO_3$ is $T_N \approx 41\,\mathrm{K}$, where the Mn moments form a spin-density-wave. Yet, the order is incomplete, as only the b-component orders. Below $T_{FE} \approx 28\,\mathrm{K}$, when the moments form a bc-spiral, the absolute ordered moment approaches the value of the isolated Mn^{3+} moment of $\mu_{eff} = 4.9\,\mu_B$ [112]. The mean field value of the Néel temperature fits relatively well the experimental values. The Weiss temperature was observed to be $\theta_N = -21.9(1)\,\mathrm{K}$ for a polycrystalline sample of $TbMnO_3$ [148]. Single crystal data showed strong deviations of this value along the major symmetric directions: $\theta_{N,a} = 17.6(1)\,\mathrm{K}$, $\theta_{N,b} = -9.3(5)\,\mathrm{K}$ and $\theta_{N,c} = -128(1)\,\mathrm{K}$. Tb moments order below T_{Tb} along $\vec{a}$, and are dominant along this direction. The same accounts along $\vec{b}$, since the Tb-moments follow the ordering of Mn-moments in the upper phase [11]. The c-direction primarily sees the Mn-moments and the measured values correspond most to the value from the mean-field approach, which considers only Mn-ordering. The frustration of the Mn-system is visible in the strong ratio of Weiss and Néel temperature $f = \theta/T_N \approx -5.7$.

Comparison with INS and IR data

In the proposed model M-II, there are two a-polarized out-of-plane modes at the magnetic zone center at $\omega_{\perp 1} = 1.0\,\mathrm{meV}$ and $\omega_{\perp 2} = 2.5\,\mathrm{meV}$. The splitting is due to the distorted easy plane anisotropy: modes polarized along $\vec{a}$ with a static b-component (rotation around $\vec{b}$) are energetically preferred to $\vec{a}$-modes with a static c-component (rotation around $\vec{c}$). These two modes correspond to a rotation of the spins around $\vec{b}$ (cycloid mode) and to a rotation around $\vec{c}$ (helical mode), referred to as $\omega_{\perp 1}$ and $\omega_{\perp 2}$. When we apply the DM mechanism to both excitations only $\omega_{\perp 1}$ changes the direction of the induced electric polarization and should thus be electrically active (see Fig. 4.4 for comparison). The rotation of the spin-plane around $\vec{b}$ leads to an oscillation of the induced electric polarization along $\vec{a}$, while a rotation around $\vec{c}$ modulates only the magnitude of P_c and leaves its direction unchanged.
Senff *et al.* separated the in-plane mode from the two out-of-plane modes at the zone center experimentally using neutron polarization analysis [12]. The extracted

energies and mode-polarizations perfectly match our model. The phase of the out-of-plane modes could not be determined. Looking at the magnetic phase diagram, the authors argue that the rotation around $\vec{b}$ is lower in energy since the electric polarization flips from P_c to P_a in modest magnetic fields $H_{a,b}$ [8]. They conclude that for the case of a perfect circular cycloid $\omega_{\perp 1} = 1.0\,\mathrm{meV}$ is the only electrically active mode, which agrees with our argumentation. In addition, Senff *et al.* point out, that the strict separation of both out-of-plane modes in the case of an elliptic structure will not be valid anymore, which would allow a mixture of modes, rendering both magnon excitations IR active [142].
Pimenov *et al.* report two electrically active modes, a stronger broad mode at $20\,\mathrm{cm}^{-1} = 2.48\,\mathrm{meV}$ and a weaker one at $10\,\mathrm{cm}^{-1} = 1.24\,\mathrm{meV}$ [57, 59]. Both positions perfectly correspond to the out-of-plane modes of our model and INS experiments, but their spectral weight seems permuted with respect to the previous discussion. Following the previous discussion, one would expect $\omega_{\perp 1}$ to be stronger relative to $\omega_{\perp 2}$.
While in INS experiments one looks at the magnetic zone center at $k_{inc} = 0.28$, in optical spectroscopy one is restricted to the wave vector of the photon which is always close to zero [59]. Yet, static modulations of the magnetic structure with the same wave vector can preserve the momentum conservation. The IR spectra are thus composed of contributions at different wave vectors, such as $k = 0$, $k = k_{inc}$ and $k = 2 \cdot k_{inc}$, and their separation is not trivial [59]. It seems thus convincing that the signal at $10\,\mathrm{cm}^{-1}$ is attributed to the zone-center mode $\omega_{\perp 1}$, which is electrically active in the DM-picture. The strong spectral weight of the upper mode may arise from a two-magnon process [65,142] or through the exchange striction mechanism [55, 114].

4.4.2. Comparison to time-of-flight data

Until now the magnon dispersion in the multiferroic phase of $TbMnO_3$ has only been reported along three main symmetry directions, as discussed in the previous section. In order to verify the proposed spin-wave model M-II, a comparison to a larger dataset is highly desired. We mounted a large single crystal ($25 \times 6 \times 6\ \mathrm{mm}^3$) in a cryostat in $[0, 1, 0/0, 0, 1]$ scattering geometry on the disk chopper time-of-flight (TOF) spectrometer IN5 at the ILL. The instrument is set in direct geometry: a monochromatic neutron pulse arrives at the sample and the position and flight time of the scattered neutrons is measured in a detector bank covering a large solid angle. The vertical angular range of the detector bank is $\pm 20.55°$ which limits the accessible range vertically to the scattering plane, i.e. the a-direction. The accessible energy and Q range as well as the resolution can be modulated by

the choice of the incident neutron wavelength. The frequency of neutron pulses is set so that the highest energy transfer is 70 % of the incident energy. The experiment has been performed at 17 K using three different incident neutron wavelengths, $\lambda_{i,1} = 2.0$ Å ($E_{i,1} = 20.5$ meV), $\lambda_{i,2} = 3.75$ Å ($E_{i,2} = 5.8$ meV) and $\lambda_{i,3} = 5.2$ Å ($E_{i,3} = 3.0$ meV). The corresponding energy resolutions determined at the elastic line were $\Delta E_1 \approx 0.84$ meV, $\Delta E_2 \approx 0.22$ meV and $\Delta E_3 \approx 0.08$ meV. The resolutions are typical for this instrument ($\Delta E_i/E_i \approx$1.7 to 3.0 meV) [86].
The treatment of the four-dimensional $S(\vec{Q}, \omega)$ datasets was done using the *Horace* suite for *MATLAB* [87]. No background subtraction was performed. Two-dimensional cuts were generated from the dataset by integrating over a specific range in Q and ω. For an incident neutron wavelength $\lambda_{i,1}$ the integration range was 0.2 $(r.l.u)$ for Q and 1 meV for E_f ($\lambda_{i,2}$: 0.1 $(r.l.u)$ and 0.4 meV, correspondingly). The 2D-cuts were reshaped using the implemented *smooth* function for 2×2 pixels for a better visualization of the data [87].
The simulation of the TOF data was done using the distorted easy-plane model described in the previous section. 2D-cuts were produced using *SpinW* by taking into account the magnetic form factor $f_m(Q)$ of Mn^{3+} and the Bose-factor for energy-loss scattering $1/(1 - \exp(\frac{-E}{k_b T}))$. For the (Q, E)-maps the energy resolution was adapted to the experimentally determined value. A finite Q-resolution and an integration over the vertical Q-component were considered to be dispensable. Accordingly, the simulated constant energy maps were integrated over a finite energy range (corresponding to the experiment) and no Q-resolution was applied. Figures 4.17 and 4.18 show the comparison of TOF data and *SpinW* simulation for selected Q-scans along the principal directions. The intensity is logarithmically color-coded. For all scans, the data could be nicely reproduced. The broadening of the modes in the TOF data relative to the calculation is partly due to the neglected Q-resolution and vertical integration of the simulation. Mainly, it arises from the intrinsic linewidth of the excitations, which has been found to be significantly larger than the best resolution used here, i.e. higher than 0.2 meV [116]. The datasets using an incident neutron wavelength of $\lambda = 2.0$ and 3.75 Å show spurious signal below 2 meV for wavelengths below the lattice constant of aluminum $\lambda < 4.8$ Å coming from the aluminum sample holder and the cryostat.
The comparison of TOF data and *SpinW* simulation for constant energy cuts in the *bc*-plane is shown in Figures 4.19 and 4.20. The difference between the linewidth of experimental data and simulation can again be attributed to the broadened intrinsic linewidth of the magnon excitations in $TbMnO_3$ and the missing Q resolution in simulation.

The comparison of TOF data in the multiferroic phase of $TbMnO_3$ at 17 K with simulated neutron intensity maps using model M-II with parameters given in Table 4.2 is very convincing, cf. Figs 4.17, 4.18, 4.19 and 4.20. The dispersion along all main symmetry directions, as well as the intensity weight is reproduced

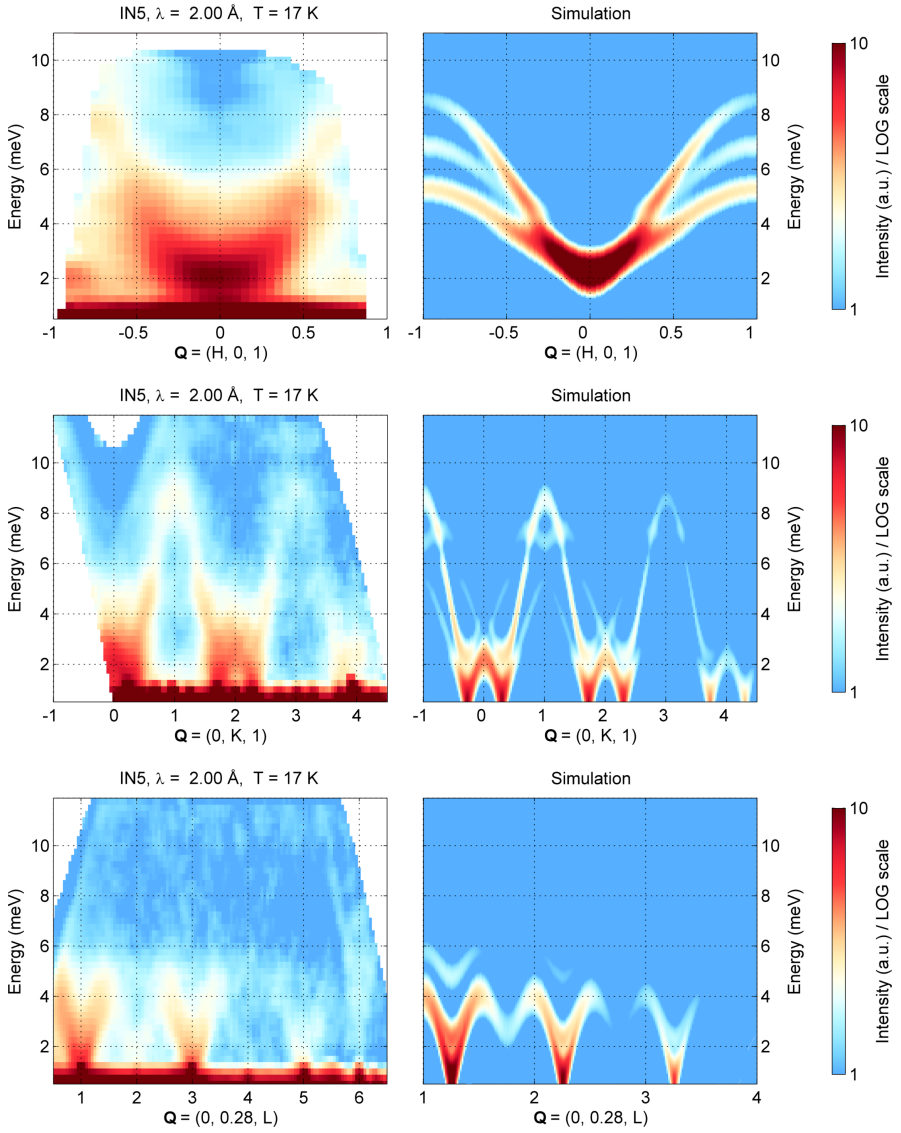

Figure 4.17.: Comparison of inelastic scattering maps of $TbMnO_3$ obtained from neutron TOF spectroscopy at IN5 (left) at $T = 17\,\mathrm{K}$) and simulation (right). The incident neutron wavelength and the energy resolution are given in the plot headers. Model M-II (cf. Tab. 4.2) was used for the simulation and the Bose factor as well as the magnetic form factor were taken into account.

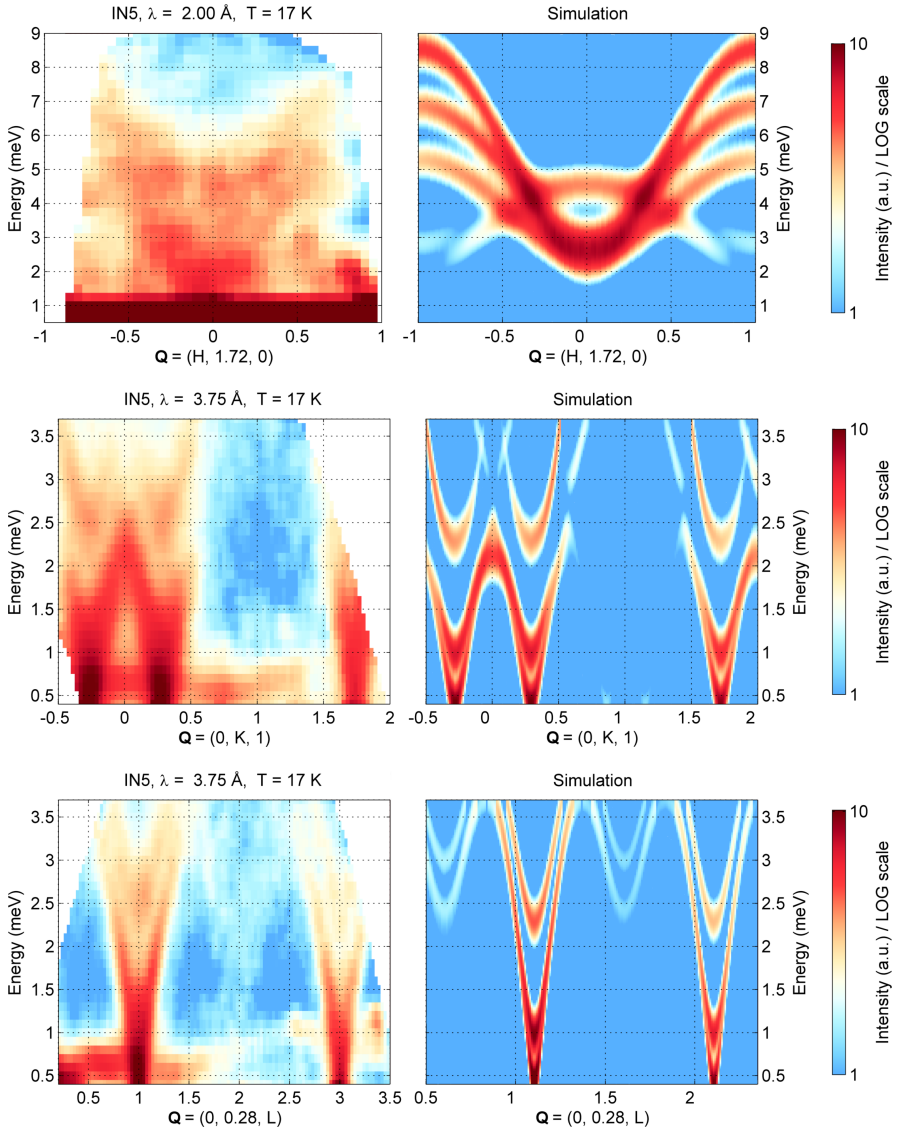

Figure 4.18.: Comparison of inelastic scattering maps of $TbMnO_3$ obtained from neutron TOF spectroscopy at IN5 (left) at $T = 17\,\mathrm{K}$) and simulation (right). The incident neutron wavelength and the energy resolution are given in the plot headers. Model M-II (cf. Tab. 4.2) was used for the simulation and the Bose factor as well as the magnetic form factor were taken into account.

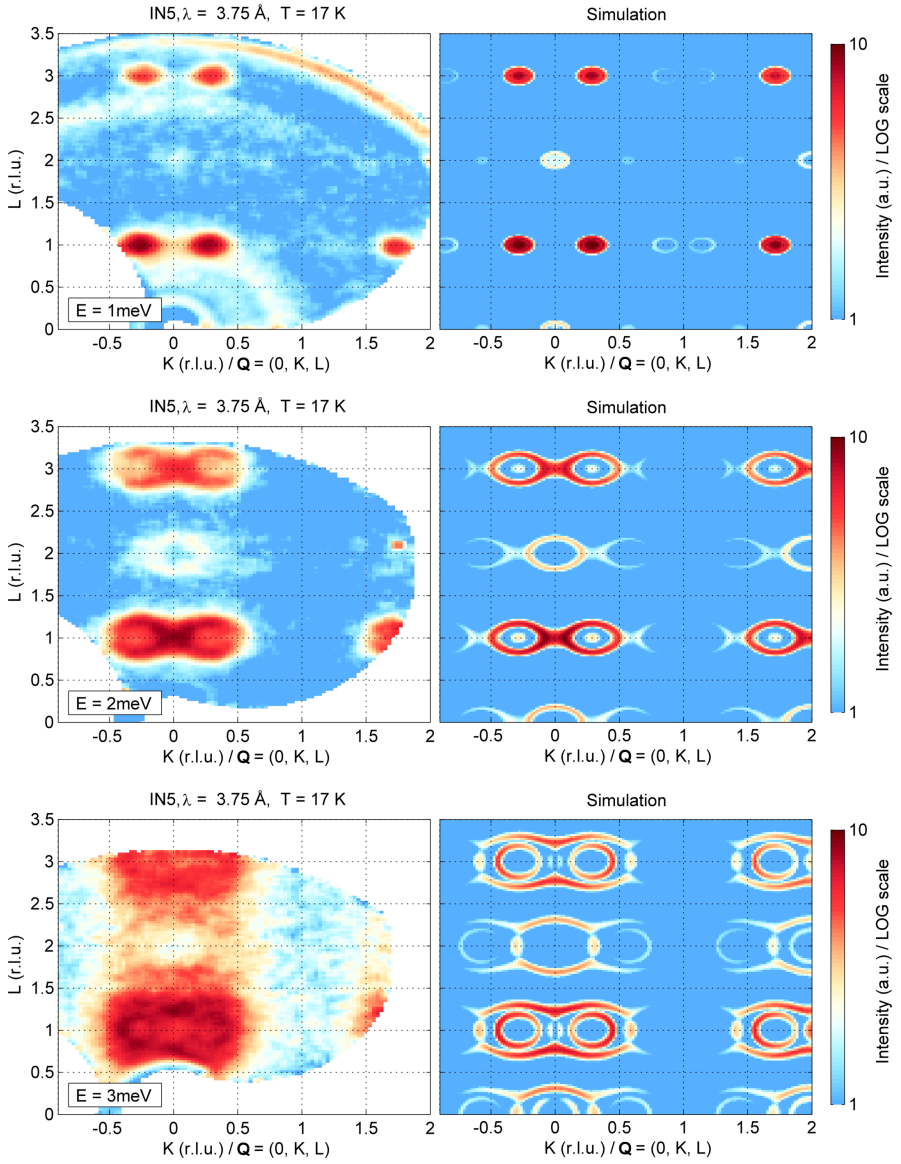

Figure 4.19.: Comparison of inelastic scattering maps of $TbMnO_3$ obtained from neutron TOF spectroscopy at IN5 (left) at $T = 17\,\mathrm{K}$) and simulation (right) in the $[0, K, L]$ plane. The incident neutron wavelength and the energy resolution are given in the plot headers. Model M-II (cf. Tab. 4.2) was used for the simulation and the Bose factor as well as the magnetic form factor were taken into account.

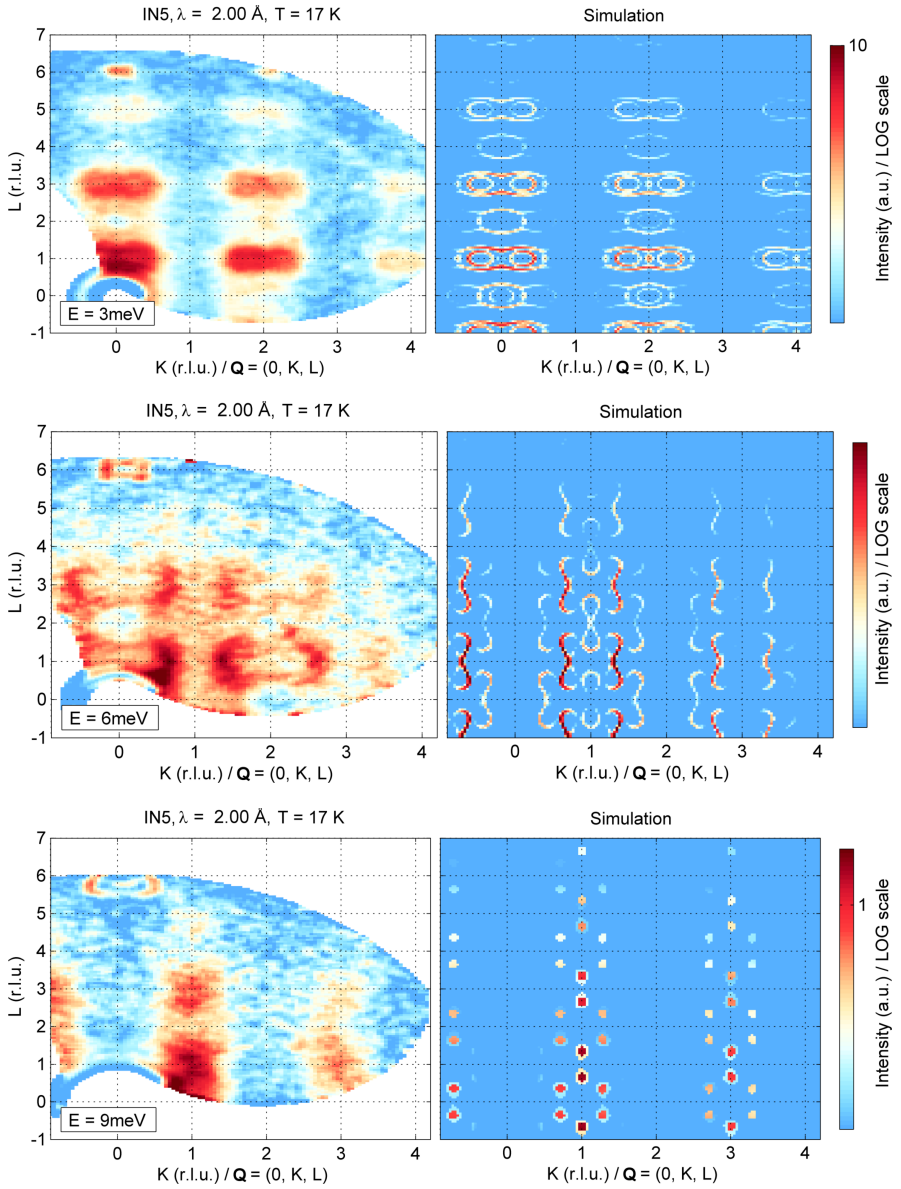

Figure 4.20.: Comparison of inelastic scattering maps of $TbMnO_3$ obtained from neutron TOF spectroscopy at IN5 (left) at $T = 17\,\mathrm{K}$) and simulation (right) in the $[0, K, L]$ plane. The incident neutron wavelength and the energy resolution are given in the plot headers. Model M-II (cf. Tab. 4.2) was used for the simulation and the Bose factor as well as the magnetic form factor were taken into account.

quite well. The model M-II assumes only the ordering and interaction of Mn moments with a distorted planar anisotropy. A qualitative description of the excitation spectra in this phase is therefore possible without considering a Tb-Mn interaction and the influence of intrinsic and ferroelectric DM interactions. These effects may be hidden in the model in the anisotropy term along $\vec{c}$, which stabilizes the spin-spiral in the *bc*-plane.

4.4.3. Chirality of excitations

Further insight of the complex excitation spectra can be gained by applying experimental techniques to separate the different branches. Polarized neutrons were successfully applied to distinguish the polarization of the three zone-center modes [12]. By the application of an electric field, it is possible to obtain a mono-domain sample and thus probe the magnetic chiral component $-i(\vec{M}_\perp \times \vec{M}^*_\perp)_x$. This technique has been been performed for $TbMnO_3$ on magnetic Bragg peaks [49], the temperature dependence of the propagation vector [128] and the magnon dispersion along $[H, 0.28, 1]$ [137].
Aim of this experiment was the investigation of the chiral components of the magnons along $\vec{Q} = (2,\ K,\ 1)$ in the multiferroic material $TbMnO_3$ using spherical polarization analysis with *Cryopad* in order to distinguish the different magnetic excitations by their origin. In a simple cycloidal incommensurate structure one may expect the phason branch to exhibit a strong chiral component which should vary with the propagation vector. Contrarily, the out-of-plane modes should not carry any chiral signal.
A large single crystal of $TbMnO_3$ was mounted in [201]/[010] scattering geometry on the cold neutron TAS instrument IN14 with *Cryopad* option at the ILL. Throughout the experiment, we worked with a final neutron energy of $E_f = 5.00\,\mathrm{meV}$ ($k_f = 1.55\,\mathrm{\AA}^{-1}$) and a Be-filter on k_f. The neutrons were polarized by a supermirror bender and analyzed by the Bragg reflection on a Heusler crystal. The flipping

Table 4.3.: Coordinate system in a polarized neutron experiment at $\vec{Q} = -(2,\ 0.28,\ 1)$ in $TbMnO_3$ mounted in [201]/[010] geometry.

	$\vec{Q}$ (r.l.u.)	$\angle(\vec{Q},\vec{a})$	$\angle(\vec{Q},\vec{b})$	$\angle(\vec{Q},\vec{c})$
x	$(-2.00, -0.28, -1.00)$	20.8°	83.2°	70.4°
y	$(\ 0.56, -5.00,\ 0.28)$	97.0°	7.5°	92.5°
z	$(\ 1.00,\ 0.00, -2.00)$	124.9°	90°	39.9°

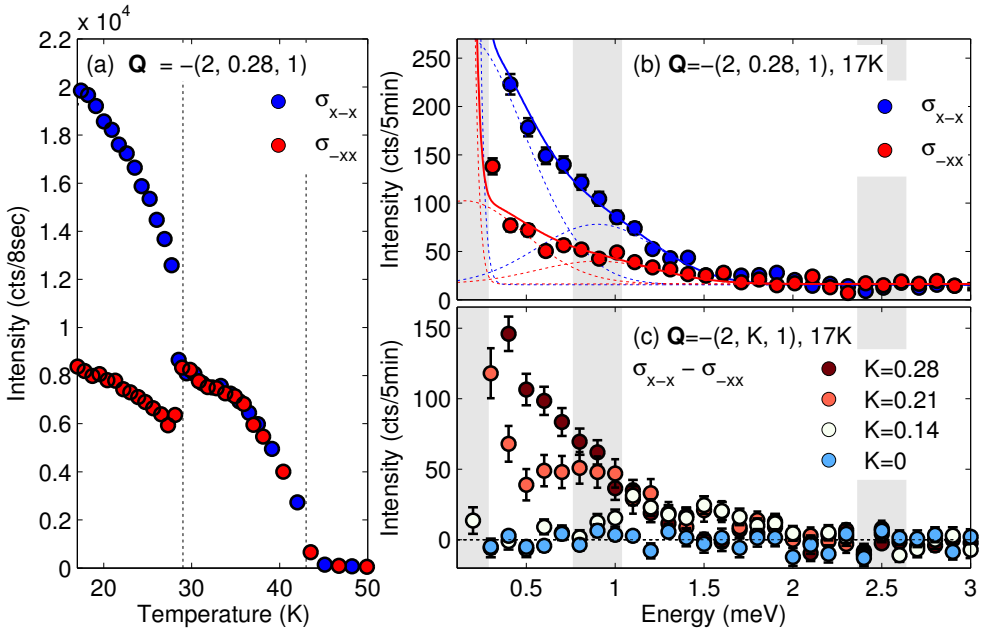

Figure 4.21.: Chiral magnetic scattering of $TbMnO_3$ measured by polarized neutrons. (a) Temperature dependence of the cross sections $\sigma_{x\bar{x}}$ and $\sigma_{\bar{x}x}$ at the magnetic Bragg peak $\vec{Q} = -(2,\ 0.28,\ 1)$ at IN14. An electric voltage of 7.8 kV ($\approx 355\,\mathrm{V\,mm^{-1}}$) was applied along $\vec{c}$. (b) Energy scan at the magnetic zone center $\vec{Q}$ for both channels at $T = 17\,\mathrm{K}$. Two Gaussian functions were fitted to each curve. (c) Evolution of the inelastic chiral intensity $\sigma_{x\bar{x}} - \sigma_{\bar{x}x}$ along $-[2, K, 1]$ at $T = 17\,\mathrm{K}$. The gray bars indicate the positions zone-center modes [12].

ratio on a magnetic Bragg peak was $FR \approx 36$ which corresponds to a polarization of the neutron beam of approximately 95 %. The resolution at the given analyzed wavelength was determined on the elastic line, $\Delta E \approx 0.24\,\mathrm{meV}$. The crystal was placed between two thin aluminum plates in order to apply an electric field along the crystallographic c-direction, the direction of the electric polarization in the multiferroic phase. The distance of about 22 mm between the two aluminum plates therefore requires a high voltage to create the electric field needed to pole the large crystal. We were able to apply a voltage of 7.8 kV corresponding to an electric field of $355\,\mathrm{V\,mm^{-1}}$.

The chirality of the magnetic scattering can be obtained straightforwardly by the determination of the chiral magnetic component. One has to ensure that the propagation vector forms an angle with the basal plane of the spin spiral. We performed the experiment around the position $\vec{Q} = -(2,\ 0.28,\ 1)$. We remind of the coordination system used in a polarized neutron experiment with x parallel $\vec{Q}$, z vertical to the scattering plane and y perpendicular to x and y. The corresponding vectors and their angles to the principal crystallographic directions are shown in

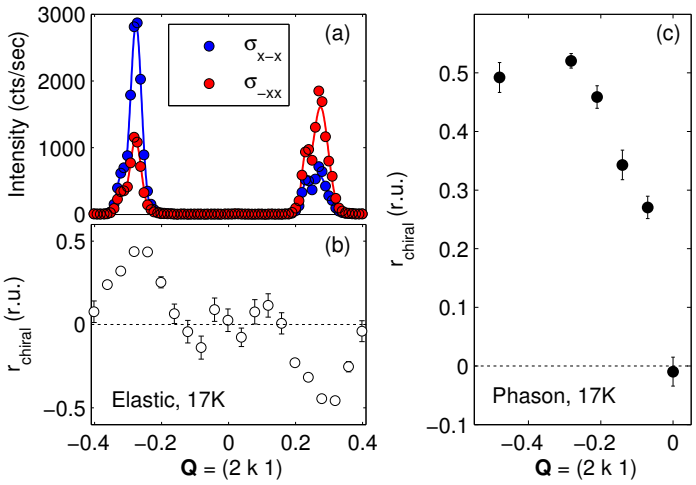

Figure 4.22: Chirality of elastic and inelastic magnetic scattering in $TbMnO_3$ along $\vec{Q} = -(2,\ k,\ 1)$ at IN14: (a) Elastic intensity of cross sections $\sigma_{x\bar{x}}$ and $\sigma_{\bar{x}x}$, (b) chiral ratio of elastic signal in two Brillouin zones, (c) chiral ratio of low-energy phason mode.

Table 4.3. The subtraction of the spin-flip channels along x, $\sigma_{x\bar{x}}$ and $\sigma_{\bar{x}x}$, directly gives the background-free intensity.

The temperature dependence of the two spin-flip channels along x at the elastic Bragg position at $\vec{Q} = -(2,\ 0.28,\ 1)$ is shown in Figure 4.21(a). The phase transitions at T_N and T_{FE} are indicated by dashed lines. The applied electric field poles the domains in the sample and the polarization analysis is able to distinguish between both vector chiralities. We obtain a ratio between both channels of about 3 : 1 at the magnetic Bragg peak which corresponds to a chiral ratio of $r_{\text{chiral}} = \frac{I_{x\bar{x}} - I_{\bar{x}x}}{I_{x\bar{x}} + I_{\bar{x}x}} \approx 0.5$. This value can only reach the maximum of $r_{\text{chiral}} = 1$ when the scattering vector $\vec{Q}$ is perpendicular to the spiral plane. From Table 4.3 an angle between $\vec{Q} = -(2,\ 0.28,\ 1)$ and the spiral plane bc of 69.2° can be deduced. One also has to take into account the elliptic shape of the spin spiral and the orientation of $\vec{Q}$ relative to the ellipse. This yields a maximum value of the chiral ratio at this position of $r_{\text{chiral,Q,max}} = 0.93$. We can conclude that more than 75 % of the sample were in one domain. In previous experiments a higher ratio of up to $r_{\text{chiral}} \approx 0.8$ was achieved [49, 137]. This was only possible using smaller samples which increased the maximum applicable electric field. In this experiment, a large sample was necessary to investigate the generally weak inelastic signal which is payed by a lower poling. The achieved value, nevertheless, is sufficiently high enough to probe the chiral component of the magnetic excitations.

The magnetic excitations at the magnetic zone center at 17 K inside the multiferroic phase are shown in Fig. 4.21(b). At this scattering vector the contribution of a-polarized out-of-plane excitations is strongly suppressed by the sizable b-component, $\sin^2(\alpha_a) = 0.12$, and the scattering intensity comes primarily from in-plane modes, $\sin^2(\alpha_{bc}) = 0.88$. In addition, one can state that according to the simple model only the low-energy phason mode carries a chiral component and should be visible in the subtraction of the spin-flip channels along x. The

positions of the in-plane phason mode ($\omega_1 \approx 0.1\,\mathrm{meV}$) and the two out-of-plane modes ($\omega_2 \approx 1.0\,\mathrm{meV}$ and $\omega_3 \approx 2.5\,\mathrm{meV}$) are indicated by gray bars. The observed chiral signal is remarkably broadened and can only be described by a combination of two Gaussian functions (dotted lines).
Figure 4.21(c) shows the dispersion of the chiral signal $\sigma_{x\bar{x}} - \sigma_{\bar{x}x}$ along $\vec{Q} = (2,\ K,\ 1)$. The intensity of the subtraction decreases away from the zone center and vanishes at the zone boundary $\vec{Q} = -(2,\ 0,\ 1)$. At all positions, the signal is significantly broadened and a pure influence from the finite resolution ellipsoid seems unlikely with the good resolution of $\Delta E \approx 0.24\,\mathrm{meV}$. As the scattering vector is almost fully aligned along the a-direction, an overlapping contribution of the out-of-plane modes can be neglected. It seems instead that the phason itself is rather complex and split into several contributions or branches. This new finding might be related to the back-folding of a split phason mode, which was theoretically predicted by Mochizuki *et al.* [114].
In the following, we will concentrate on the low-energy chiral signal whose energy corresponds to the phason mode. In Figure 4.22 the chirality of the Bragg peak signals (a) and (b) is compared with the dispersion of the chirality of the phason mode. The elastic scan along $\vec{Q} = -(2,\ K,\ 1)$ shows two magnetic Bragg reflections with opposite chiral ratio. This is due to the scattering geometry when $\vec{Q}$ changes the sign. It explains the decrease of the phason chirality when approaching the zone boundary in Fig. 4.22(c) to zero at the zone boundary $\vec{Q} = -(2,\ 0,\ 1)$. It should be mentioned that by the application of an inverted electric field, the sign of chirality of the Bragg peaks *and* the phason mode is fully reversed.
During the experiment it was not observed that the application of an electric field resulted in a variation of the positions of the mode. The energy of the field applied to the electric dipoles seems to be negligible in comparison to the magnetic interactions. Accordingly, the magnon dispersion could be modeled without considering the ferroelectric ordering in the spiral phase (cf. Section 4.3).
The investigation of the chiral components of the magnon modes in the spiral phase of $TbMnO_3$ revealed another interesting finding. Figure 4.23(a) shows the chiral component, i.e. the subtraction of both xSF channels $\sigma_{x\bar{x}} - \sigma_{\bar{x}x}$, of the excitation spectrum at the magnetic zone center $\vec{Q} = -(2,\ 0.28,\ 1)$ at 17 K. The same scan was measured at IN14, as described above, and at the thermal TAS instrument IN20 at the ILL using $k_f = 2.66\,\mathrm{\AA}^{-1}$ performed by M. Baum [168]. The latter experimental setting allows to measure at higher energy transfer, with the cost of a relaxed resolution. Both spectra where matched by multiplying the IN14 data by a factor of 20, which accounts for the higher flux on thermal instruments. For both scans the sample was poled by an electric field. At low energies, the intensity of the chiral component is strongly positive and exceeds the vertical scale (see Fig. 4.21(c) for the full scale). Surprisingly, at higher energies, the intensity not only decreases, but chances its sign at an energy transfer of approximately 4 meV.

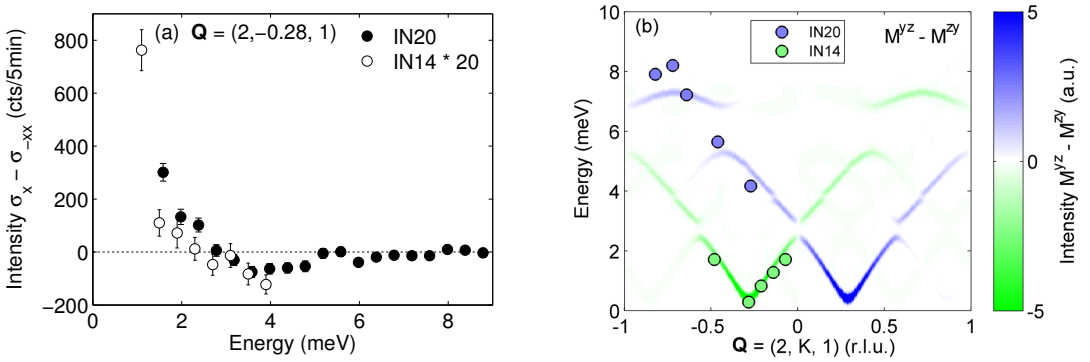

Figure 4.23.: Dispersion of chiral magnetic scattering in $TbMnO_3$ at $T = 17\,\mathrm{K}$, poled by an electric field of $E \approx 355\,\mathrm{V\,mm^{-1}}$. (a) Chirality component, $\sigma_{x\bar{x}} - \sigma_{\bar{x}x}$, of zone-center modes measured on IN14 and IN20 [168]. The intensity of the IN14 scan was multiplied by a factor of 20. (b) Simulation of chiral magnetic scattering $\mathrm{Im}(M^{yz} - M^{zy})$ in $TbMnO_3$ along $\vec{Q} = (2,\ K,\ 1)$. The sign of chirality is color-coded. The simulation is compared to data obtained at IN14 (this thesis) and IN20 [168] at $T = 17\,\mathrm{K}$. The color of the symbols corresponds to the sign of chirality of the modes.

This observation is visible in both scans and cannot be explained by statistical variations. We can state that there is a high-energy mode at the zone center which bears an opposite chirality with respect to the static Bragg peak.
The mode of opposite chirality could be followed through the Brillouin zone on IN20 (data not shown) [168]. We will simulate the chiral magnetic scattering using the model M-II, developed in this chapter, to investigate the origin of this mode. Figure 4.23(b) shows the calculated neutron intensity $M^{yz} - M^{zy}$ (which corresponds to the magnetic chiral component) along $\vec{Q} = (2,\ K,\ 1)$. The color scale ranges from negative (green) to positive (blue) values. The calculation can directly be compared to experimental values. Green dots denote the position and sign of chirality of the phason mode. The values have been determined by Gaussian fits to the data (an example is shown in Fig. 4.21). In addition, we show values of the high-energy mode obtained at IN20. This mode shows a reversed chirality, with respect to the static Bragg peak. The data extracted from both experiments confirm the calculated opposite sign of the mode chirality arising from back-folding of the phason mode of the neighboring Brillouin zone. The coexistence of modes with different sign of chirality has been reported in $Ba_3NbFe_3Si_2O_{14}$ whose structure is intrinsically chiral [169, 170].
We can conclude that the chiral component of the in-plane phason mode could be well described by model M-II. The high energy modes of reversed chiral component can be attributed to a back-folding of the phason mode. The discrepancy between experiment and simulation is found in the width of the chiral component. While the simulation predicts only a chiral component for the phason mode, the experi-

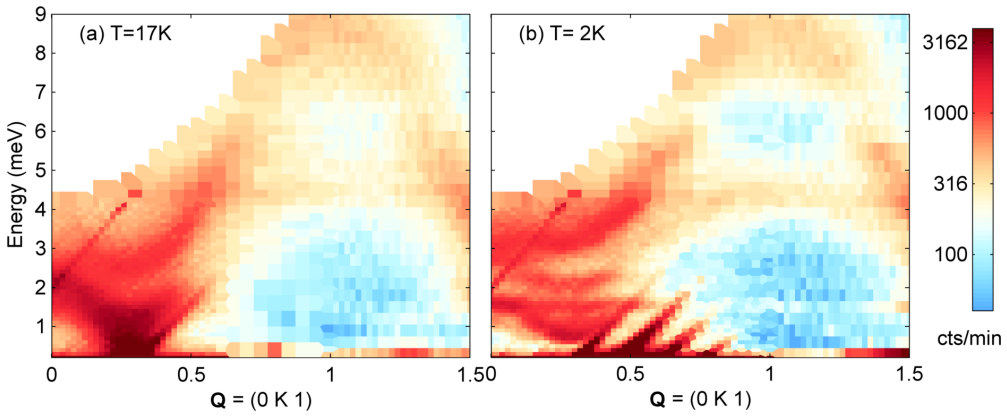

Figure 4.24.: Inelastic neutron intensity of $TbMnO_3$ along $\vec{Q} = (0,\ K,\ 1)$ at $T = 17\,\mathrm{K}$ (a) and $T = 2\,\mathrm{K}$ (b) at Thales. The intensity is logarithmically color-coded. The sharp diagonal features can be attributed to spurious signals arising from strong Bragg peak scattering.

mentally observed chiral signal is significantly broadened and cannot be described by a single mode.

4.4.4. Influence of the Tb-subsystem

The Tb-subsystem orders at $T_{Tb} = 7\,\mathrm{K}$ with a propagation vector of $\vec{k}_{Tb} = (0,\ 0.42,\ 0)$ and with moments aligned parallel to the a-direction. It has been proposed that below this temperature the propagation vectors of Mn and Tb order are connected via $3k_{Tb} - k_{Mn} = 1$ which implies a sizable interaction J_{Mn-Tb} [131]. Even at 15 K, a sizable polarized moment of Tb was found [11]. The rare-earth magnetic ordering has a clear impact on the multiferroic phase [171] and Kajimoto *et al.* found the development of additional Mn structures (G, C and F type) which may arise due to the Tb-subsystem [123]. Furthermore, Voigt *et al.* reported the induced ordering of $4f$ moments in the multiferroic phase [132].
The investigation of the magnon dispersion in $TbMnO_3$ has so far been performed at 17 K or higher temperatures in order to avoid a stronger influence from the rare-earth ions [142]. Nevertheless, it seems possible that, even in this temperature range of the multiferroic phase, the influence cannot be neglected due to the observations given above. A direct comparison of the spin excitations below and well above the transition temperature of the T_{Tb} may help to understand the relevant changes induced by the Tb ordering.
The same large crystal used in the previous section was installed on the cold-neutron TAS instrument Thales at the ILL in [010]/[001] scattering geometry. The

experiment was performed with a fixed final neutron energy of $E_f = 4.64\,\mathrm{meV}$ ($k_f = 1.50\,\mathrm{\AA}^{-1}$) and a velocity selector on k_i. PG-monochromator and analyzer were set to be double-focusing. The instruments energy resolution of $\Delta E \approx 0.19\,\mathrm{meV}$ was determined on the elastic line. It has been verified that the measured linewidth of the magnetic excitations are intrinsic and did not sharpen with higher instrument resolution at $k_f = 1.20\,\mathrm{\AA}^{-1}$.

Figure 4.24 compares the excitation spectrum in $TbMnO_3$ along $\vec{Q} = (0,\ K,\ 1)$ at 17 K, in the multiferroic phase, and at 2 K, below T_{Tb}. The sharp features can be attributed to scattering of the magnetic Bragg reflections. Usually these spurious effects are eliminated using a Be-filter on k_f, which was not available during the experiment. At the higher temperature, only two spurions from the Mn Bragg reflections are visible and at the lower temperature also the Tb Bragg reflections are visible. The overall features of the dispersion are recovered below T_{Tb} but especially at the zone center significant changes occur. All modes shift to higher energies and at least one additional mode can be identified.

The changes of the spectra are studied in more detail in Figure 4.25(a)-(c). The temperature dependencies in the range of 2 to 17 K are given for energy scans at (a) $\vec{Q} = (0,\ 0,\ 1)$, (b) $\vec{Q} = (0,\ 0.28,\ 1)$ and (c) $\vec{Q} = (0,\ 0.28,\ 1.5)$. First we look at the magnetic zone center. A peak appears at a finite but still low energy (at 2 K well below the Tb ordering this peaks lies at about 0.7 meV). The smooth temperature dependence enables us to interpret this low-energy peak as the phason mode which acquires finite energy due to enhanced pinning at low temperatures. Furthermore, the position of the mode at 2 K agrees well to an antiferromagnetic resonance mode at $5\,\mathrm{cm}^{-1} = 0.625\,\mathrm{meV}$ measured in IR spectroscopy [59, 144]. At higher temperatures this mode shifts to smaller energies and moves out of the energy range accessible by IR. The two a-polarized modes, i.e. the electromagnons, harden upon cooling in perfect agreement with the IR studies [59, 144]. The upper one shows a kink at the inset of the Tb order. More surprisingly, the lower of both modes either splits up into two modes below T_{Tb} or a new mode appears. This mode splitting is also visible at the zone boundary $\vec{Q} = (0,\ 0,\ 1)$, cf. Fig. 4.25(a). The comparison of the magnon dispersion of the Mn-oder above and below the ordering temperature of the Tb-subsystem revealed drastic changes of the dynamics. At low temperatures we find a splitting of modes and it is possible, that an overlap of modes leads to the significant broadening of inelastic signal at higher temperatures. Further investigations and a more complex simulation including the Tb-order are necessary in order to fully describe the dispersion below T_{Tb}.

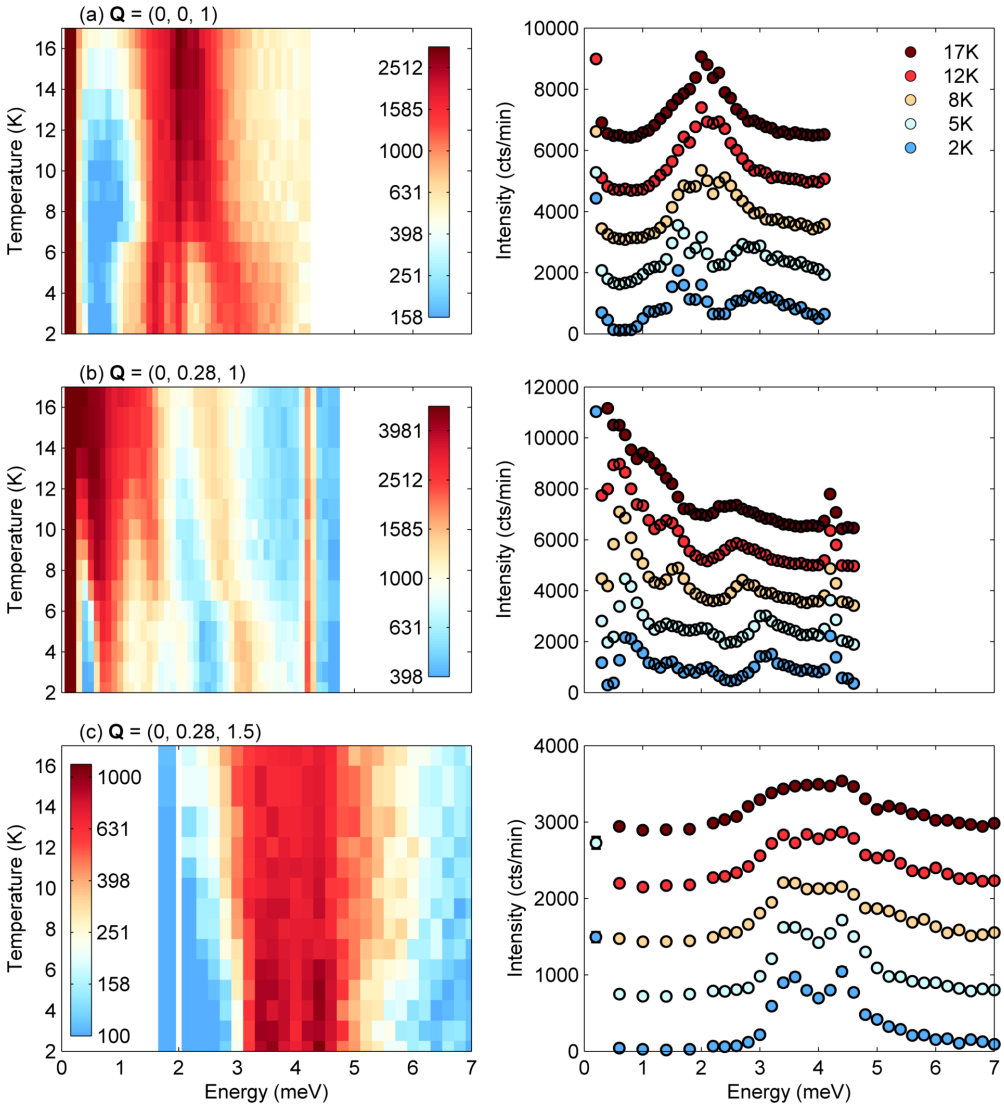

Figure 4.25.: Temperature dependence of inelastic neutron scattering of $TbMnO_3$ at (a) $\vec{Q} = (0,\ 0,\ 1)$, (b) $\vec{Q} = (0,\ 0.28,\ 1)$ and (c) $\vec{Q} = (0,\ 0.28,\ 1.5)$ at Thales. The intensity is logarithmically color-coded. Selected energy scans corresponding to the color map are shown on the right side.

4.5. Magnetic excitations in commensurate high-field phase phase

$TbMnO_3$ shows a 90° flop of ferroelectric polarization (P_c to P_a) and spin-spiral plane (*bc*-plane to *ab*-plane) in magnetic fields applied along $\vec{a}$ and $\vec{b}$, resulting from the giant magnetoelectric effect in spin-inducted multiferroics [8]. The polarization flop can perfectly be explained with the DM model of the static structure [48, 139]. A discrepancy was found when looking at the magnetic and electric excitations. An INS experiment in fields H_a revealed an excitation spectrum at the zone center which is consistent with the flop of the spin-spiral plane [56] (a model is shown in Fig. 4.4). According to the DM mechanism, the polarization of the electromagnon mode should also rotate from $\vec{a}$ to $\vec{c}$, which could not be confirmed by IR spectroscopy [59].
Recently, Shuvaev *et al.* reinvestigated the field-induced flop in magnetic fields H_b and their IR experiments showed an electromagnon polarized along $\vec{a}$ in the commensurate high field phase HF-C. This mode would correspond to the out-of-plane excitation of an *ab*-spiral and match the DM mechanism [60]. We used inelastic neutron scattering in the H_b high field phase to be able to directly compare IR and INS results.

Experiment details

The experiment was performed at the cold TAS instrument IN14 at the ILL. A single crystal of $TbMnO_3$ was mounted with the scattering plane defined by the directions $[1, 0, 0]$ and $[0, 0.25, 1]$ in a 10 T vertical cryomagnet. The (0, 0, 2)-reflection of pyrolytic graphite was used to monochromate and analyze the energy of the neutrons. The energy of the analyzed neutrons was fixed to $E_f = 4.66\,\text{meV}$ ($k_f = 1.50\,\text{Å}^{-1}$). Selected scans were repeated with $E_f = 3.44\,\text{meV}$ ($k_f = 1.29\,\text{Å}^{-1}$) to verify with better resolution that the broadening of the observed excitations was intrinsic. We used vertical (monochromator) and horizontal (analyzer) focusing in order to increase the neutron flux on the sample. A cooled beryllium filter was mounted behind the sample in the neutron path to suppress contaminations by higher-order neutrons. The measurements were done at two temperatures in the multiferroic phase, 12 K and 2 K, in order to investigate the influence of the Tb-subsystem and to compare the data with previous experiments.
In order to reach the magnetic propagation vector of the HF-C phase, $\vec{k}_{com} = (0,\ 0.25,\ 0)$, the *b*-axis had to be tilted relative to the vertical axis by $\alpha = 11.2°$. An applied magnetic field thus has components along $\vec{b}$ and $\vec{a}$, respectively (98 %$\|$ H_b

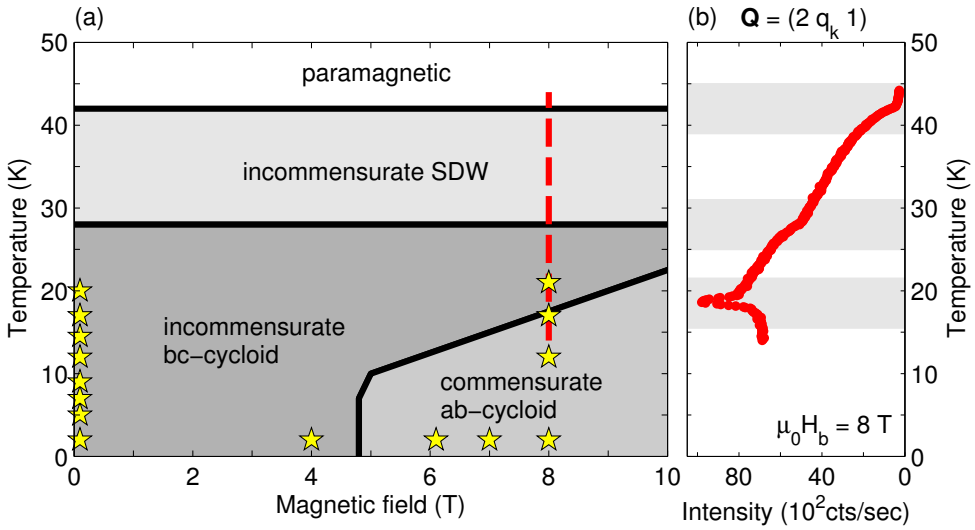

Figure 4.26.: (a) Schematic phase diagram of $TbMnO_3$ for magnetic fields applied along $\vec{b}$ [8]. Stars denote the positions of the recorded spin-wave spectra, the line highlights the position of the temperature scan in (b). (b) Neutron intensity of the Bragg peak position $\vec{Q}_2 = (2,\ q_k,\ 1)$ as function of temperature in 8 T applied along $\vec{b}$. The gray bars indicate the magnetic phase transitions.

and 19 %$\|$ H_c). As an example, at the maximum applied field of 8 T, we get a distribution of 7.9 T along H_b and 1.6 T along H_c. The induced transition in magnetic fields H_c occurs at all temperatures above 5 T [8]. We conclude that the small tilting of the magnetic field with respect to the b-axis has only a minor influence on the system and in particular on the magnetic phase. No significant changes are expected in both, the transition temperatures and the incommensurate character of the phase. In this section, we will refer to a magnetic field applied along $\vec{b}$ for simplicity.
In the high-field phase HF-C, the propagation vector $\vec{k} = (0,\ q_k,\ 0)$ changes from $q_k \approx 0.28$ to $q_k = 0.25$. This small difference has no significant impact on the experimental setup, since both vectors are within the vertical resolution of the spectrometer and the dispersion along b is known to be rather flat [142]. In the following, we will refer to the zone center positions as $\vec{Q}_1 = (0,\ q_k,\ 1)$ and $\vec{Q}_2 = (2,\ q_k,\ 1)$ for both spiral phases, in zero field and in fields H_b.

Phase transition

The magnetic phase diagram of $TbMnO_3$ in magnetic fields applied along $\vec{b}$ is schematically shown in Figure 4.26(a), after Ref. [8]. Black solid lines indicate the

different magnetic phases: an incommensurate SDW phase at higher temperatures, an incommensurate *bc*-spiral phase in low fields (LF-IC) and a commensurate *ab*-spiral phase (HF-C) at high fields. Both spiral phases develop a ferroelectric polarization P_c and P_a, respectively. Stars denote the positions in the phase diagram of INS spectra investigated in this section.
The temperature dependence of the neutron intensity at magnetic Bragg peak position $\vec{Q}_2 = (2,\ q_k,\ 1)$ in $H_b = 8\,\mathrm{T}$ is given in Fig. 4.26(b). The position in the phase diagram is indicated as a red dashed line. The evolution of scattered intensity with decreasing temperature can be understood as follows: Below $T_N = 42\,\mathrm{K}$, the Mn-moments order in a SDW, leading to an increase of intensity. The transition into the LF-IC phase at $T_{FE} = 28\,\mathrm{K}$ results in a strong enhancement of intensity. In this phase, the magnetic structure develops a $\vec{c}$-component, to which the scattering vector $\vec{Q}_2 = (2,\ q_k,\ 1)$ is sensitive.
At about 17 K, the neutron intensity shows a sharp feature at the LF-IC→HF-C transition, which is followed by a decrease of intensity. Here, the spin-spiral plane flops from *bc* to *ab* [48]. The magnetic moment which contributs to the scattering $\vec{M}_\perp$ changes with $\vec{Q}$. This is why the scattering vector $\vec{Q}_2 = (2,\ q_k,\ 1)$ is less sensitive to magnetic components parallel to $\vec{a}$, which results in a loss of scattered intensity. The flop of the spin-spiral plane is accompanied by a change of the propagation vector $\vec{k} = (0,\ q_k,\ 0)$ from $q_k \approx 0.28$ to the commensurable value of $q_k = 0.25$. This may explain the sharp peak at the transition under the given experimental conditions.

4.5.1. Zone-center modes in the HF-C phase

In the following, we will discuss the magnetic excitation spectra in the zero field and the high-field multiferroic phase. Inelastic scans at the magnetic zone centers $\vec{Q}_1 = (0,\ q_k,\ 1)$ and $\vec{Q}_2 = (2,\ q_k,\ 1)$ are presented in Fig. 4.27. The spectra were recorded in the LF-IC phase at $H_b = 0\,\mathrm{T}$ and in the HF-C phase at $H_b = 8\,\mathrm{T}$. Two different temperatures were chosen: well above (12 K) and below (2 K) the ordering temperature of the Tb-subsystem.
Strong magnetic signals are present in all four spectra. A weak feature is common in all spectra at an energy transfer of approximately 4.5 K. This feature has been identified in an INS study in zero field as a contribution of the crystal field (CF) excitation of the Tb-subsystem [12]. Crystal field calculations done on $TbMnO_3$ agree with this interpretation and find $\omega_{Tb} = 4.6\,\mathrm{meV}$ [172]. We will ignore this CF excitation in the following, as no significant changes can be observed in all spectra above 4 meV. In contrast, the applied magnetic field has a remarkable of influence on the low energy excitations at both investigated temperatures.

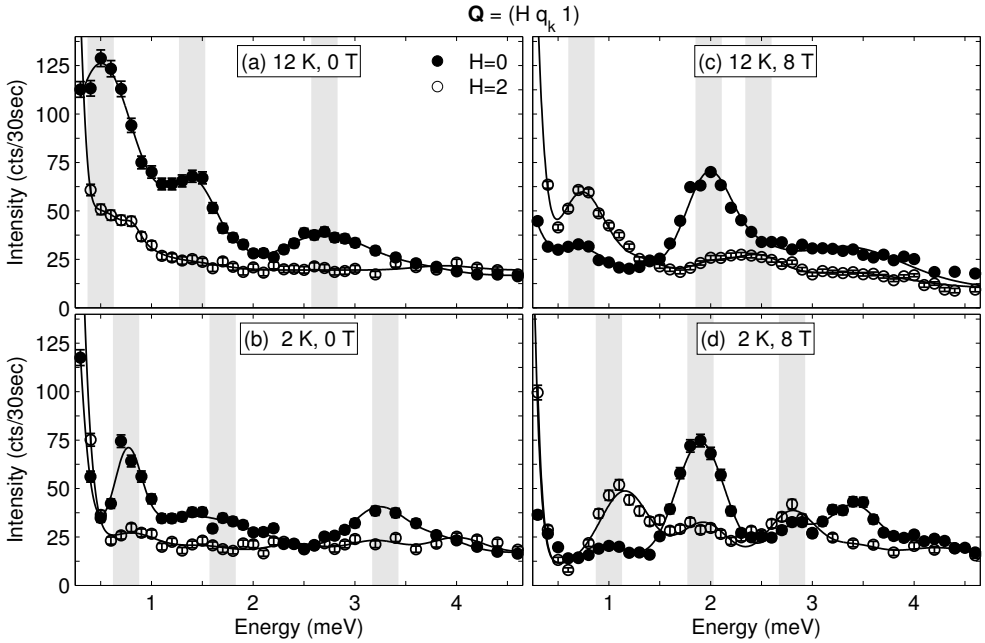

Figure 4.27.: Zone center excitations at the magnetic Bragg positions $\vec{Q}_1 = (0,\ q_k,\ 1)$ and $\vec{Q}_2 = (2,\ q_k,\ 1)$ at IN14. The spectra were recorded at (a) 12 K and 0 T, (b) 2 K and 0 T, (c) 12 K and 8 T and (d) 2 K and 8 T, with the magnetic field applied along $\vec{b}$. The gray bars denote the positions of the low-energy magnon modes of the Mn-order.

At zero field, the magnon spectrum consists of three different low-energy branches which are indicated with gray bars in Fig. 4.27(a). These features can be attributed to the Mn-order, which has been shown by the comparison of the $\vec{Q}$-dependence of the inelastic signal with the magnetic form factor of Mn^{3+} by Senff *et al.* [12]. Furthermore, the authors applied longitudinal neutron polarization analysis and were able to unambiguously identify the phason mode (low-energy mode) as well as two *a*-polarized modes [12].
The zone center excitations could be well described by fitting three Gaussian functions to the data. The positions of the peak energies are indicated as gray bars in Figs. 4.27(a-d). The energies found at 12 K and 8 T are slightly higher than those in Reference [12], where the spectrum was recorded at 17 K. This observation is consistent with the hardening of modes in lower temperatures and is even more pronounced at 2 K in Fig. 4.27(b). The temperature dependence of the magnetic excitations will be discussed in a separate section.
The change of the spectra form the LF-IC phase to the HF-C phase is similar at both investigated temperatures. At 12 K in the high field phase, the spectrum can be decomposed into two strong excitations, centered around 0.7 meV and 2.0 meV, as well as a weaker excitation around 2.5 meV, indicated by gray bars

in Fig. 4.27(c). These three modes shift to slightly higher energies at 2 K, see Fig. 4.27(d). In addition, a fourth peak appears at this temperature at approximately 3.5 meV. At 12 K, this peak transforms into a broad signal, which shows the same Q-dependence. From the temperature dependence, we may assign this mode to arise from Tb-ordering. In the following, this feature will be excluded from the analysis and discussion.

Polarization of HF-C magnetic excitations

A systematic analysis of the $\vec{Q}$-dependence of the magnetic excitations will be applied in order to determine their polarization character. Only magnetic components perpendicular to the scattering vector, $\vec{S}_\perp$, contribute to the neutron scattering intensity. The observed intensity of the modes is proportional to the magnetic form factor of Mn^{3+} and the angle α between $\vec{Q}$ and the magnetic polarization:

$$I \propto f_m^2(Q) sin^2(\alpha) \ . \tag{4.6}$$

The excitation spectrum in the HF-C field was recorded at two different zone centers $\vec{Q}_1 = (0,\ q_k,\ 1)$ and $\vec{Q}_2 = (2,\ q_k,\ 1)$. Fig. 4.27(c) spectra recorded 12 K and 8 T. The magnon frequencies extracted from fitting are identical at these two $\vec{Q}$ points: $\hbar\omega_1 = 0.73$ meV, $\hbar\omega_2 = 1.98$ meV and $\hbar\omega_3 = 2.47$ meV. Their spectral weight changes drastically at both positions: The mode ω_1 is stronger for $\vec{Q}_2$ and ω_2 is enhanced for $\vec{Q}_1$. The identification of the weak mode ω_3 suffers from the fact, that it slightly overlaps with the stronger mode at ω_2. A comparison with the low temperature data helps to reveal their $\vec{Q}$ dependence, which is the same as for ω_1.
We can state that $\vec{Q}$-dependence of the three investigated modes is similar at both temperatures in 8 T in the HF-C phase. In this phase, the Mn-moments form a spin-spiral in the *ab*-plane. In-plane (*ab*-polarized) and out-of-plane (*c*-polarized) modes can be distinguished with the help of Eq. 4.6 by looking at the angle α between $\vec{Q}$ and $\vec{c}$. This angle can be calculated to be $\alpha_1 = 17.5°$ for $\vec{Q}_1$ and $\alpha_2 = 70.4°$ for $\vec{Q}_2$. For magnetic fluctuation polarized predominantly perpendicular to $\vec{c}$, one expects increasing of scattered intensity towards higher α. We will show that this is the case for ω_2: For an entirely *ab*-polarized mode, one expects an intensity ratio of $I_{\vec{Q}_1}{:}I_{\vec{Q}_2} = 4.4$. The experimentally observed ratio of $I^{exp}_{\vec{Q}_1}{:}I^{exp}_{\vec{Q}_2} = 4.0$ supports the assumption. The ω_2 mode may thus be identified as the phason mode of the *ab*-cycloid.
The same analysis will be applied to the the modes ω_1 and ω_3. Their $\vec{Q}$-dependence shows the opposite behavior: a decrease of scattered intensity for increasing α. This

suggests that these modes are polarized parallel to the c-axis. The intensities at both positions, ω_1 and ω_3, yield an intensity ratio of $I^{exp}_{\vec{Q}_1}$:$I^{exp}_{\vec{Q}_2} = 0.2$. This is in good agreement with the expected value for a purely c-polarized mode, $I_{\vec{Q}_1}$:$I_{\vec{Q}_2} = 0.4$. This comparison allows the assumption that the modes ω_1 and ω_3 are out-of-plane modes of the ab-cycloid.
The analysis of the zone center spectra in the HF-C phase, shown in Fig. 4.27(c-d), revealed the presence of a in-plane mode (ω_2) and two out-of-plane modes (ω_1 and ω_3) of the ab-spiral. We can show that our observations are fully consistent with the field-induced flop of the magnetic cycloid from the bc to the ab-plane. The strong mode ω_2 is polarized within the ab-plane and should correspond to the phason mode of the commensurate spiral. The energy of the phason mode is strongly enhanced in comparison with the LF-IC phase, from ≈ 0.1 meV at 0 T to 1.9 meV at 8 T. This enhancement can be attributed to the strong pinning of the commensurate spiral at high fields. The same pinning effect of the phason mode was found for the H_a transition [56]. The two other modes, ω_1 and ω_3, are polarized perpendicular to the spiral plane and correspond thus to the two out-of-plane modes of the zero field spiral. A sketch of the zone-center modes in the LF-IC and the HF-C phase is shown in Fig. 4.4. The two out-of-planes differ from each other as one consists of a static a-component (rotation of spins around $\vec{a}$: helical mode), while the other consists of a static b-component (rotation of spins around $\vec{b}$: cycloid mode). The latter mode is expected too strongly couple to an alternating electric field along $\vec{c}$ and should be visible in optical spectroscopy [54].

Comparison to IR spectroscopy

Shuvaev *et al.* reported an optical experiment in the HF-C phase for magnetic fields along $\vec{b}$ [60]. The authors indeed find evidence for an electromagnetic excitation around 2.6 meV at 6 K, which is electrically polarized in c-direction. The signal was associated with the dominating peak reported by the previous INS experiment in the HF-C phase [60]. This interpretation, however, does not seem plausible, as this strong mode clearly can be identified as the phason mode, which should not be magnetoelectrically active [56]. The previous INS experiment was performed in magnetic fields along $\vec{a}$ and a direct comparison with the optical data cannot be made. Our experiment shows, that the magnon modes polarized perpendicular to the cycloidal plane are significantly different in the HF-C phases induced by magnetic field along $\vec{a}$ [56] or $\vec{b}$. Senff *et al.* reported mode frequencies of 0.5 meV, 2.25 meV and 3.0 meV at 17 K and in 12 T applied along $\vec{a}$.
The modulation of magnon energies with the direction of the magnetic field can be understood by simple considerations. A magnetic field along $\vec{b}$ will favor the reduc-

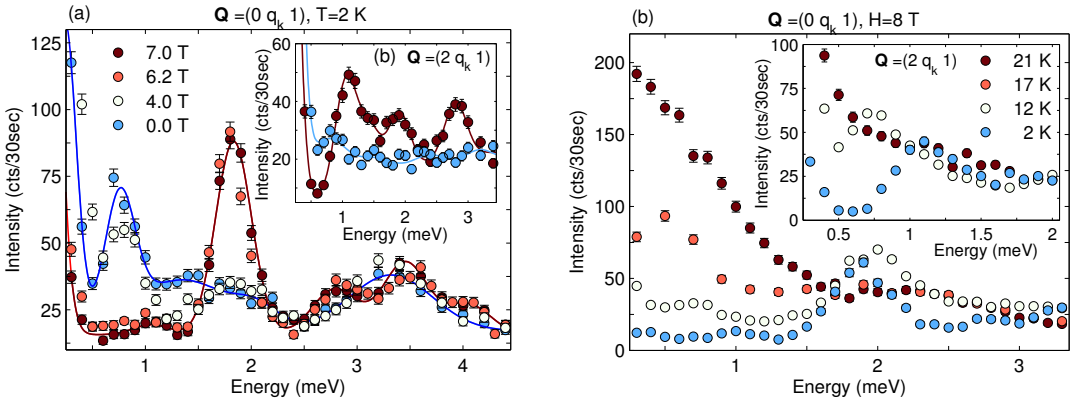

Figure 4.28.: (a) Magnetic field dependence of the zone center excitations at the magnetic Bragg positions $\vec{Q}_1 = (0,\ q_k,\ 1)$ and $\vec{Q}_2 = (2,\ q_k,\ 1)$ for field applied along $\vec{b}$ at 2 K at IN14. (b) Temperature dependence of the zone center excitations at the magnetic Bragg positions $\vec{Q}_1 = (0,\ q_k,\ 1)$ and $\vec{Q}_2 = (2,\ q_k,\ 1)$ in 8 T applied along $\vec{b}$.

tion of the antiferromagnetically ordered moment along $\vec{b}$, so that the magnetic polarization does not need to overcome the exchange. Following this approach, we suppose that the lower of the out-of-plane modes, ω_1, corresponds to the mode in which mainly the b-component oscillates in c-direction, the helical mode. Subsequently, the mode ω_3 is likely to correspond to the rotation around the direction of the magnetic propagation vector $\vec{b}$, the cycloid mode. This mode rotates the spiral plane and is expected to induce a strong dielectric oscillation via the DM mechanism [54]. The frequency of ω_3 only changes slightly with temperature and thus perfectly matches with the optical experiment performed at 6 K [60]. An electrically active c-mode in both HF-C phases has also been detected at the same energy by Raman spectroscopy, hardening our interpretation [173]. In an INS experiments performed on $DyMnO_3$ [55], the cycloid rotation mode was also found at the same frequencies as a low-energy optical signal, which matches our conclusion for the HF-C phase in $TbMnO_3$.

4.5.2. Dependency of modes on H_b, T and Q

The evolution of the magnetic zone center spectra with increasing magnetic field along $\vec{b}$ is shown in Figure 4.28(a) at 2 K. The spectra were recorded at two zone center positions $\vec{Q}_1 = (0,\ q_k,\ 1)$ and $\vec{Q}_2 = (2,\ q_k,\ 1)$. Within the LF-IC phase and the HF-C phase, the spectra are practically identical and show no influence of the field and can be described using the same frequencies. Between 4 T and 6.2 T the excitation spectrum changes drastically, when the spiral-plane flops from bc to ab.

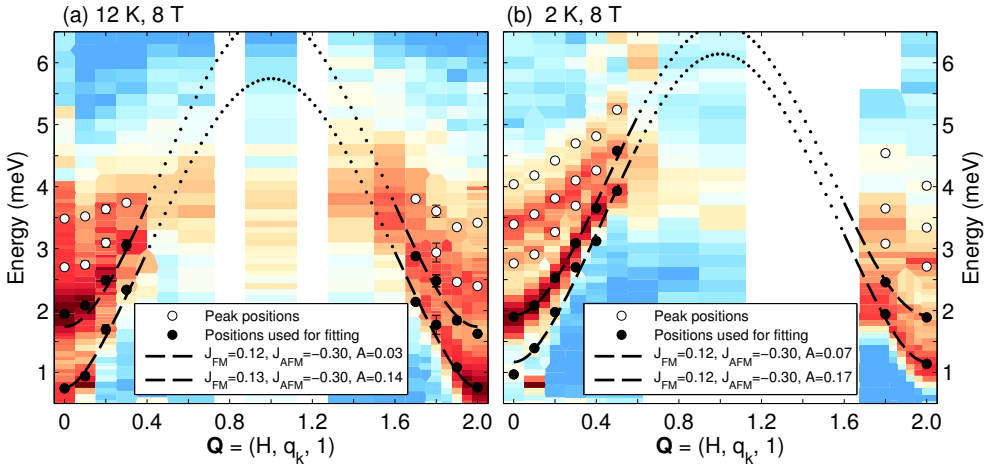

Figure 4.29.: Intensity mapping of the spin-wave excitations at (a) 12 K and (b) 2 K along $\vec{Q} = (H,\ q_k,\ 1)$ in 8 T applied along $\vec{b}$ at IN14. The dispersion was fitted applying the same model as the one described in Ref. [56] using the parameters given in the plot.

The data reflects the strong first-order character of the LF-IC to HF-C transition. Figure 4.28(b) shows the temperature dependence of the magnetic excitations in $H_b = 8$ T at the same zone center positions $\vec{Q}_1 = (0,\ q_k,\ 1)$ and $\vec{Q}_2 = (2,\ q_k,\ 1)$. From the phase diagram in Fig. 4.26, we can deduce that the system is in the LT-IC phase at 21 K. The spectral weight is centered at low energies at this temperature, in agreement to previous reports [142]. At 17 K, the system is close to the LT-IC phase transition, but the feature at low energies is still enhanced and the phason pinning can be incomplete. Finally, at 12 K the Mn-moments are ordered in the HF-C phase and the spin-wave spectrum changes significantly. The intensity at low energies is suppressed, whereas a strong mode centered around 2 meV evolved. Between 12 K and 2 K the modes slightly shift towards higher energies.
In the given experimental geometry, it was possible to follow the magnetic excitations in the HF-C phase along $\vec{Q} = (H,\ q_k,\ 1)$. Figure 4.29(a-b) shows a logarithmic intensity mapping of energy scans along the a-direction between the two magnetic zone centers $\vec{Q}_1 = (0,\ q_k,\ 1)$ and $\vec{Q}_2 = (2,\ q_k,\ 1)$ in $H_b = 8$ T at temperatures of 12 K and 2 K. Open and filled circles denote the position of the modes obtained by fitting Gaussian functions to the spectra. Filled points were used to fit the spin-wave dispersion along $\vec{a}$. A simple spin-only Hamiltonian model was used assuming a FM exchange J_{FM} between nearest neighbors within the ab-planes, an AFM exchange J_{AFM} along $\vec{c}$, and a single-ion anisotropy A. This model has been used before to describe the dispersion in the zero field multiferroic LF-IC phase and the HF-C phase in H_a [56, 142]. The interaction J_{AFM} along $\vec{c}$ has been fixed to the value used in Ref. [56]. The simple model fails to describe the splitting of the different branches and the incommensurability along

$\vec{b}$. Nevertheless, it allows to estimate values for J_{FM} and the anisotropy A in the HF-C phase, which can be compared to the zero field phase and the HF-C phase in fields H_a. The overall dispersion is very similar in all phases. Accordingly, the obtained value for $J_{FM} \approx 0.13\,\text{meV}$ at both temperatures does not differ from the zero field phase. It indicates that the magnetic field influences the Mn-anisotropies without a significant change in the Mn-interactions. The most pronounced effect on the dispersion is the strong enhancement of the phason mode in the high-field phase.

4.6. Conclusion

The magnetic properties of the multiferroic phase of $TbMnO_3$ were investigated by unpolarized and polarized neutron scattering. It was possible to characterize the magnetic fluctuations in the system and to accurately describe the spin wave dispersion in the multiferroic phase. $TbMnO_3$ is a prototype material for multiferroic materials of spin origin [5]. It is also the first material in which electromagnetic excitations were observed [12, 57].
We find diffuse magnetic scattering in $TbMnO_3$, which is present well above the antiferromagnetic transition temperature at $T_N = 42\,\text{K}$. The fluctuations could be separated into contributions from Mn and Tb moments by using neutron polarization analysis. Magnetic fluctuations could also be observed in the ordered SDW phase. They can be seen as precursor of the ferroelectric transition at $T_{FE} = 28\,\text{K}$ and indicate an almost continuous transition towards the spin-spiral phase. The fluctuations in the paramagnetic phase could be well described by a mean-field approach.
The magnetic excitations spectrum in the multiferroic phase was investigated in detail by time-of-flight spectroscopy. The comprehensive dataset was used to develop a spin-wave model in oder to describe the magnon dispersion using linear spin wave theory. We were able to achieve a convincing agreement between experimental data and simulation along all crystallographic directions. The model takes into account the nearest-neighbor exchanges along $\vec{c}$ and in the ab-plane, as well as the next-nearest-neighbor exchange along $\vec{b}$. The latter one accounts for the frustration of the system [12]. At the zone center, we find an in-plane mode and two out-of-plane modes of the spiral. The splitting of the out-of-plane mode was achieved by introducing a distorted easy-plane anisotropy. The spin-wave model accurately describes the polarization of modes observed by INS [12] and allows to identify the electromagnon of the DM mechanism. Its energy at the zone center perfectly agrees to observations from IR spectroscopy [57].
Neutron polarization analysis was used in order to investigate the chiral component of the excitation spectrum. The application of an electric field enables to pole

the domains of the spin-spiral in the multiferroic phase. The dispersion of the chiral component is well reproduced by the developed spin-wave model. The model simulation allows us to explain the observation of modes with reversed chirality in the same Brillouin zone by a back-folding of branches.
The influence of the Tb moments on the magnetic excitations of the Mn-order was analyzed by a comparison of the excitation spectra above and below the ordering temperature of the Tb-subsystem. At the onset of the Tb-order, the excitation spectrum shows significant changes. We observe a separation of modes below the transition temperature indicating a significant Tb-Mn interaction.
Finally, the excitation spectrum in the commensurate high field phase of $TbMnO_3$ was investigated. In this phase, the spin spiral flops to the *ab*-plane which coincides with a flop of ferroelectric polarization [48]. It was possible to analyze the polarization character of the zone center excitations in this high-field phase and to compare the energies with results from IR spectroscopy [60]. The good agreement of the dataset allows for the conclusion that there is an electromagnon in $TbMnO_3$ which is of DM-origin.

Chapter 5

Magnetic fluctuations in $MnWO_4$

After the discovery of the multiferroic behaviour of $TbMnO_3$, many other compounds were found in which a magnetic structure induces an electric polarization [34]. One among these materials is $MnWO_4$, which was found to be multiferroic independently by three groups [17, 46, 47]. The study of this compound benefits from the fact that, unlike in the case of RMnO$_3$ materials, only one type of magnetic ion is present and it is considered to be a prototype multiferroic. In the past, neutron polarization analysis has been a valuable tool in order to reveal information about the multiferroic phase in $MnWO_4$ [13, 50, 51, 176].

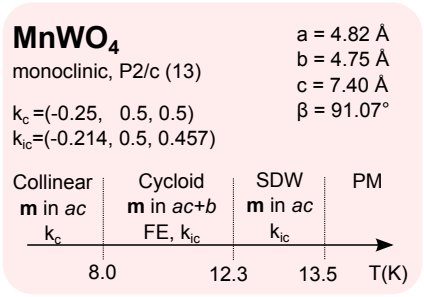

Figure 5.1.: Crystal parameters and magnetic phase transitions in $MnWO_4$ [47, 174, 175].

In this chapter, three different polarized neutron scattering techniques were used in order to investigate the successive magnetic phase transitions in this material. Furthermore, the close coupling of ferroelectricity and magnetic order allowed to study the magnetic excitations in dependence of an applied electric field.

5.1. Introduction

5.1.1. Crystal and magnetic structure

Manganese tungstate crystallizes in a wolframite structure, which is described by the monoclinic space group $P2/c$ with the following lattice parameters: $a = 4.84\,\text{Å}$, $b = 5.76\,\text{Å}$, $c = 4.99\,\text{Å}$ and a monoclinic angle of $\beta = 91.08°$ at room temperature [174]. Characteristic properties of the system are summarized in Figure 5.1. The crystal structure is shown in Figure 5.2. Manganese and tungsten ions are surrounded by distorted edge-sharing [O_6]-octahedra, which form zig-zag chains along the crystallographic c-direction. Chains of manganese and tungsten are arranged in bc-planes which alter along the a-axis. The nuclear structure is centrosymmetric and thus non-polar.
In this material, only the transition-metal carries a magnetic moment (Mn^{2+}, $3d^5$, $S = 5/2$ and $L = 0$ for single ion). The moments occupy the $2e$ position on a two-fold rotational center. Upon cooling, $MnWO_4$ undergoes three successive magnetic phase transitions as determined by neutron diffraction [174, 175, 177]:

- AF3 at $T_{N3} = 13.5\,\text{K}$, $\vec{k}_{ic} = (-0.214,\ 0.5,\ 0.457)$
  The magnetic moments form an incommensurate sinusoidal spin density wave (SDW). The moments are collinear along the easy axis $\vec{e}_{ac}$ in the ac-plane, forming an angle of 35° with the a axis.

- AF2 at $T_{N2} = 12.3\,\text{K}$, $\vec{k}_{ic} = (-0.214,\ 0.5,\ 0.457)$
  Inside this phase, an additional spin component evolves along b-direction yielding transformation towards an elliptical spin spiral with the major axis along $\vec{e}_{ac}$ and the minor axis along $\vec{b}$.

- AF1 at $T_{N1} = 8.0\,\text{K}$, $\vec{k}_c = (-0.25,\ 0.5,\ 0.5)$
  The system undergoes a first order transition towards a collinear antiferromagnetic structure with a commensurate propagation vector. The magnetic moments are aligned along the easy axis $\vec{e}_{ac}$.

The magnetic structures where derived by Lautenschläger *et al.* by applying group theory considerations [126, 175, 178]. A magnetic propagation vector of the form $\vec{k} = (k_x,\ 1/2,\ k_z)$ reduces the crystal symmetry from $P2/c$ to Pc. The corresponding little group $G_{\vec{k}} = \{1, c\}$ contains two irreducible representations, denoted as $\Gamma^{\vec{k}1}$ and $\Gamma^{\vec{k}2}$ in the literature. The Mn moments are located at the Wyckoff position $2e$ at $(0, y, 1/4)$ and are connected by symmetry via the glide reflection c. Two such moments have a phase shift of $e^{-2\pi r_z k_L}$, depending on their distance along $\vec{c}$, r_z, and the incommensurability k_L. The SDW of the AF3 phase can be described by a single irreducible representation. In this phase, the

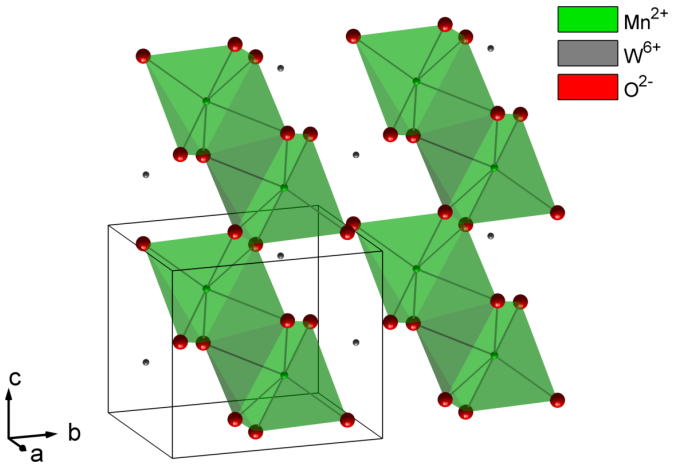

Figure 5.2: Crystal structure of $MnWO_4$: manganese (green) and tungsten (grey) are surrounded by oxygen (red) octahedra. These octahedra form planes perpendicular to $\vec{a}$. The size of the atoms reflects their relative ion radius [118]. [MnO_6]-octahedra form zig-zag chains along $\vec{c}$.

b-component of the magnetic moments is unordered [175]. The development of the b-component in the spiral AF2 phase is only possible by taking into account a combination of both irreducible representations. The sequel of second-order phase transitions, PM→SDW and SDW→spiral, can be attributed to the onset of the corresponding irreducible representations and has also been observed in the spiral multiferroics $TbMnO_3$ and $Ni_3V_2O_3$ [11, 179]. The transition towards the commensurate phase AF1 is of first-order and the magnetic structure can be described in the space group C_a2/c [178].
Sketches of the three magnetic phases are shown in Fig. 5.3. The crystallographic unit cell consists of two manganese positions which are connected by symmetry. In the figure, the unit cell is extended ten times along $\vec{c}$, the direction of the zig-zag chains. Similar to the case of $TbMnO_3$, the magnetic moments in $MnWO_4$ order first in a collinear spin density wave before a spiral structure is realized with the onset of an ordered component along $\vec{b}$. The ground state structure is again collinear with a commensurate propagation vector. The transitions at T_{N3} and T_{N2} are reported to be of second order, whereas the incommensurate-commensurate transition at T_{N1} is of first order [175]. The AF2 spiral phase coincides with the presence of a ferroelectic polarization along $\vec{b}$, which only exists in this phase [17, 46, 47]. Further details of this multiferroic phase will be discussed in the next section. The development of an incommensurate spiral structure and a ferroelectric polarization in $MnWO_4$ is unique among the family of transition-metal tungstates, which order in a commensurate antiferromagnetic structure (e.g. MWO_4 with M = Cr, Fe, Co, Ni, Cu) [174, 180, 181].
Noncollinear spin arrangements generally occur in order to reduce the extent of geometric spin frustration [53]. Indeed, a moderate degree of frustration can be derived from the comparison of Curie-Weiss and Néel temperature, $f = -\theta/T_N \approx 5$ (with $\theta = -75\,\mathrm{K}$ and $T_N = 13.5\,\mathrm{K}$ [47, 177]). The frustration is driven by the distortion of [O_6]-octahedra which decreases the nearest-neighbor exchange along

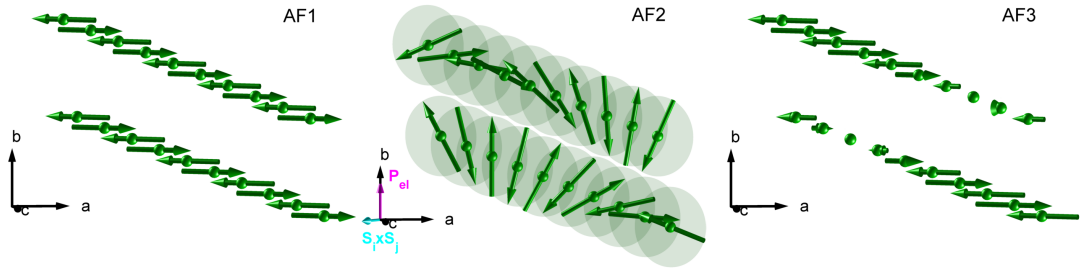

Figure 5.3.: Magnetic phases of $MnWO_4$. The Mn moments order successively in an incommensurate spin density wave (AF3, $T_{N3} \approx 13.2\,\mathrm{K}$), an incommensurate spin spiral (AF2, $T_{N2} \approx 12.3\,\mathrm{K}$) and at last in a commensurate antiferromagnetic structure (AF1, $T_{N1} \approx 8.0\,\mathrm{K}$). The easy magnetization axis lies in the monoclinic plane and forms an angle of approximately 35° with the a-axis. The multiferroic AF2 phase exhibits a ferroelectric polarization P_{el} which is connected to the spin spiral via the DM mechanism, $\vec{P}_{el} \propto \vec{r}_{i,j} \times \vec{S}_i \times \vec{S}_j$.

the edge-sharing chains [182]. Hence, the analysis of the magnon dispersion in $MnWO_4$ yields a competition of nine to eleven long-range exchange interactions [182, 183, 184].

5.1.2. Multiferroic AF2 phase

Between $T_{N2} = 12.3\,\mathrm{K}$ and $T_{N1} = 8.0\,\mathrm{K}$, the Mn-moments in $MnWO_4$ form an elliptic spiral with the major axis along $\vec{e}_{ac}$ and the minor axis along $\vec{b}$. In this phase, the antiferromagnetic structure coexists with a ferroelectric ordering, rendering it multiferroic. Even more, both orders are closely coupled because the spiral magnetic structure directly induces the electric polarization ($P_b \approx 50\,\mu\mathrm{C/m^2}$ at 8 K) [17, 46, 47]. Similar to the case of the multiferroic phase of $TbMnO_3$, the induced ferroelectricity in $MnWO_4$ can be explained by the inverse Dzyaloshinskii-Moriya interaction [15]. The spins form zig-zag chains along $\vec{c}$. The cross product of two neighboring spins lies in the ac-plane. In such a configuration, a ferroelectric polarization along $\vec{b}$ is expected by applying Eq.2.6, which perfectly matches the experimental observation. The sign of the polarization $\vec{P}_{el}$ can be assigned to the direction of rotation of the spin spiral, i.e. the vector chirality of the spiral.
The accuracy of the proposed DM mechanism in the case of $MnWO_4$ was demonstrated by probing the influence of the electric field on the magnetic ordering. Using polarized neutron scattering, one can measure the chiral magnetic term $-i(\vec{M}_\perp \times \vec{M}^*_\perp)_x$, which is of opposite sign for the two chiral domains for the choice of an appropriate scattering geometry, cf. Tab. 3.1. The appearance of the chiral magnetic term coincides with the ferroelectric polarization [137]. Sagayama *et al.*

were the first to show that the magnetic chirality in $MnWO_4$ can be switched by alternating the applied electric field upon field-cooling through T_{N2} [13]. Subsequent application of this experimental technique revealed full hysteresis cycles of the chirality [50, 176, 185] and switching time of chiral domains in the order of milliseconds [51]. The values of the derived switching times of the spiral match values determined from second harmonic generation [186] and dielectric measurements [187, 188].

Effect of applied magnetic fields and doping

The magnetic field vs. temperature phase diagram for $MnWO_4$ was at first investigated by Ehrenberg *et al.* [189], before the discovery of the multiferroic phase. Fields applied along the easy axis $\vec{e}_{ac}$ stabilize the spiral phase AF2, while this phase is completely suppressed in fields applied along the monoclinic axis $\vec{b}$. Magnetic fields applied perpendicular to $\vec{e}_{ac}$ and $\vec{b}$ only slightly shift the transition temperatures of all phases. It was confirmed by pyroelectric measurements that the findings also apply for the ferroelectricity [17, 47]. In addition, Taniguchi *et al.* find a flop of ferroelectric polarization from $\vec{P}_{el} \parallel \vec{b}$ to $\vec{P}_{el} \parallel \vec{a}$ for $H_b > 10\,\mathrm{T}$ [17]. Using neutron diffraction techniques, this flop could be connected to the flop of the spin spiral plane [190]. The Zeeman energy induces a spin flop at high magnetic fields aligning the moments perpendicular to the field direction [53]. The coexisting flop of the ferroelectric polarization is another support for the validity of DM mechanism explaining the multiferroicity in $MnWO_4$. A similar field-induced flop of polarization is present in the $R\mathrm{MnO_3}$ series (cf. Section 4.1.3). There, the flop is most probably related to a strong influence of the rare-earth ion moments [43]. The frustration of the magnetic order in $MnWO_4$ discussed in this section is also visible in the strong influence of small doping. As an example, doping with Fe^{2+} [191, 192] and Cu^{2+} [193] suppresses the multiferroic AF2 phase, while the AF2 phase becomes the ground state for Co^{2+} [194] and Zn^{2+} [195] doping. The frustrated system appears to be very sensitive to the varying single-ion anisotropies of the doped elements on the one hand, and an interruption of Mn exchanges on the other hand.

Magnetic and electric excitations

The spin wave dispersion in $MnWO_4$ has been investigated by inelastic neutron scattering (INS) by Ehrenberg *et al.* [182, 196]. They report four magnon modes in the commensurate AF1 phase and are able to describe their dispersion using nine

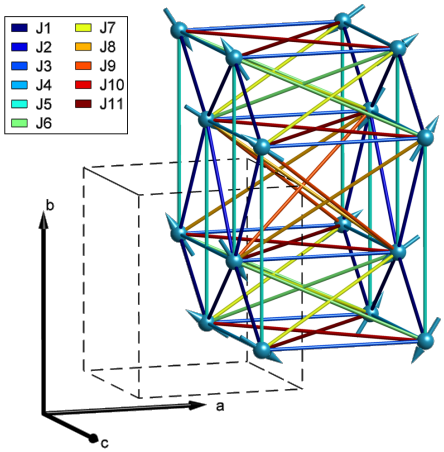

Figure 5.4: Magnetic exchange interactions in $MnWO_4$. The model shows magnetic moments in the AF2 phase in a $2 \times 2 \times 2$ unit cell with exchange paths along 11 closest distances, which were used to describe the magnon dispersion in the AF1 phase in Ref. [184].

exchange interactions and an easy-axis anisotropy (see Fig. 5.4). The magnetic interaction occurs by superexchange via one or two oxygen ions. Surprisingly, even the long-range exchange parameters are of sizable strength and are necessary to describe the systems properties, whereas the intra-chain interaction along $\vec{c}$ is rather small. The authors conclude, that the strength of this nearest-neighbor interaction is significantly reduced by the $[MnO_6]$-octahedra distortion. The distortion results in an enhanced Mn-O-Mn bond angle of approximately 95° [174], which reduces the nearest-neighbor exchange J_1 within the chains [196]. For isostructural compounds $M WO_4$ with M =Fe, Co and Ni, this angle is almost rectangular and the exchange J_1 is strongly ferromagnetic [196]. For M =Mn and Cu, the angle is enhanced, weakening J_{NN} relative to next-nearest-neighbor exchanges. This is believed to be one of the major differences relative to other MWO_4, leading to a strong degree of frustration in $MnWO_4$.
Density functional calculations and classical spin analysis were later used to determine the magnetic structure in the AF1 and AF2 phase, which revealed a different result for the AFM coupling between the spin chains along b-direction [183]. In a successive neutron time-of-flight (TOF) study by Ye *et al.*, the model had to be extended to eleven exchange parameters in order to properly describe the dispersion along different directions, using yet again a different set of magnetic interaction parameters [184]. First-principle calculations support this set of exchanges [197]. Nevertheless, it has been pointed out by Matityahu *et al.* [198] that especially the calculated Curie-Weiss temperatures from all proposed sets of exchanges strongly deviate from the experimental value of $\theta_{CW} \approx -75$ [47]. They attribute the discrepancy to a wrong choice of exchanges. Indeed, all models assume only an easy-axis anisotropy which might oversimplify the problem. For example, in an X-ray absorption study, a more complex situation was reported for the Mn moments, including two principal axes for the magnetic anisotropy and a DM term of similar size [199].

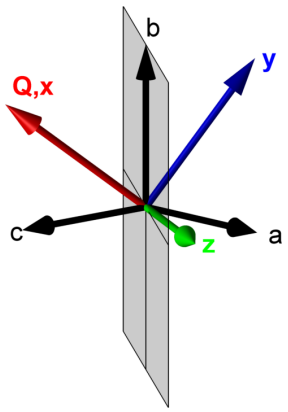

Figure 5.5: Sketch of neutron polarization analysis geometry at $\vec{Q} = (-0.21,\ 0.5,\ 0.45)$ in $MnWO_4$ in the $[-0.21, 0, 0.45]/[0, 1, 0]$ scattering plane. The dedicated coordination system is defined as x parallel $\vec{Q}$, z vertical and y perpendicular to x and z. The gray plane is spanned by $\vec{b}$ and the easy axis $\vec{e}_{ac}$ and symbolized the orientation of magnetic moments in the spiral AF2 phase. The easy axis lays in the ac-plane and is canted by approximately 35° relative to $\vec{a}$.

In the AF2 phase, the excitation spectra change drastically, and surprisingly, there are until today no reports of the spin wave dispersion in this ferroelectric phase. Only at the magnetic zone center, the excitation spectrum in this phase has been investigated by INS by Finger *et al.* [137]. As in the case of the multiferroic phase of $TbMnO_3$, three excitations have been found. Using polarization analysis, these modes could be distinguished in a low energy phason mode and two modes being polarized perpendicular to the plane of the magnetic spiral [137].
The multiferroicity in both $TbMnO_3$ and $MnWO_4$ is explained by the same DM mechanism and thus, one would expect both to show hybridized electromagnetic excitations [15]. These electromagnons have been observed in $TbMnO_3$ in optical spectroscopy [57] and neutron spectroscopy [12] (see Section 4.1.4 for details). The zone center excitations in the multiferroic AF2 phase in $MnWO_4$ are below 1.0 meV and an upper boundary was estimated for the spectral weight of a possible electromagnon of less than 0.1 % of the total weight, which renders them difficult to be accessed by optical spectroscopy [200]. No excitations of electromagnetic origin have been found in the region between ν =5 to 80 cm^{-1} (E =0.62 to 9.92 meV) [201], but there is evidence for an electromagnon mode around 4 cm^{-1} (0.5 meV) [202].
In a recent study by Niermann *et al.* using broadband dielectric spectroscopy, the critical slowing down of an electric fluctuation has been observed at the AF3→AF2 phase transition [203]. The fact that the order parameter of this transition is of magnetic origin, combined with the determination of the critical exponent led to the conclusion that these fluctuations are electromagnetic. The finding thus shows the softening of an electromagnon at the phase transition.

5.2. Diffuse magnetic scattering

The high degree of magnetic frustration in $MnWO_4$ leads to the presence of magnetic correlations outside of the magnetically ordered phases. Powder data reveal the presence of diffuse magnetic scattering at the position of the magnetic AF3 and AF2 Bragg reflections in the paramagnetic phase [175]. Even inside the ordered AF3 phase, a broadening of the reflections has been observed, yielding an almost continuous transition from the SDW paraelectric phase to the cycloidal ferroelectric phase. We used different unpolarized and polarized neutron scattering techniques to investigate the magnetic fluctuations above and inside the ordered phases.
For all presented experiments single crystals cut from the same rod were used. The crystal was grown by C. Tölzer and C. Lee by using the floating zone technique in a mirror furnace [204]. The measurement of the magnetic susceptibility showed three successive transitions at $T_{N3} = 13.47\,\mathrm{K}$, $T_{N2} = 12.32\,\mathrm{K}$ and $T_{N1} = 8.04\,\mathrm{K}$ which correspond perfectly to values reported by Lautenschläger *et al.* [175]. Two samples were prepared by J. Stein [205]: a smaller one with parallel planes cut along $\vec{b}$ (1.9 g, thickness 3.65 mm) and a larger one of cylindrical shape (4.0 g).
The propagation vector is $\vec{k}_{ic} = (-0.214,\ 0.5,\ 0.457)$ for the incommensurate phases AF3 and AF2 and $\vec{k}_c = (-0.25,\ 0.5,\ 0.5)$ for the commensurate phase in relative length units of the $P2/c$ structure. The two propagation vectors form an angle of only 3° and are similar in length ($k_{ic} = 0.89\,\mathrm{\AA}^{-1}$ and $k_c = 0.85\,\mathrm{\AA}^{-1}$). By taking advantage of the instruments goniometers, it is feasible to tilt the scattering plane by several degree, rendering Bragg reflections at both positions accessible.
Also the following geometry analysis holds for both propagation vectors. Figure 5.5 shows the typical scattering geometry for a polarization analysis at $\vec{Q} = (-0.21,\ 0.5,\ 0.45)$ in the $[-0.21, 0, 0.45]/[0, 1, 0]$ scattering plane in $MnWO_4$. The polarization axes are the following: $x \parallel \vec{Q}$, $z \parallel [2, 0, 0.9]$ and $y = z \times x$. The gray plane symbolizes the rotation plane of Mn moments in the AF2 phase. Magnetic scattering occurs for the magnetic components parallel to the scattering vector. Furthermore, the polarization analysis is based on the fact that scattering on magnetic moments perpendicular to the spin of the neutron $\vec{m}_{neutron}$ flip $\vec{m}_{neutron}$ by 180°, this is the spin-flip (SF) process. Scattering on moments parallel to $\vec{m}_{neutron}$ does not flip the neutron spin (non spin-flip process). Figure 5.5 nicely illustrates the separation of magnetic scattering along $\vec{b}$ and along $\vec{e}_{ac}$: M_y is composed of 60 %$||\vec{b}$ and 99 %$||\vec{e}_{ac}$ and M_z is composed of 100 %$||\vec{b}$ and 15 %$||\vec{e}_{ac}$. We can conclude, that intensity in the channel ySF sees M_z and is thus sensitive to the b-component, while the intensity in zSF sees M_y which is mainly sensitive to the $\vec{e}_{ac}$-component.

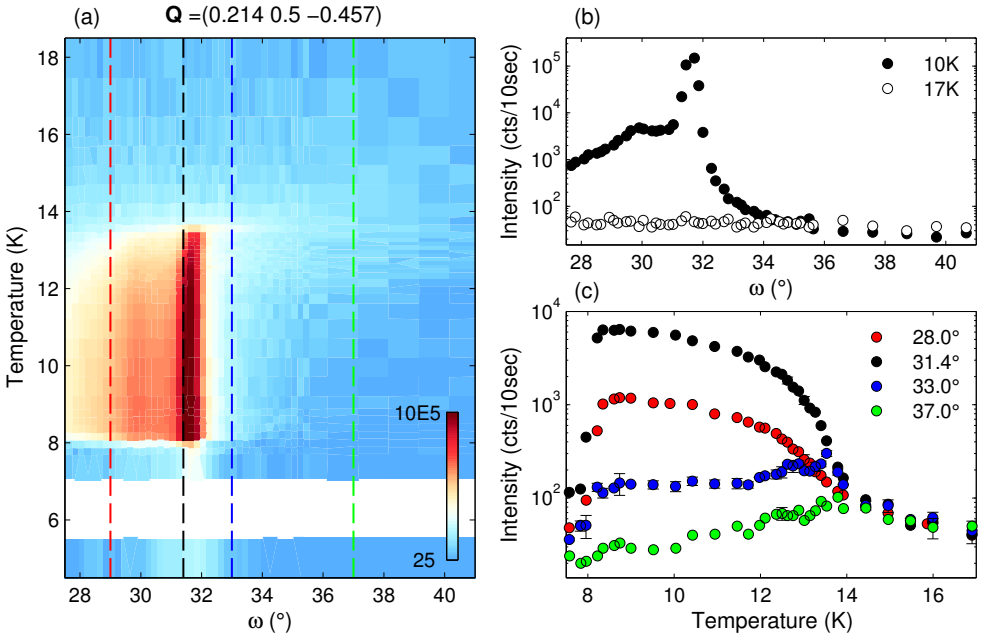

Figure 5.6.: Temperature dependence of rocking scans in $MnWO_4$ at IN3. (a) Intensity mapping of rocking scan over the magnetic Bragg peak position at $\vec{Q} = (0.214,\ 0.5, -0.457)$ at several temperatures. The intensity is logarithmically color coded. (b) Horizontal cuts at two temperatures, showing the initial scans. (c) Vertical cuts at several angles.

5.2.1. Sample characterization

In order to get an overview of the elastic and diffuse scattering in $MnWO_4$, a single crystal was mounted in $[-0.21, 0, 0.45]/[0, 1, 0]$ scattering geometry in a cryostat on the thermal neutron TAS instrument IN3 at the ILL. The neutron energy was fixed to $E = 14.7\,\mathrm{meV}$ ($k = 2.66\,\mathrm{\AA}^{-1}$). Beam collimation (30′ on $\vec{k}_i$ and 40′ on $\vec{k}_f$) and a PG filter on $\vec{k}_f$ were used to get a low background with high angular resolution. A high instrument resolution and a low mosaicity of the sample are indispensable for a meaningful separation of elastic and quasi-elastic contributions to the neutron scattering.
Figure 5.6(a) shows a logarithmic color mapping of a rocking scan (sample rotation ω) at the magnetic Bragg peak position at $\vec{Q} = (0.214,\ 0.5, -0.457)$ in the temperature range from 5 to 18 K. The original scan is shown at two temperatures in Fig. 5.6(b). The signal at the Bragg peak position shows a sharp peak below the ordering temperature T_{N3}. On one side of the peak, the signal rapidly decreases to the value of the background (cf. data at 17 K). On the other side the intensity decreases rapidly by almost two orders before it reaches a plateau of almost constant

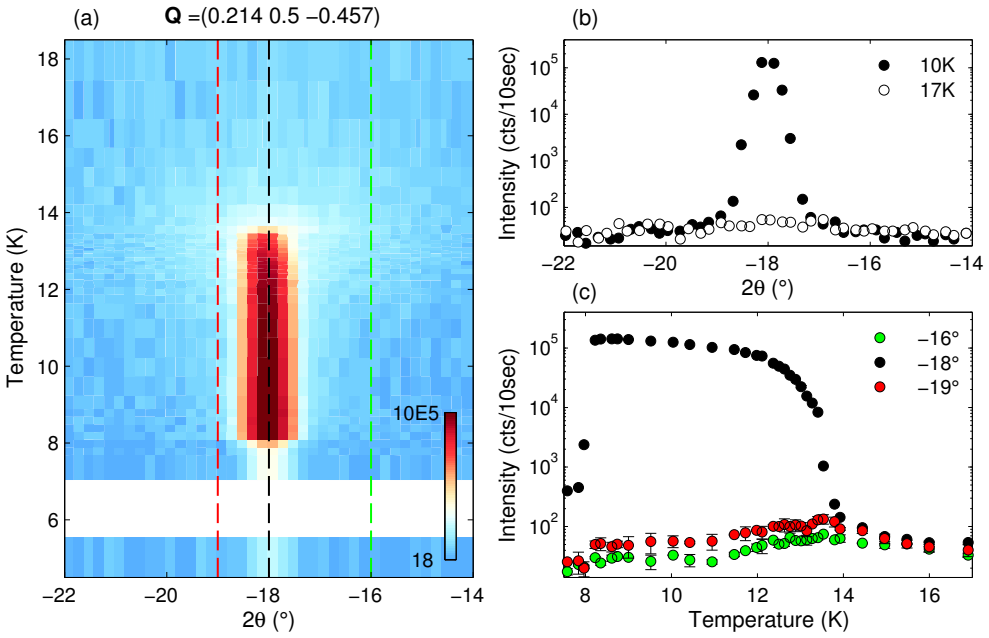

Figure 5.7.: Temperature dependence of 2θ-scans in $MnWO_4$ at IN3. (a) Intensity mapping of rocking scan over the magnetic Bragg peak position at $\vec{Q} = (0.214,\ 0.5, -0.457)$ at several temperatures. The intensity is logarithmically color coded. (b) Horizontal cuts at two temperatures, showing the initial scans. (c) Vertical cuts at several angles.

intensity which spreads over more than 3°. The maximum intensity of this plateau is only 1/100 of the intensity of the strong peak. It can be attributed to magnetic Bragg scattering from small crystallites, which are slightly tilted with respect to the larger single crystal. Nuclear reflections showed the same peak profile. A removal of the small misaligned crystallites was not possible.
Vertical cuts through the (T, ω)-map are shown in Figure 5.6(c). The corresponding scans are indicated by colored dashed lines in Fig. 5.6(a). The temperature dependencies at $\omega = 28.0°$ and 31.4° show the development of the AF3 Bragg reflection, an increase of intensity at the transition to the AF2 phase and finally a rapid drop at the AF2→AF1 first-order transition, where the propagation vector becomes commensurate. This is the expected behaviour of the long-range magnetic order.
The behaviour slightly away from the Bragg peak position, at ω =33.0° and 37.0°, differs significantly from the one at the static signal. At both positions, we find an increase of intensity when approaching the PM→AF3 transition, similar to the Bragg signal. After the transition, the intensity decreases again, until the second transition AF2, where it rises again. Inside the AF2 phase the intensity continuously decreases and finally drops to the background value at the first-order transition T_{N1}. Away from the position of the strong Bragg peak position, it

is possible to see short-range magnetic fluctuations. Fluctuations only persist over a limited time scale. Neutron scattering from fluctuations appears as broad Lorentzian-shaped peaks in Q-space, which correspond to the Fourier-transform of an exponential decay. Bragg peak scattering, in contrast, comes from a static (long-range) arrangement, which Fourier-transforms into a delta function in Q-space. These only appear broadened in Q-space due to the finite instrument resolution. The observation of diffuse magnetic scattering inside the ordered phase in this preliminary test renders the sample suitable for further investigations.
Figure 5.7(a-c) shows the same scenery for a rotation of scattering angle 2θ (almost transversal scan in Q-space) across $\vec{Q} = (0.214,\ 0.5, -0.457)$. The contamination of the small, misaligned crystallites is not visible in this scan, because it arises from the same Bragg peak as the bigger single crystal. Again, we find diffuse scattering near the Bragg peak which is pronounced around the phase transitions at T_{N3} and T_{N2}.
Finally, we investigate the temperature behaviour of neutron at the commensurate magnetic Bragg peak position at $\vec{Q} = (0.25,\ 0.5, -0.5)$. In order to do so, the scattering plane was changed by tilting the cryostat by approximately 3°. The sample could be investigated under the same conditions as in the case of the incommensurate phase. The corresponding temperature dependencies are shown in Figure 5.8(a-c) (ω-scan) and Figure 5.9(a-c) (2θ-scan). The AF2→AF1 transition is of first order and no fluctuations are expected above and below. Indeed, the intensities away from the Bragg peak position are constant with temperature.
The 2θ-scans in Figure 5.9(a-c) show another sharp signal at a slightly different scattering angle. This signal comes from the incommensurate Bragg reflection of the AF2 phase. Both, incommensurate and commensurate, Bragg reflections are close in Q-space and due to the finite instrument resolution, we only capture a weak signal from the incommensurate peak. The temperature dependence nicely illustrates a small overlap of both signals, which is typical for a first-order transition. It is in sharp contrast to the second-order AF3→AF2 transition, which is almost continuous.

5.2.2. Antiferromagnetic transition at T_{N3}

The magnetic fluctuations above the antiferromagnetic phase transition T_{N3} were investigated at the diffuse scattering spectrometer D7 with xyz polarization analysis at the ILL. A single crystal of $MnWO_4$ was mounted in $[0, 1, 0]/[0.21, 0, 0.45]$ scattering geometry. Throughout the experiment, we worked with a fixed incident neutron wavelength of $E_i = 3.46\,\text{meV}$ ($k_i = 1.29\,\text{Å}^{-1}$, $\lambda_i = 4.86\,\text{Å}$). The instrument D7 only analyzes the polarization of the scattered neutrons, not their energy.

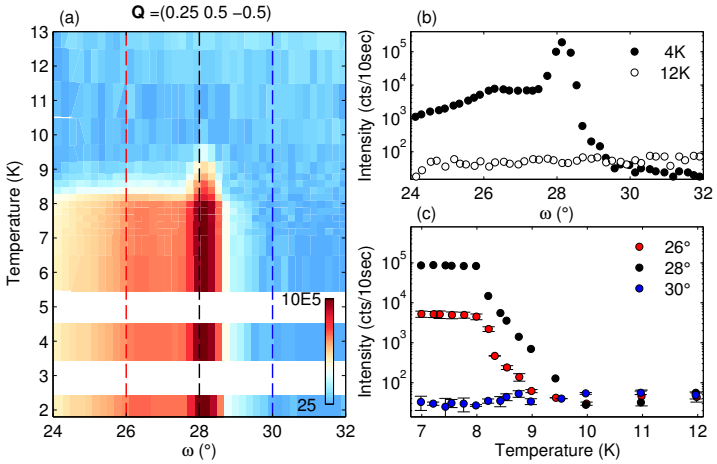

Figure 5.8: Temperature dependence of rocking scans in $MnWO_4$ at IN3. (a) Logarithmic intensity mapping of rocking scan over the magnetic Bragg peak position at $\vec{Q} = (0.25,\ 0.5, -0.5)$ at several temperatures. (b) Horizontal cuts at two temperatures, showing the initial scans. (c) Vertical cuts at three angles.

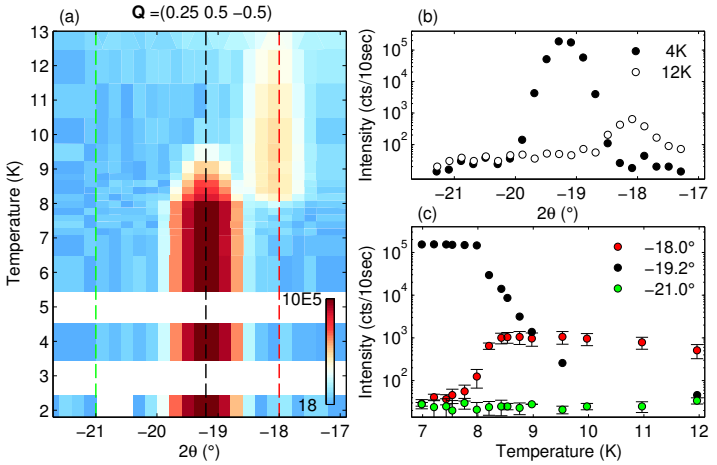

Figure 5.9: Temperature dependence of 2θ-scans in $MnWO_4$ at IN3. (a) Logarithmic intensity mapping of rocking scan over the magnetic Bragg peak position at $\vec{Q} = (0.25,\ 0.5, -0.5)$ at several temperatures. (b) Horizontal cuts at two temperatures, showing the initial scans. (c) Vertical cuts at three angles.

This allows the investigation of fast fluctuations, which are cut-off by the energy analysis in a TAS experiment.
The D7 instrument consists of three detector banks, each one having 44 single detectors [105], which allows for a large coverage of solid-angle within the scattering plane. This has some influences on the geometry for polarized neutrons and the separation of directions becomes more complicated as shown in Fig. 5.5. The direction of the magnetic field is fixed relative to the direct beam. The angle between x and the incident beam is called *Schärpf-angle*, which is approximately 26° at the D7 [106]. At each value of 2θ, we thus have a linear combination of x and y, since x is no longer parallel $\vec{Q}$. Table 5.1 summarizes the scattering angles and linear combination of x and y for the three accessible magnetic Bragg reflections in the chosen scattering plane. The values are deduced from the relative angle between $\vec{Q}$ and the polarization axis, taking into account the quadratic relation between the ordered moment and the scattered intensity, $I \propto \vec{M}^2_{\perp\vec{Q}}$. In

$\vec{Q}$ (r.l.u)	$2\theta(^\circ)$	$\angle(\vec{Q},x)(^\circ)$	$\angle(\vec{Q},y)(^\circ)$
$(-0.21,\ 0.5,\ 0.45)$	37.4	82.7	-7.3
$(-0.21,\ 1.5,\ 0.45)$	85.4	106.7	16.7
$(-0.79,\ 0.5,\ 1.55)$	121.5	124.8	34.8

Table 5.1: Scattering geometry for polarization analysis at D7 for $MnWO_4$ with $\lambda = 4.86\,\text{Å}$ and a *Schärpf-angle* of 26°. Listed are the angle between reciprocal vectors and the polarization directions along x and y, which are fixed at D7.

all cases, the y-part is dominant which means a reversal of polarization channels with respect to the notation used in Fig. 5.5. The z-direction is not affected by the *Schärpf-angle*, as it is always perpendicular to the scattering plane.
The data obtained on D7 was corrected for varying detector efficiency, detector solid angle, and analyzer transmission using a Vanadium standard with the program *LAMP* [206]. The varying detector flipping ratios are corrected by measuring a standard Quartz sample. A mean flipping ratio of about 20 was reached throughout the experiment. The influence of the scattering from the instrument environment was determined by measuring the background with a Cadmium sample and subtracted from the raw data. The procedures of data correction are described in detail in References [207] and [208]. The data was plotted using the *fcplot* routine for *MATLAB* [85].
Figure 5.10 shows an elastic scattering map in the spiral AF2 phase for non-spin flip processes along the neutron polarization axis z. This corresponds to the channel zNSF, i.e. the cross section σ_{zz}. The scattering plane spanned by the vectors $[0,1,0]$ and $[0.21,0,0.45]$. The axis show the length of the reciprocal vectors and dotted red lines indicate integer multiples of the scattering vectors. No symmetrization has been done, the sample was rotated by 360° to obtain the scan. Two contributions can be distinguished: nuclear Bragg reflections at $\vec{Q} = (0,-1,\ 0)$ and $\vec{Q} = (0,-1,\ 0)$ (black circles) and magnetic satellites at $\vec{Q} = (-0.21,\ 0.5,\ 0.45)$, $\vec{Q} = (-0.21,-1.5,\ 0.45)$ and $\vec{Q} = (-0.79,-0.5,\ 1.55)$ (green circles). All Bragg reflections show a tail on one side. It has been discussed in the previous section that this feature arises from smaller crystallites of the sample. The powder line in the intermediate region comes from nuclear scattering from the aluminum sample holder. The symmetry of the dataset documents the perfect alignment of the sample. In order to use the limited beam time efficiently, only 180° scans were performed in the paramagnetic phase. The datasets were symmetrized by a two-fold rotation for a better visibility.
We continue with the polarization analysis of the diffuse scattering in the paramagnetic phase in $MnWO_4$. In Figure 5.11, the intensities of the diagonal spin-flip cross

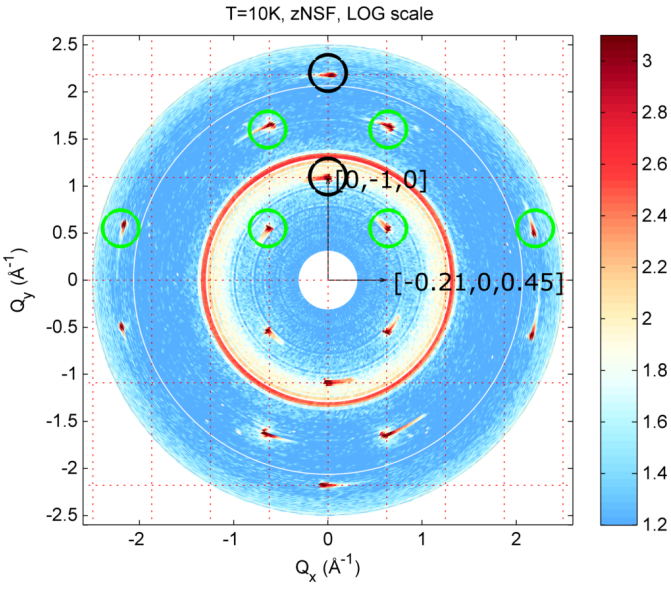

Figure 5.10: Elastic scattering map of $MnWO_4$ at 10 K at D7. The non-spin-flip intensity along z (σ_{zz}, zNSF) was determined by a 360° rocking scan in the scattering plane spanned by the vectors $[0, 1, 0]$ and $[-0.21, 0, 0.45]$ at D7. Nuclear reflections (black) and magnetic satellites (green) are marked by circles. The powder line in the intermediate region can be attributed to the aluminum environment.

sections $\sigma_{x\bar{x}}$, $\sigma_{y\bar{y}}$, $\sigma_{z\bar{z}}$ and non spin-flip cross sections σ_{xx}, σ_{yy}, σ_{zz} are shown at 14 K, well above $T_{N3} = 13.5$ K. The maps on the left side show spin-flip scattering, which is purely magnetic. The main contributions arise at the positions of the magnetic Bragg peaks of the AF3 phase, listed in Table 5.1. We discussed that, for all three positions (and their symmetry equivalents) the guide field for y is almost parallel $\vec{Q}$. Hence in the ySF channel we see the sum of the channels xSF and ySF. Furthermore, the xSF channel is more sensitive to scattering from moments along the easy axis $\vec{e}_{ac}$ and the zSF sees the scattering in the scattering plane, i.e. along $\vec{b}$. This separation works most accurately at $\vec{Q} = (-0.21,\ 0.5,\ 0.45)$.
At $T_{N3} = 13.5$ K, the Mn moments order in an incommensurate SDW along the easy axis $\vec{e}_{ac}$. We thus expect the fluctuations close to the phase transition to also be mainly polarized along $\vec{e}_{ac}$, which can be confirmed by comparing the intensities in the channels xSF and zSF. Two other observations can be made from the scattering maps. First, we see diffuse scattering at the second-order Bragg position $\vec{Q} = (-0.42,\ 1.0,\ 0.90)$. Structural modulations of half the period arise in incommensurate collinear magnetic structures due to the effect of exchange-striction. The scattering of the second-order modulation has been studied in detail by Finger *et al.* [185]. They find enhanced magnetic and nuclear scattering at this position even in the spiral AF2 phase and relate their presence to pinning of magnetic and ferroelectric domains [185]. Second, magnetic diffuse scattering can be observed around the positions of nuclear Bragg reflections. Small contaminations from non spin-flip scattering (nuclear scattering) are visible due to the finite flipping ratio. They arise from the nuclear Bragg reflections and the aluminum holder.
The non spin-flip scattering maps on the right side of Fig. 5.11 are composed of nuclear and magnetic scattering. Only when $\vec{Q}$ is parallel to the polarization axis,

the magnetic scattering is absent. This is the case for the yNSF channel, where we find only scattered signal from the nuclear Bragg reflections and the aluminum powder line.
The xyz polarization analysis on D7 provides full and unambiguous separation of the magnetic, nuclear and spin-incoherent cross sections in the paramagnetic phase of magnetic systems. The different cross sections can be decoupled by taking into account the directions of polarization (defined by the *Schärpf-angle*) and the Moon-Riste-Koehler equations for an uniaxial polarized neutron beam [99] (see Ref. [105] for details). Figure 5.12 shows the obtained intensities for nuclear and magnetic scattering. The magnetic contribution can be calculated from NSF (Figure 5.12(b)) and SF (Figure 5.12(c)) channels. Both maps show a similar pattern, with the difference, that the statistics for the NSF maps are lower. The magnetic scattering can be deduced from either SF or NSF channels. The result of the component separation nicely confirms our interpretation of the data.
The diffuse scattering in $MnWO_4$ could be followed up to 30 K, which is almost three times the Néel temperature of the compound. Figure 5.13 shows symmetrized intensity maps of the magnetic intensity obtained by component separation averaged from spin-flip and non spin-flip channels. The signal is thus purely magnetic. The intensity is linearly scaled using the same scale for all temperatures. The intensity at the magnetic Bragg peak positions continuously decreases with temperature and vanishes at 60 K.
The Q-dependence of diffuse magnetic scattering in the paramagnetic phase bears a characteristic shape, which is most pronounced close to the transition temperature at 14 to 20 K. The scattering is strongly anisotropic and it is particularly enhanced diagonal away from the Bragg positions. This characteristic shape may be helpful in order to determine the correct setting of exchange parameters by comparison with simulations of diffuse scattering maps. The diffuse magnetic scattering was simulated by a mean-field model, taking into account the interaction exchanges of the AF1 phase proposed in literature [184, 196]. While this approach worked properly for the paramagnetic phase of $TbMnO_3$ (see Figure 4.8), the characteristics of the diffuse scattering in $MnWO_4$ could not be reproduced by the simple model. The strong reduction of the nearest-neighbor exchange in $MnWO_4$ strongly frustrates the magnetic system [196]. The magnetic system becomes very complex and a proper spin-wave calculation has to be performed in order to model the diffuse magnetic scattering.
The intensity maps at 60 K and 100 K show enhanced scattering left and right of the center. This intensity might be partly related to the shape of the sample holder. The sample is placed between aluminum plates with a normal vector parallel $[0, 1, 0]$. This may result in an anisotropic background from the sample holder.
We can quantitatively analyze the diffuse scattering data by looking at specific

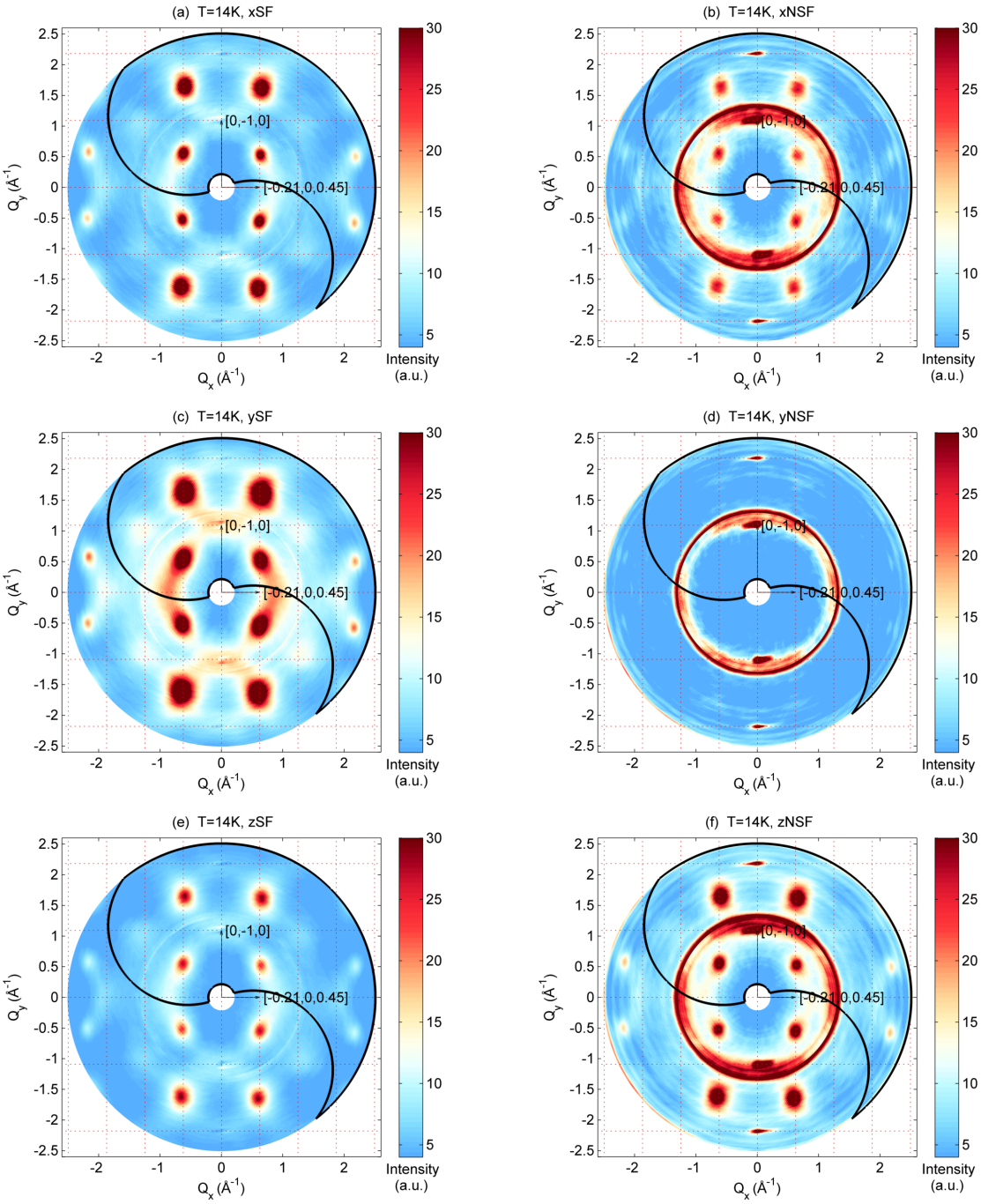

Figure 5.11.: Polarization analysis of diffuse scattering in $MnWO_4$ in $[0, 1, 0]/[-0.21, 0, 0.45]$ scattering geometry at D7. The intensity maps were collected on D7 by 180° rocking scans (black frame) at 14 K and symmetrized by a 2-fold rotation. Six linear non-spin-flip and spin-flip cross sections are shown: (a) $\sigma_{x\bar{x}}$, (b) σ_{xx}, (c) $\sigma_{y\bar{y}}$, (d) σ_{yy}, (e) $\sigma_{z\bar{z}}$ and (f) σ_{zz}.

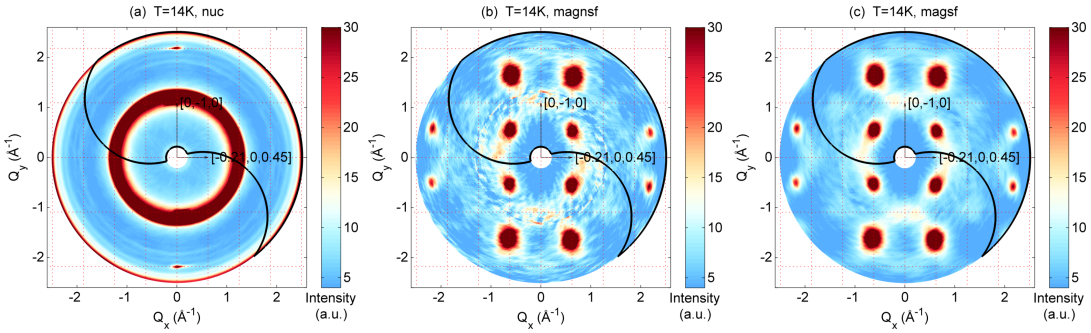

Figure 5.12.: Component separation of neutron scattering in $MnWO_4$ in $[0, 1, 0]/[-0.21, 0, 0.45]$ scattering geometry at D7. The use of polarized neutrons allows to separate the contribution of (a) nuclear, (b) magnetic non spin-flip and (c) magnetic spin-flip scattering. The intensity maps were collected on D7 by 180° rocking scans (black frame) at 14 K and symmetrized by a 2-fold rotation.

directions within the scattering plane. Figure 5.14 shows cuts along $[0, 1, 0]$ and $[-0.21, 0, 0.45]$ taken from scattering maps in the channels xSF and zSF at several temperatures in the paramagnetic phase. The scan directions are indicated with dashed lines in Fig. 5.13. This allows the comparison of magnetic correlations along two different directions in the crystal. Moreover, the polarization analysis allows for differentiating between scattering of moments along the easy axis $\vec{e}_{ac}$ (xSF) and along the monoclinic axis $\vec{b}$ (zSF). The experimental data was fitted using two Lorentzian functions and a linear background. For the scans along $[0, 1, 0]$ some points were removed to avoid the small contribution of the powder line.
The results of the Lorentzian fit for the scans at $T = 14$, 16, 20 and 30 K are summarized in Figure 5.15. The plot shows the temperature dependence of the peak intensity and the correlation length, which is given by $\xi = |\vec{Q}|^{-1} \cdot \mathrm{HWHM}$, determined along two different scan direction and polarization axes. A power law function was fitted to the data, using two different transition temperatures $T_{C3} = 13.4$ K and $T_{C2} = 12.3$ K, which are similar to those obtained from magnetic susceptibility measurements on the same sample [204].
We start with the differentiation of scattering in the two polarization channels by looking at the temperature dependence of the scattered intensity, shown in Fig. 5.15(a). The intensity in xSF increases strongly with decreasing temperature and its temperature dependence corresponds to a transition at $T_{C3} = 13.4$ K to a static magnetic order. This channel is sensitive to magnetic scattering along $\vec{e}_{ac}$ the direction of moments in the SDW AF3 phase. The temperature dependence of the zSF deviates from this behaviour. The fit indicates that it corresponds to a transition at lower temperature. This channel is sensitive for magnetic scattering along $\vec{b}$, and indeed, the b-component orders only below $T_{C2} = 12.3$ K, where the AF3→AF2 transition towards a spin spiral occurs. Furthermore, we can deduce

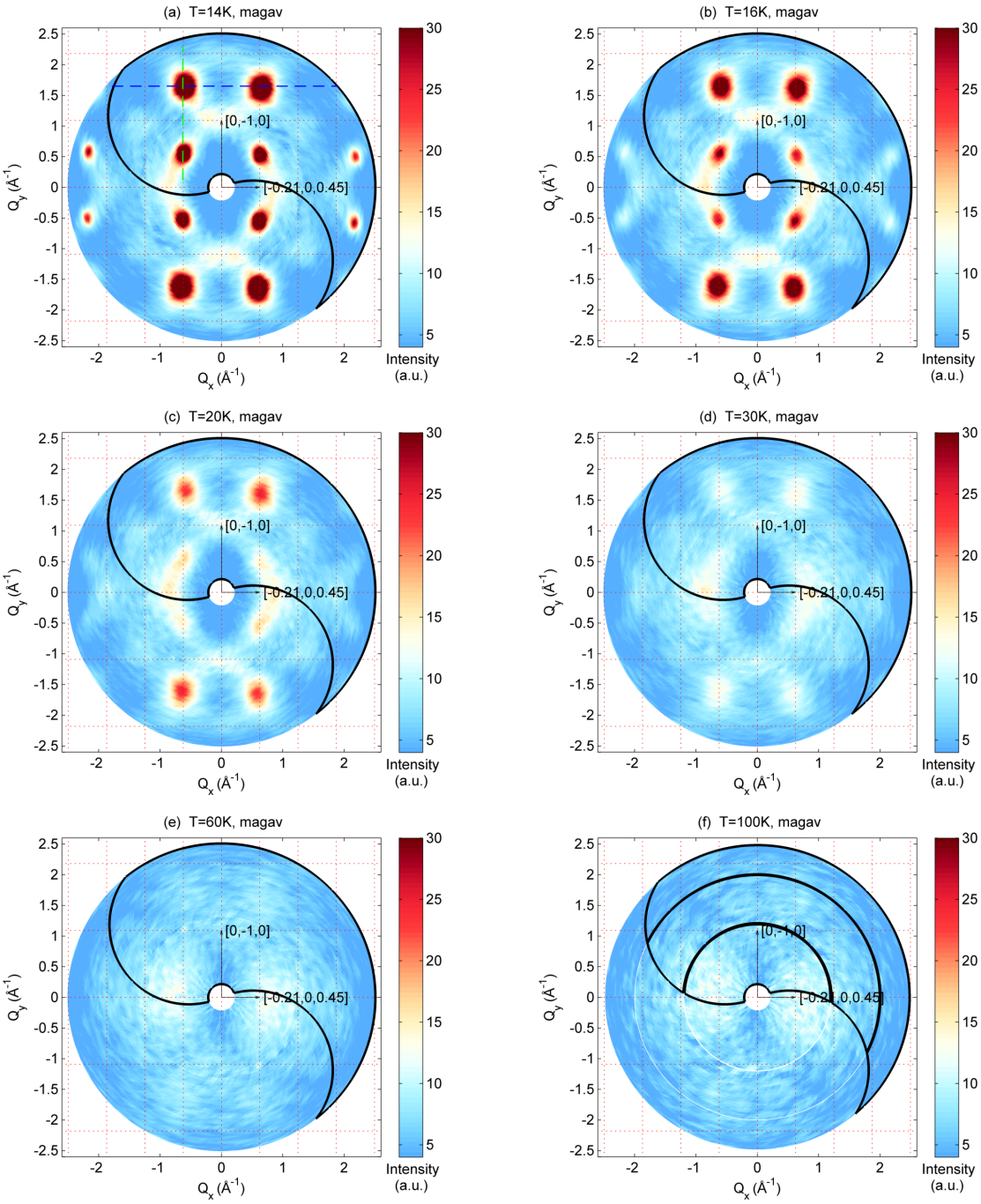

Figure 5.13.: Temperature dependence of magnetic scattering in $MnWO_4$ in $[0, 1, 0]/[-0.21, 0, 0.45]$ scattering geometry at D7. The magnetic intensity was deduced using polarization analysis. The intensity maps were collected on D7 by 180° rocking scans (black frame) and symmetrized by a 2-fold rotation. Diffuse magnetic scattering is present up to 30 K.

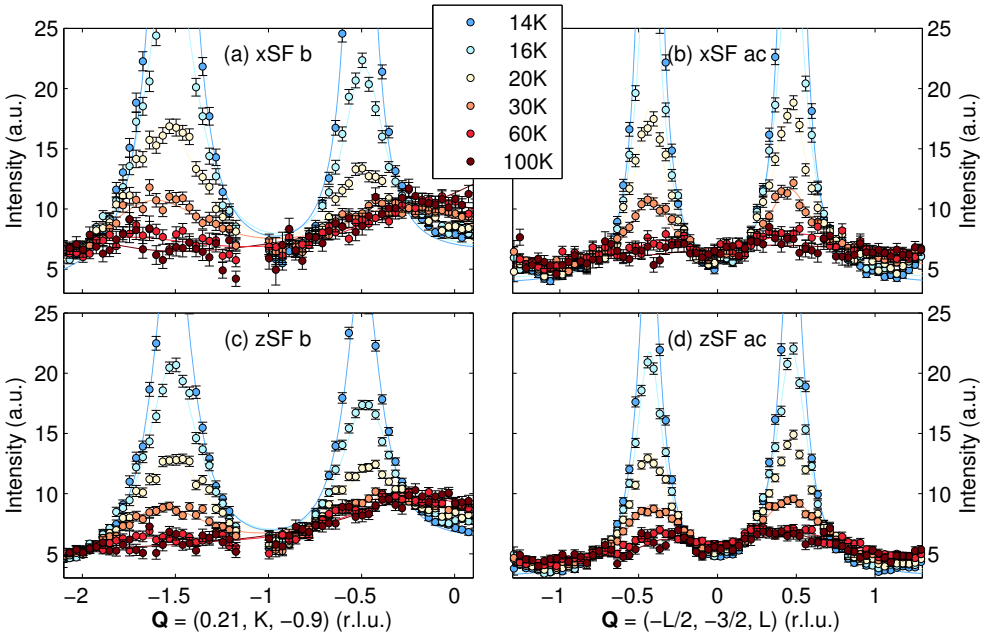

Figure 5.14.: Magnetic scattering in $MnWO_4$ along $[0, K, 0]$ and $[-0.5L, 0, L]$ at different temperatures in the paramagnetic phase at D7. The line scans were extracted from D7 scattering maps: (a-b) xSF and (c-d) zSF. Lorentzian functions were fitted to the data.

that only at the highest temperature shown, $T = 30\,\mathrm{K}$, the diffuse magnetic scattering becomes isotropic, i.e. the scattered intensities are similar in the spin-flip channels along x and z. The intensities from the different scan directions, $[0, K, 0]$ and $[-0.5, L, 0, L]$, show the same results. This is expected since the scans go along the same Q-positions.

The analysis of the temperature dependence of the correlation lengths, shown in Fig. 5.15(b), bears additional information. It allows us to differentiate scattering from magnetic fluctuations along different directions. The temperature dependence of the correlation length in xSF clearly deviates from the other spin-flip channel zSF. The fit of a power law function supports the temperature behaviour shown in the previous section: the correlation length of fluctuations along the easy axis $\vec{e}_{ac}$ (in xSF) diverges at $T_{C3} = 13.4\,\mathrm{K}$, while fluctuations along $\vec{b}$ (in zSF) seem to diverge at the lower temperature $T_{C2} = 12.3\,\mathrm{K}$.

Furthermore, we can deduce information from the different scan directions. At higher temperatures the correlation lengths in 'xSF ac' and 'zSF ac' are enhanced. This means that the fluctuations are isotropic and extend mainly along the easy axis $\vec{e}_{ac}$. At lower temperatures, close to the upper transition at T_{N3}, channels 'xSF b' and 'xSF ac' strongly increase. This corresponds to anisotropic fluctuations of moments along the easy axis $\vec{e}_{ac}$. The correlation length of these fluctuations increase along both directions in the crystal, $\vec{e}_{ac}$ and $\vec{b}$.

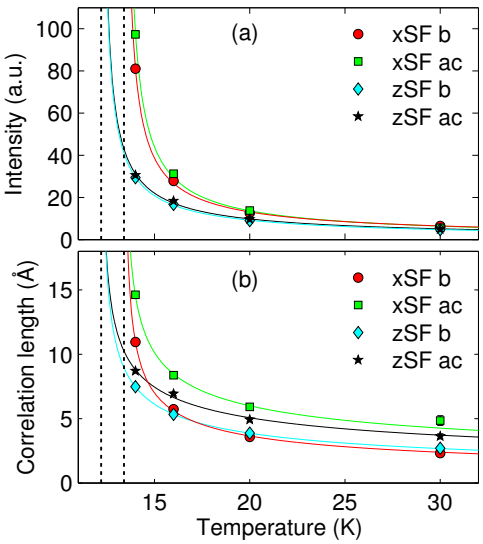

Figure 5.15: Properties of diffuse magnetic scattering in $MnWO_4$ at the magnetic Bragg position $\vec{Q} = (-0.21, -1.5,\ 0.45)$ at D7. The intensity and FWHM was determined by Lorentzian functions along two directions, $[0, K, 0]$ (b) and $[-0.5L, 0, L]$ (ac), and two spin-flip polarization axes, xSF and zSF (cf. Fig. 5.14). The correlation length was calculated from the width of the Lorentzian fits. A power law was fitted to the curves using $T_{N3} = 13.4\,\mathrm{K}$ and $T_{N2} = 12.3\,\mathrm{K}$ denoted by dashed lines.

The analysis of the critical magnetic behaviour in $MnWO_4$ along $\vec{e}_{ac}$ and $\vec{b}$ imposes the assumption, that the fluctuations in the paramagnetic phase in $MnWO_4$ are composed of two contributions. Only one part, the fluctuations along $\vec{e}_{ac}$, become static at T_{N3}. Contrarily, the temperature dependence of the other part, the fluctuations along $\vec{b}$, suggests that they become static below T_{N3}. This would imply that these b-polarized fluctuations persist even in the ordered AF3 phase. The attempt was made to investigate the fluctuations in the AF3 phase on D7. The presence of strong overlapping magnetic Bragg peaks renders it very difficult to follow the relatively weak scattering of fluctuations. A different experimental approach was necessary, which is described in the following section.

5.2.3. Multiferroic transition at T_{N2}

We already established the fact, that diffuse scattering surrounds the static magnetic Bragg peaks in the AF2 phase in $MnWO_4$ (see Section 5.2.1 for details). In order to characterize these fluctuations, a single crystal was installed at the cold neutron TAS instrument IN14 at the ILL. A set of Helmholtz coils was mounted in combination with a supermirror bender and a Heusler analyzer in order to use linear neutron polarization analysis. The sample was placed between parallel aluminum plates to enable the application of an electric field along the direction of ferroelectric polarization $\vec{b}$ and was mounted in $[-0.21, 0, 0.45]/[0, 1, 0]$ scattering geometry. The neutron energy was fixed to $E = 4.7\,\mathrm{meV}$ ($k = 1.5\,\mathrm{\AA}^{-1}$). Beam collimation ($40'$ on $\vec{k}_f$), a beryllium filter and a flat analyzer were used in order to reduce the background and achieve a high angular resolution. The flipping ratio

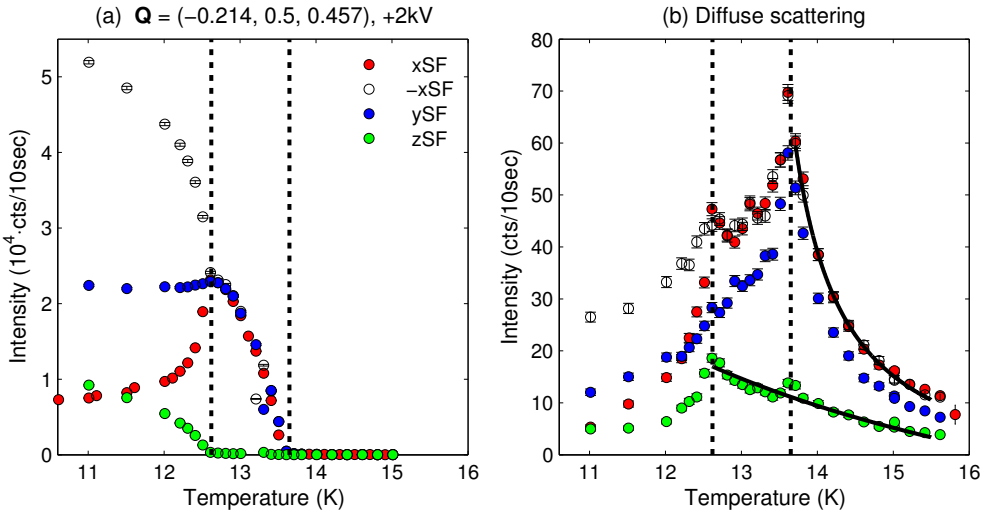

Figure 5.16.: Polarization analysis of magnetic Bragg peak and diffuse scattering in $MnWO_4$ at IN14. (left) Temperature dependence of scattered neutron intensity at $\vec{Q} = (-0.214,\ 0.5,\ 0.457)$. (right) Temperature dependence of diffuse scattering slightly away from the Bragg peak ($+4°$ in ω). The dashed lines indicate the magnetic transitions T_{N3} and T_{N2}. The black solid lines serve as guide to the eye. An electric field of $+550\,\mathrm{V\,mm^{-1}}$ was applied to the sample along $\vec{b}$.

at the nuclear Bragg reflection $\vec{Q} = (0,\ 1,\ 0)$ was $FR \approx 27$, which corresponds to a neutron polarization higher than 92 %.

The temperature dependence of the magnetic Bragg reflections was summarized in Section 5.2.1 using unpolarized neutron scattering. We investigated the behaviour of neutron scattering of the static magnetic structure and the fluctuations in the ordered phase. At the Bragg position, the weak signal from the diffuse scattering lays on top of a strong static background. It is nevertheless possible to detect scattering from fluctuations slightly away from the peak position, since diffuse scattering is significantly broadened in Q-space relative to static Bragg scattering. Figure 5.16 shows the temperature dependence of neutron scattering at the magnetic Bragg peak position $\vec{Q} = (0.214,\ 0.5, -0.457)$ (left) and slightly away from the peak (right, 4° sample rotation). An electric voltage of 2 kV was applied to the sample ($E \approx 550\,\mathrm{V\,mm^{-1}}$) and the intensity of four spin-flip cross sections was collected: $\sigma_{x\bar{x}}$ (xSF), $\sigma_{\bar{x}x}$ (-xSF), $\sigma_{y\bar{y}}$ (ySF) and $\sigma_{z\bar{z}}$ (zSF). The orientation of the polarization axes x, y and z is shown in Figure 5.5. The polarization analysis allows to separate scattering from moments along the monoclinic axis $\vec{b}$ (zSF) and the easy axis $\vec{e}_{ac}$ (ySF). Furthermore, the comparison of the spin-flip channels along x permits the detection of the chiral magnetic term $-i(\vec{M}_\perp \times \vec{M}^*_\perp)_x$, cf. Tab. 3.1. The intensity at the Bragg peak position increases at T_{N3} and is almost fully polarized in the ySF channel in the temperature range of a few Kelvin above T_{N3}.

The ySF channel is sensitive to direction of moments in the SDW. The intensity in the zSF channel was corrected for contamination from the zNSF channel through the finite flipping ratio[a]. About 3 % of the intensity in zNSF (which is sensitive to moments parallel $\vec{e}_{ac}$) is visible in this channel. The intensity after correction slowly increases during cooling from 0 to 300 cts/10sec.
At the second transition T_{N2}, the structure transforms into a spin spiral, which comes along with the development of a b-component, visible in zSF. The ellipticity $e = m_b/m_{\text{easy}}$, which can be estimated by the ratio of ySF and zSF scattering, increases continuously and is $e \approx 0.9$ at 9 K [13]. The chiral ratio can be calculated as $r_{\text{chiral}} = \frac{I_{x\bar{x}} - I_{\bar{x}x}}{I_{x\bar{x}} + I_{\bar{x}x}} \approx 0.76$ at 11 K, which matches well reported values [50]. The saturation value of 1 can only be reached when $\vec{Q}$ is parallel to the rotation axis of the spiral. At the present position a maximum value of $r_{\text{chiral}} = 0.96$ is possible for a monodomain sample.
The diffuse scattering slightly away from the Bragg position is similar in the paramagnetic phase. When coming from higher temperatures, the intensity increases towards the upper phase transition. The scattering becomes more anisotropic and the major part is polarized along $\vec{e}_{ac}$ at the transition. Below T_{N3}, the scattering behaviour significantly changes and differs completely from the scattering from the Bragg peak. The overall intensity decreases when the Bragg peak sharpens. More surprisingly, the polarization of the magnetic scattering changes: the intensity in zSF increases, whereas the ySF-intensity decreases. This shows the development of a b-component scattering from the paramagnetic and through the AF3 phase (black line). The dip at T_{N3} is caused by a contamination of the increasing zNSF. Finally below T_{N2}, the diffuse scattering decreases in all channels.
The temperature dependence of the diffuse scattering in $MnWO_4$ demonstrates the continuous transition from the spin density wave to the spin spiral and shows that even in the paramagnetic phase precursors of the spiral phase are present.

Chiral diffuse scattering

The observed diffuse scattering in the AF3 phase arises from correlated fluctuations of moments along $\vec{b}$. Such fluctuations should transform the SDW into a spiral, which carries a chirality within the corresponding correlation length and time. The polarization analysis allows us to identify such a parameter by comparing the two spin-flip channel along x. The difference will be small in comparison to the static, non-chiral signal and a excellent statistic is necessary to obtain meaningful data. The experimental setup was optimized by replacing the polarized Heusler analyzer by an unpolarized PG analyzer with larger surface area and higher efficiency

[a] The flipping ratio adds a contamination of the non spin-flip channel as $\frac{1}{FR} \cdot NSF$.

leading to a increase of flux by a factor of two. Without the analyzer we are no longer able to differentiate between spin-flip and non spin-flip processes. This separation is not necessary, as it was already verified that no nuclear scattering is present at the investigated Q-position.
The temperature evolution of the scattered intensities in the cross sections parallel x is shown in Figure 5.17(a-b) at the Bragg peak position $\vec{Q} = (0.214,\ 0.5, -0.457)$ and slightly away. Beginning in the paramagnetic phase, the sample was cooled in an electric field of approximately $550\,\mathrm{V\,mm^{-1}}$. The plots show a close-up around the multiferroic transition T_{N2}, which is indicated by a dashed line. The temperature was determined by fitting the xSF intensity using a power law function as described by Tolédano *et al.* [178]. Above the transition, the intensity is equally distributed in both channels, which is expected for the scattering from a spin density wave. Below the transition, both channels become unequal, with their difference being the chiral magnetic component, $-i(\vec{M}_\perp \times \vec{M}^*_\perp)_x$, arising from the spiral spin structure. The application of a reversed electric field lead to the complete switched-over of the scattered intensities in both channels. With this test, we could approve that the difference purely arises from the chiral domains poled by an electric field.
The diffuse scattering slightly away from the Bragg reflection shows a similar behaviour, shown in Fig. 5.17(b). While cooling, the intensities in the two channels separate due to a poling of chiral fluctuations in the electric field. At the transition T_{N2}, the intensity increases when the fluctuations become static. Their correlation length diverges and they are no longer visible away from the Bragg peak position. The remarkable observation in this scan is the presence of chiral scattering above T_{N2}, inside the SDW phase. This diffuse chiral scattering is only visible up to 12.67 K, which is about 1 % above the transition. The scans were performed using a temperature step of 0.005 K and a counting time of $\Delta T = 120\,\mathrm{s}$, yielding an optimal statistic with neutron counts of the order of 10^6. It is surprising that the chiral diffuse scattering is limited to about 0.15 K above the transition, whereas diffuse magnetic scattering was observed up to 1 K above (cf. Fig. 5.16). The chiral diffuse scattering was measured using a higher instrument resolution of $\Delta E \approx 0.13\,\mathrm{meV}$ at $k = 1.2\,\mathrm{\AA}^{-1}$ (compared to $\Delta E \approx 0.25\,\mathrm{meV}$ at $k = 1.5\,\mathrm{\AA}^{-1}$). This corresponds to accessible time scale of approximately 30 GHz for scattering from fluctuations. The energy analysis in a TAS experiment defines the limit for the accessible energy and time range.
Our results agree with the observation of the critical slowing down of ferroelectric fluctuations in $MnWO_4$ reported by Niermann *et al.* [203]. Using broadband dielectric spectroscopy, they followed the softening of an electric mode between T_{N2} and 1.5 % above in the range of 0 to 8 GHz. These electric fluctuations are coupled via the DM mechanism to the vector chirality of the magnetic structure, rendering them visible using polarized neutrons. One is tempted to assume that

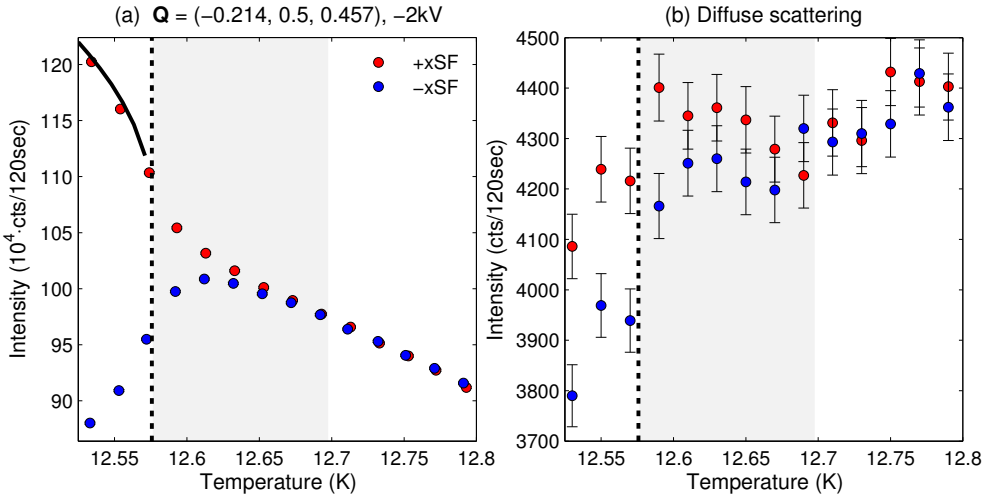

Figure 5.17.: Chiral magnetic scattering in $MnWO_4$ at IN14. Temperature dependence of scattered neutron intensity in the cross sections $\sigma_{x\bar{x}}$ (+xSF) and $\sigma_{\bar{x}x}$ (-xSF) at the Bragg peak position $\vec{Q} = (-0.214,\ 0.5,\ 0.457)$ (a) and slightly away (+4° in ω) (b). An electric field of $+550\,\mathrm{V\,mm^{-1}}$ was applied to the sample along $\vec{b}$ upon cooling. The transition temperature T_{N2} determined by a power law fit (solid line) is indicated by a dashed line.

both experimental observations, from this section and from Ref. [203], arise from the same microscopic phenomenon.

We find a similar scenario in $TbMnO_3$, where the ferroelectric polarization is likewise induced by a spiral spin structure via the DM interaction [15]. On one hand, Finger *et al.* documented the existence of chiral diffuse magnetic scattering in a range of 2 K above the multiferroic phase [137]. Diffuse magnetic scattering, on the other hand, is present in the entire SDW phase ranging from 28 to 42 K, as demonstrated in Section 4.2.2.

We can state that in $MnWO_4$, chiral magnetic fluctuations were only observed in a limited region above the multiferroic transition, whereas magnetic fluctuations are visible even at higher temperatures, similar to the fluctuations in $TbMnO_3$ [137]. One possibility to explain this discrepancy is the effect of electric poling. Chiral fluctuations can only be detected in polarized neutron experiments when the fluctuations are poled by an electric field (which applies also to the observation of corresponding ferroelectric polarizations).

The energy induced by the electric field can be estimated by assuming a simple model of electric dipoles. The potential energy of a dipole $\vec{p} = Q \cdot \vec{l}$ in an electric field $\vec{E}$ is given as $D = \vec{E} \cdot \vec{p}$. The microscopic dipole moment is connected to the electric polarization via the volume, $\vec{P}_{el} = d\vec{p}/dV$. When the AF2 structure is static, the volume is equal to the volume of the crystal for a monodomain state.

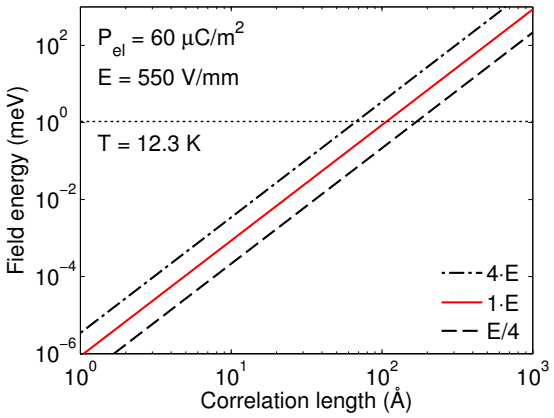

Figure 5.18: Energy induced by an constant electric field on correlated ferroelectric regions in a double-logarithmic scale. The field energy was calculated using Equation 5.1 with the values given in the plot. The horizontal dashed line denotes the thermal energy of $T_{N2} = 12.3\,\mathrm{K}$.

Above the ferroelectric transition T_{N2}, the volume of correlated ferroelectric regions decreases drastically and changes strongly with temperature. For fluctuations with an isotropic correlation length ξ, we obtain:

$$D = \frac{4\pi}{3} \cdot \vec{E} \cdot \vec{P}_{el} \cdot \xi^3 \ . \tag{5.1}$$

The relation between induced field energy and size of correlated regions is shown in Fig. 5.18. The curve was calculated using the value of the electric field applied during the experiment, $E \approx 550\,\mathrm{V\,mm^{-1}}$, and the maximum electric polarization measured in $MnWO_4$, $P_{el,b} = 60\,\mu\mathrm{C\,m^{-2}}$ [17]. The chiral component of the magnetic fluctuations could be measured up to 12.55 K, slightly above the ferroelectric transition $T_{N3} = 12.3\,\mathrm{K}$. The thermal energy T_{N3} is indicated by a horizontal dashed line in the graph. This value can be understood as a threshold. With increasing temperature, the correlation length decreases and so does the field energy. Below the threshold, at $\xi \approx 100\,\text{Å}$, the thermal energy overcomes the field energy and the fluctuations are no longer poled by the electric field. This cancels out the net polarization as well as the chiral component, to which our experiment is sensitive.
Experimentally, it is very difficult to directly access the correlation length of fluctuations in the AF3 phase, since the diffuse signal is dominated by static Bragg peak scattering. At D7 it was possible to separate AF2 and AF3 type fluctuations in the paramagnetic phase using neutron polarization analysis (cf. Fig 5.15). Looking at the temperature dependence of fluctuations along $\vec{b}$, it seems likely that the threshold correlation length is only exceeded in a narrow range above the transition temperature.
The comparison of our simple estimation with experimental data thus supports the assumption that the field energy can only pole the ferroelectric fluctuations in a narrow range above the phase transition.

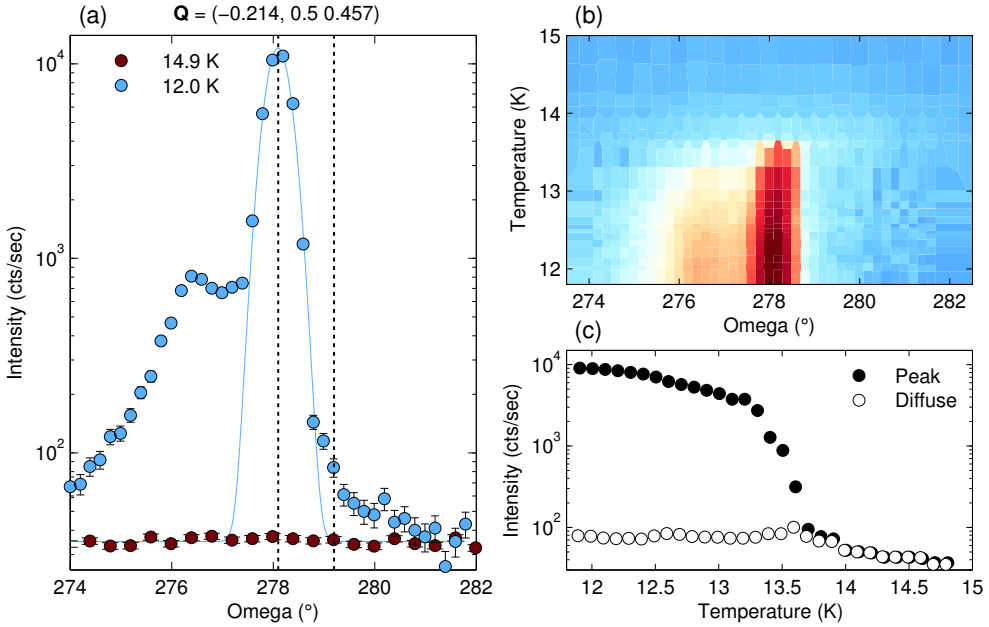

Figure 5.19.: Rocking scan over the magnetic Bragg peak position at $\vec{Q} = (-0.214,\ 0.5,\ 0.457)$ in $MnWO_4$ at IN11. (a) Scan above and below the antiferromagnetic phase transition. A Gaussian function was fitted to the data. (b) Intensity mapping at several temperatures, the intensity is logarithmically color coded. (c) Temperature dependence of intensity at the Bragg peak position and slightly away. The corresponding angles are indicated by dashed lines in (a).

5.2.4. Relaxation times of magnetic fluctuations

An experimental technique which is perfectly suited to investigate fluctuations in a material over a huge time scale is neutron spin-echo spectroscopy (NSE). It has been successfully demonstrated in $TbMnO_3$, that magnetic fluctuations within the ordered phase can be observed using the spin-echo spectrometer IN11 at the ILL [209, 210]. In the following, we will describe the determination of relaxation times of magnetic diffuse scattering in the paramagnetic and the SDW phase.
Throughout the experiment, both samples described at the beginning of this chapter were investigated, yielding consistent data. The experiment was done in paramagnetic NSE mode around $\vec{Q} = (0.214,\ 0.5, -0.457)$, a magnetic Bragg position of the SDW-structure. The NSE spectra were normalized by xyz-polarization analysis, where z was the vertical, x parallel to $\vec{Q}$ and y complementing the Cartesian set (cf. Fig. 5.5). In a NSE experiment, the incident neutron beam is not restricted to be

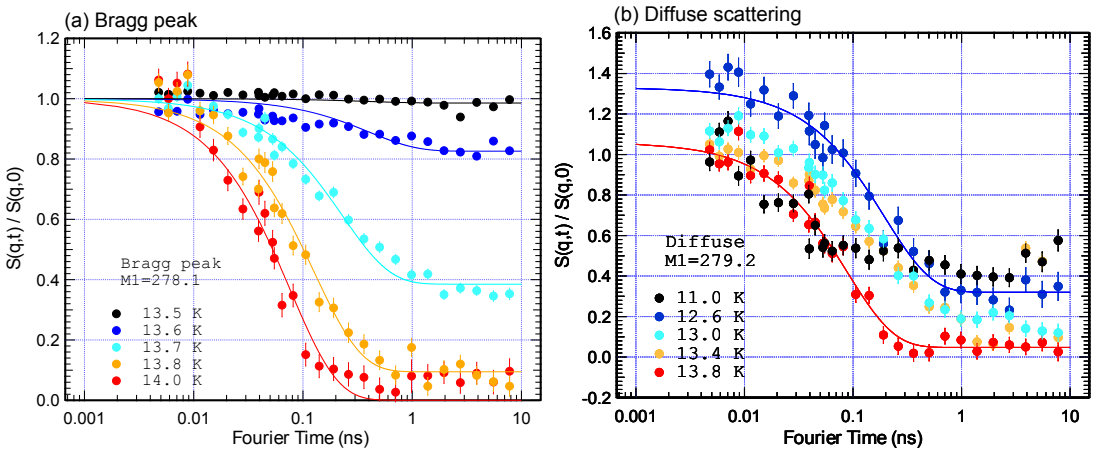

Figure 5.20.: Neutron spin echo spectra in $MnWO_4$ at IN11. The spectra were obtained at several temperatures in the PM, AF3 and AF2 phases at: (a) Bragg peak position $\vec{Q} = (-0.214,\ 0.5,\ 0.457)$ and (b) after a rotation of $\omega = 1.1°$ away from the peak position. An exponential decay function was fitted to the data.

monochromatic. We worked with a range of $\pm 18\,\%$ around a neutron wavelength of $\lambda_i = 5.5\,\text{Å}$ ($E_i = 2.7\,\text{meV}$ and $k_i = 1.14\,\text{Å}^{-1}$). The flipping ratio was $FR = 20$. The instrument was used in the IN11A setting with a two-dimensional multi-detector arm with a length of approximately 5 m [79]. This provides a good angular resolution, which is optimal for the study of fluctuations near a strong static signal.

Figure 5.19(a-b) shows the profile of the magnetic Bragg reflection determined by sample rotation at $\vec{Q} = (0.214,\ 0.5, -0.457)$ at 12.0 K. A Gaussian function was fitted to the peak. The particular profile matches the TAS data described previously in Section 5.2.1: one side of the peak is contaminated by small misoriented crystallites, whereas the intensity on the other side rapidly decreases to the value of the background. Dashed lines indicate two exemplary sample positions $\omega = 278.1°$ (Bragg peak scattering) and 279.2° (diffuse scattering). The evolution of scattered intensity at these two positions is shown in Fig. 5.19, reproducing the same behaviour of static and diffuse scattering in the paramagnetic and the ordered AF3 phase as presented in the previous sections.

Figure 5.20(a) shows the NSE spectra at the magnetic Bragg position for temperatures from the paramagnetic phase to the ordered AF3 phase. The data nicely shows the slowing down of the fluctuations at the onset of the magnetic Bragg peak at T_{N3}. An exponential function of the form $S = S_0 e^{-\tau \cdot t}$ was fitted to the data to describe the decay of polarization. The resulting relaxation times are the red points of Figure 5.21. Similarly, the NSE spectra slightly away from the magnetic Bragg peak at $\omega_{\text{diffuse}} = \omega_{\text{Bragg}} + 1.1°$ are shown in Figure 5.20(b) for several temperatures in the AF3 and AF2 phase. The resulting relaxation times

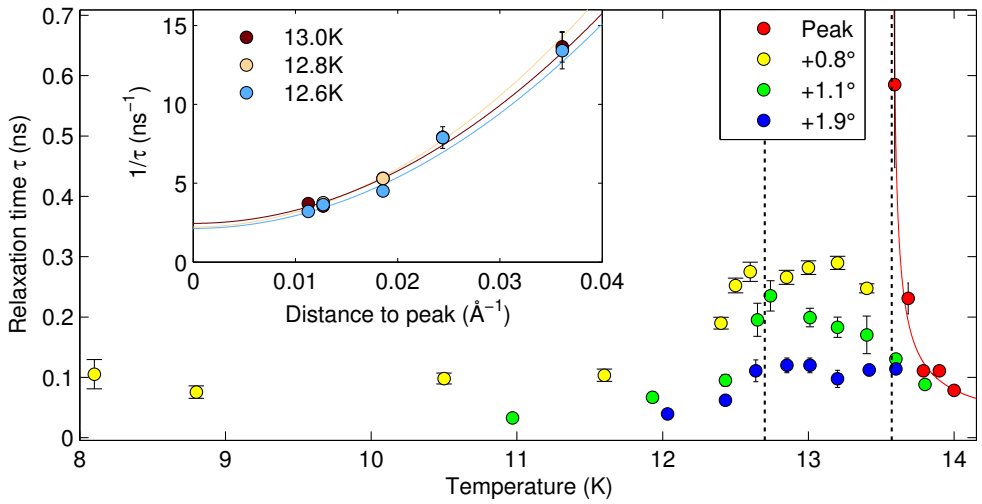

Figure 5.21.: Characteristic relaxation times obtained by neutron spin echo spectra at the Bragg peak position $\vec{Q} = (0.214,\ 0.5, -0.457)$ and after a small sample rotation at several temperatures at IN11. A power law was fitted to the peak values yielding a critical exponent $\nu = 0.66(15)$. Dashed lines indicate the phase transitions T_{N3} and T_{N2}. The inset shows the Q-dependence of the relaxation time. A quadratic function was fitted to extrapolate the value at the Bragg peak position.

are marked as green points in Figure 5.21.
Finally, the relaxation times extracted from the NSE spectra at different temperatures and positions relative to the magnetic Bragg peak are summarized in Figure 5.21. The temperature dependence at the Bragg peak position was fitted using a power law function. The resulting critical exponent $\nu = 0.66(0.15)$ perfectly matches the value of a three-dimensional XY transition $\nu = 0.669$ [149], expected for the PM→AF3 transition [150].
The critical phenomena in $R\mathrm{MnO_3}$ multiferroics were investigated by Harris *et al.* using Landau theory. Their approach may also be applied to $MnWO_4$, which shows similar successive transitions PM→SDW→spiral [198]. Following this approach, the upper PM→AF3 belongs to the universality class of the XY model, which implies a critical exponent of $\nu = 0.669$ ($D = 2$, $d = 3$[b]) [149]. The ferroelectric transition AF3→AF2 is in the 3d-Ising universality class, yielding $\nu = 0.707$ ($D = 1$, $d = 3$) [149].
The surprising finding, which has strong similarities with the previous results on $TbMnO_3$, is that the diffuse scattering is unaffected by the magnetic transition at T_{N3}, whereas it clearly bears the signature of a Q-dependent slowing down at T_{N2}. The relaxation time of fluctuations inside the AF3 phase the Bragg peak position

[b] One differs between the dimensionality of the order parameter D and the dimension of system d.

could not be accessed experimentally due to the strong overlaying signal of the static structure. It was attempted to extrapolate this value by measuring the Q-dependence of fluctuations. The inset of Figure 5.21 shows the Q-dependence of the inverse relaxation times at different temperatures above T_{N2} versus the relative distance to the magnetic Bragg reflection. A quadratic function was fitted to extrapolate the value at the Bragg peak. We obtain a value of about $2.2\,\mathrm{ns}^{-1}$ for the fluctuation at $q = 0$, which varies only slightly with temperature. This corresponds to a frequency of approximately 0.5 GHz. This value is of the same order of the ferroelectric fluctuations close to the multiferroic transition measured by broad dielectric spectroscopy [203].
While Niermann *et al.* find a critical slowing down of the relaxation times close to T_{N2}, our results show almost no temperature dependence in the temperature range from 12.6 to 13.0 K [203]. The neutron experiment suffers from the fact that the weak scattering from fluctuations in the AF3 phase is dominated by strong scattering from the static structure. We succeeded to measure the fluctuations slightly away from the static Bragg peak position, due to the broadening of quasi-elastic scattering. The circumstances, nevertheless, change close to the AF2 transition: at the critical slowing down the correlation lengths of fluctuations diverges which results inevitably in a sharpening of the scattered signal. Therefore we are no longer able to detect these fluctuations away from the Bragg peak position.
Another difference to the results from Niermann *et al.* is, that their experimental technique only resolves ferroelectric fluctuations which can be unambiguously addressed to the multiferroic AF2 phase. The presented approach using spin-echo spectroscopy sees all magnetic fluctuations in the system, which renders it very difficult to isolate those who purely arise from the AF2 phase.

5.3. Magnetic excitations in the multiferroic phase

The study of the chiral magnetic component, which helped investigating the diffuse magnetic scattering, can also be applied to the excitation spectrum of spiral spin structures. It has been demonstrated in Section 4.4.3, that in the case of $TbMnO_3$ such experiments can give substantial information helping to understand the systems dynamics.
Until now, only the magnon dispersion in the commensurate AF1 phase has been studied experimentally in $MnWO_4$ [182, 184]. In the AF2 phase, the excitation spectra change drastically, shown by a recent INS investigation at the magnetic zone center [137]. Similar to the case of the multiferroic phase of $TbMnO_3$, three

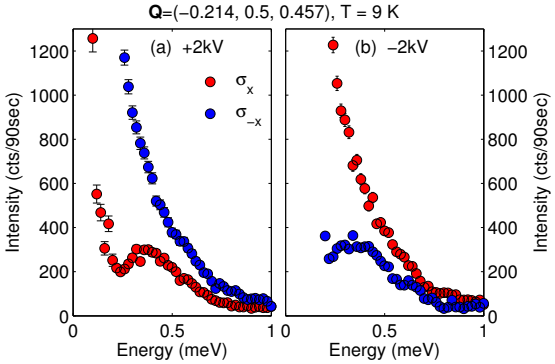

Figure 5.22.: Zone center modes at the magnetic Bragg peak position $\vec{Q} = (-0.214,\ 0.5,\ 0.457)$ in $MnWO_4$ at 9 K at IN14. An electric field of $+550\,\mathrm{V\,mm^{-1}}$ (a) and $-550\,\mathrm{V\,mm^{-1}}$ (b) was applied to the sample along $\vec{b}$. The intensity of the spin flip cross sections along $x \parallel \vec{Q}$ follow the reversal of the electric field.

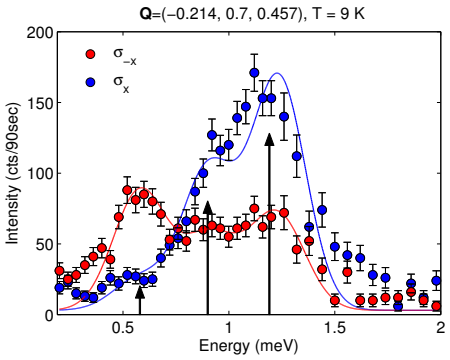

Figure 5.23.: Magnon modes at $\vec{Q} = (-0.214,\ 0.7,\ 0.457)$ in $MnWO_4$at IN14 at 9 K. The intensities of the two spin flip cross sections along $\vec{Q}$ reveal the coexistence of both chiral states. Arrows denote the position of Gaussian functions fitted to the data. An electric field of $+550\,\mathrm{V\,mm^{-1}}$ was applied to the sample along $\vec{b}$.

excitations have been found, which were distinguished as a low energy phason mode and two modes being polarized perpendicular to the plane of the magnetic spiral.

The experiment presented in this section directly followed the investigation of diffuse scattering reported in Section 5.2.3. A single crystal[c] was installed at the cold neutron TAS instrument IN14 at the ILL. The sample was placed between parallel aluminum plates to enable the application of an electric field along the direction of ferroelectric polarization $\vec{b}$ and was mounted in $[-0.21, 0, 0.45]/[0, 1, 0]$ scattering geometry. The analyzed neutron energy was fixed at $E_f = 3.0\,\mathrm{meV}$ ($k_f = 1.2\,\mathrm{\AA}^{-1}$) and a beryllium filter was used to eliminate higher order reflections. Longitudinal polarization analysis was achieved by a supermirror bender in the incident neutron beam and a set of Helmholtz coils at the sample stage. The neutron flux at the sample was increased by using a vertical focusing monochromator and a double-focusing PG analyzer. This is called a half-polarized setup, because the PG analyzer is insensitive to the polarization of neutrons. The energy resolution was determined to be $\Delta E \approx 0.13\,\mathrm{meV}$ at the elastic line. An additional experiment was performed at the cold neutron TAS instrument 4F1 at the LLB, Saclay, yielding consistent results.

The experiment was performed in half-polarized setup, where in the two channels

[c]The crystal was grown by C. Tölzer and C. Lee [204] and prepared by J. Stein at the University of Cologne.

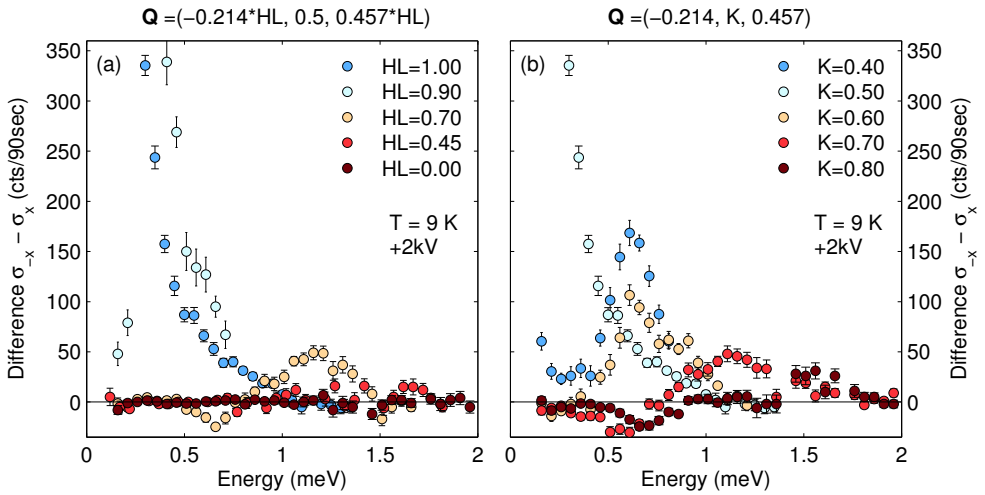

Figure 5.24.: Dispersion of the chiral magnetic component, $\sigma_{\bar{x}} - \sigma_x$, in $MnWO_4$ at 9 K along $\vec{Q} = (-0.24 \cdot HL, 0.5,\ 0.457 \cdot HL)$ (a) and $\vec{Q} = (-0.24, K,\ 0.457)$ (b) at IN14. An electric field of $+550\,\mathrm{V\,mm^{-1}}$ was applied to the sample along $\vec{b}$.

with the spin parallel and anti-parallel to the scattering vector, the chiral contributions appear with opposite sign. This particular setup has the advantage of simplicity and significantly higher count rates, rendering inelastic measurements more efficient. Spin-flip and non spin-flip channels along one polarization direction can no longer be distinguished in this setup (e.g. $\sigma_{x\bar{x}}$ and σ_{xx}). We will use the following notation: σ_x for a polarization parallel to $\vec{Q}$ and $\sigma_{\bar{x}}$ for a polarization antiparallel to $\vec{Q}$. It was verified before that all inelastic signal was purely magnetic. The zone center excitation spectrum at 9 K, inside the ferroelectric AF2 phase, is shown in Figure 5.22 at the magnetic Bragg peak $\vec{Q} = (-0.214,\ 0.5,\ 0.457)$. The intensity significantly differs in both channels, indicating chiral magnetic component. At low energies, the difference is enhanced. The low energy mode is believed to be the in-plane phason mode which should carry a chirality. At higher energies, the deviation is smaller and so is the chiral component. The upper modes were identified as out-of-plane modes and should thus possess no chirality (just as in the case of $TbMnO_3$, see Section 4.4.3). Our results thus agree with the interpretation of Finger *et al.* [137]. The scan was performed with two electric field configurations, $550\,\mathrm{V\,mm^{-1}}$ and $-550\,\mathrm{V\,mm^{-1}}$, proving that the deviating intensity in both channels originates from the reversed chiral domain of the magnetic spiral.
Further away from the magnetic Bragg peak, the chiral character of the modes significantly. An exemplary scan at $\vec{q} = (0,\ 0.2,\ 0)$ (relative moment transfer within a Brillouin zone) is shown in Fig. 5.23. The spectra in both channels could be well described by fitting three Gaussian functions. Their positions are

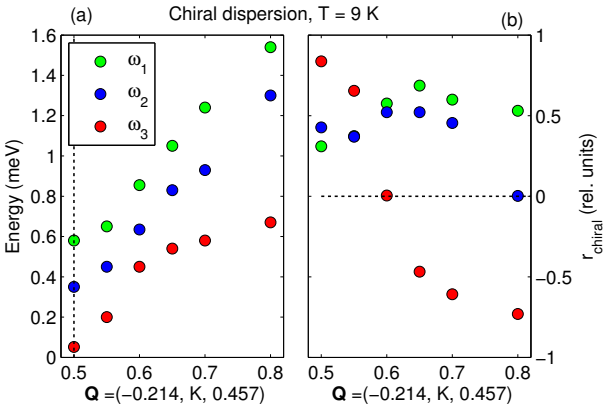

Figure 5.25: Dispersion and chiral ratio of magnon modes in $MnWO_4$ at 9 K along $[0, 1, 0]$ at IN14. The positions and chiral components of the three low-energy modes were determined by Gaussian fits (cf. Figs. 5.24 and 5.25). An electric field of $+550\,\mathrm{V\,mm^{-1}}$ was applied to the sample along $\vec{b}$.

indicated by black arrows. We find the coexistence of both chiral states at one position. A similar observation was made in the multiferroic phase of $TbMnO_3$ (see Chapter 4.4.3 for more details). In $TbMnO_3$, the coexisting modes of opposite chirality were found at higher energies. By modeling the spin wave dispersion, it could be shown that these modes are dispersing from the adjacent Brillouin zone. In the present case of $MnWO_4$, the origin of opposite chirality might be more complex.

The dispersion of magnetic excitations and especially of the chiral component was followed along the directions of the scattering plane. Figure 5.24 shows the subtraction of both channels along $[-0.21, 0, 0.45]$ (left) and $[0, 1, 0]$ (right). The subtraction yields $\sigma_{x\bar{x}} - \sigma_{\bar{x}x} = -i(\vec{M}_\perp \times \vec{M}^*_\perp)_x \cdot 2$. Along both directions, the presence of a mode with opposite chirality can be observed. Furthermore the chirality is completely lost at the magnetic zone boundary $\vec{Q} = (0,\ 0.5,\ 0)$. The loss of chirality can be explained by symmetry, when changing the Brillouin zone at the zone boundary. The coexistence of both chirality states inside one zone must be due to folding of modes, and has also been observed in the multiferroic spiral phase of $TbMnO_3$, cf. Section 4.4.3.

The results from the fitting of the excitation spectra along $[0, 1, 0]$ are summarized in Figure 5.25. At all positions the spectra in both channels could be described using three Gaussian functions. Figure 5.25(a) shows the energy dispersion of modes, and Figure 5.25(b) shows the corresponding chiral ratio. The colors denote the different modes. By looking at the dispersion it seems possible that a mode crossing occurs at $K \approx 0.6$. The most remarkable observation is the strong opposite chirality of the low-energy mode.

It was attempted to model the magnon modes in the multiferroic AF2 phase using linear spin wave theory. As described in Section 4.4.3, the chirality of modes in the multiferroic phase of $TbMnO_3$ was successfully modeled using the program *SpinW* [94]. Until now only the dispersion in the collinear AF1 phase could be modeled, using a set of nine to eleven exchange interaction parameters [182, 184].

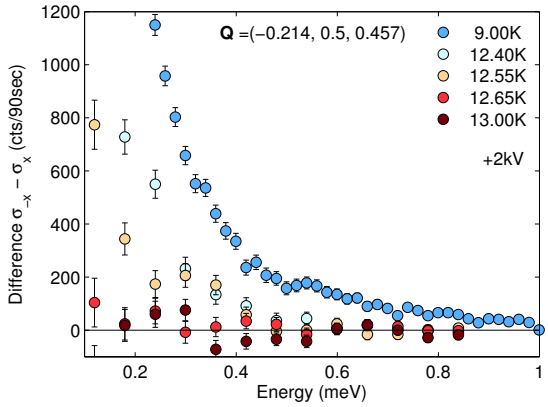

Figure 5.26: Temperature dependence of the chiral component, $\sigma_{\bar{x}x} - \sigma_{x\bar{x}}$, at the magnetic zone center $\vec{Q} = (-0.214,\ 0.5,\ 0.457)$ in $MnWO_4$ at IN14. An electric field of $+550\,\mathrm{V\,mm^{-1}}$ was applied to the sample along $\vec{b}$. The chirality disappears above the ferroelectric transition at T_{N2}.

The complexity of the system, given by the large number of competing exchanges, renders it difficult to describe the frustrated spiral phase and no satisfying model could be obtained by spin wave calculation.
Finally we discuss the evolution with temperature of the chiral magnetic component. Figure 5.26 shows the subtraction of both channels along x for various temperatures in the AF2 and AF3 phase. Upon increasing temperature, the spectral weight continuously decreases and shifts to lower energies. This is in agreement with the temperature dependence of the zone center excitations, which shift to lower energies for increasing temperatures [137, 182]. The chirality of modes decreases upon cooling and is lost at the AF2→AF3 transition at T_{N2}. This agrees with the understanding that magnetic excitations of a collinear SDW should not carry a chiral component. This is the case for the AF3 phase in $MnWO_4$.

5.4. Conclusion

This chapter presents a comprehensive study of magnetic fluctuations in the spin-induced multiferroic $MnWO_4$. Different neutron scattering techniques with polarization analysis were applied in order to investigate the correlation length and the direction of the fluctuations. We were able to separate contributions from the SDW and the spiral order. The temperature dependence of the contributions along $\vec{b}$ demonstrates the almost continuous nature of the PM→SDW→spiral transition. Diffuse magnetic scattering, which arises from magnetic fluctuations, is present in the system up to two times the transition temperature of $T_{N3} = 13.5\,\mathrm{K}$, which indicates the strong frustration of competing exchange interactions. It could be shown that the fluctuations close to T_{N3} are mainly polarized along the direction of the easy-axis anisotropy $\vec{e}_{ac}$, while they become isotropic at higher temperatures. In addition, the usage of polarized neutrons helped to analyze fluctuations along

$\vec{b}$ which arise from the spiral phase. The comprehensive dataset documents a characteristic shape of the magnetic fluctuations, which is directly linked to the complex magnetic exchange interactions in $MnWO_4$.
These fluctuations along $\vec{b}$ could also be observed and characterized inside the ordered AF3 phase, which shows the almost continuous transition towards the spin spiral phase. Relaxation times of the fluctuations determined by neutron spin echo spectroscopy confirm this assumptions. The fluctuations along $\vec{b}$ seem to be unaffected from the ordering of moments along $\vec{e}_{ac}$ at T_{N3}, the transition of the spin-density-wave.
The spin-spiral structure of the AF2 phase induces a ferroelectric polarization via the DM mechanism [17], and the sign of polarization can be attributed to the sign of vector chirality [13]. This vector chirality should also be an intrinsic property of the fluctuations along $\vec{b}$ in the AF3 phase. By applying an electric field, it was shown that these magnetic fluctuations can be electrically poled in the dielectric phase. The magnetic fluctuations of chiral character can be compared to the critical slowing down of electric fluctuations observed by dielectric spectroscopy [203].
In addition, the excitation spectrum in the multiferroic phase was investigated. The magnon modes possess a strong chiral component, which could be poled by an applied electric field. The chiral component of the magnon modes could be followed along two directions in reciprocal space. Remarkable is the observation of modes of reversed chirality relative to the static Bragg peak. These modes may arise due to back-folding of magnon branches and could help to validate models for the spin-wave dispersion in the multiferroic phase.

Chapter 6

Magnetic phase diagram of $NaFe(WO_4)_2$

The discovery of a spin-driven multiferroic phase in $MnWO_4$ in 2006 [17, 46, 47] motivated the research for multiferroicity in other materials of the tungstate family [212]. The metal ion M^{2+} in MWO_4 can be substituted by a magnetic ion with the same valency or by a combination of mono- and trivalent ions. Instead of the spin-spiral of $MnWO_4$, the resulting compounds often develop a simple collinear antiferromagnetic structure [174, 180, 211] and no electric polarization was observed [212].

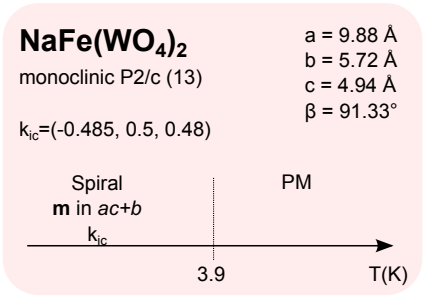

Figure 6.1.: Crystal parameters and magnetic phase transitions in $NaFe(WO_4)_2$ [187, 211].

First dielectric experiments on $NaFe(WO_4)_2$ indicated the presence of an electric polarization in the low temperature phase [212]. This experimental observation and the complex magnetic phase diagram [187, 213] are in contradiction to the simple collinear structure proposed in the literature [211], rendering this material interesting for further investigations.
In this chapter, a detailed neutron diffraction study of the magnetic phase diagram of $NaFe(WO_4)_2$ is presented for magnetic fields applied along the monoclinic axis.

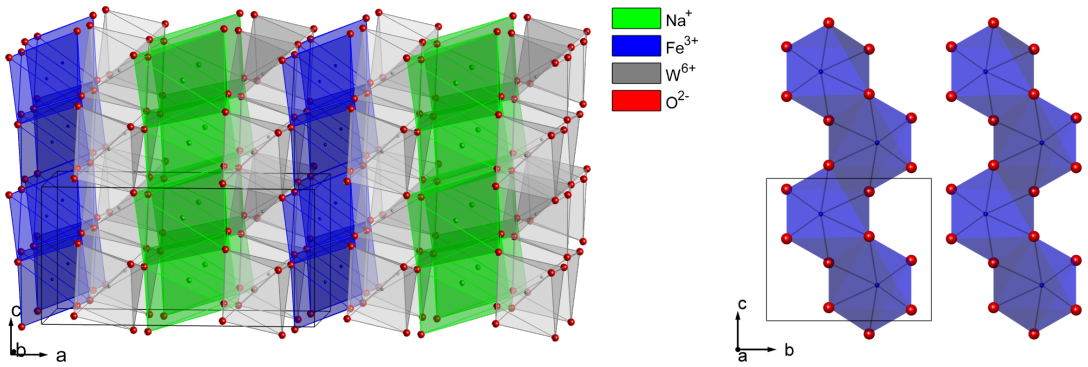

Figure 6.2.: (a) Crystal structure of $NaFe(WO_4)_2$. Tungsten (grey), iron (blue) and sodium (blue) ions are surrounded by oxygen (red) octahedra. These octahedra form planes perpendicular to $\vec{a}$. The size of the atoms reflects their relative ion radius [118]. (b) Iron octahedra form chains along $\vec{c}$.

6.1. Introduction

6.1.1. Crystal and magnetic structure

The crystal structure of the double tungstate $NaFe(WO_4)_2$ can be described in the monoclinic space group *P2/c* with lattice parameters $a = 9.88\,\text{Å}$, $b = 5.72\,\text{Å}$, $c = 4.94\,\text{Å}$ and a monoclinic angle of $\beta = 90.33°$ [214]. An overview of the crystal and magnetic structure of $NaFe(WO_4)_2$ is given in Fig. 6.1. The metal ions are surrounded by edge-sharing $[O_6]$-octahedra and aligned in planes parallel to the *bc*-plane. The structure is shown in Figure 6.2(a). Layers containing $[NaO_6]$ octahedra and $[FeO_6]$ octahedra, respectively, are separated by layers that contain $[WO_6]$ octahedra only. Hence, the unit cell of $NaFe(WO_4)_2$ is doubled along $\vec{a}$, with respect to the natural wolframites $MnWO_4$ and $FeWO_4$ [174, 180].
In $NaFe(WO_4)_2$, the Fe^{3+} ions carry a finite magnetic moment. Similar to the case of $MnWO_4$, the magnetic Fe^{3+} ions form zig-zag chains along the *c*-axis (see Fig. 6.2(b)). In spite of the long distance between the Fe^{3+}-planes, $NaFe(WO_4)_2$ develops a three-dimensional magnetic structure at temperatures below 5 K. The analysis of neutron powder diffraction yielded a collinear antiferromagnetic structure with magnetic moments aligned parallel to the *a*-axis [211]. The magnetic reflections were indexed with a commensurable propagation vector of $\vec{k}_c = (0.5,\ 0.5,\ 0.5)$. Nyam-Ochir *et al.* claim the antiferromagnetic super-superexchange coupling along $\vec{b}$ and $\vec{c}$ causes the doubling of the magnetic unit cell along these directions, whereas the mechanism for the coupling along the extended *a*-axis remains unclear [211]. The substitution of the magnetic site with Cr^{2+} also leads to a long-range three-dimensional magnetic order but a mixed occupation of Fe^{3+} and Cr^{3+} destroys the magnetic order [211].

Figures 6.3(a-c) show the magnetic susceptibility of $NaFe(WO_4)_2$ along the principal crystallographic directions measured on a single crystal. The high temperature part was fitted using the inverse Curie-Weiss function $\chi_m^{-1} = C^{-1}(T + \theta)$ yielding Weiss-temperatures around $\theta = -8.5\,\mathrm{K}$ in the monoclinic plane and an effective magnetic moment of $\mu_{eff,exp} = 5.932(15)\,\mu_B$, which matches perfectly the expected value of $\mu_{eff} = 2\sqrt{S(S+1)} = 5.92\,\mu_B$ for a spin-only moment of Fe^{3+} with $S = 5/2$ [53]. The results agree with values determined from powder [211].
The low temperature part of the susceptibility is shown in Fig. 6.3(a). All three curves show a broad maximum at about 14 K. At lower temperatures the behaviour is different along each direction. Perpendicular to the monoclinic axis, along $\vec{a}^*$ and $\vec{c}^*$, the susceptibility drops rapidly, whereas along $\vec{b}$ only a small decrease is seen[a]. In a uniaxial antiferromagnet, the temperature dependence of the susceptibility strongly depends on the relative direction of the applied magnetic field and the ordered magnetic moments. Fields applied parallel to the moments yield a decrease of susceptibility below the phase transition. For fields applied perpendicular the susceptibility is constant for decreasing temperatures [53]. From this we can deduce that the magnetic moments in $NaFe(WO_4)_2$ are mainly aligned in the *ac*-plane with a small component along $\vec{b}$. We find a transition temperature of 3.9 K which is indicated by a black dotted line in the inset. The ratio of Curie-Weiss and Neel temperature, $f = \theta_{CW}/T_N \approx 2.2$, shows that the system is frustrated [215]. The Neel temperature was confirmed by specific heat measurements upon heating and cooling [216]. The transition along $\vec{b}$ is slightly shifted towards lower temperatures due to the applied magnetic field along this direction.
Finally in Figure 6.3(c), we show the induced magnetization for fields applied along $\vec{b}$ and $\vec{c}^*$. The magnetization per field (cf. Figure 6.3(d)) changes at magnetic fields of about 1.5 K giving a hint for a spin-flop transition.

6.1.2. Magnetic phase diagram and dielectric measurements

The phase diagram of $NaFe(WO_4)_2$ for a magnetic field applied along the principal axes was determined by M. Ackermann and Y. Sanders at the University of Cologne [213]. We will present the performed macroscopic measurements to demonstrate the complexity of the system. Figure 6.4(a) shows the thermal expansion of $NaFe(WO_4)_2$ along the monoclinic axis $\vec{b}$ for magnetic fields applied along the same direction. The curves are shown for selected fields upon cooling and heating. A transition below 4 K is visible in magnetic fields up to 11 T. In the

[a] Note that in the monoclinic system $\vec{b} \| \vec{b}^*$ is valid.

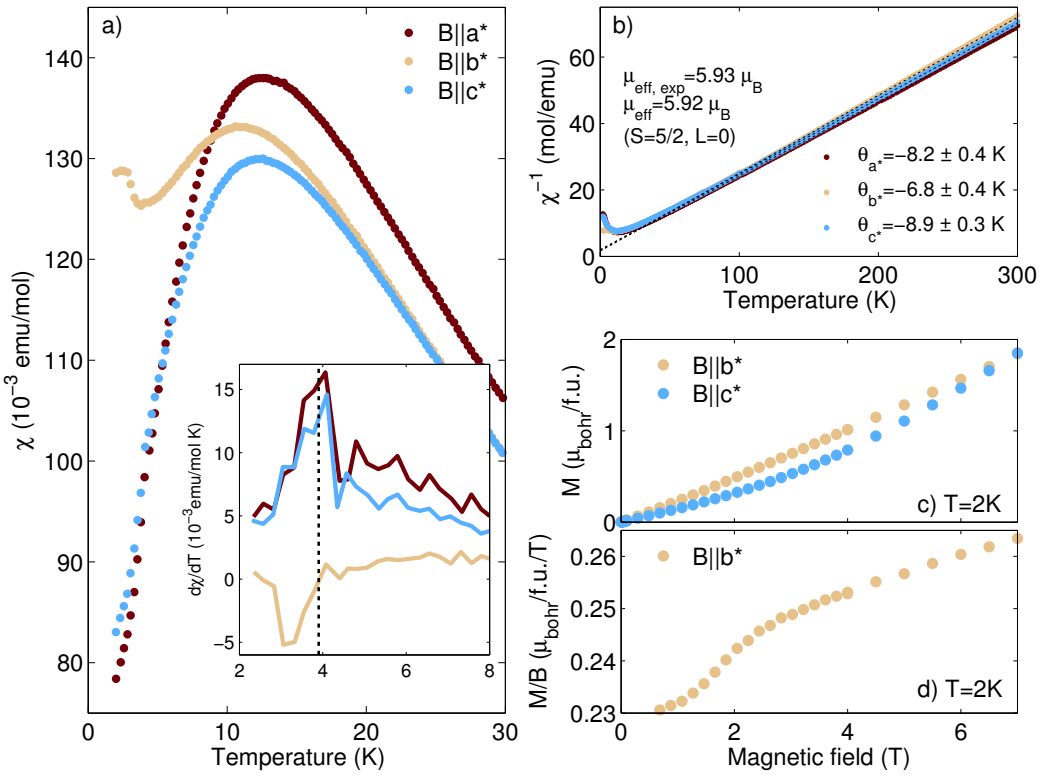

Figure 6.3.: Magnetic susceptibility of $NaFe(WO_4)_2$ along principal crystallographic directions: (a) low temperature behaviour and (b) Curie Weiss fit to the high temperature part. The inset in (a) shows the derivative of the susceptibility with respect to the temperature. A magnetic field of 0.1 T was applied to the sample. (c) Magnetization on $NaFe(WO_4)_2$ for magnetic fields applied along $\vec{b}$ and $\vec{c}^*$. (d) Magnetization per applied magnetic field for $B||b$. Measurements were performed by S. Heijligen.

case of increasing magnetic fields, the transition shifts towards lower temperatures. In low fields up to 1 T a hysteresis is visible which disappears in higher fields. The perturbations in the curves at 2 K are caused by stabilization problems of the temperature controller [213].

The magnetostriction of $NaFe(WO_4)_2$ along the monoclinic axis $\vec{b}$ for magnetic fields applied along the same direction at selected temperatures is shown in Figure 6.4(b). The measurements were performed after cooling from the paramagnetic phase in increasing and decreasing magnetic fields at constant temperatures. At temperatures below 3 K, two transitions occur when the field is increased, at about 2 T and 12 T. The upper transition shifts towards lower fields at higher temperatures. When the field is decreased again only one sharp feature is visible. At the field of the lower transition only a minor anomaly can be detected. The magnetostriction curves confirm the transition temperatures determined by thermal

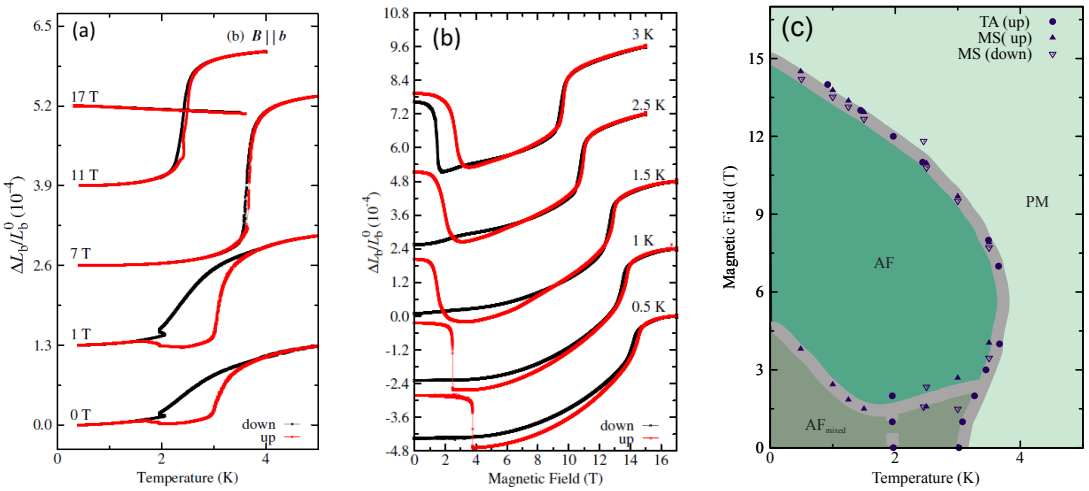

Figure 6.4.: (a) Thermal expansion and (b) magnetostriction of $NaFe(WO_4)_2$ along the monoclinic axis for magnetic fields applied along $\vec{b}$. The data was obtained upon decreasing and increasing temperature or magnetic field (black and red curves). (c) Resulting magnetic-field versus temperature phase diagram. All figures are taken from Ref. [213].

expansion at higher fields.
The resulting phase diagram determined by anomalies in the macroscopic measurements is shown in Figure. 6.4(c). Ackermann comes to the conclusion that $NaFe(WO_4)_2$ undergoes a glass-like transition in low fields into a mixed partially magnetically ordered phase AF_{mixed}. In higher fields applied along $\vec{b}$, the antiferromagnetic order AF is completed and the phase is stable even in decreasing fields [213].
The phase diagrams along $\vec{a}^*$ and $\vec{c}^*$ are rather complex and show several transitions in high magnetic fields which might as well be explained by the incomplete magnetic order at zero-field [213]. We will focus in the following on the case of magnetic fields applied along the monoclinic axis.
Preliminary pyro-electric current experiments have been performed by S. Jodlauk and S. Albiez [212,213]. They found evidence of an electric current but it could not be surely attributed to a ferroelectric phase. The experiments have been revised and repeated on single crystals along the principal crystallographic directions with the application of a magnetic field. Upon cooling, no electric current could be detected. Upon heating, an electric signal could be detected along $\vec{a}^*$ and $\vec{c}^*$ which was interpreted as an effect of frozen charge carriers. The authors conclude that $NaFe(WO_4)_2$ is neither multiferroic nor linear magnetoelectric [213].

6.2. Neutron diffraction in the zero field phase

Neutron scattering experiments were conducted at the triple-axis spectrometers (TAS) IN3 (thermal) and IN14 (cold) at the ILL to investigate the temperature dependence of the zero field magnetic phase. In a TAS experiment, one is restricted in $\vec{Q}$ space to a scattering plane spanned by two vectors. In order to access the incommensurability along all three crystallographic directions, the experiment had to be repeated with three different crystal orientations. At IN14, we worked with an analyzed neutron energy of 3.5 meV ($k_f = 1.3\,\text{Å}^{-1}$) and a sample orientation of $[1,1,0]/[0,0,1]$. At IN3, we worked with an analyzed neutron energy of 14.7 meV ($k_f = 2.66\,\text{Å}^{-1}$) and a sample orientation of $[1,0,1]/[0,1,0]$ and $[0,1,1]/[100]$. The single crystal ($13 \times 8 \times 2\text{mm}^3$) used for the experiment has been grown from melt by P. Becker at the University of Cologne [212].

6.2.1. Temperature dependence of magnetic order

The temperature dependence of the magnetic transition in $NaFe(WO_4)_2$ determined by macroscopic measurements was discussed in Section 6.1.2. The thermal expansion curves showed a hysteresis-like behaviour of the phase transition which was interpreted as a glass-like transition towards a partially ordered magnetic phase [213].
Figures 6.5(a) and (b) show intensity maps of $\vec{Q}$ scans along $[1,1,1]$ over the magnetic satellites at $\vec{Q} = (-0.5,\ 0.5,\ 0.5)$ upon cooling and heating. At about 4 K, two strong incommensurate Bragg peaks develop whose positions are temperature dependent. The incommensurate splitting of the magnetic Bragg peaks in the zero field magnetic phase have been observed first during the diploma thesis [187]. The magnetic satellites are accompanied by weak third-order reflections and scattered signal at the commensurate Bragg peak position. Above the transition temperature, diffuse scattering is visible. Three Gaussian functions were fitted to the data to take into account the intensities at the two incommensurate positions and the commensurate position in the center. The signal at the commensurate Bragg position is weak in comparison to the incommensurate peaks but cannot be attributed to $\lambda/2$ contamination from a structural peak since its intensity varies with temperature. A detailed analysis of this finding is restricted by the weakness of the effect and the fact that the magnetic satellites are so close to each other. Our data suggests that the commensurate signal grows towards lower temperatures which comes along with a broadening of the width of the incommensurate satellites. A development of a second magnetic phase would lower the correlation length of the primary structure which would be visible in a broadening of the magnetic

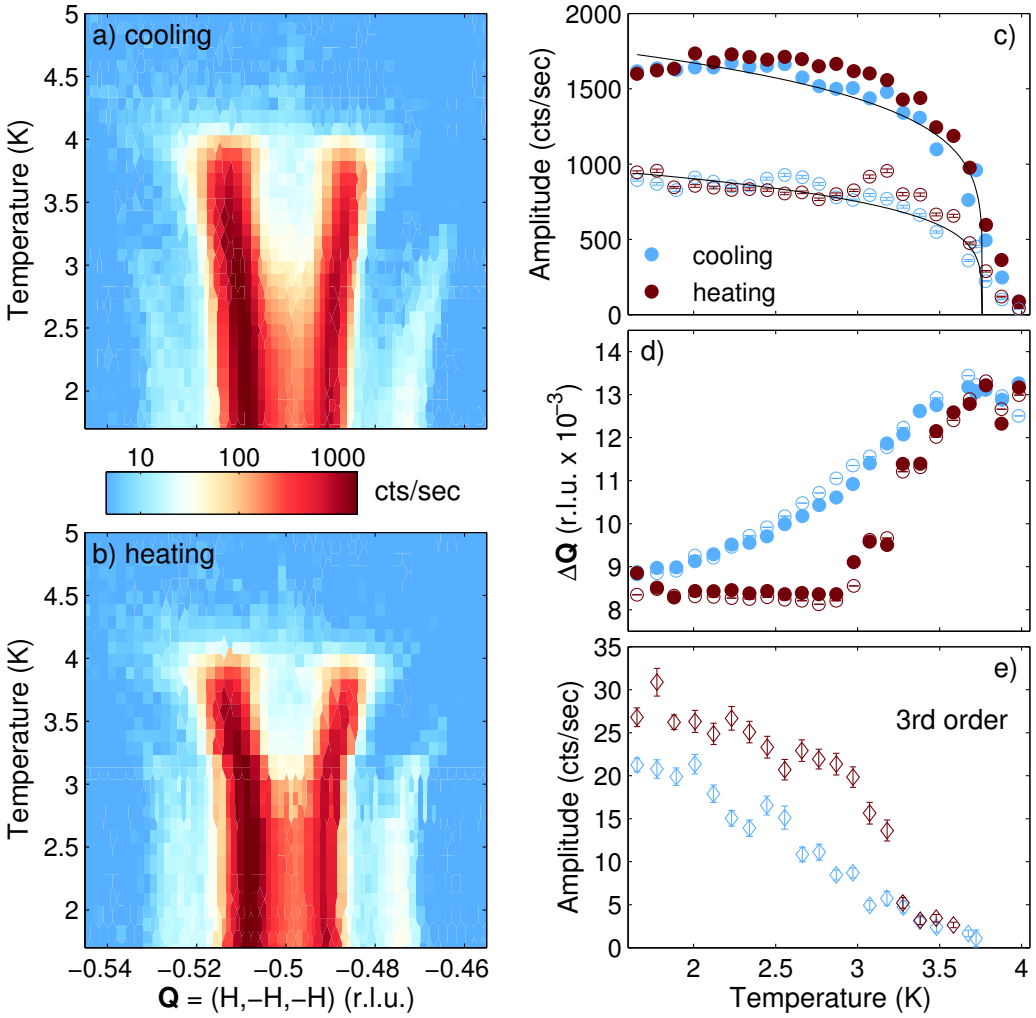

Figure 6.5.: Magnetic phase transition in $NaFe(WO_4)_2$ upon cooling and heating at IN3. (a), (b) Intensity mapping of $\vec{Q}$ scans along the position of the magnetic Bragg reflection $\vec{Q} = (-0.5,\ 0.5,\ 0.5)$ upon cooling and heating through the phase transition. The color is logarithmically coded. Gaussian peaks were fitted to the data. (c) Peak intensities of both magnetic satellites. The fitted power law function $M^2 = c(T_C - T)^{2\beta}$) yields a transition temperature of $T = 3.76(2)\,\mathrm{K}$ and a critical exponent of $\beta = 0.10(2)$. (d) positions of the satellites relative to the commensurate Bragg point, (e) Peak intensity of the incommensurate third-order signal upon heating and cooling. The onset of the third-order reflections coincides with the modulation of the propagation vector.

reflections. The presence of a commensurate magnetic signal and higher order reflections of the incommensurate satellites are both indicators that the present magnetic structure is perturbated.
The appearance of the third-order reflections may be attributed to an anharmonic perturbation of the incommensurate structure. A perturbated sinusoidal wave can be described by additional wave vectors using Fourier transformation. Higher order harmonics often indicate squaring-up of the magnetic structure. This is an expected feature at low temperatures as an incommensurate sinusoidal spin-density wave cannot be the ground state of a local moment system [217]. The ratio of first and third-order satellites is in the order of $I_{1st}/I_{3rd} \approx 100/1$ in the present case.
Figure 6.5(c) shows the temperature dependence of the fitted peak intensity of the first-order satellites. Unlike expected from the thermal expansion data we did not find a hysteresis behaviour of the transition temperature and only minor variations in the peak intensity. Fitting a power law to the data, we get the same transition temperature of about 3.8 K for the cooling and heating cycle. This finding perfectly agrees with the temperature determined from the magnetic susceptibility within the accuracy of the used cryostat.
In Figure 6.5(d), the fitted peak position of the first-order magnetic satellites are shown for the cooling and heating cycles. The distance to the commensurate position is plotted against the temperature. Both satellites show the same behaviour within a cycle, but the temperature dependence is different for heating and cooling. Upon cooling, the incommensurability decreases continuously with temperature. Upon heating, the value of the incommensurability is locked-in up to 3.0 K and increases in higher temperatures. The temperatures match the hysteresis-like behaviour found in the thermal-expansion data (cf. Fig. 6.4(a)). The fluctuation of intensity in the heating curve may be assigned to a non-perfect temperature stabilization of the cryostat.
Finally in Figure 6.5(e), we show the temperature dependence of the relative peak intensities of the third-order magnetic satellites. Again we find the same hysteresis behaviour upon heating and cooling as in the thermal-expansion data. The corresponding transition temperatures match perfectly the quasi lock-in temperatures of the incommensurability.
We can conclude that the magnetic transition temperature of $NaFe(WO_4)_2$ is at 3.9 K and that the hysteresis-like behaviour found in thermal-expansion data can be assigned to perturbations of the magnetic ordering. These perturbations are visible as third-order magnetic satellites in the neutron diffraction data. The presence of scattered magnetic intensity at the commensurate Bragg positions may reflect a coexistence of incommensurate and commensurate magnetic order. A spin-glass behaviour can be excluded as the present magnetic structure leads to sharp Bragg reflections. This result is further supported by measurements of the field-cooled and non-field-cooled magnetic susceptibility. No field dependence is

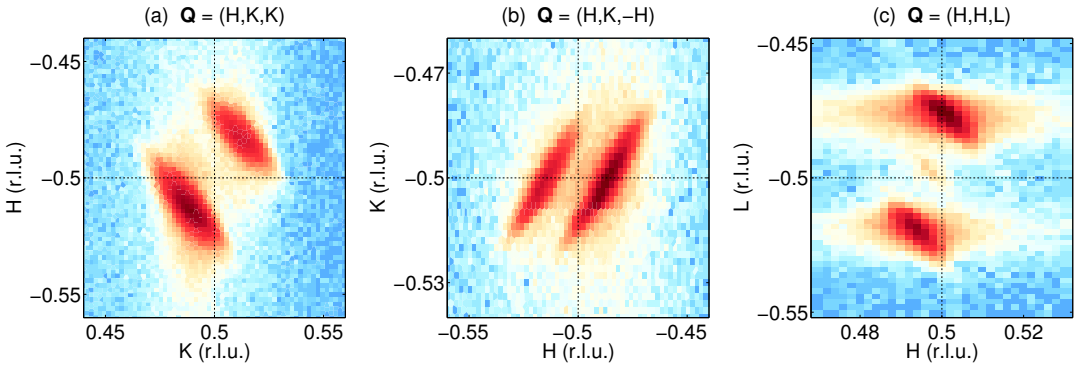

Figure 6.6.: Intensity mapping of $\vec{Q}$ scans along magnetic Bragg peaks of $NaFe(WO_4)_2$ at 3.8 K in three different orientations: (a) $\vec{Q} = (-0.5,\ 0.5,\ 0.5)$ in $[1,0,0]/[0,1,1]$, (b) $\vec{Q} = (-0.5,-0.5,\ 0.5)$ in $[0,1,0]/[1,0,1]$ and (c) $\vec{Q} = (0.5,\ 0.5,-0.5)$ in $[0,0,1]/[1,1,0]$. The color is logarithmically coded. Dashed lines indicate the commensurate Bragg peak position.

visible, whereas for a spin-glass system one would expect an irreversibility of the susceptibility below the transition [218].

6.2.2. Magnetic propagation vector

Figures 6.6(a-c) show two-dimensional intensity maps of $\vec{Q}$ scans along two magnetic satellites in $NaFe(WO_4)_2$ in three different crystal orientations at 3.8 K. The black cross indicates the commensurate peak position. This temperature is slightly below the magnetic transition temperature, where the splitting of the satellites is most pronounced (cf. Section 6.2.1). The intensity is logarithmically coded and diffuse scattering is visible around the static Bragg peaks. The images can be understood as two-dimensional cuts through the three-dimensional $\vec{Q}$ space. In Figure 6.6(a), the single crystal was oriented along $[1,0,0]/[0,1,1]$ and was measured at the spectrometer IN3. The splitting of the incommensurate magnetic satellites occurs along both axes of the scattering plane. The splitting along $[1,0,0]$ can be projected to be $\Delta_H = 0.03$. Figure 6.6(b) was recorded at IN3 in the scattering plane $[0,1,0]/[1,0,1]$. In this orientation the splitting is only present along $[1,0,1]$. Within the experimental precision we cannot determine a splitting along the monoclinic axis and $\Delta_K = 0$. Finally at the spectrometer IN14 the crystal was oriented along $[0,0,1]/[1,1,0]$. The splitting is again present along both axes and we can project a value of $\Delta_L = 0.04$ for the incommensurability along $\vec{c}^*$.
We can conclude that the incommensurable splitting of the magnetic propaga-

tion vector in the zero-field phase of $NaFe(WO_4)_2$ only occurs perpendicular to the monoclinic axis $\vec{b}$. This is a symmetry plane of the Brillouin zone for the space group $P2/c$. The propagation vector at 3.8 K was determined to be $\vec{k}_{ic} = (-0.485,\ 0.5, -0.48)$.

6.2.3. Diffuse magnetic scattering

In the previous sections, we mentioned the presence of diffuse magnetic scattering in the paramagnetic phase of $NaFe(WO_4)_2$. Aim of this section will be to investigate the temperature and $\vec{Q}$ dependence of the diffuse scattering. The experiment was performed at the spectrometer IN3 using a single crystal of $NaFe(WO_4)_2$ in the orientation $[1,0,0]/[0,1,1]$.
Figures 6.7(a) and (b) show two-dimensional intensity maps along the commensurate Bragg peak $\vec{Q} = (-0.5,\ 0.5,\ 0.5)$ at 4.0 K and 4.2 K, inside the paramagnetic phase. At 4.0 K the diffuse scattering is well centered around the incommensurate Bragg peak positions. The signal is rather sharp along $[0,1,1]$ and significantly broadened along $[1,0,0]$. At 4.2 K this situation is even more pronounced. The diffuse scattering remains centered at the commensurate value along $[0,1,1]$ and is nearly constant along the a^* axis.
Figure 6.7(c) shows $\vec{Q}$ scans along $[0,1,1]$ over the commensurate Bragg peak position $\vec{Q} = (-0.5,\ 0.5,\ 0.5)$ at different temperatures above the magnetic transition. Diffuse scattering is present up to 6 K which is almost twice the transition temperature of $T_N = 3.9$ K suggesting a low-dimensional or frustrated character of the system. This finding is in perfect agreement with the magnetic susceptibility data, cf. Figure 6.3(a). Magnetic resonance studies on $NaFe(WO_4)_2$ revealed a two-dimensional character of the magnetic order and the ratio of intralayer J to interlayer exchange J' was estimated to be $J' \approx 10^{-6} J$ [219].
We now focus on the anisotropy of the magnetic correlations. Figure 6.7(d) shows the temperature dependence of $\vec{Q}$ scans along $[1,0,0]$. The diffuse scattering is significantly broadened along this direction. By fitting the data with a Lorentzian function, one can determine the correlation length of the diffuse order. The finite instrument resolution can be neglected in the investigated temperature range because the diffuse signal is significantly broadened.
The temperature dependence of the correlation length along both directions is shown in Figure 6.7(e). $NaFe(WO_4)_2$ crystallizes in a layered structure with separated planes of Na, Fe and W parallel bc (see Fig. 6.2 and [214]). The distance of the magnetic ions along $\vec{a}^*$ is almost 10 Å. The weakness of the coupling along $\vec{a}^*$ is visible in the two-dimensional diffuse scattering in the paramagnetic phase. Correlations between the magnetic moments first occur below 10 K inside the

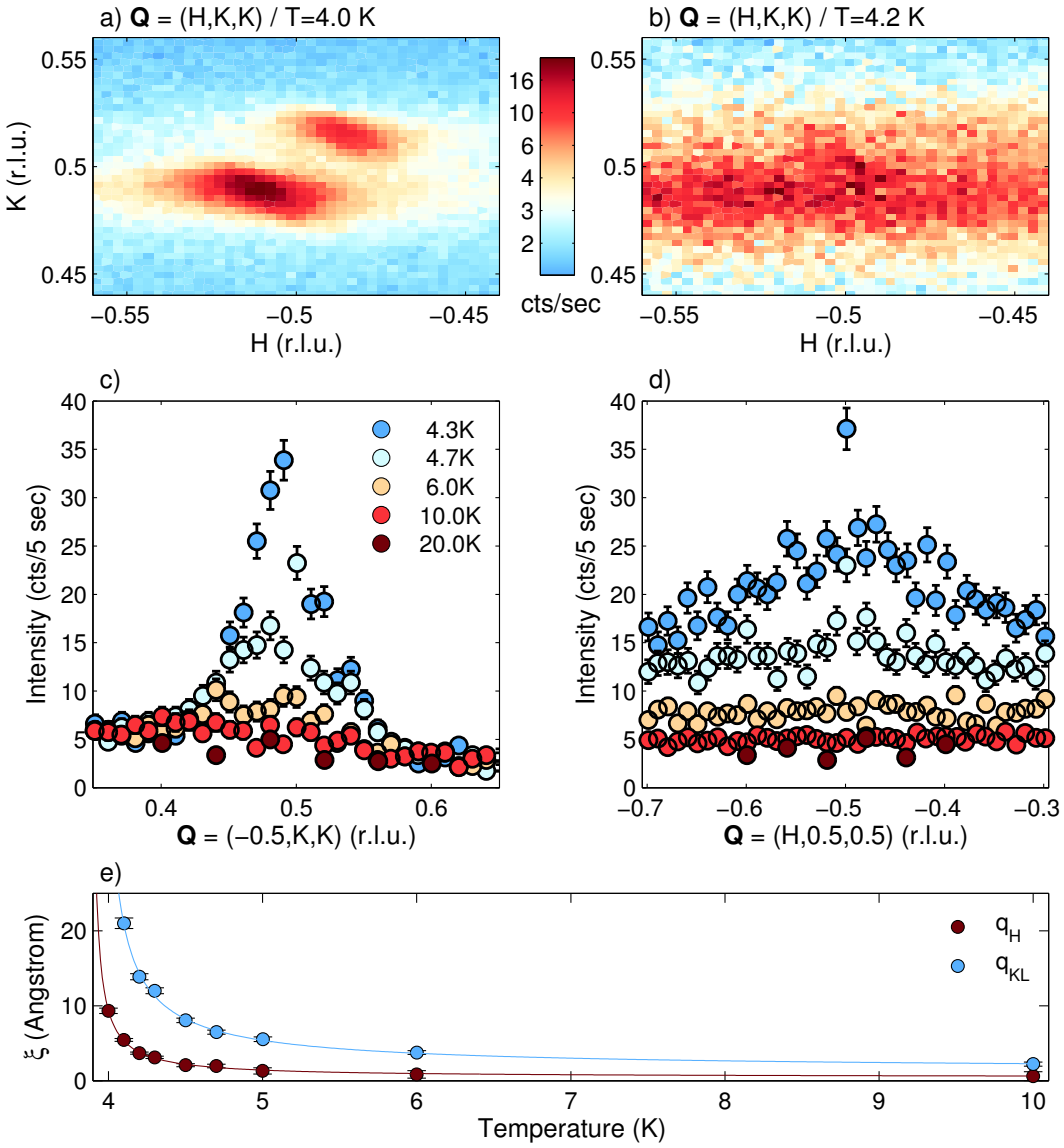

Figure 6.7.: Diffuse scattering in $NaFe(WO_4)_2$. Two-dimensional intensity mapping of $\vec{Q}$ scans along magnetic Bragg $\vec{Q} = (-0.5,\ 0.5,\ 0.5)$ upon heating through the phase transition in the orientation $[1,0,0]/[0,1,1]$ at (a) 4.0 K and (b) 4.2 K at IN3. The color is logarithmically coded. (c) and (d) show $\vec{Q}$ scans through commensurate Bragg position along $[0,1,1]$ and $[1,0,0]$ at several temperatures above the magnetic transition. Diffuse magnetic scattering is present up to 6 K. The correlation length ξ determined by Lorentzian fits for both directions is given in (e). A power law function $\xi = c(T - T_c)^{\nu}$ was fitted to the data yielding a transition temperature of $T_c = 3.90(5)$ K and a critical exponent of $\nu = -0.90(10)$.

bc-plane, where the magnetic moments form zig-zag chains. The planes are first decoupled along $\vec{a}$ leading to two-dimensional diffuse scattering. Only at lower temperatures the system develops correlations between the planes.

6.3. Symmetry analysis

A symmetry analysis of $NaFe(WO_4)_2$ has been done using *BasIreps* (implemented in the *FullProf* suite [81]) in order to solve the complex magnetic structures of the low field and high field phases of $NaFe(WO_4)_2$. The program is based on the method of representation analysis developed by Bertaut [126, 221, 222]. The crystallographic space group is $P2/c$ (13), its symmetry elements are listed in Table. 6.1. The magnetic moments of Fe^{3+} are located at the special Wyckoff site $2e$ at $(0, y, 1/4)$ which has two-fold symmetry and a multiplicity of two.
Nyam-Ochir *et al.* were able to describe the magnetic neutron powder data with a commensurate propagation vector of $\vec{k}_c = (0.5,\ 0.5,\ 0.5)$ [211]. The corresponding little group is $G_{\vec{k}_c} = \{1, 2, \bar{1}, c\}$ which is identical to the space group of the structure. It contains one two-dimensional irreducible representation Γ_1. The character table and the corresponding symmetry conditions for the magnetic moments are given in Table 6.2. In the case of the commensurate propagation vector, $\vec{k}_c$ and $-\vec{k}_c$ are equivalent and the star of $\vec{k}_c$ consists of one vector. The two-dimensional representation allows the two symmetry connected moments in the crystallographic unit cell to be either collinear or canted. For a given moment (u, v, w), the second moment can align according to the four possibilities: (u, v, w), $(u, \bar{v}, w)$, $(\bar{u}, v, \bar{w})$ and $(\bar{u}, \bar{v}, \bar{w})$.
In Section 6.2.2, it has been shown that the propagation vector of the zero-field magnetic phase is incommensurate in the monoclinic plane and is of the form $\vec{k}_{ic} = (\delta_H,\ 0.5,\ \delta_L)$ (see also Section 6.5.1 and [187]). With the incommensurability along $\vec{a}^*$ and $\vec{c}^*$ the little group of the magnetic structure changes to $G_{\vec{k}_{ic}} = \{1, c\}$. It contains two one-dimensional irreducible representations $\Gamma_{1,2}$. The character table and the corresponding symmetry conditions for the magnetic moments are

Table 6.1: Symmetry elements of the monoclinic space group $P2/c$ (no. 13) with the unit axis $\vec{b}$ [220].

Element		Symmetry operation
1		x, y, z
2	$0, y, 1/4$	$\bar{x}, y, \bar{z} + 1/2$
$\bar{1}$	$0, 0, 0$	$\bar{x}, \bar{y}, \bar{z}$
c	$x, 0, z$	$x, \bar{y}, z + 1/2$

	1	2	$\bar{1}$	c	x, y, z	$\bar{x}, \bar{y}, \bar{z}$
Γ_1	1 0 0 1	1 0 0 -1	0 1 1 0	0 1 -1 0	u, v, w	p, q, r

Table 6.2: Character table and symmetry conditions of the little Group $G_{\vec{k}_c} = P2/c$, $\vec{k}_c = (0.5,\ 0.5,\ 0.5)$.

	1	c	x, y, z	$x, \bar{y}, z + 1/2$
Γ_1	1	a	u, v, w	$a \cdot (u, \bar{v}, w)$
Γ_2	1	-a	u, v, w	$a \cdot (\bar{u}, v, \bar{w})$

Table 6.3: Character table and symmetry conditions of the little Group $G_{\vec{k}_{ic}} = Pc$, $\vec{k}_{ic} = (\delta_H,\ 0.5,\ \delta_L)$ with $a = e^{-2\pi i \cdot \delta_L \cdot r_z}$.

given in Table 6.3. In the case of the incommensurate propagation vector, $\vec{k}_{ic}$ and $-\vec{k}_{ic}$ are not equivalent and the star of $\vec{k}_{ic}$ contains two vectors. Since the c glide plane connects the two Fe sites in the unit cell and since c belongs to $G_{\vec{k}_{ic}}$, both sites thus belong to one orbit and can be described by three parameters u, v, w, cf. Table 6.3.

6.4. Structure determination of the zero-field phase

The magnetic structure of the zero field magnetic phase of $NaFe(WO_4)_2$ was investigated at the single-crystal four-circle diffractometer D10 at the ILL. Two single crystals of similar size ($13 \times 8 \times 2$ mm^3 and $6 \times 7 \times 2$ mm^3) were used for the experiment. The D10 diffractometer was equipped with a $80 \times 80\,\text{mm}^2$ microstrip area detector and was used with two wavelengths 1.26 Å and 2.36 Å. Magnetic Bragg reflections were recorded at 1.75 K and structural Bragg reflections were recorded at 12 K, well above the magnetic phase transition. The magnetic propagation vector $\vec{k}_{ic} = (0.485,\ 0.5,\ 0.48)$ of $NaFe(WO_4)_2$ is incommensurate (see Sections 6.5.1 and 6.2.2). The resolution of the chosen neutron wavelength did not allow to measure the magnetic satellites separately as the values of the incommensurabilities are close to the commensurate vector $\vec{k}_c = (0.5,\ 0.5,\ 0.5)$ and the reflections overlap. The collection of magnetic peaks has been done by long scans at the positions in Q-space generated by the commensurate propagation vector. The refinement was done in the space group $P2/c$ with the lattice parameters given in Figure 6.1 and was done using *FullProf* [81]. The datasets from both single crystals yield quantitatively the same results and we will present only the results from one dataset. The single crystal sample was the same as the one used for the neutron diffraction experiment discussed in Section 6.2.

Crystal structure

Structural reflections were recorded at 12 K in the paramagnetic phase. At a neutron wavelength of 1.26 Å, a total of 766 reflections were collected. For the refinement 367 independent nuclear reflections were used. The internal and weighted R-values are 1.64 and 1.83, respectively. The results of the refinement of the structural parameters are given in Table 6.4. Isotropic temperature factors and anisotropic extinction correction (model 4 in *FullProf*) were used for the refinement. The values for the atomic positions correspond very nicely to the results obtained from powder data [211] and the anisotropic extinction parameters well describe the plate like shape of the crystal. One can estimate the necessity of an absorption correction for cylindrical shaped crystals by calculating the product of the linear attenuation factor of the scattered sample with the radius of the sample. In the case of $NaFe(WO_4)_2$, the attenuation factor is $\mu = 0.194\,\mathrm{cm}^{-1}$ and the average diameter of the sample is approximately 0.5 cm. For products well below a value of 1, a correction for absorption is not necessary, which is the case for our sample [223]. The structural dataset can also be used to verify the occupation of the different atomic sites. It was mentioned before that the mechanism of the magnetic coupling along the extended a-axis is still matter of question. One possible explanation could be stacking faults of Na^+ and Fe^{3+} which would decrease the distance along this axis. The coherent neutron scattering length of sodium and iron are $b_{Na} = 3.63$ fm and $b_{Fe} = 9.45$ fm which makes a differentiation of both elements possible. The refinement with *FullProf* yields a deviation of only 1 to 2 % per site. The layered structure is thus well ordered and an influence of stacking faults on the magnetic structure can be a-priori excluded.

Magnetic structure

Magnetic Bragg reflections were recorded at 2 K in the ordered phase. At a neutron wavelength of 1.26 Å, a total of 423 reflections were collected. For the refinement 411 independent magnetic reflections were used. As mentioned before, the incommensurate satellites could not be measured independently. The resolution at the given wavelength was not high enough to separate the two satellites corresponding to $\vec{k}_{ic,1} = (0.485,\ 0.5,\ 0.48)$ and $\vec{k}_{ic,2} = (-0.485,\ 0.5, -0.48)$. Instead we used the commensurate propagation vector to measure the magnetic reflections and integrated over both peaks. The refinement program *FullProf* allows to treat the list of measured intensities in a way that the contribution of two neighboring

Table 6.4.: Structural parameters of $NaFe(WO_4)_2$ at 12 K. The data was recorded at the diffractometer D10 and the refinement was done using *FullProf* [81].

	x	y	z	U_{iso} ($\mathring{A}^2$)
Fe	0.0	0.67074(19)	0.25	0.04(2)
Na	0.5	0.6971(6)	0.25	0.35(5)
W	0.23704(14)	0.1831(2)	0.2572(3)	0.12(3)
O1	0.35385(12)	0.3813(3)	0.3816(3)	0.25(3)
O2	0.10888(13)	0.6226(3)	0.5923(3)	0.22(2)
O3	0.33177(13)	0.0897(2)	0.9533(3)	0.22(3)
O4	0.12606(13)	0.1215(3)	0.5757(3)	0.17(2)
$R_{F^2} = 3.70$, $R_{wF^2} = 3.55$, $R_F = 2.87$, $\chi^2(I) = 4.13$				

magnetic satellites is summed up in clusters and the incommensurate propagation vector could be used for the refinement.
Different models were used to describe the data. In a first step, a general symmetry of $P1$ was assumed with two independent Fe sites in the crystallographic unit cell. The two sites were described by identical Fourier coefficients and a phase shift $\phi_{\vec{k},c}$ between those two moments. This condition is necessary since both sites are still connected by symmetry (cf. Table 6.3) which requires an equal distribution of the magnetic moment. A comparison of the refinements using different models is given in Table 6.5. Analysis of neutron powder data yielded a model with a commensurate propagation vector and moments aligned antiparallel along $\vec{a}$ [211]. This model, however, is not compatible with the single crystal data from the D10 diffractometer. The fit can be improved by allowing the spins to align in the *ac*-plane. Another minor improvement can be achieved when we allow an additional component along the monoclinic axis. This result agrees with the analysis of the magnetic susceptibility. As discussed in Section 6.2.1, we expect an ordered magnetic moment in the *ac*-plane with a small additional component along the monoclinic axis.
The fit results are similar for a collinear spin density wave (SDW) and a spin spiral rotating in the $\vec{e}_{ac}$-$\vec{b}$ plane. The vector $\vec{e}_{ac}$ denotes the direction of the easy axis in the *ac*-plane. Spin spirals with a different rotation axis are not compatible with the data. We now take into account the symmetry analysis for the case of an incommensurate propagation vector $\vec{k}_{ic,1} = (0.485,\ 0.5,\ 0.48)$, cf. Table 6.3. Both Fe sites are connected by a glide plane c along the monoclinic axis and have a phase difference of $\phi_{\vec{k}} = 2\pi \times 0.24$. The refinement gives the best result for the case

Table 6.5.: Residual values for the refinements of the magnetic reflections of $NaFe(WO_4)_2$ taken at 2 K on D10 using different models.

	COM a	SDW a	SDW *ac*	SDW *abc*	Spiral $\vec{e}_{ac}$-$\vec{b}$ (1)	Spiral $\vec{e}_{ac}$-$\vec{b}$ (2)
R_{F^2}	47.8	47.9	15.0	14.9	15.1	11.7
R_{wF^2}	51.8	51.8	16.0	15.6	15.5	13.3
R_F	29.2	29.2	9.1	9.1	9.0	7.1
$\chi^2(I)$	239.0	240.0	22.7	22.1	21.6	9.9

of an elliptical spin spiral with moments rotating in the $\vec{e}_{ac}$-$\vec{b}$ plane. This model is compatible with either of the two irreducible representations Γ_1 and Γ_2 and the fit results do not allow to distinguish between them. A combination of both representation does not improve the fit and it can be stated that one representation is sufficient to describe the zero-field magnetic structure in $NaFe(WO_4)_2$. The difference of the two spiral models, $\vec{e}_{ac}$-$\vec{b}$ (1) and $\vec{e}_{ac}$-$\vec{b}$ (2), is the rotation of the two moments in the crystallographic unit cell relative to each other. In the model 'Spiral $\vec{e}_{ac}$-$\vec{b}$ (1)', which is the combination of both irreducible representations, the moments rotate along the same direction, whereas using only one irreducible representation, the moments rotate in the opposite direction (model 'Spiral $\vec{e}_{ac}$-$\vec{b}$ (2)').

The lengths of the major and the minor principal axis of the elliptical spiral are $M_{max} = \sqrt{(M_x^2 + Mz^2)} = 4.88\,\mu_B$ and $M_{min} = M_y = 1.09\,\mu_B$, with a ratio of $M_{min}/M_{max} = 0.22$. The angle between the major principal axis and the a-axis is 47.8°. A model of the magnetic structure is shown in Figure 6.8. Given the strong deformation of the ellipse, the magnetic moments cannot order at every position in the lattice, similar to the case of a spin-density-wave. After integration over the ellipse, we get an average oriented moment of about $3.5\,\mu_B$ which is less than 60 % of the moment of Fe^{3+}. The model described by *FullProf* only accounts for the harmonic incommensurate spin spiral. The anharmonic perturbations ('squaring up') and the coexisting commensurate phase (cf. Section 6.2.1) are not taken into account and lower the ordered magnetic moment.

The incommensurate spin spiral of this model breaks the inversion symmetry of the crystal which opens the possibility for a magnetoelectric effect and a ferroelectric polarization in this phase [6]. In Section 6.1.2, we discussed the dielectric experiments that have been performed on $NaFe(WO_4)_2$ [213]. In the zero field phase no pyro-electric current was detected and the material is thus not ferroelectric. The inverse Dzyaloshinskii-Moriya effect $\vec{D}_{ij} \times (\vec{S}_i \times \vec{S}_j)$ is nonzero in the proposed magnetic structure but it does not lead to a net electric polarization. The two magnetic moments in the crystallographic unit cell rotate in the opposite direction,

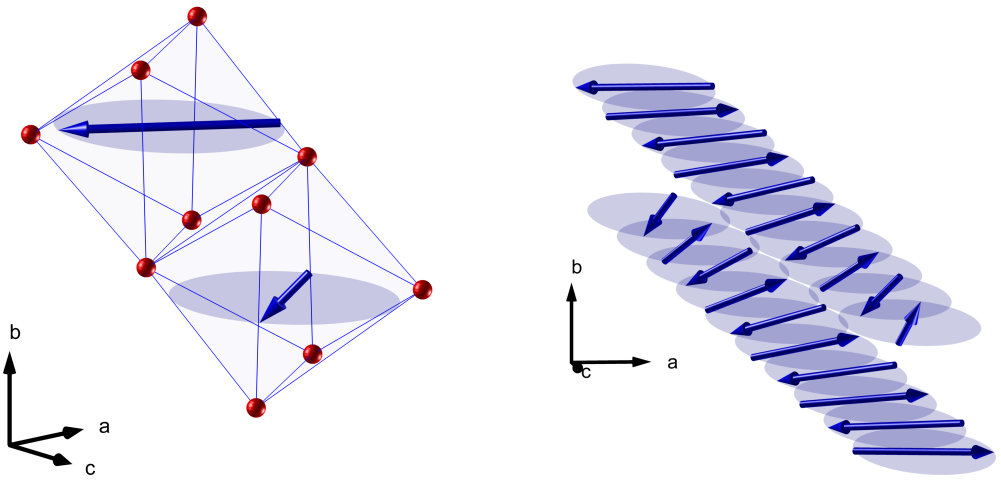

Figure 6.8.: Magnetic structure of $NaFe(WO_4)_2$ at 2 K as determined by single crystal diffraction on D10: (a) Crystallographic unit cell with magnetic moments and oxygen ions and (b) evolution of the spiral along $\vec{c}$. The ellipses show the rotation plane of the magnetic moments with the principal axes $\vec{e}_{ac}$ and $\vec{b}$.

relative to each other, and thus the effect cancels out as the cross product of neighboring spins switches sign during one period of the spiral [197, 224]. A similar situation was discussed for the AF3 phase in $MnWO_4$ where two opposing spirals prohibit a ferroelectric polarization [225].
In Figure 6.9, we compare our determined magnetic model with the one proposed on the basis of neutron powder diffraction data [211]. The program *FullProf* was used to simulate neutron diffractograms for nuclear and magnetic scattering at a wavelength of 2.4 Å. For the calculation of the magnetic scattering, two different models were taken into account. To simulate the powder data from the literature, a collinear magnetic structure with moments along $\vec{a}$ and a commensurate propagation vector of $\vec{k}_c = (0.5,\ 0.5,\ 0.5)$ was used. For the 'Spiral $\vec{e}_{ac}$-$\vec{b}$' curve, the incommensurate spin spiral model determined in this section was used. The resolution was adapted to the neutron powder data from the literature. The small incommensurability is difficult to be resolved within the given resolution from powder diffraction. The different orientation of the moments in both models only results in minor changes in the diffractograms which can easily be overseen or misinterpreted. Nyam-Ochir *et al.* mention that an additional component along $\vec{c}$ also described the data well but did not improve the fit. In $NaFe(WO_4)_2$, the lattice parameters are $a = 9.88$ Å, $b = 5.72$ Å, $c = 4.94$ Å and $\beta = 90.33(4)°$ [214]. The distance along $\vec{a}$ and $\vec{c}$ are connected by almost a factor of two and it is difficult to distinguish them in a powder experiment. We argue that both datasets, from powder and single crystal diffraction, can be described by the model determined in this section.

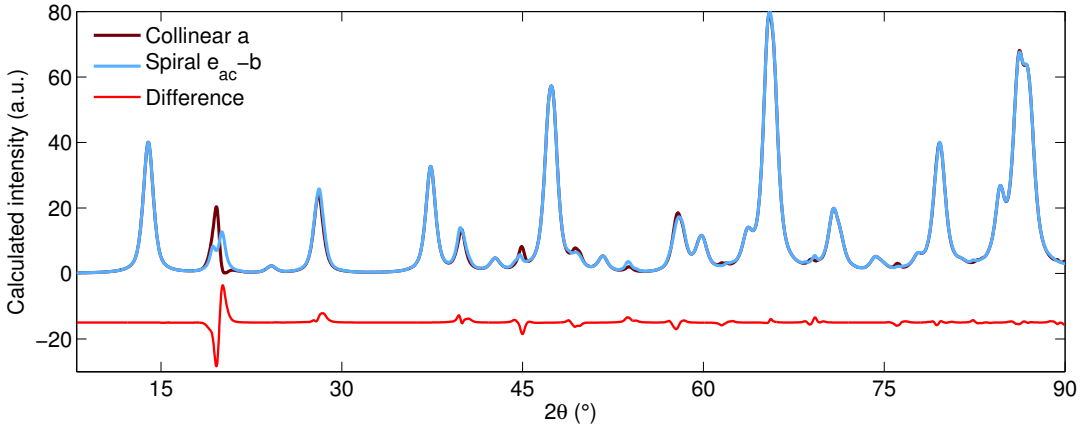

Figure 6.9.: Calculated neutron powder diffractograms for nuclear and magnetic scattering at a wavelength of 2.4 Å using *FullProf*. The brown line corresponds to the model proposed by Nyam *et al.* and the blue line corresponds to single crystal model found in this work [211]. The subtraction of both curves is shown below in red.

6.5. Neutron diffraction of high-field phases

6.5.1. Magnetic field dependence of the propagation vector

The influence of magnetic fields applied along the monoclinic axis $\vec{b}$ on the magnetic structure of $NaFe(WO_4)_2$ was investigated by neutron diffraction in the diploma thesis [187]. The experiment was performed at the four-circle diffractometer 6T2 at the LLB in Saclay, France. The same single crystal was used for the experiment as for experiments previously described. We will briefly summarize the results in this section.
Figure 6.10(a) shows the intensity map of rocking scans along the magnetic Bragg peak position $\vec{Q} = (\ 0.5, -0.5, -0.5)$ for magnetic fields applied along the monoclinic axis $\vec{b}$. The intensity is logarithmically color coded. The application of the magnetic field along the monoclinic axis strongly affects the incommensurate splitting of the satellites. At a magnetic field of about 1.2 T, the satellites merge into one commensurate peak. The field was first increased to a maximum field of 5 T and then decreased to zero field at constant temperature. In decreasing fields, only a modulation of the intensity is visible and the scattered intensity remains at the commensurate position. Gaussian functions have been fitted to the data

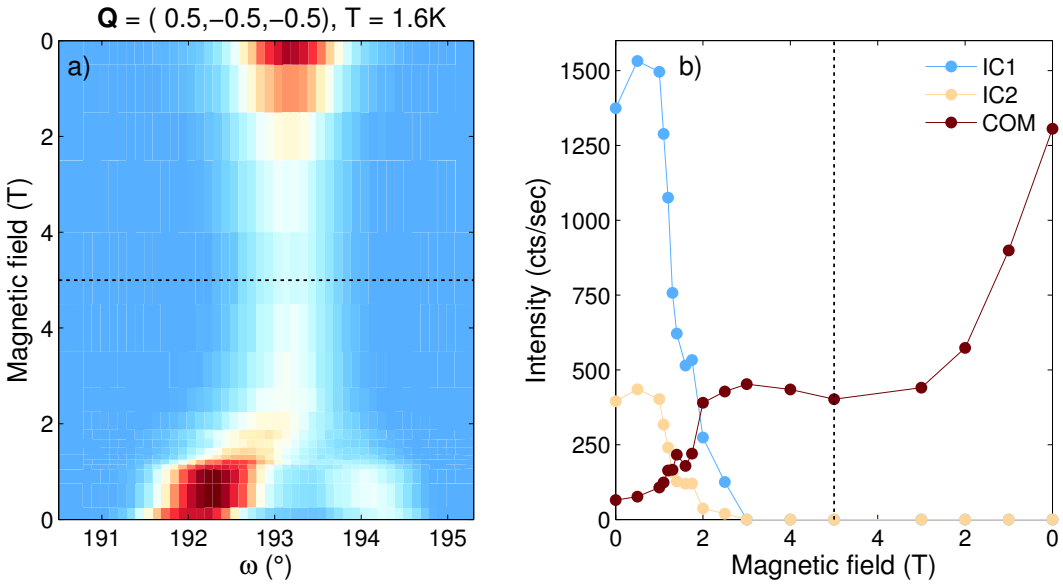

Figure 6.10.: Magnetic field dependence of the magnetic structure in $NaFe(WO_4)_2$ at 6T2. (a) Intensity mapping of rocking scans along the magnetic Bragg peak position $\vec{Q} = (0.5, -0.5, -0.5)$ in magnetic fields applied along $\vec{b}$ at 1.6 K. (b) Corresponding Bragg peak intensities of incommensurate (IC1 and IC2) and commensurate (COM) reflections fitted by Gaussian functions. Lines between points are a guide to the eye. Data taken from [187].

and resulting amplitudes are shown in Figure 6.10(b). The first transition at 1.2 T perfectly matches the phase transition observed in the magnetostriction data (cf. Figure 6.4(b)). The system undergoes a phase transition from a paramagnetic towards an incommensurate magnetic structure with a propagation vector of $\vec{k}_{ic} = (\delta_H,\ 0.5,\ \delta_L)$ at low temperatures. When the magnetic field is decreased again, the system stays in the commensurate magnetic phase and only a modulation of the scattered intensity of the Bragg peaks is visible. We can thus assign three different magnetic phases as low-field incommensurate (LF-IC), high-field commensurate (HF-C) and low-field commensurate (LF-C).

6.5.2. Commensurate magnetic structures

The results from the zero field diffraction data will help to analyze the data collected in the high field magnetic phase of $NaFe(WO_4)_2$. In Section 6.5.1. we summarized the results of the experiment at the 6T2 diffractometer. In addition to the temperature and magnetic field dependence of the propagation vector, 36

Table 6.6.: Comparison of magnetic structures in $NaFe(WO_4)_2$ in magnetic fields applied parallel $\vec{b}$. The orientation of the moments in the crystallographic unit cells are given and the corresponding propagation vectors are $\vec{k}_c = (0.5,\ 0.5,\ 0.5)$ (C) and $\vec{k_{ic}} = (0.485,\ 0.5,\ 0.48)$ (IC). The models were determined from experiments at D10 and 6T2 using *FullProf*. We list the Fourier coefficients $\vec{M}_{AF}$ for site 1 and the symmetry relation for site 2, with $a = e^{-2\pi i \cdot k_z \cdot r_z}$. The induced ferromagnetic magnetization, $M_{FE}(B)$, is deduced from SQUID data (Fig. 6.3(c)).

$B\|\|b$ (T)	$M_{FM}(B)$ (μ_B)	Phase	$\vec{M}_{AF}$ (μ_B)	Symmetry	$\angle(\vec{e}_{ac}, \vec{a})$ (°)
0	0	LF-IC	(3.3,-i·1.1, 3.6)	$a \cdot (u, \bar{v}, w)$	47.7
5	1.28	HF-C	(2.5, 0.8, 2.1)	$(\bar{u}, \bar{v}, \bar{w})$	39.7
3	0.75	HF-C	(3.0, 0.8, 3.0)	$(\bar{u}, \bar{v}, \bar{w})$	44.8
2	0.50	HF-C	(3.0, 0.5, 3.3)	$(\bar{u}, \bar{v}, \bar{w})$	48.1
1	0.25	LF-C	(2.7, 1.5, 3.3)	$(u, \bar{v}, w)$	50.4
0	0	LF-C	(2.5, 2.1, 3.1)	$(u, \bar{v}, w)$	50.7

magnetic reflections were collected at 1.6 K in 0 T, 5 T and again 0 T. The instrument was equipped with a cryomagnet which cannot be used in combination with the Eulerian cradle. One was thus restricted to a two-dimensional scattering plane. The installed lifting counter geometry made it nevertheless possible to move the detector up to 30° perpendicular out of the scattering plane in order to increase the accessible $\vec{Q}$ space. The small number of reflections and the absence of reflections along the $\vec{b}$ lowers the completeness and of the data. A precise refinement of the magnetic structure is not possible but the data gives significant information about the orientation of the moments in the different magnetic phases.
The 6T2 zero field data confirms the model for the magnetic structure determined from the D10 data in the LF-IC phase. As a result, we get the same incommensurate spin spiral with main axes along $\vec{e}_{ac}$ and $\vec{b}$. The ratio between the components along $\vec{c}$ and $\vec{a}$ is $M_z/M_x \approx 1.1$ which corresponds to an angle of 47.7° to the a-axis. A model of the magnetic structure is shown in Figure 6.8(a).
Figure 6.11(a) shows a model of the magnetic structure determined from the 6T2 data in a magnetic field of 5 T applied along the monoclinic axis. The figure shows the addition of the commensurate antiferromagnetic phase and the induced ferromagnetic moment along $\vec{b}$ (see also Table 6.6). The propagation vector of the HF-C phase changes to a commensurate $\vec{k}_c = (0.5,\ 0.5,\ 0.5)$. The moments in the crystallographic cell are collinear antiferromagnetically ordered with components along all three axis: $M_x = 2.54(10)\,\mu_B$, $M_y = 0.84(14)\,\mu_B$ and $M_z = 2.12(10)\,\mu_B$ yielding a total ordered moment of $M = 3.4\,\mu_B$. This model only describes the

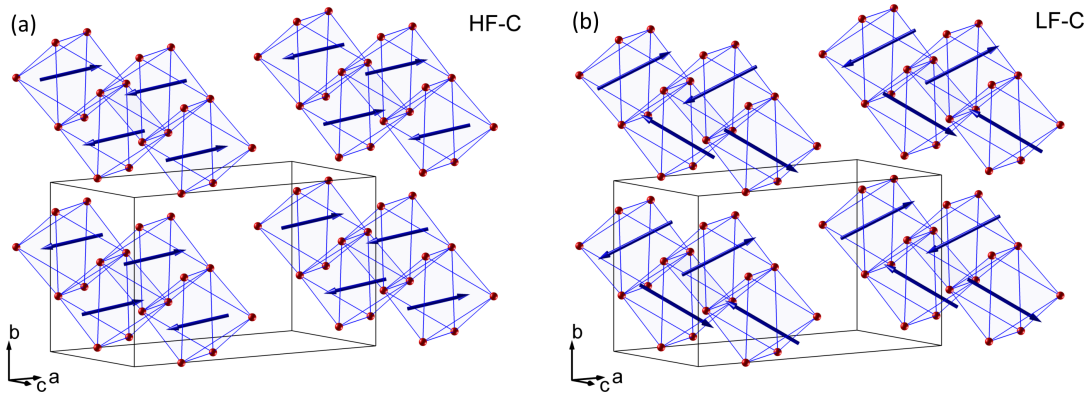

Figure 6.11.: Magnetic structures of $NaFe(WO_4)_2$ at 1.6 K as determined by single crystal diffraction on 6T2 with magnetic fields applied along $\vec{b}$: (a) High-field commensurate phase at 5 T and (b) low-field commensurate phase zero field. The induced ferromagnetic magnetization was not taken into account.

moments ordered according to the commensurate propagation vector. We can deduce from the magnetization at 2 K (cf. Fig. 6.3(c)) that fields applied along $\vec{b}$ induce an additional ferromagnetic moment of about $M_{FM} = 1.3\,\mu_B$. This induced moment leads to an increase of intensity at the nuclear Bragg peak positions. The ratio between the components along $\vec{c}$ and $\vec{a}$ is $M_z/M_x \approx 0.8$ which corresponds to an angle of 39.7° to the a-axis. This value is significantly smaller than in the incommensurate zero field phase.
Finally, Figure 6.11(b) shows the model of the magnetic structure determined with the zero field data, directly after decreasing the field from 5 to 0 T at a constant temperature of 1.6 K. The propagation vector in the LF-C phase is the same as in the high field phase, $\vec{k}_c = (0.5,\ 0.5,\ 0.5)$. The best fit was achieved with canted moments in the crystallographic unit cell with components along all three axis: $M_x = 2.5(3)\,\mu_B$, $M_y = 2.1(2)\,\mu_B$ and $M_z = 3.1(4)\,\mu_B$ yielding a total ordered moment of $M = 4.5\,\mu_B$. The ratio between the components along $\vec{c}$ and $\vec{a}$ is $M_z/M_x \approx 1.2$ which corresponds to an angle of 50.7° to the a-axis. This value is similar to the one in the high field phase. The transition from the HF-C to the LF-C phase is visible in a modulation of scattered intensity (Fig. 6.10(a)) and as a spin-flop transition in the magnetization data (cf. Fig. 6.3(d)). A comparison of the models in the incommensurate low field phase (IC-LF), commensurate high field phase (C-HF) and the commensurate low field phase (C-LF) is given in Table 6.6. The analysis of the crystallographic space group combined with the commensurate propagation vector of the magnetic structure yield a little group of $G_{\vec{k}} = \{1, 2, \bar{1}, c\}$, cf. Table 6.2). To determine the magnetic space group of the two distinct magnetic structures we now have to take into account the orientation of the moments and their transformation under different symmetry operations. In a classical description,

magnetic moments are represented by axial vectors (or pseudo-vectors). These vectors transform like polar vectors under proper rotations, but change sign under improper symmetry operation such as inversion and mirrors [222]. In the case of the collinear moments in the HF-C phase, we determine a loss of the glide plane c and the two-fold rotation which is due to the canting with respect to the monoclinic plane. The inversion has to be combined with the time reversal operator $1'$ which switches the sign of the moment. This leaves us with a magnetic space group of $P\bar{1}'$ for the HF-C phase. From the magnetic symmetry one can also derive the compatibility of the system with magnetoelectric invariants, following the Neumann principle [226]. The corresponding magnetic point group $\bar{1}'$ does not allow a linear magnetoelectric effect (only the quadratic term EHH is allowed) [31, 227].
Similarly we determined the magnetic space group for the LF-C phase as Pc'. Here, the relative canting of the two moments in the unit cell destroys the two-fold rotation and the inversion symmetry. The corresponding magnetic point group m allows the linear magnetoelectric effect EH [31, 227].
In all three magnetic structures, the centrosymmetry of the crystallographic space group $P2/c$ is broken which opens the possibility of a ferroelectric polarization [228]. We already discussed the absence of such a polarization induced by the DM effect in the LF-IC phase. In the HF-C phase, all magnetic moments are (anti-)parallel and the DM mechanism would again not lead to a polarization. The case is different for the LF-C phase where the moments in the unit cell are canted. Applying Equation 2.6 to the spin chain along $\vec{c}$ leads to a net ferroelectric polarization along the monoclinic axis. The pyrocurrent was measured along $\vec{b}$ in the LF-C phase but no evidence for a ferroelectric polarization was found.

6.6. Conclusion

The double tungstate $NaFe(WO_4)_2$ is isostructural to the well studied spiral multiferroic $MnWO_4$. The magnetic phase diagram of $NaFe(WO_4)_2$ was investigated intensively using elastic neutron scattering in the zero-field phase and in the high field phases in magnetic fields applied along the monoclinic axis $\vec{b}$. An analysis of the different magnetic structures together with the study of the complex temperature and magnetic field dependence of the propagation vector helped to explain the magnetic phase diagram.
At zero field, it could be demonstrated that the Fe magnetic moments order directly in a spin spiral with a incommensurate propagation vector $\vec{k_{ic}} = (0.485,\ 0.5,\ 0.48)$ at 3.9 K. The spiral is elliptically distorted with the major axis of the spiral along $\vec{e}_{ac}$ and the minor axis along $\vec{b}$. The incommensurability decreases with temperature and freezes in at a temperature of 2.0 K. Upon heating, the incommensurability

shows a hysteresis-behaviour, which could be related to an anharmonic distortion of the spiral. The hysteresis effect of the propagation vector allows to explain features visible in thermal expansion data, which do not show the transition but the change of incommensurability [213].
The direct transition into the spiral state is in contrast to other systems such as $MnWO_4$ and $TbMnO_3$, where the spiral phase follows a sinusoidal modulated phase [11, 175]. The spiral transition can be described by a single irreducible representation, which explains the absence of an electric polarization in this phase. Spin spirals of opponent rotation direction are equally present in the system and cancel out the effect of the DM mechanism. In $MnWO_4$, the spiral state is described by two representations, which allow the rotation direction to be along the same direction, inducing a finite electric polarization.
In magnetic fields applied along $\vec{b}$, the magnetic structure becomes commensurate with a propagation vector of $\vec{k_c} = (0.5,\ 0.5,\ 0.5)$. The collinear ordered magnetic moment develops components within the monoclinic plane, as well as perpendicular to it. When the field is decreased again, at a constant temperature, the magnetic order shows a spin-flop. The propagation vector remains commensurate but the magnetic moments in the unit cell are canted relative to each other. This phase is similar to the commensurate ground state of $MnWO_4$ [175].
From the magnetic phase diagram, we can assume that the magnetic ground state of $NaFe(WO_4)_2$ is the commensurate low-field phase [229]. Upon cooling, the system first orders incommensurately and subsequently remains in this local minimum, due to a loss of thermal energy. Magnetic fields applied along $\vec{b}$ lead to a transition into the commensurate state.

Chapter 7

$Ni_{0.42}Mn_{0.58}TiO_3$, a magnetoelectric spin glass

The discovery of spin-induced ferroelectricity and giant magnetoelectric effects in magnetically frustrated transition-metal oxides attracted much interest due to their exciting physical mechanism and their potential applications [5]. In most materials studied, the magnetoelectric properties are coupled with the spin chirality via the inverse Dzyaloshinskii-Moriya interaction [15,43]. Generally, the effect is studied in systems that exhibit long-range magnetic order. However, very recently Yamaguchi *et al.* showed that long-range order actually is not needed [18]. They find a finite magnetoelectric effect in a material with only short-range ordering.

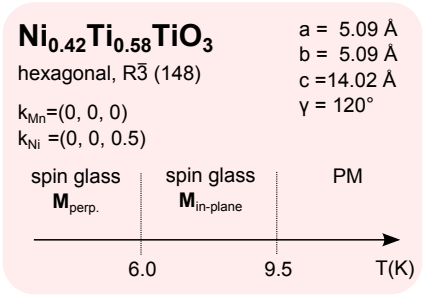

Figure 7.1.: Crystal parameters and magnetic phase transitions in $Ni_{0.42}Mn_{0.58}TiO_3$ [230, 231].

The $Ni_xMn_{1-x}TiO_3$-system develops a spin-glass (SG) phase at low temperatures for Ni concentrations between $x = 0.4$ and 0.5. An electric polarization could be induced in this phase by crossed magnetic and electric fields [18]. This off-diagonal linear magnetoelectric effect was explained by an induced ferrotoroidal order in the short-range order [18, 232].

In this chapter, the study of the spin glass system $Ni_{0.42}Mn_{0.58}TiO_3$ using unpolarized and polarized neutron scattering methods is presented. The ordering in the frustrated spin-glass phase and the behavior of the short-range order in applied magnetic and electric fields will be discussed. Finally, the magnetic excitations in the spin-glass phase were measured and compared to simulation using linear spin wave theory.

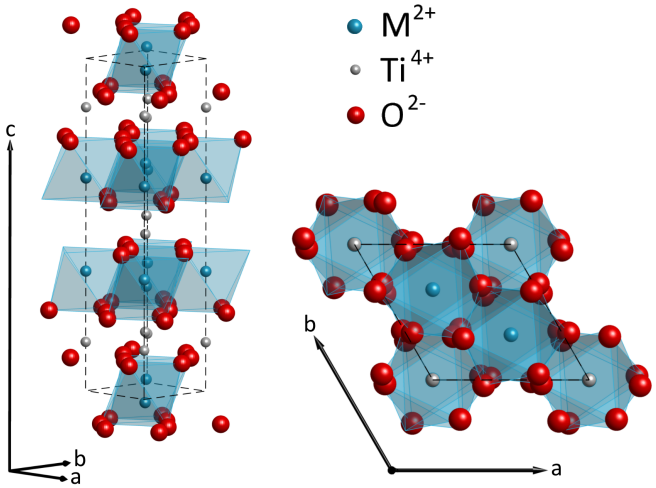

Figure 7.2: Ilmenite-type crystal structure of the $M\mathrm{TiO_3}$ series, with M^{2+} being a transition metal ion. M^{2+} and Ti^{4+} ions are in an octahedral environment and form sheets in the hexagonal plane which are alternately stacked along $\vec{c}$. Each metal ion is surrounded by six oxygen ions.

7.1. Introduction

7.1.1. The $Ni_xMn_{1-x}TiO_3$ system

Materials of the $\mathrm{Ni}_x\mathrm{Mn}_{1-x}\mathrm{TiO_3}$ system crystallize in a trigonal centrosymmetric structure which can be described in the space group $R\bar{3}$ (no. 148) [230, 231]. The system is isostructural to ilmenite ($\mathrm{FeTiO_3}$), such as other $M\mathrm{TiO_3}$ systems with a magnetic transition metal ion M =Mn^{2+}, Co^{2+}, Ni^{2+} and Zn^{2+} [233, 234, 235]. Throughout this chapter, the trigonal system is described in the hexagonal setting which is commonly used nowadays. In some publications, the rhombohedral setting was applied[a]. The crystal structure is shown in Fig. 7.2. Tetravalent Ti and divalent M-ions form well defined planes parallel to the hexagonal ab-plane and and are regularly stacked. Since Ti^{4+} is non-magnetic, the magnetic layers are only weakly coupled, forming a 2D honey-comb lattice in the hexagonal ab-plane. The members of the $M\mathrm{TiO_3}$ group show only small deviations in their crystallographic parameters, which makes them suitable for studying compounds with mixed magnetic moments. These mixed systems are of particular interest when competing exchange interactions or anisotropies of the end members lead to frustration. This is the case for the $\mathrm{Ni}_x\mathrm{Mn}_{1-x}\mathrm{TiO_3}$ system [236]. We will first discuss the end compounds of this series before we focus on the mixed state.

[a]The conversion of Miller indices of the rhombohedral setting (h, k, l) to the hexagonal setting (H, K, L) is: $H = h - k$, $K = k - l$ and $L = h + k + l$.

$NiTiO_3$

The magnetic structure in $MnTiO_3$ and $NiTiO_3$ was investigated in an early neutron diffraction study by Shirane *et al.* [233]. In $NiTiO_3$, the magnetic moments were found to order in an layered antiferromagnetic structure below $T_N \approx 23.2\,\mathrm{K}$ [237, 238]. Ferromagnetic layers in the hexagonal plane are coupled antiferromagnetically along $\vec{c}$. The resulting magnetic unit cell is doubled along $\vec{c}$ with a propagation vector of $\vec{k}_{Ni} = (0,\ 0,\ 0.5)$. The moments are oriented within the hexagonal plane but the precise direction within the plane could not be determined [233]. Both, crystal and magnetic structure, have inversion symmetry $\bar{1}$ and thus do not allow for a magnetoelectric effect. A high temperature phase of $M\mathrm{TiO}_3$ exists, which is non-centrosymmetric, and which is metastable at room temperature [239]. Ferro- and magnetoelectric properties in this phase have been predicted [240] and measured in $NiTiO_3$ [241, 242].
A detailed theoretic study of the magnetic properties in the $M\mathrm{TiO}_3$ ilmenites was published by Goodenough *et al.* [234]. Looking at the electron occupation of interacting orbitals, they argue that for Ni^{2+} the superexchange couplings in the hexagonal *ab*-plane are ferromagnetic, which is also the case for systems with M =Fe^{2+} and Co^{2+}. The super-superexchange interaction via the non-magnetic Ti^{4+} layer should accordingly be antiferromagnetic and weak relative to the intra-layer exchange [234]. The ordered magnetic moment of $\mu_{eff} = 2.25\,\mu_B$ determined by neutron diffraction at 4.2 K is smaller than the spin-only moment $\mu_{eff} = 2.83\,\mu_B$ for Ni^{2+}, with $S = 2/2$ and a quenched orbital moment [233]. Shirane *et al.* mention the possibility of incomplete order of Ni and Ti sites that can lead to the reduction of the ordered moment (also observed by Ohgaki *et al.* [243]). The cation disorder in $NiTiO_3$ seems to strongly depend on the crystal quality, because there are also reports of an complete order [235]. Susceptibility measurements yield a larger effective magnetic moment of $\mu_{eff} = 3.24\,\mu_B$ indicating a contribution of a slightly unquenched orbital moment [244]. This could explain the observed finite single-ion-anisotropy of Ni^{2+} which overcomes the spin-dipol interaction and confines the magnetic moments in the hexagonal plane [238].

$MnTiO_3$

In $MnTiO_3$, the magnetic moments order below $T_N \approx 63.6\,\mathrm{K}$ and are aligned along the hexagonal axis $\vec{c}$ [245]. The moments form an antiferromagnetic G-type structure with propagation vector $\vec{k}_{Mn} = (0,\ 0,\ 0)$ [233]. This can be explained by the magnetic exchange interactions. The e_g orbitals of Mn are single-occupied yielding an antiferromagnetic coupling along $\vec{c}$, as it is the case for other ilmenite systems $M\mathrm{TiO}_3$ with M=Ni, Co and Fe. The t_{2g} orbitals in the hexagonal plane are single-

occupied, which leads to an antiferromagnetic superexchange interaction [234]. This is in contrast to other $M\mathrm{TiO}_3$, where the strongest in-plane exchange is ferromagnetic [234]. The intra-plane interactions were found to be significantly stronger compared to inter-plane interactions ($\sum J_{inter}/\sum J_{intra} \approx 0.035(5)$), resulting in a 2D-like character of the magnetic susceptibility. Furthermore, Akimitsu *et al.* report the observation of 2D-like diffuse magnetic scattering above T_N and the investigation of the critical exponents suggests a cross-over effect from 2D to 3D behaviour above T_N [246].
The isolated Mn^{2+} ion has a spin of $S = 5/2$ and zero orbital momentum, yielding $\mu_{eff} = 5.92\,\mu_B$. No spin-orbit coupling is expected and the weak confinement of moments along $\vec{c}$ can be explained purely by dipole interaction, which favors moments to be aligned along the long axis [245]. An ordered magnetic moment of only $\mu_{eff} = 4.55\,\mu_B$ at about 4 K was determined by neutron diffraction [233, 247]. The origin of the reduced moment is unclear and was attributed to either an incomplete Mn-Ti order [233] or the existence of di- and trivalent Mn ions [248].
The magnetic space group of MnTiO_3 is $R\bar{3}'$ and allows for the linear magnetoelectric effect, which is in contrast to NiTiO_3 [233]. By symmetry, $\alpha_{xx} = \alpha_{yy}$, α_{zz}, and $\alpha_{xy} = -\alpha_{yx}$ of the magnetoelectric tensor are allowed to be non-zero. The material is thus dielectric at zero-magnetic field but can be polarized in applied electric and magnetic fields. It was demonstrated by Mufti *et al.* by measuring P_{el} as function of H that the diagonal term α_{zz} of the magnetoelectric tensor in MnWO_4 is finite [249]. The microscopic origin of the ME effect could be explained by spin-dependent metal-ligand hybridization [250].

Phase diagram of $\mathbf{Ni_{0.42}Mn_{0.58}TiO_3}$

The end members of the system, MnTiO_3 and NiTiO_3, exhibit simple antiferromagnetic structures, which are coupled antiferromagnetically along the hexagonal c-axis and are not frustrated in the honey-comb lattice. Differences between both magnetic structures consists of their orthogonal easy magnetization directions and the sign of the nearest intra-plane exchange interaction. Both should result in a strong frustration for intermediate concentrations.
Figure 7.3 shows the schematic magnetic phase diagram of $\mathrm{Ni}_x\mathrm{Mn}_{1-x}\mathrm{TiO}_3$ for varying temperature and Ni-concentration determined by Ito *et al.* [230]. At low Ni-concentrations, the system orders in the magnetic structure of MnTiO_3, denoted as AF-$\mathrm{Mn}_{\parallel}$. An increase of Ni introduces frustration into the system, visible in a reduction of T_N, and the development of a second phase transition. The in-plane single-ion-anisotropy of Ni competes with the dipole interaction. As a result, the direction of moments rotates from the c-axis to the ab-plane. The angle between the ordered magnetic moment $\vec{m}$ and the hexagonal plane is strongly dependent

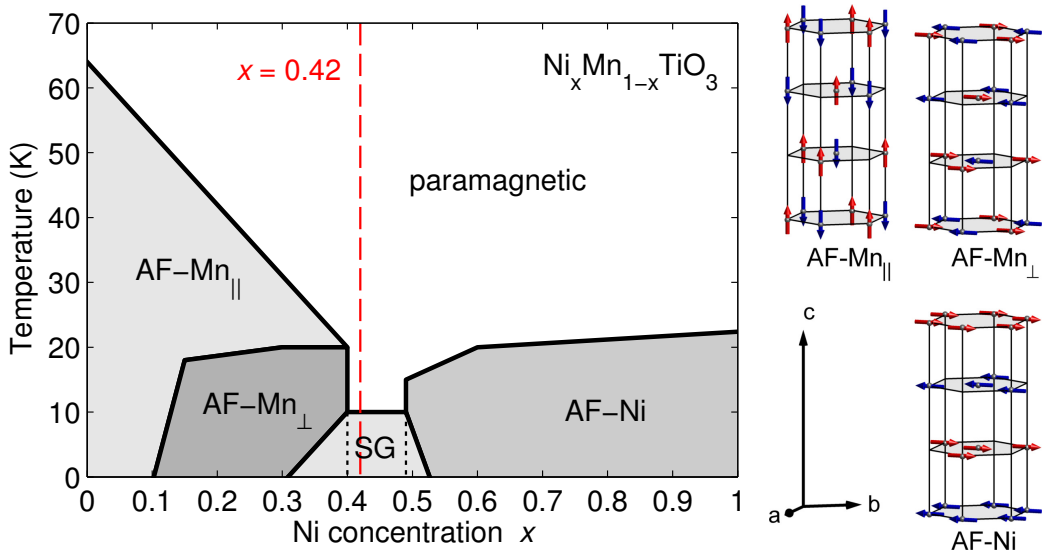

Figure 7.3.: Schematic diagram of magnetic phases of the $Ni_xMn_{1-x}TiO_3$ system, reproduced from Ref. [230]. The relative spin orientations of the ordered phases AF-$Mn_{\parallel}$, AF-$Mn_{\perp}$ (both G-type) and AF-Ni (A-type) are illustrated on the right. Black dotted lines separate the spin glass (SG) phase from the reentrant spin glass regions. The concentration investigated in this work is indicated by a red dashed line.

on the Ni concentration x and T in this region. In the diagram, this region is simplified as one area, denoted AF-$Mn_{\perp}$. Yoshizawa *et al.* revealed that this region is subdivided in at least four different phases [236]. At high Ni-concentrations $x > 0.5$, the system orders in the magnetic A-type structure of $NiTiO_3$ (AF-Ni). This phase is stable almost down to an equal concentration of Ni and Mn. It seems plausible that due to the stronger anisotropy of Ni moments, the phase is less perturbed by Mn doping. The three magnetic structures are schematically shown on the right side of Fig. 7.3.

For an intermediate Ni-concentration between $x = 0.4$ to 0.5, the absence of long-range magnetic order has been deduced from the lack of an anomaly in specific heat measurements [230]. These compounds were proposed to exhibit a spin-glass transition that is visible in a clear splitting of the magnetization curves measured in magnetic field or in zero-field cooling [230]. Ni and Mn ions are randomly distributed on the M-sites and their competing intra-plane interaction destroys the development of a long-range order. In analogy to a glass state of matter, a frozen state of disordered atoms, the spin glass state describes the freeze-in of magnetic moments with short-range order only.

The freezing of magnetic moments in the spin glass phase has been furthermore investigated by neutron diffraction. Kawano *et al.* find weak intensity at the

AF-Ni Bragg peak positions arising from quasi-elastic magnetic scattering [231]. The temperature dependencies from the magnetic susceptibility as well as the magnetic scattering show two anomalies which Kawano *et al.* interpret as successive spin glass transitions. They argue that the single-ion-anisotropy of Ni leads to a separation of in-plane and out-of-plane magnetic components, following the theory of SG systems with planar anisotropy [251]. Accordingly, they distinguish the transition of the component in the *ab*-plane, $T_{SG}^{\parallel} = 9.5(10)\,\mathrm{K}$, and the transition of the component along $\vec{c}$, $T_{SG}^{\perp} = 6.0(5)\,\mathrm{K}$ [231]. In general, such systems with planar anisotropy are referred to as XY spin glasses [252].
Such a spin glass phase at an intermediate region of concentration has also been observed for the systems $Fe_xMn_{1-x}TiO_3$ [253] and $Co_xMn_{1-x}TiO_3$ [254]. In all cases, the magnetic frustration is due to the unique position of Mn ions among the other transition metal ions in the $MTiO_3$ series in terms of exchange interaction and single-ion-anisotropy [234].

7.1.2. Magnetoelectric effect in the spin-glass phase

The end compounds of the $Ni_xMn_{1-x}TiO_3$ system not only differ from each other in magnetic nearest-neighbor in-plane exchange and anisotropy, but also in their magnetoelectric properties. While the magnetic structure of $MnTiO_3$ allows for the linear magnetoelectric effect, it is excluded by symmetry in $NiTiO_3$. Yamaguchi *et al.* investigated the electric polarization P in dependence of applied magnetic fields for several Ni concentrations in the region of the SG phase [18, 232]. For concentrations of $x = 0.40$ and $x = 0.42$, they find an induced polarization in crossed magnetic and electric fields. The corresponding magnetoelectric tensor has non-zero off-diagonal terms $\alpha_{xy} = -\alpha_{yx}$[b]. All diagonal terms were found to be zero, which is in contrast to the case of $MnTiO_3$ [249]. It is thus likely that the induced electric polarization in $Ni_{0.42}Mn_{0.58}TiO_3$ is caused by another effect.
The linear magnetoelectric (ME) effect is allowed only in magnetic insulators in which time reversal and space inversion symmetry are simultaneously broken. The ordering of magnetic moments breaks the time reversal symmetry. The space inversion is an element of the centrosymmetric space group $R\bar{3}$ and can only be broken by a specific arrangement of moments. This explains the existence of the ME effect in $MnTiO_3$ and its absence in $NiTiO_3$. The linear ME effect is mostly discussed in terms of ordered magnetic structures and only few reports exist about such an effect in disordered systems (e.g. Ref. [255]).
In most materials studied, the magnetoelectric properties are coupled with the spin chirality $\vec{S}_i \times \vec{S}_j$ via the inverse DM interaction [15,16]. Another multi-spin variable

[b]The following coordinate system was applied: $X \parallel [110]$, $Y \parallel [\bar{1}10]$, $Z \parallel [001]$.

that couples directly with magnetoelectric properties is the toroidal moment, which is given by the cross product between the positions $\vec{r}_i$ of the magnetic ions and their spins $\vec{S}_i$:

$$\vec{t} \propto \sum_i \vec{r}_i \times \vec{S}_i \ . \tag{7.1}$$

The sign of the toroidization $\vec{t}$ changes with both, space reversal and time inversion but it is invariant against the simultaneous inversion of both [31, 256]. A non-vanishing $\vec{t}$ can be achieved by a ring of magnetic moments. In the presence of such an order, antisymmetric ME effects are allowed, i.e. $\vec{P}_{FE} \propto \vec{t} \times \vec{H}$ and $\vec{M} \propto \vec{t} \times \vec{E}$ [31, 256]. The field, which directly couples to a ferrotoroidal order, is an inhomogeneous magnetic field with a non-vanishing curl that may align with the ring of magnetic moments. Such a magnetic field, however, can only exist in the presence of electric currents. Crossed magnetic and electric fields are also able to pole the ferrotoroidal moments profiting from the non-diagonal terms in the magnetoelectric tensor [256].
Yamaguchi *et al.* use this approach to describe the linear off-diagonal magnetoelectric effect observed in $Ni_{0.42}Mn_{0.58}TiO_3$ [18]. They argue that for the case of zero-field cooling, the spins freeze completely randomly which cancels out the toroidization. However, by cooling the system under crossed magnetic and electric fields, the formation of a net toroidization would give rise to a gain in energy. This renders the system magnetoelectric, even in the lack of long-range magnetic order [18].
Recently, Chi *et al.* investigated the $Ni_xMn_{1-x}TiO_3$ system with $x = 0$, 0.33, 0.5 and 0.68 by neutron diffraction and pyroelectric measurements [257]. The authors find additional elements of the ME tensor for $x = 0.33$, which are excluded in $MnTiO_3$. Chi *et al.* relate this finding to the rotation of Mn moments. For increasing Ni concentration, the Mn moments rotate from $\vec{c}$ towards the *ab*-plane. While the AF-$Mn_{\parallel}$-order has $\bar{3}'$ symmetry, the rotation axis is lost in AF-$Mn_{\perp}$ and the magnetic space group reduces to $P\bar{1}'$ [257]. In this space group there are no restrictions for the ME tensor [227].

7.2. Magnetic properties of the spin-glass phase

The surprising finding of a linear magnetoelectric effect in the spin glass phase of $Ni_xMn_{1-x}TiO_3$ raises the question of the microscopic origin of the effect. The proposition of a ferrotoroidal spin arrangement induced by crossed magnetic and electric fields by Yamaguchi *et al.* can be verified by neutron diffrac-

tion. There are three reports about neutron studies of the spin glass phase in $Ni_{0.42}Mn_{0.58}TiO_3$ [230, 231, 236]. All of them were performed well before the discovery of the ME effect and focus primarily on the temperature dependence of specific magnetic reflections.
This section will focus on the magnetic properties of $Ni_{0.42}Mn_{0.58}TiO_3$ at low temperatures and in zero-field.

7.2.1. Sample characterization

A large single crystal of $Ni_{0.42}Mn_{0.58}TiO_3$ has been grown in a floating-zone furnace by A. A. Nugroho at the University of Cologne. The constant Ni concentration of $x = 0.42$ was verified using energy-dispersive X-ray spectroscopy.
The temperature dependence of the magnetization in the hexagonal plane along $[1, 1, 0]$ is shown in Fig. 7.4, carried out with a SQUID magnetometer. The curves were measured upon heating after cooling the sample in a magnetic field (FC), and in zero-field (ZFC). Both curves show an anomaly at about 10 K, indicating a magnetic phase transition. This temperature can be assigned to the spin glass transition of spins in the easy plane. At lower temperatures the curves split up in a typical manner of spin glass systems: in the absence of a magnetic field, the moments freeze-in randomly at the spin-glass transition, while during field-cooling,

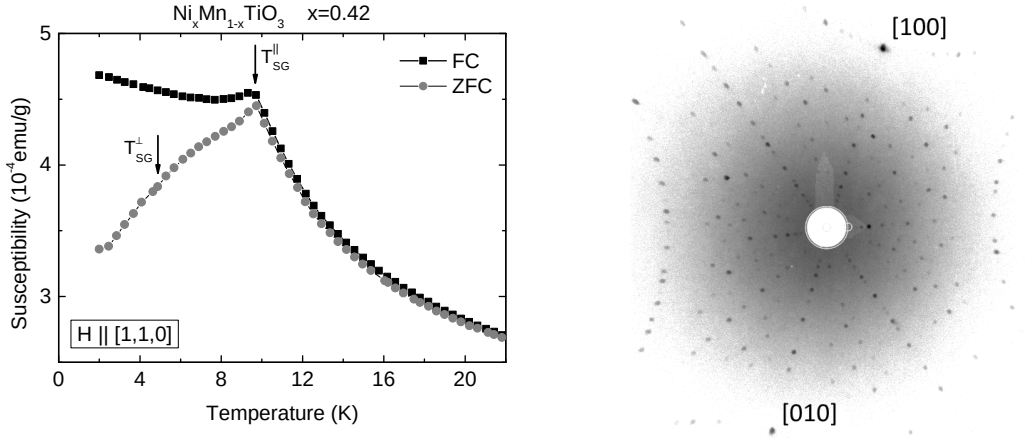

Figure 7.4.: (left) Temperature dependence of field-cooled (FC) and zero-field-cooled (ZFC) magnetic susceptibility of $Ni_{0.42}Mn_{0.58}TiO_3$ in a field of 0.5 mT applied parallel to $[1, 1, 0]$. The spin glass transitions parallel ($T^{\parallel}_{SG}$) and perpendicular ($T^{\perp}_{SG}$) to the easy-plane anisotropy are marked by black arrows. (right) X-ray Laue image of a single crystal of $Ni_{0.42}Mn_{0.58}TiO_3$ with the $[1, 1, 0]$ direction parallel to the beam.

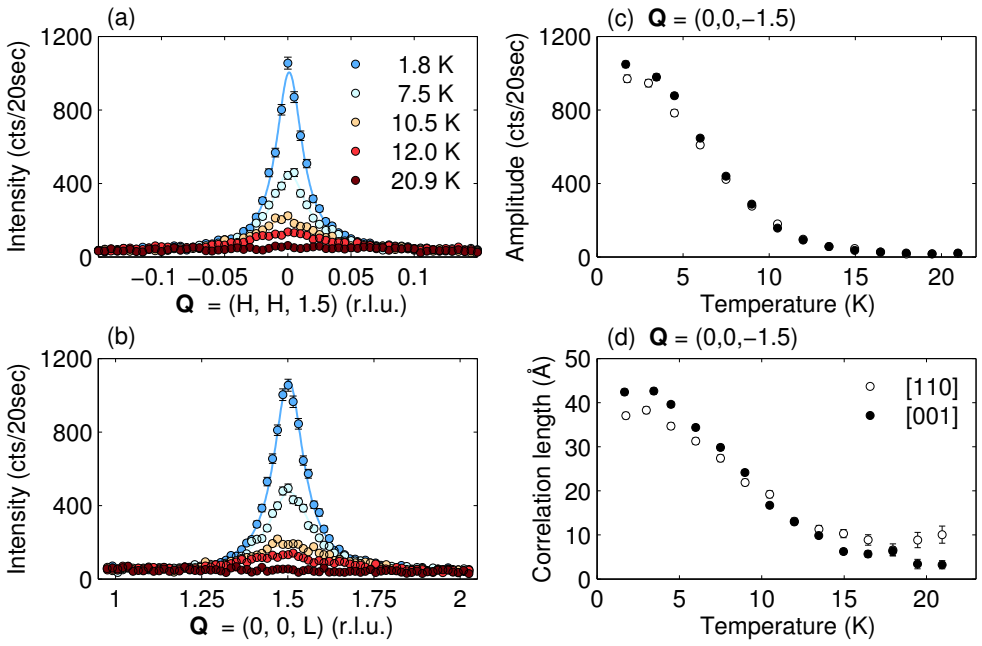

Figure 7.5.: Temperature dependence of neutron scattering at the position of the AFM-N order in $Ni_{0.42}Mn_{0.58}TiO_3$ at IN3. (a) and (b) show Q-scans in the hexagonal plane and perpendicular at selected temperatures along the Bragg peak position $\vec{Q} = (0,\ 0, -1.5)$. The amplitude (c) and correlation length (d) determined by fitting of a Lorentzian function are given on the right.

moments tilt along the direction of the applied magnetic field [218]. The second transition, where the magnetic components perpendicular to the planar anisotropy freeze-in, occurs at about 6 K and is visible as a kink in the ZFC magnetization. The magnetization of the sample perfectly agrees with the one reported in reference [18] and should thus exhibit the same spin glass phase.
The right site of Fig. 7.4 shows an image of nuclear Bragg reflections obtained with an X-ray Laue camera. The single crystal was aligned with $[1, 1, 0]$ being parallel to the beam. The image testifies the good sample quality and shows no defects. The Bragg reflections could be well described using the following crystal parameters and the space group $R\bar{3}$: $a = b = 5.09\,\text{Å}$, $c = 14.02\,\text{Å}$ and $\gamma = 120°$.

7.2.2. Temperature dependence of magnetic reflections

In order to get an overview of the temperature dependence of magnetic scattering in $Ni_{0.42}Mn_{0.58}TiO_3$, a single crystal was mounted in $[1, 1, 0]/[0, 0, 1]$ scattering geometry in a cryostat on the thermal neutron TAS instrument IN3 at the ILL.

The neutron energy was fixed to $E = 14.7\,\mathrm{meV}$ ($k = 2.66\,\mathrm{\AA}^{-1}$).
Figure 7.5(a-b) shows elastic Q-scans at the magnetic Bragg peak position $\vec{Q} = (0,\ 0,\ -1.5)$ of the AF-Ni phase along two directions for several temperatures above and below the SG transition. From the temperature dependence we can deduce that the signal is of purely magnetic origin as it vanishes at higher temperatures. Even at 1.8 K, the scattered intensity is weak in comparison to the scattering from nuclear Bragg peaks (cf. $I_{(0,0,3)}$ $5 \cdot 10^4$ cts/20sec). The onset of magnetic scattering at a temperature of $T_{N,Ni} \approx 10\,\mathrm{K}$ coincides with the kink of magnetization in Fig. 7.4(a). The increase of intensity is rather strong and the correlation length in the hexagonal plane and perpendicular to it spans up to 40 Å at 2 K. The AF-Mn order is thus almost long-ranged in $Ni_{0.42}Mn_{0.58}TiO_3$.
The scattered intensities at nuclear and magnetic Bragg reflections allows to estimate the ordered magnetic Ni-moment in the AF-Ni phase. The ratio of structure factors of nuclear and magnetic Bragg peak at both positions is $r_{Ni,calc} = I_{(0,0,3)}/I_{(0,0,1.5)} \approx 1.23$. The ratio was calculated assuming the structure factor of $Ni_{0.42}Mn_{0.58}TiO_3$ and a complete ordering of Ni moments with an effective magnetic moment of $\mu_{eff} = 2.25\,\mu_B$ determined by neutron diffraction [233]. To obtain a value for the corresponding experimental ratio, one has to take into account the different linewidth of nuclear and magnetic order. The AF-Ni reflections are enlarged along $[0, 0, L]$ by a factor of 1.5 in comparison to nuclear reflections. For simplicity, we assume that this factor is isotropic, i.e. that the correlation of the Ni-order is isotropic in the crystal. In general on a TAS instrument, the resolution is relaxed along the vertical direction, and we can neglect the enlargement factor along this direction. The magnetic intensity has thus to be multiplied with the square of the enlargement factor, accounting for the enlargement in the scattering plane. We determine an experimental ratio of nuclear and magnetic intensity as $r_{Ni,exp} = I_{(0,0,3)}/I_{(0,0,1.5)} \approx 20$. The intensity of scattered neutrons is proportional to the square of the structure factor, which itself is proportional to the magnetic moment of the scattering object:

$$I \propto F^2 \propto \mu_{eff}^2\ . \tag{7.2}$$

From this considerations, we can estimate that about 25 % of the Ni-moments in $Ni_{0.42}Mn_{0.58}TiO_3$ contribute to the magnetic scattering at 2 K.
Furthermore, the diffuse nature of magnetic scattering is visible by the broad shape of the reflections. A Lorentzian function was fitted to the data in order to determine the intensity and linewidth. Fig. 7.5(c) shows the temperature dependence of determined peak intensities along both directions. The resulting smooth increase of scattered intensity perfectly agrees with a previous neutron study at this Bragg position [231]. The linewidths were used to calculate the correlation length of the diffuse scattering, which is shown in Fig. 7.5(d). Above the transition, magnetic

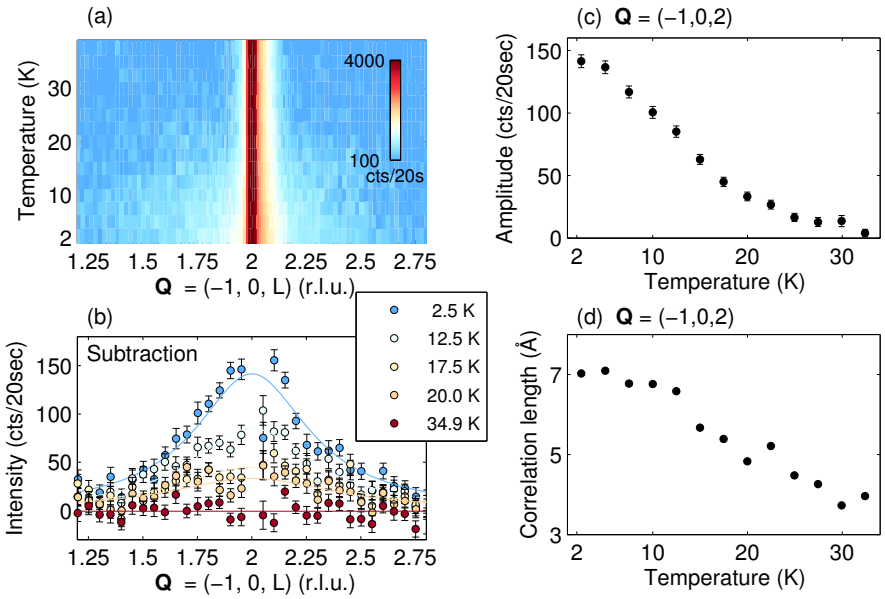

Figure 7.6.: Temperature dependence of neutron scattering at the position of the AFM-M order in $Ni_{0.42}Mn_{0.58}TiO_3$ at IN3. (a) Intensity mapping of scans along $[0, 0, L]$ at the Bragg peak position $\vec{Q} = (-1,\ 0,\ 2)$ in a logarithmic scale. (b) Scattered intensities determined by subtraction of the high temperature curve at 37 K arising from magnetic order. A Lorentzian function was fitted to the scans to extract the amplitude (c) and the correlation length (d).

correlations primarily exist in the hexagonal plane, while below the SG transition the correlations are similar along and perpendicular to the hexagonal plane.
Let us turn to Bragg positions of the AF-$Mn_{\parallel}$ and AF-$Mn_{\perp}$ structure. The difference of both $MnTiO_3$-type structures is the orientation of magnetic moments relative to the hexagonal axis. The precise orientation of moments was investigated using spherical neutron polarization analysis and will be discussed in Section 7.3. Both structures have zero propagation vector and the magnetic reflections overlap with the reflections from the crystal structure [233].
Figure 7.6(a) shows a logarithmic intensity mapping of Q-scans along the Bragg position $\vec{Q} = (-1,\ 0,\ 2)$. The Bragg peak signal is dominated by temperature-independent nuclear scattering. The temperature-dependent magnetic scattering is visible as diffuse scattering around the peak position. In order to study the evolution of magnetic scattering with temperature, the intensity from the high-temperature scan at $T = 38$ K was subtracted from intensities at lower temperatures. Fig. 7.6(b) shows the resulting curves, which can be well described using a Lorentzian function. Both temperature dependencies, of the scattered intensity and the correlation length, differ from the behaviour of the AF-Ni reflection, shown in Figures. 7.6(c-d). While significant magnetic intensity persists already at 20 K, well above the SG

transition temperature, the correlation length of the AF-$Mn_{\parallel}$ phase only spans over a limited range along $\vec{c}$. The reduced correlation length of Mn moments may arise due to the perturbation by the single-ion-anisotropy of Ni moments which rotates the orientation of Mn moments from $\vec{c}$ into the *ab*-plane.
Again, it is possible to estimate the ordered magnetic moment by a comparison of experimental and calculated intensities. For this, we assume a complete ordering of Mn moments in $Ni_{0.42}Mn_{0.58}TiO_3$ with an effective magnetic moment of $\mu_{eff} = 4.55\,\mu_B$ determined by neutron diffraction [233]. The AF-Mn-type reflections are significantly broadened, resulting in an enlargement factor of 9.2 relative to a nuclear reflection in the scattering plane. By applying Eq. 7.2 and the same assumptions as described before, we can estimate a contribution of about 25 % of Mn-moments to the broad scattering at the AF-$Mn_{\parallel}$ positions.
The presented data allow the conclusion that frozen fluctuations of both magnetic structures, $MnTiO_3$-type AF-$Mn_{\parallel}$ and $NiTiO_3$-type AF-Ni, coexist in the spin-glass phase of $Ni_{0.42}Mn_{0.58}TiO_3$. The magnetic reflections could be well described with a Lorentzian function suggesting a cluster glass type ordering of moments. While the AF-Ni-reflections are sharp, indicating an almost long-range order of Ni moments, the Mn-reflections are significantly broadened, indicating a short-range order of AF-Mn-type order. The simple comparison of nuclear and magnetic intensities yield a equal contribution of about 25 % of Ni and Mn moments to the magnetic intensities.

7.2.3. *Q*-dependence of magnetic reflections

A different experimental setup was used in order to investigate the Q-dependence of magnetic scattering in the spin-glass phase of $Ni_{0.42}Mn_{0.58}TiO_3$. A large single crystal ($30 \times 6 \times 6$ mm^3) was mounted in $[1,0,0]/[0,0,1]$ scattering geometry in a cryostat on the thermal neutron TAS instrument IN8 at the ILL. The incident neutrons were selected using the (1, 1, 1) Bragg reflection of a silicon monochromator. Instead of a single-detector, the multi-detector *FlatCone* was installed, which covers a wide scattering angle [84]. The neutron energy was set to $E = 18.6$ meV ($k = 3.0\,\mathrm{\AA}^{-1}$).
The instrumental procedure with the *FlatCone* analyzer persist of a rotation of the sample at a constant energy transfer. Such a scan creates a surface in $(\vec{Q}, \omega))$ space which is defined by the vectors spanning the scattering plane. At zero energy transfer one obtains an intensity map of elastic nuclear and magnetic scattering. For a better comparison with the comprehensive experimental data, we calculated the structure factors in $Ni_{0.42}Mn_{0.58}TiO_3$ arising from the nuclear structure, and the magnetic phases AF-$Mn_{\parallel}$, AF-$Mn_{\perp}$ and AF-Ni. The magnetic intensities were

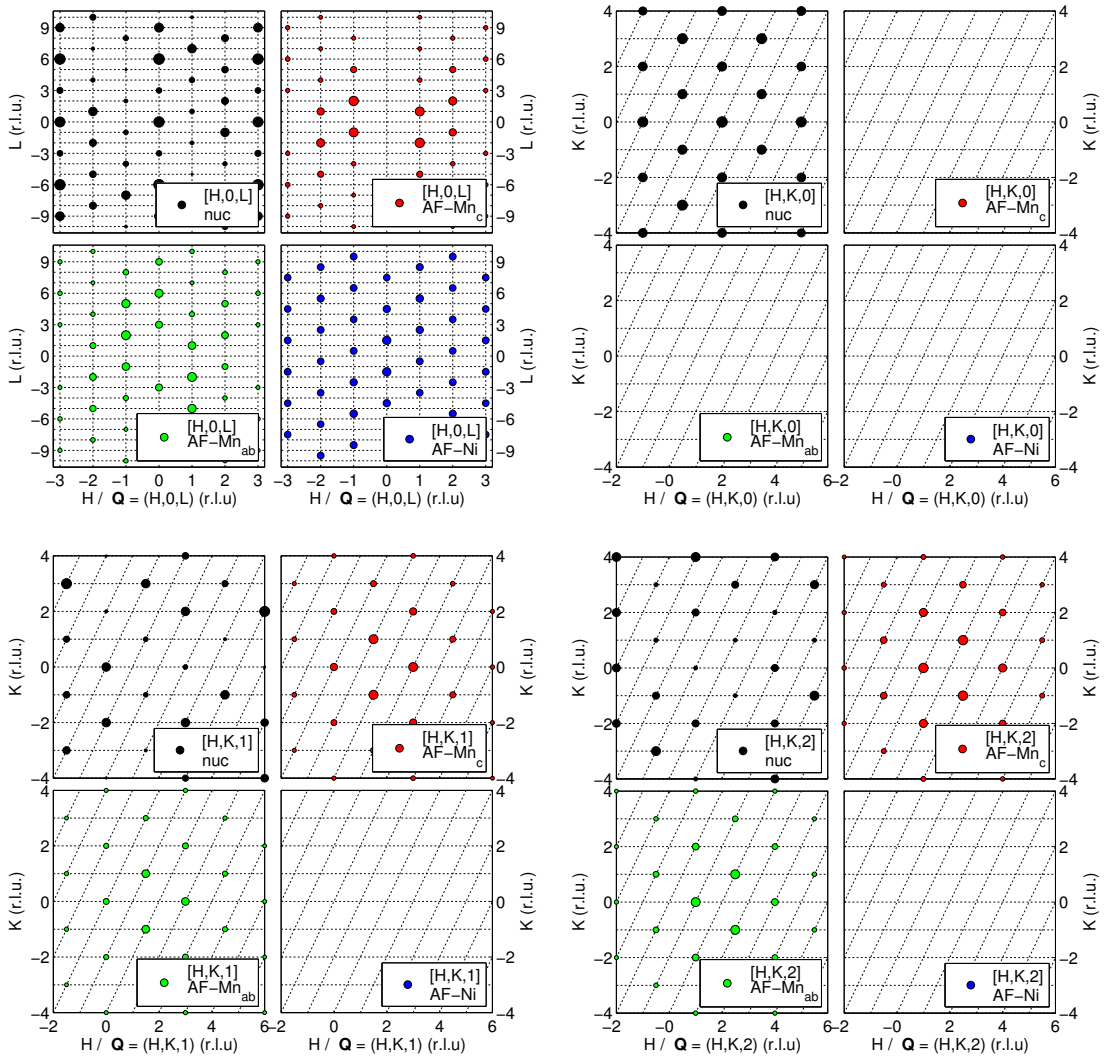

Figure 7.7.: Calculated intensities neutron scattering in $Ni_{0.42}Mn_{0.58}TiO_3$ in several scattering planes. The structure factor was calculated for the nuclear structure (nuc) and the magnetic phases AF-$Mn_{\parallel}$, AF-$Mn_{\perp}$ and AF-Ni. The reflection condition for the nuclear $R\bar{3}$ structure is $-h+k+l=3n$. The size of the dots corresponds to the logarithmic value of the structure factor within one scattering map. A different intensity scale was used for each map.

calculated assuming a equal distribution of antiferromagnetic domains. The logarithmic peak intensities are shown in Figure 7.7 for the scattering planes $[H, 0, L]$, $[H, K, 0]$, $[H, K, 1]$ and $[H, K, 2]$. Nuclear Bragg reflections obey the reflection condition for the space group $R\bar{3}$: $\vec{Q}_{nuc} = (h,\ k,\ l)$ with $-h + k + l = 3n$ [220]. This condition is modified for the different magnetic structure structures. In the AF-$Mn_{\parallel}$-phase, the moments are parallel $\vec{c}$ and scattering at Bragg positions $\vec{Q} = (0,\ 0,\ L)$ is excluded due to the condition for magnetic scattering. In addition, the structure factors sums up to zero at $\vec{Q} = (H,\ K,\ 0)$ for the G-type magnetic structures AF-$Mn_{\parallel}$ and AF-$Mn_{\perp}$. Magnetic scattering of the AF-Ni-phase is only visible at half-integer L, due to the finite propagation vector of the structure along the c-axis.

Figures 7.8(a-b) show the intensity mapping of neutron scattering in the $[H, 0, L]$ plane at 30 K and below the spin-glass transition at 2 K. The experimental data (black frame) was symmetrized by a two-fold rotation. The same logarithmic scale was used for both maps. Nuclear reflections are found at the expected positions and the extinction rules are preserved, indicating a monodomain crystal structure. Remarkable is the enhanced intensity along the hexagonal axis $\vec{c}$ at integer h. The diffuse scattering along $\vec{c}$ has also been reported for $Ni_xMn_{1-x}TiO_3$ with $x = 0$ and 0.33, in a diffuse neutron scattering study [257]. They may arise due to partial disorder of M^{2+} and Ti^{4+}, resulting in stacking faults [233]. Another remarkable observation is the existence of super-structure reflections at $\vec{Q} = (\pm 1.5,\ 0, \pm 3)$, which could indicate an ordering of Mn and Ni ions. These super-structure reflections have also been found in X-ray diffraction at half-integer h [258].

The difference in the scattering maps at both temperatures can be attributed to magnetic scattering from the spin-glass phase. The subtraction $I_{2K} - I_{30K}$ is shown in Fig. 7.8(c) in a linear color scale. Magnetic reflections are visible at the positions of the nuclear reflections, arising from the AF-$Mn_{\parallel}$ order, and at positions indicated by the propagation vector $\vec{k} = (0,\ 0,\ 0.5)$, arising from the AF-Ni order. Dashed lines indicate cuts through the 2D-data along $[H, 0, H]$ and $[0, 0, L]$ which are shown in Fig. 7.8(d).

The sample was reorientated in order to access the scattering in the hexagonal ab-plane. Figures 7.9(a-b) show the intensity mapping of neutron scattering in this plane at 30 K and 2 K. The experimental data (black frame) was symmetrized by a two-fold rotation and the same logarithmic scale was used for both maps. Strong nuclear reflections are visible at positions corresponding to the $R\bar{3}$ space group.

The cut along the hexagonal plane at both investigated temperatures reveals an odd shape of nuclear reflections, that was not visible in the $[H, 0, L]$ diffraction maps. The intensity at the Bragg position is accompanied by smaller reflections at a larger scattering angle. From the experiment, we can deduce two informations for the nuclear satellites: their intensity does not change with temperature and they are only visible in the hexagonal plane. An ordering of Mn and Ni ions

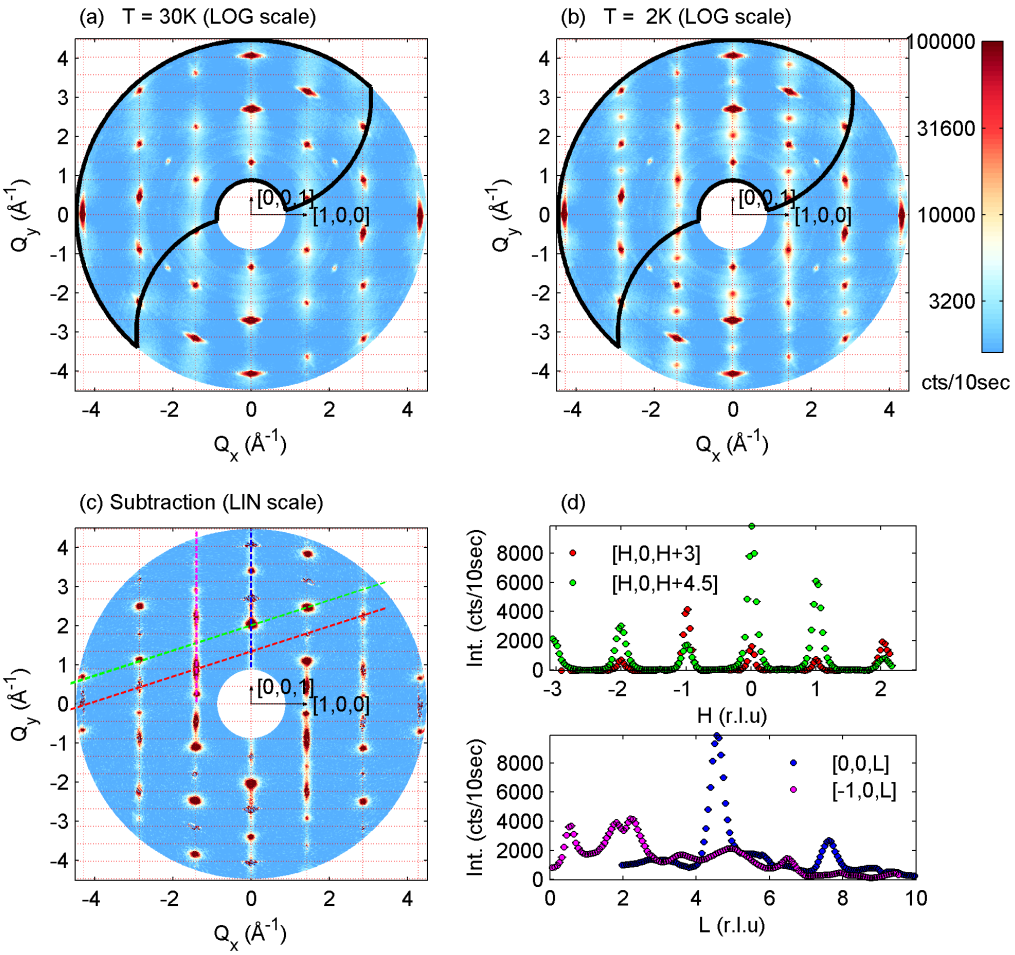

Figure 7.8.: Intensity mapping of neutron scattering in the $[H, 0, L]$ plane in $Ni_{0.42}Mn_{0.58}TiO_3$ at IN8. (a) and (b) show scattering maps at 30 K and 2 K in a logarithmic scale. The black curve highlights the measured data, the other half was symmetrized. (c) Subtraction of the high temperature data to show the magnetic scattering in a linear scale. Dashed lines indicate the directions of line cuts shown in (d).

in the hexagonal plane may lead to these features. Further investigations are necessary to determine the origin of this nuclear satellites. Due to the weakness of these anomalies and their nuclear nature, we will exclude them from the following analysis of the magnetic scattering.

The subtraction of both intensity maps reveals the contribution of magnetic scattering in Fig. 7.9(c). Cuts along different directions are indicated as dashed lines and are shown in Fig. 7.9(d). Weak scattering is present at the Bragg positions of the nuclear structure, even though one would not expect magnetic scattering

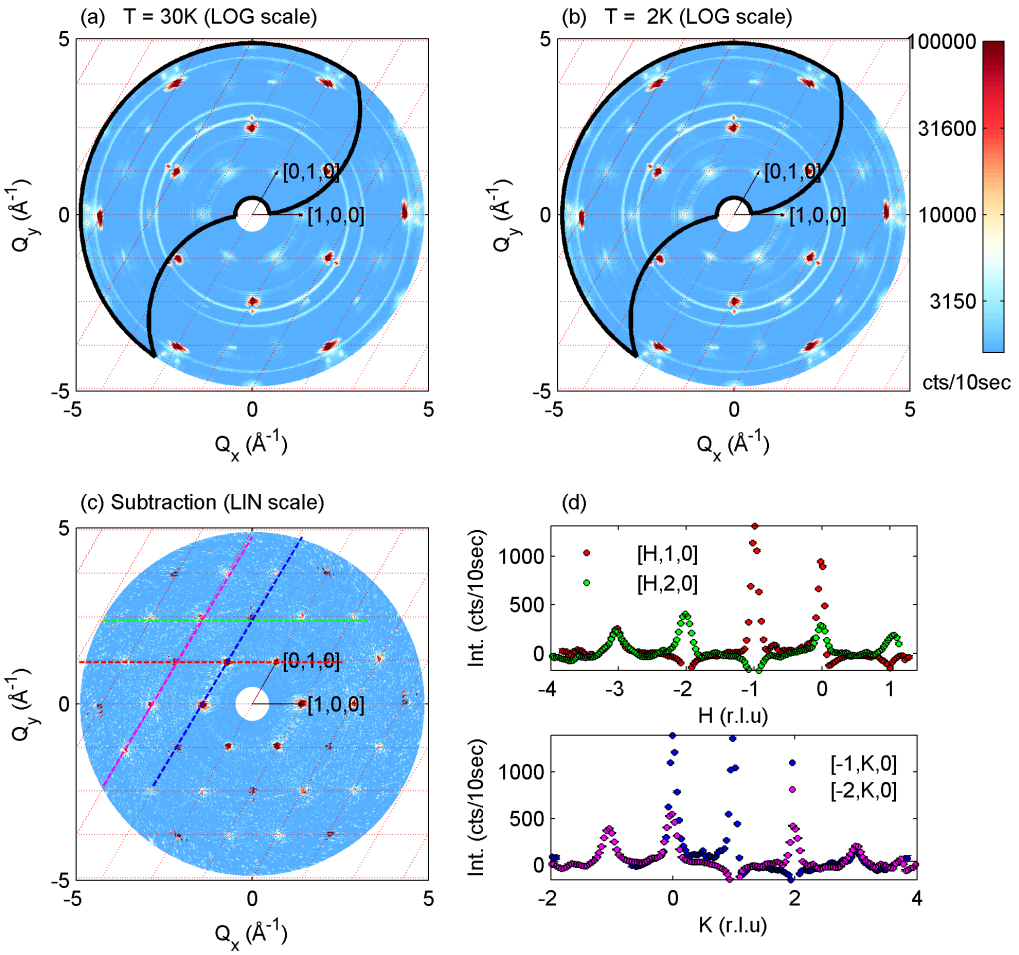

Figure 7.9.: Intensity mapping of neutron scattering in the $[H, K, 0]$ plane in $Ni_{0.42}Mn_{0.58}TiO_3$ at IN8. (a) and (b) show scattering maps at 30 K and 2 K in a logarithmic scale. The black curve highlights the measured data, the other half was symmetrized. (c) Subtraction of the high temperature data to show the magnetic scattering in a linear scale. Dashed lines indicate the directions of line cuts shown in (d).

in the $[H, K, 0]$ plane. Scattering from the AF-Ni phase is not visible due to the finite length of the propagation vector along $\vec{c}$. And the G-type orientation of moments in the AF-$Mn_{\parallel}$ structure leads to a cancellation of the magnetic structure factor for any Bragg position with $L = 0$. The presence of scattering at this positions is likely due to disorder along $\vec{c}$, which breaks the symmetry of the structure.

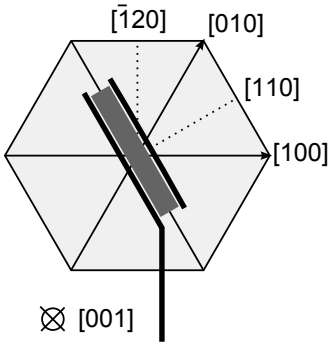

Figure 7.10: Sketch of the scattering geometry of $Ni_xMn_{1-x}TiO_3$ for neutron polarization analysis. The disc-shaped sample is placed between aluminum plates along $[1, 1, 0]$. An electric field can be applied along this direction. The sample is aligned in a way that $[1, 0, 0]$ and $[0, 0, 1]$ span the horizontal scattering plane, with $[\bar{1}, 2, 0]$ being vertical at all times. The hexagonal *ab*-plane, indicated as light gray plane, is perpendicular to the scattering plane.

7.3. Polarized neutron diffraction

Further insight into the alignment of the magnetic moments of Ni and Mn in the spin-glass phase of $Ni_{0.42}Mn_{0.58}TiO_3$ can be gained by looking at the polarization dependence of scattered intensity. Spherical neutron polarization analysis is a powerful tool, which is perfectly suited to determine the orientation of magnetic moments in a crystal [102].
A single crystal of $Ni_{0.42}Mn_{0.58}TiO_3$ was mounted in a cryostat at the cold neutron TAS instrument IN14 at the ILL. The instrument was equipped with the *Cryopad-III*, a zero-field polarimeter which enables to independently choose the orientation of incident and scattered neutron spin [109]. The flat shaped crystal ($d = 2.5\,\mathrm{mm}$) was held between two aluminum plates in order to apply a homogeneous electric field along the $[1, 1, 0]$ direction. Throughout the experiment, we worked worked with a fixed neutron energy of $E = 4.0\,\mathrm{meV}$ ($k = 1.55\,\mathrm{\AA}^{-1}$) and a beryllium filter on $\vec{k}_f$ to suppress scattering from higher orders. The neutron beam was polarized by a supermirror bender and analyzed using the (1, 1, 1) reflection of a Heusler monochromator. The flipping ratio on a magnetic Bragg peak was almost 34, which corresponds to a neutron polarization approx. 94 %.
The geometry of the experiment is schematically shown in Fig. 7.10. The scattering plane is spanned by the directions $[1, 0, 0]$ and $[0, 0, 1]$ and the direction vertical to the plane is $[\bar{1}, 2, 0]$ in the hexagonal setting. The polarization directions always fulfill the conditions: $x \parallel \vec{Q}$, z vertical, $y \parallel z \times x$.
The first part of the experiment was done in zero-field, in order to determine the orientation of the magnetic moments in the frustrated spin-glass phase. The second part is dedicated to the influence of magnetic and electric fields on the magnetic structure.

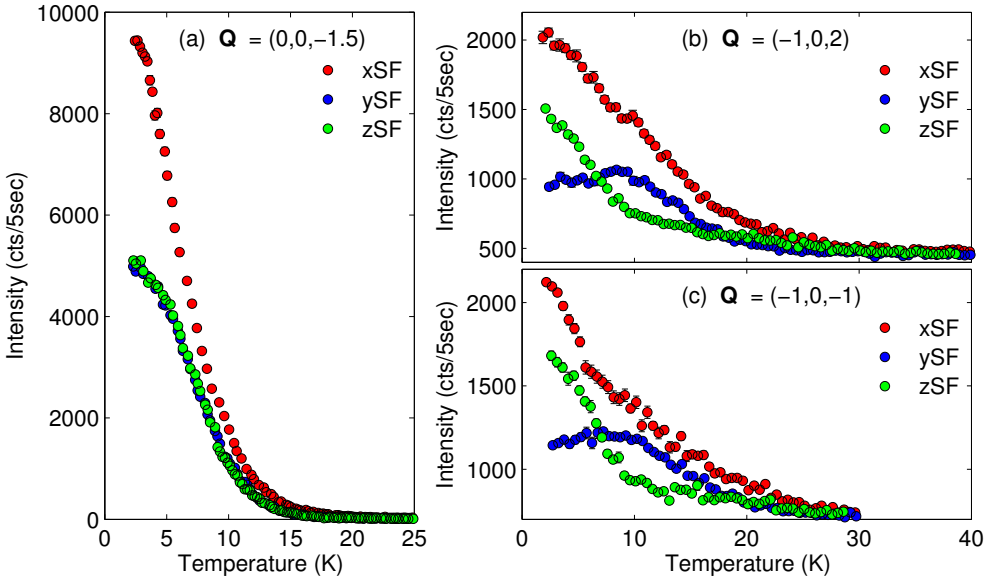

Figure 7.11.: Polarization analysis of temperature dependent magnetic scattering in $Ni_{0.42}Mn_{0.58}TiO_3$ at IN14. The scattered spin-flip intensity along the polarization axes x, y and z are shown at the Bragg positions (a) $\vec{Q}_{AF-Ni} = (0,\ 0, -1.5)$, (b) $\vec{Q}_{AF-Mn} = (-1,\ 0,\ 2)$ and (c) $\vec{Q}_{AF-Mn} = (-1,\ 0, -1)$. The orientation is chosen so that x is aligned parallel $\vec{Q}$, z is parallel $[1, 2, 0]$ and y is perpendicular to x and z.

7.3.1. Temperature dependence and polarization of ordered magnetic moments

In agreement with the experimental results from the previous section, we find diffuse magnetic signals at low temperatures at positions corresponding to both magnetic structures of the mother compounds $MnTiO_3$ (AF-$Mn_{\|}$) and $NiTiO_3$ (AF-Ni). Figure 7.11(a) shows the temperature dependence of spin-flip cross sections along the polarization directions at a Bragg position of the AF-Ni structure, $\vec{Q}_{AF-Ni} = (0,\ 0, -1.5)$. The scattered intensity increases when approaching the SG-transition at 10 K. The ratio of intensity of the polarization channels along y and z is constant with temperature. Table 7.1 summarizes the polarization directions at the investigated Q-positions. The equal distribution of intensity along y and z allows the assumption that the magnetic moments of the AF-Ni order lay in between those axis in the hexagonal plane.
The temperature dependence of the polarized intensities at the AF-Mn Bragg positions $\vec{Q} = (-1,\ 0,\ 2)$ and $\vec{Q} = (-1,\ 0, -1)$ are shown in Fig. 7.11(b-c). At both positions, the scattered intensity increases below 25 K, which has been observed before in the unpolarized neutron experiment. Unlike the case for the AF-Ni reflection, where the intensity vanishes at higher temperatures, we find strong scattering

$\vec{Q}$, x (r.l.u)	y (r.l.u)	z (r.l.u)
$(0,\ 0,\ 1.\bar{5})$	$(1,\ 0,\ 0)$	$(\bar{1},\ 2,\ 0)$
$(\bar{1},\ 0,\ 2)$	$(\bar{1},\ 0,\ \bar{5})$	$(\bar{1},\ 2,\ 0)$
$(\bar{1},\ 0,\ \bar{1})$	$(\bar{1},\ 0,\ 10)$	$(\bar{1},\ 2,\ 0)$

Table 7.1: Polarization directions in $Ni_{0.42}Mn_{0.58}TiO_3$ for specific Bragg positions at IN14.

even at 40 K. Spin-flip processes are purely magnetic and should thus unambiguously distinguish nuclear from magnetic scattering. Nevertheless, the incomplete polarization of neutrons leads to a mix of non-spin-flip and spin-flip processes, defined by the flipping ratio. With the given flipping ratio, 6 % of the neutrons are polarized in the opposite direction. The finite temperature-independent intensity at high temperatures can thus completely be attributed to scattering from the strong nuclear scattering at the same Bragg position.
At both positions, the ratio of scattering along y and z changes with temperature, indicating a rotation of magnetic moments in the sample. The directions of the polarization axes, given in Tab. 7.1, allow one to understand the process. At about 10 K, the scattering is mainly in the ySF channel, which is sensitive to moments perpendicular to $\vec{Q}$ and y. This implies that the moments are oriented in the hexagonal plane. At this temperature, the ordering of Ni-moments sets in, and their planar anisotropy seem to influence the alignment of Mn-moments. $Ni_{0.42}Mn_{0.58}TiO_3$ was discussed to show the behaviour of a XY spin-glass, in which moments parallel to the planar anisotropy freeze-in at $T_{SG}^{\parallel} = 12$ K [231]. At this temperature the Mn-ordering corresponds to a AF-$Mn_{\perp}$-type.
Below $T = 10$ K the polarization scheme changes drastically and scattering in the zSF channel dominates at 2 K. It can be explained by the ordering of moments primarily along $\vec{c}$, the moment direction of the AF-$Mn_{\parallel}$ structure. The increase of intensity perfectly coincides with the freeze-in temperature of moments perpendicular to the planar anisotropy at 6.0(10) K [231]. The scattered intensity in the ySF channel persists down to base temperature, which suggests either a coexistence of AF-$Mn_{\parallel}$ and AF-$Mn_{\perp}$ order, or a tilt of magnetic moments between $\vec{c}$ and the hexagonal plane.
The polarization analysis can be used to determine the different nuclear and magnetic components that contribute to the scattered intensity. Table 7.2 summarizes the obtained values at different AF-$Mn_{\parallel}$ and AF-Ni Bragg reflections at 2 K for the following components: nuclear scattering (NN^*), total magnetic scattering ($\vec{M}_{\perp} \cdot \vec{M}_{\perp}^*$), magnetic scattering along y and z (M_yM_y and M_zM_z) and the chiral magnetic term ($-i(\vec{M}_{\perp} \times \vec{M}_{\perp}^*)_x$). The terms were calculated from spin-flip and non-spin-flip cross sections measured at the corresponding Bragg peak positions (see Tab. 3.1 for their composition).
The experimental values can be compared to the values obtained by a structure fac-

Table 7.2.: Experimental nuclear and magnetic scattering components determined by neutron polarization analysis at different Bragg positions in $Ni_{0.42}Mn_{0.58}TiO_3$ at 2 K. The intensities were normalized to a monitor of 200 (cts/0.5 s).

$\vec{Q}$ (r.l.u.)	NN^*	$\vec{M}_\perp \cdot \vec{M}^*_\perp$	M_yM_y	M_zM_z	$-i(\vec{M}_\perp \times \vec{M}^*_\perp)_x$
$(0,\ 0,\ \bar{3})$	852(2)	2.0(6)	0.9(6)	1.1(6)	0.2(4)
$(\bar{1},\ 0,\ \bar{1})$	250(2)	5.6(5)	4.0(4)	1.6(4)	-0.6(4)
$(1,\ 0,\ \bar{2})$	287(2)	7.1(4)	5.1(4)	2.0(4)	-0.1(3)
$(0,\ 0,\ 1.\bar{5})$	0.13(40)	28.2(5)	14.5(6)	13.7(5)	-0.6(5)
$(1,\ 0,\ 2.5)$	1.4(3)	7.3(3)	2.0(3)	5.4(3)	-0.1(2)

tor calculation. The nuclear part was calculated assuming a random distribution of Ni and Mn ions, a perfect order of M^{2+} and Ti^{4+} sites and no atomic displacement factors. The magnetic part was calculated assuming a contribution of AF-$Mn_\parallel$-, AF-$Mn_\perp$- and AF-Ni-type ordering. The effective moment was calculated as:

$$\mu_{eff} = c_{\text{crystal}} \cdot c_{\text{magnetic}} \cdot \mu_{\text{total}} \ , \tag{7.3}$$

with the moment-concentration c_{crystal}, the ordering of moments c_{magnetic} and the effective moment of the fully ordered structure. The parameters were the following:

AF-$Mn_\parallel$: $c_{\text{crystal}} = 0.58$, $c_{\text{magnetic}} = 0.30$, $\mu_{Mn} = 4.55\,\mu_B$
moments parallel $\vec{c}$.

AF-$Mn_\perp$: $c_{\text{crystal}} = 0.58$, $c_{\text{magnetic}} = 0.15$, $\mu_{Mn} = 4.55\,\mu_B$
moments in *ab*-plane (equal distribution of 120° domains).

AF-Ni: $c_{\text{crystal}} = 0.42$, $c_{\text{magnetic}} = 0.25$, $\mu_{Ni} = 2.25\,\mu_B$
moments in *ab*-plane (equal distribution of 120° domains).

The calculated nuclear and magnetic components at the same Bragg peak positions as the experiment are summarized in Tab. 7.3. In Section 7.2.3, it was discussed that the magnetic reflections were significantly broadened, relative to the nuclear reflections, due to the short-range magnetic order. The experimental values in Tab. 7.2 were obtained by counting at the Bragg peak position. In order to be able to compare experimental values with the calculated structure factors, one has to correct for the broadening of the reflections. We use the same enlargement factors as described in Section 7.2.3, while assuming an isotropic broadening within the scattering plane and an neglectable vertical broadening, due to the relaxed

Table 7.3.: Calculated nuclear and magnetic scattering components at different Bragg positions in $Ni_{0.42}Mn_{0.58}TiO_3$. The intensities were normalized to the experimentally observed nuclear scattering intensity at $\vec{Q}_{AF-Mn} = (-1,\ 0,\ 2)$. The magnetic intensities were calculated assuming a superposition of AF-$Mn_{\parallel}$-, AF-$Mn_{\perp}$- and AF-Ni-type structures, as described in the text.

$\vec{Q}$ (r.l.u.)	NN^*	$\vec{M}_\perp \cdot \vec{M}_\perp^*$	M_yM_y	M_zM_z	$-i(\vec{M}_\perp \times \vec{M}_\perp^*)_x$
$(0,\ 0,\ \bar{3})$	1130.75	1.27	0.64	0.64	0.00
$(\bar{1},\ 0,\ \bar{1})$	604.56	6.87	5.33	1.53	0.00
$(1,\ 0,\ \bar{2})$	287.00	9.13	6.82	2.31	0.00
$(0,\ 0,\ \bar{1.5})$	0.00	25.47	12.74	12.74	0.00
$(1,\ 0,\ 2.5)$	0.00	9.23	2.53	6.70	0.00

instrumental resolution.
The calculated intensities were scaled to the experimental nuclear cross section at $\vec{Q} = (1,\ 0, -2)$. The calculated nuclear cross sections at $\vec{Q} = (0,\ 0, -3)$ and $\vec{Q} = (-1,\ 0, -1)$ overestimate the experimental values. Without further corrections, such as the nuclear displacement factors and a Lorentz-correction, such deviations are possible. Our qualitative analysis aims at the polarization dependence at specific Bragg positions, for with our model is sufficient.
The magnetic part can be relatively well described by the given model. The ratios between scattering along y and z are consistent, and both, experiment and calculation, find a vanishing chiral component. Deviations exist in the intensities of the strong nuclear reflections.
The scattering at the AF-Ni Bragg positions is purely magnetic. The finite experimental values for NN^* are due to statistical deviations. For the calculation of the AF-Ni-phase, we assumed an equal distribution of 120°-domains in the ab and a contribution of 25 % of Ni-moments in $Ni_{0.42}Mn_{0.58}TiO_3$ to the scattering. The absolute values, as well as the component separation along y and z, of the calculation nicely match the experimental values.
The contribution of magnetic scattering at the AF-Mn-type positions is more complex. The component separation suffers from the strong nuclear part, which inserts strong statistical errors for the magnetic components. In addition, the direction of magnetic moments is uncertain and is probably canted relative to the $\vec{c}$. The calculation at the nuclear Bragg positions was done assuming a superposition of AF-$Mn_{\parallel}$- AF-$Mn_{\perp}$-type ordering. The experimental data can be relatively well described assuming a contribution of 30 % of Mn-moments to the AF-$Mn_{\parallel}$ ordering and 15 % of Mn-moments to the AF-$Mn_{\perp}$ ordering. The values are given for Mn-moments in $Ni_{0.42}Mn_{0.58}TiO_3$. This would correspond to

a tilting of Mn-moments of $\alpha \approx 26°$ relative to the c-axis. Chi *et al.* observed an angle of $\alpha \approx 80°$ for a Ni concentration of $x = 0.33$, which was temperature dependent and could be significantly reduced in magnetic field applied along $\vec{c}$ [257].

7.3.2. Influence of magnetic and electric fields

After the discussion of the zero-field spin-glass phase, we can continue with the investigation of influences of crossed magnetic and electric fields on the alignments of magnetic moments in $Ni_{0.42}Mn_{0.58}TiO_3$. Yamaguchi *et al.* proposed the evolution of a toroidal moment which accounts for the observed magnetoelectric effect [18]. Induced toroidal moments modulate the zero-field alignment of magnetic moments which can be detected by spherical neutron polarization analysis. This technique has already been successfully applied to detect different antiferromagnetic domains in magnetoelectric [259] and ferrotoroidal compounds [260].
The *Cryopad* option at IN14 allows, in addition to the diagonal terms, the determination of off-diagonal terms of the polarization matrix, where incident and scattered neutron are polarized along different directions [108]. Taking into account the three polarization axes, there exists a total of 36 spin-flip and non-spin-flip cross-sections, cf. Table 3.1. Furthermore, this allows to separate nuclear-magnetic interference terms NM_i (with $i = y, z$). A net toroidal moment may arise due to a reorientation of magnetic moments or a structural displacement of magnetic ions (cf. Eq. 7.1). The first one can be detected even by linear polarization analysis. The latter one leads to a relative shift of nuclear and magnetic phases which can directly be measured by looking at term NM_i, requiring spherical neutron polarimetry [102].
The control of neutron polarization with *Cryopad* is done using a zero-field environment at the sample stage. This prohibits the use of external magnetic fields. It is nevertheless possible to cool the sample in magnetic and electric fields outside of the *Cryopad* and return the sample at constant temperature. Toroidal moments, if present, would freeze-in below the spin-glass transition and persist even in the absence of applied fields. The same scattering geometry was used as described in Fig. 7.10. An electric field of 200 to 600 $\mathrm{V\,mm^{-1}}$ was applied along $[1, 1, 0]$ and a magnetic field of 1 T was applied along vertical to the scattering plane along $[\bar{1}, 2, 0]$, creating an angle of 60° between the fields. Between each field setting, the sample was heated up to 30° in the paramagnetic phase.
The comparison of several AF-$Mn_{\parallel}$ and AF-Ni reflections revealed no significant change in the scattered magnetic intensities. Also, no additional magnetic reflections were observed. This is consistent with the measurement of the specific heat in applied magnetic fields of equal strength. No anomaly was observed in the

curves which lead Yamaguchi *et al.* to the conclusion that no long-range order is induced by the field [18].
Specific scattering components derived from the polarization analysis at different settings of the magnetic and electric field are summarized in Table 7.4. The corresponding cross sections were determined at the AF-Mn Bragg position $\vec{Q} = (-1,\ 0,\ 2)$ at 2 K. We start with the discussion of magnetic scattering along the polarization direction y and z. In an applied magnetic field, the scattering in M_z increases, which is the direction of the magnetic field. The magnetic moments seem to tilt along the direction of the field. This is equivalent to a poling of antiferromagnetic domains. The scattering in M_y increases in positive magnetic field, while it decreases in negative magnetic fields. The scattering in M_y and M_z seems to be unaffected by the electric field.
The nuclear-magnetic interference terms also show strong deviations by the applied fields. While both real terms are close to zero at all settings, the imaginary parts change drastically. $\mathrm{Im}M_y^*N$ and $\mathrm{Im}M_z^*N$ increase in positive magnetic fields and change their sign in negative magnetic fields. The electric field again appears to have no influence on the scattering components.
The same scattering components, that have been derived from experimental neutron polarization analysis, were calculated from the magnetic and nuclear structure factor of $Ni_{0.42}Mn_{0.58}TiO_3$. The results are given in the same Table 7.4, below the experimental values. The table reads as follows: the first three rows were calculated assuming the AF-$Mn_{\parallel}$-phase with an equal distribution of domains (top), and the positiv (middle) and negative (bottom) 180°-domains. The seven subsequent rows were calculated assuming the AF-$Mn_{\perp}$, which consists of 60°-domains. The first row was calculated assuming equal distribution of antiferromagnetic domains, while for the rows below the direction of the moments is given on the left. The simulated intensities were normalized to $M_yM_y^*$ of AF-$Mn_{\parallel}$. The different correlation length of the magnetic and nuclear reflections has not been taken into account. It is thus not possible to compare the absolute values of the simulated and experimental intensities. Nevertheless, the comparison of relative changes of intensities due to the influence of the applied field can be analyzed.
The nuclear-magnetic interaction terms allow to investigate antiferromagnetic domains. For example, the AF-$Mn_{\parallel}$-phase consists of two 180° domains. The reversal of the magnetic moments is visible in this terms, as shows the comparison of the imaginary part $\mathrm{Im}M_y^*N$ for both domains in Table 7.4. The AF-$Mn_{\perp}$ phase contains six equivalent antiferromagnetic domains. These domains show a finite M_y and M_z component and are thus distinguishable via $\mathrm{Im}M_y^*N$ and $\mathrm{Im}M_z^*N$.
First, we compare the zero-field experimental data in Table 7.4 with the simulated values. The finite intensities in $M_yM_y^*$ and $M_zM_z^*$ yield a tilt of magnetic moments away from the c-axis, which can be described by a superposition of AF-$Mn_{\parallel}$- and AF-$Mn_{\perp}$-type order. For an equal distribution of antiferromagnetic domains, the

Table 7.4.: Magnetic and electric-field dependence of magnetic scattering components in $Ni_{0.42}Mn_{0.58}TiO_3$, determined at $\vec{Q}_{AF-Mn} = (-1,\ 0,\ 2)$ at 2 K. The intensities were normalized to a monitor of 200 (cts/0.5 s). The electric field was applied along $[1, 1, 0]$ and the magnetic field applied along $[\bar{1}, 2, 0]$. Below, simulated intensities are shown for different domain constellations of the AF-$Mn_{\parallel}$ and AF-$Mn_{\perp}$ order. The simulated intensities were normalized to $M_yM_y^*$ of AF-$Mn_{\parallel}$.

B (T)	E (kV)	$M_yM_y^*$	$M_zM_z^*$	ReM_yN	ReM_z^*N	ImM_y^*N	ImM_z^*N
0	0	5.1(4)	2.0(4)	-0.3(5)	0.5(6)	0.7(7)	8.2(7)
+1	-1.5	8.1(7)	30.3(6)	-1.4(7)	-0.5(7)	8.2(6)	74.9(7)
+1	+0.9	8.0(6)	16.2(5)	0.5(7)	0.3(5)	6.6(7)	54.4(6)
-1	-1.2	0.8(4)	12.1(4)	-0.2(4)	-0.6(4)	-2.6(4)	-38.8(5)
-1	+0.5	-0.9(7)	18.9(6)	-0.3(7)	0.2(7)	-6.2(7)	-65.1(9)

Simulation	$M_yM_y^*$	$M_zM_z^*$	ReM_y^*N	ReM_z^*N	ImM_y^*N	ImM_z^*N
AF-$Mn_{\parallel}$	1.00	0.00	0.00	0.00	0.00	0.00
$[0, 0, 1]$	1.00	0.00	0.00	0.00	-0.50	0.00
$[0, 0, \bar{1}]$	1.00	0.00	0.00	0.00	0.50	0.00
AF-$Mn_{\perp}$	0.19	0.70	0.00	0.00	0.00	0.00
$[1, 0, 0]$	0.39	0.00	0.00	0.00	-0.31	0.00
$[\bar{1}, 0, 0]$	0.10	1.04	0.00	0.00	0.15	0.51
$[0, \bar{1}, 0]$	0.10	1.04	0.00	0.00	0.15	0.51
$[1, 0, \bar{1}]$	0.39	0.00	0.00	0.00	0.31	0.00
$[0, 1, 0]$	0.10	1.04	0.00	0.00	-0.15	-0.51
$[\bar{1}, 0, 1]$	0.10	1.04	0.00	0.00	-0.15	-0.51

NM interaction terms should all cancel to zero. The fact, that the interaction term $\mathrm{Im}M_z^*N$ shows a significant intensity indicates a preferred direction of domains in the crystal, which breaks the symmetry.
In all field settings, the experimental values for $\mathrm{Re}M_y^*N$ and $\mathrm{Re}M_z^*N$ are close to zero within the error bars. This is in agreement to the simulated values, which are zero for all domain configurations. The imaginary parts $\mathrm{Im}M_y^*N$ and $\mathrm{Im}M_z^*N$ are strongly enhanced when the field are applied. The value of $\mathrm{Im}M_z^*N$ even exceeds the values $M_yM_y^*$ and $M_zM_z^*$. This enhancement is probably due to the strong nuclear part N, which enters the interaction NM. The term $\mathrm{Im}M_z^*N$ is only present for domains of the AF-$\mathrm{Mn}_\perp$-order. This shows that the applied magnetic field further rotates the moment in the *ab*-plane, with is also visible in an enhancement of M_z. Finally, we can analyze the change of sign of the experimental interaction terms. In an positive magnetic field, $\mathrm{Im}M_y^*N$ and $\mathrm{Im}M_z^*N$ are positive. A negative magnetic field switches the sign of both terms. This behaviour is also shown by the simulated intensities of the AF-$\mathrm{Mn}_\perp$-domains $[0, \bar{1}, 0]$ and $[0, 1, 0]$. The comparison of experimental and simulated nuclear-magnetic interaction terms thus indicate, that it was possible to switch antiferromagnetic domains in the spin-glass phase of $\mathrm{Ni_{0.42}Mn_{0.58}TiO_3}$. The analysis at the AF-Mn Bragg positions $\vec{Q} = (-1,\ 0, -1)$ and $\vec{Q}_{AF-Mn} = (0,\ 0, -3)$ is shown in appendix C.
Yamaguchi *et al.* observed finite ME tensor elements $\alpha_{xy} = -\alpha_{yx}$. By the application of crossed magnetic and electric field, one would expect a sign change by the reversal of either one of the fields. Our experimental data report a switching of domains by the reversal of the magnetic field. The sign of the electric field, nevertheless, seems not to affect the domain population. This might be related to a memory effect. For example in $\mathrm{MnWO_4}$ it has been observed, that the first field-cooling set a preferred direction for the magnetic moments [50]. This preferred direction was only removed after heating up to room temperature. In the presented experiment, the crystal was heated to 30 K between the field-cooling.
The presented results from the neutron polarization analysis may indicate that the short range AF-Mn order alone accounts for the ME effect in $\mathrm{Ni_{0.42}Mn_{0.58}TiO_3}$. The AF-Mn structure breaks the inversion symmetry and allows for the linear magneto-electric effect [257]. The magnetoelectric tensor of $\mathrm{MnTiO_3}$ has non-zero diagonal and off-diagonal terms [249]. The terms α_{xx} and α_{xy} were also measured by Yamaguchi *et al.* in $\mathrm{Ni}_x\mathrm{Mn}_{1-x}\mathrm{TiO_3}$ at $x = 0.38$. Nevertheless, the diagonal term α_{xx} vanished at $x = 0.40$ and above, while the off-diagonal term persisted up to $x = 0.42$. The explanation for this behaviour cannot be deduced from the given dataset.

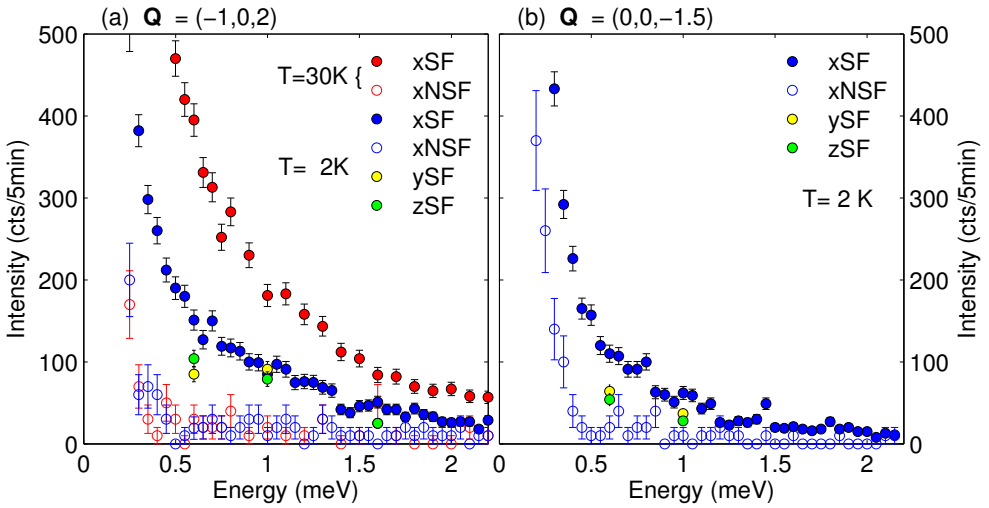

Figure 7.12.: Polarization analysis of zone center excitations in $Ni_{0.42}Mn_{0.58}TiO_3$ at IN14. (a) Excitation spectrum at $\vec{Q}_{AF-Mn} = (-1,\ 0,\ 2)$ at 30 K and 2 K. (b) Excitation spectrum at $\vec{Q}_{AF-Ni} = (0,\ 0, -1.5)$ at 2 K. For each spectrum the scattering for spin-flip (filled circles) and non spin-flip (open circles) processes along the polarization axis x are shown. At 2 K, the intensities in the spin-flip channels along y and z are given for specific energies.

7.4. Magnetic excitations in the spin-glass phase

The coexistence of AF-$Mn_{\parallel}$ and AF-Ni type magnetic order in $Ni_{0.42}Mn_{0.58}TiO_3$ raises the question of the interaction of magnetic moments in the spin-glass phase. The diffuse scattering maps shown in Section 7.2.3 indicate short-range order in the hexagonal plane which is only weakly coupled along $\vec{c}$. The study of the excitation spectrum allows one to investigate determine the coupling constants and anisotropies from the spin-wave dispersion.
In the following we will discuss the origin of the zone center excitations and present a complete picture of their Q-dependence. Finally, the dispersion of modes is compared to the excitation spectrum of pure $MnTiO_3$.

7.4.1. Zone center excitations

Subsequently to the polarization analysis of elastic scattering, we investigated the polarization analysis of zone center excitations at AF-$Mn_{\parallel}$ and AF-Ni Bragg reflections. A single crystal of $Ni_{0.42}Mn_{0.58}TiO_3$ was mounted in [100/[001] scattering geometry on IN14 with *Cryopad*, as described in Section 7.3. We worked with a

fixed final neutron energy of $E_f = 4.0\,\mathrm{meV}$ ($k_f = 1.55\,\mathrm{\AA}^{-1}$). An energy resolution of $\Delta E \approx 0.18\,\mathrm{meV}$ was determined on the elastic line.
The polarization analysis of the zone center spectra at $\vec{Q}_{AF-Mn} = (-1,\ 0,\ 2)$ is shown in Fig. 7.12(a) for the spin-flip and non-spin-flip channels along x. The spectrum is rather broad at the superposed nuclear and magnetic reflection. The polarization analysis verifies the origin of the inelastic signal to be purely magnetic. In addition, the full xyz polarization analysis at specific energies enables to state, that the magnetic spectra is nearly isotropic.
The energy scan at $\vec{Q}_{AF-Ni} = (0,\ 0, -1.5)$ reveals a similar picture, cf. Fig. 7.12(b). The intensity shows the same energy dependence as at the AF-$Mn_{\parallel}$ zone center and purely arises from magnetic excitations. The similarity of the data indicates once more a weak coupling between hexagonal planes. A differentiation between AF-$Mn_{\parallel}$ and AF-Ni modes is not possible. The broadening of the excitation spectrum is intrinsic to the system, which has been verified using $k_f = 1.2\,\mathrm{\AA}^{-1}$ with increased energy resolution.
The application of polarized neutrons verified the magnetic nature of zone center excitations and their isotropic character. This is a non-trivial information as the Bragg reflections of nuclear and AF-$Mn_{\parallel}$ structure overlap. Experiments using polarized neutrons suffer from the reduced neutron intensity, rendering especially inelastic scans very time-consuming. The following study can be done using unpolarized neutrons which has the advantage of an increased neutron flux and the possibility to cover a larger region in Q-space.

7.4.2. Q-dependence of magnetic excitations

The dispersion of the magnetic excitations in the spin-glass phase of $Ni_{0.42}Mn_{0.58}TiO_3$ was investigated at the cold neutron TAS instrument Panda at the FRM II. The large single crystal ($30 \times 6 \times 6\ \mathrm{mm}^3$), that had been used for previous experiments, was installed in the same [100]/[001] scattering geometry. The experiment was performed with a final neutron energy of $E_f = 4.0\,\mathrm{meV}$ ($k_f = 1.55\,\mathrm{\AA}^{-1}$), double focusing monochromator and analyzer and a Be-filter on $\vec{k}_f$. The energy resolution was comparable to the previous experiment, $\Delta E \approx 0.14\,\mathrm{meV}$.
Figure 7.13(a) shows zone center scans at several AF-$Mn_{\parallel}$ and AF-Ni Bragg peak positions at 2 K. The data strengthens the assumption that the inter-plane interaction is weak, as they seem to differ only in scattered intensity modulated by the magnetic form factor.
A different situation is visible within the hexagonal plane. Figure 7.13(b) shows scans along Q_H at a different energy transfer around $\vec{Q}_{AF-Mn} = (-1,\ 0, -2)$. Above 4 meV the peak at the center splits up, showing a dispersion-like be-

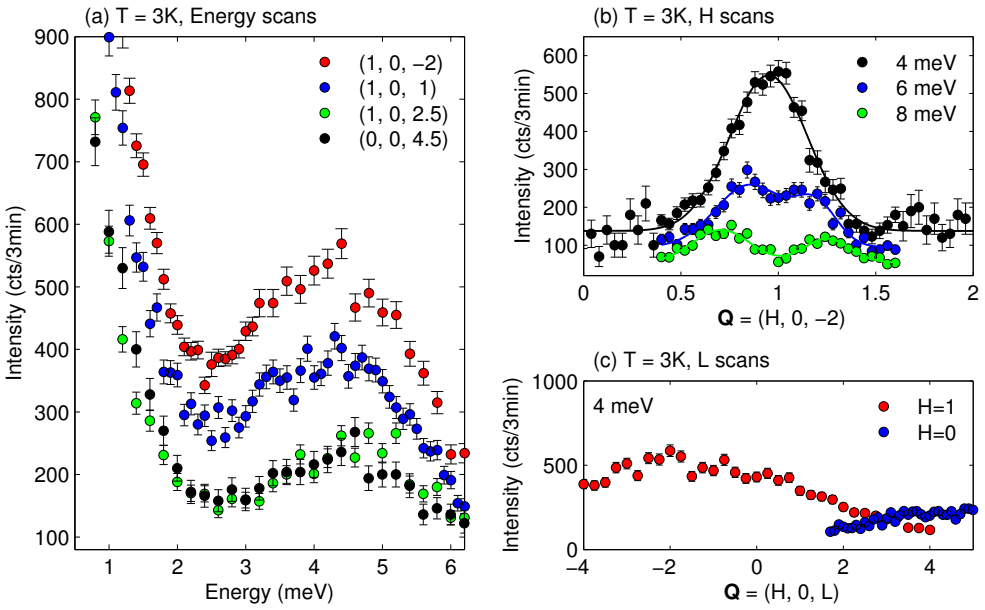

Figure 7.13.: Q-dependence of magnetic excitations in $Ni_{0.42}Mn_{0.58}TiO_3$ at 3 K indicating correlations in the hexagonal plane: (a) Energy scans at several AFM-M and AFM-N zone center positions, (b) Constant Q-scans at the Bragg peak position $\vec{Q}_{AF-Mn} = (-1,\ 0, -2)$, (c) extended Q-scans perpendicular to the hexagonal plane at 4 meV, measured at PANDA.

haviour. The observation of collective magnetic excitations in the spin-glass phase of $Ni_{0.42}Mn_{0.58}TiO_3$ is quite remarkable. Elastic diffraction studies have obtained an order of approximately 25 to 45 % of magnetic moments and the correlation length only spans over some 10 Å (cf. Section 7.2).
Similar scans along Q_L do not show any evidence of a dispersion. Figure 7.13(c) shows two of such scans at 4 meV. The scattered intensity only diminishes in accordance to the magnetic form factor showing no correlation along $\vec{c}$.
The dispersion-like feature in $Ni_{0.42}Mn_{0.58}TiO_3$ turned out to exceed the maximum energy transfer on instruments with cold neutrons. A subsequent experiment was performed at the thermal neutron TAS instrument IN8 at the ILL, in order to access the whole energy range of the dispersion. The instrument was equipped with the *FlatCone* multi-detector, which covers a large area in Q-space. The same large crystal of the previous experiment was mounted in two different scattering geometries, [100]/[001] and [100]/[010], in order to obtain a complete picture of the excitation spectrum in the spin-glass phase of $Ni_{0.42}Mn_{0.58}TiO_3$. The final energy of the neutrons was $E_f = 18.6$ meV ($k_f = 3.0$ Å^{-1}) and the energy resolution can be estimated to be $\Delta E \approx 0.8$ meV.
Experiments with *FlatCone* are generally conducted by performing sample rota-

tions at a constant energy transfer at two or more positions of the multi-detector. The resulting data forms a concentric surface at constant energy in (Q, ω)-space. Figure 7.14 shows a collection of these maps obtained along $[H, 0, L]$ at 2 K ranging from 2 to 12 meV (see Fig. 7.8 for the corresponding elastic map). Black frames indicate the original data which was symmetrized by a two-fold rotation to fill the map. All maps were produced using the same linear color scale and can directly be compared. The maps demonstrate the absence of dispersion along Q_L and thus confirm the assumption provided by previous experiments. Modulation of scattered intensity along $\vec{c}$ only arises from a combination of magnetic structure factor and the magnetic form factor.
The regions of strong intensity split up above 6 meV, showing a dispersion in the hexagonal plane. The dispersion extends up to 12 meV. Additional maps at higher energies have been collected to verify the absence of inelastic scattering. Sharp spots, which are present in all maps, can be attributed to spurious effects from strong nuclear Bragg peak scattering.
The excitation spectrum inside the hexagonal plane $[H, K, 0]$ is presented in Figure 7.15 (see Fig. 7.9 for the corresponding elastic map). At low energies the scattered intensity is located at lattice positions indicated with $(h,\ k,\ 0)$, $h+k = 2n$. Towards higher energies the modes disperse concentrically and before they disappear above 12 meV.
At this point it should be mentioned again that this system does not exhibit a completely ordered magnetic structure at low temperatures. Instead the magnetic moments freeze-in in a spin-glass manner with short-ranged regions of AF-$Mn_{\parallel}$ and AF-Ni type order (cf. Section 7.2).
The excitation spectrum seems to be dominated by the AF-Mn order. This can be understood by a comparison of the ordered magnetic moment of Mn and Ni ions in $Ni_{0.42}Mn_{0.58}TiO_3$. In Section 7.3.1 we estimated an ordering of 25 % of Ni moments and 45 % of Mn moments. In addition, we have to take into account the maximum effective moment of Ni and Mn as determined by neutron diffraction [233], $\mu_{eff,NiTiO3} = 2.25\mu_B$ and $\mu_{eff,MnTiO3} = 4.55\mu_B$. By using Equation 7.3, we can derive the ratio as follows:

$$\frac{\mu_{eff,Ni}}{\mu_{eff,Mn}} = \frac{0.42}{0.58} \cdot \frac{0.25}{0.45} \cdot \frac{2.25\mu_B}{4.55\mu_B} \approx 0.20 \ . \tag{7.4}$$

The intensity of magnetic neutron scattering is proportional to the square of the ordered magnetic moment, $I \propto M_{\perp}^2$, yielding a ratio of intensity of $I_{Ni}/I_{Mn} \approx 0.04$. This comparison explains that the inelastic signal is dominated by the AF-Mn order from the Mn moments in $Ni_{0.42}Mn_{0.58}TiO_3$.
Intensity maps in the $[H, K, 1]$ plane and the temperature dependence of inelastic neutron scattering maps in the $[H, K, 0]$ plane are presented in the appendix C.2.

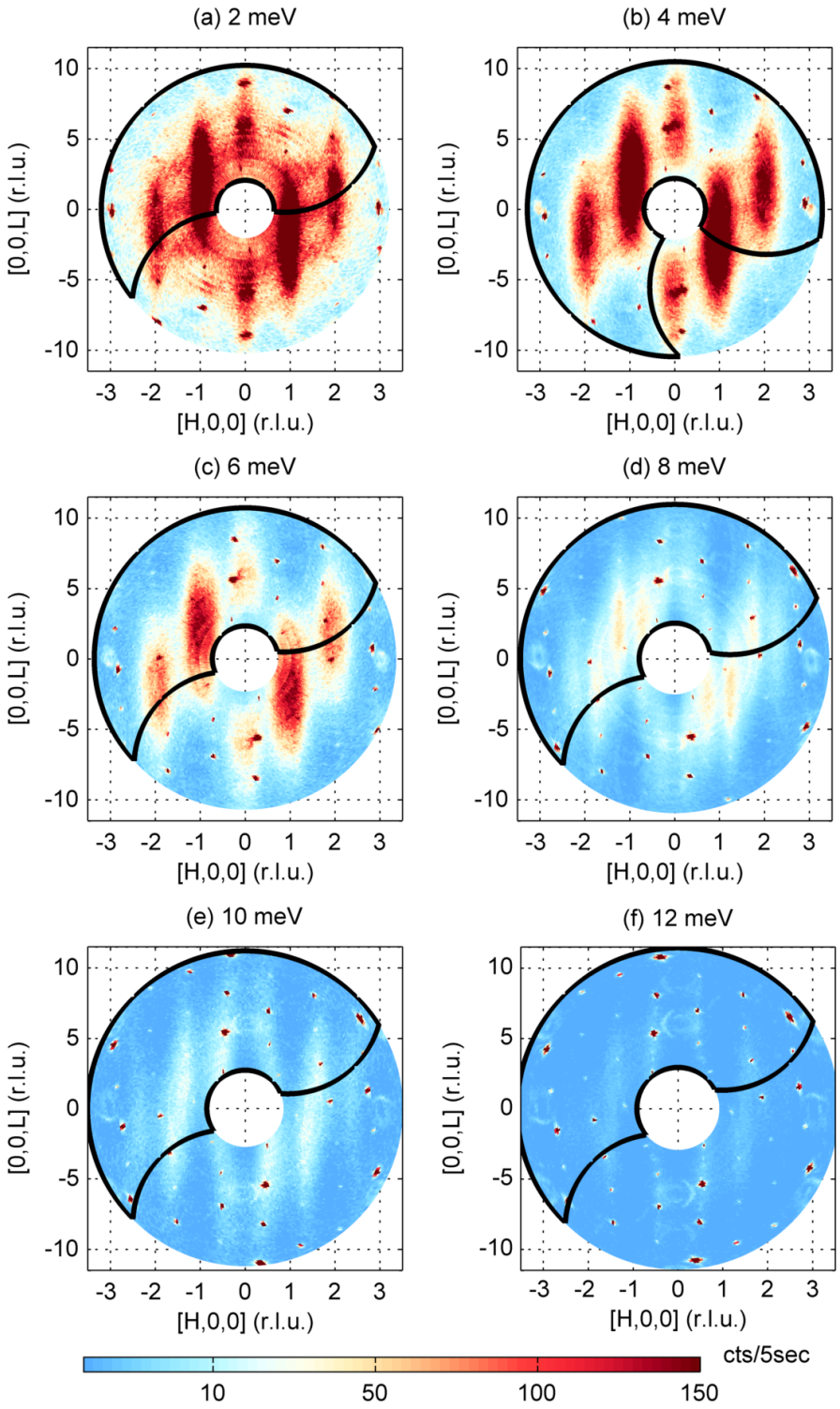

Figure 7.14.: Intensity mapping of magnetic excitations in $Ni_xMn_{1-x}TiO_3$ in the $[H, 0, L]$ plane in $Ni_xMn_{1-x}TiO_3$ at 2 K at IN8. The scattered neutron intensity was collected at constant energies from 2 to 12 meV. The same linear color scale was used for all maps. Black lines surround the measured data, the maps were completed by symmetrization.

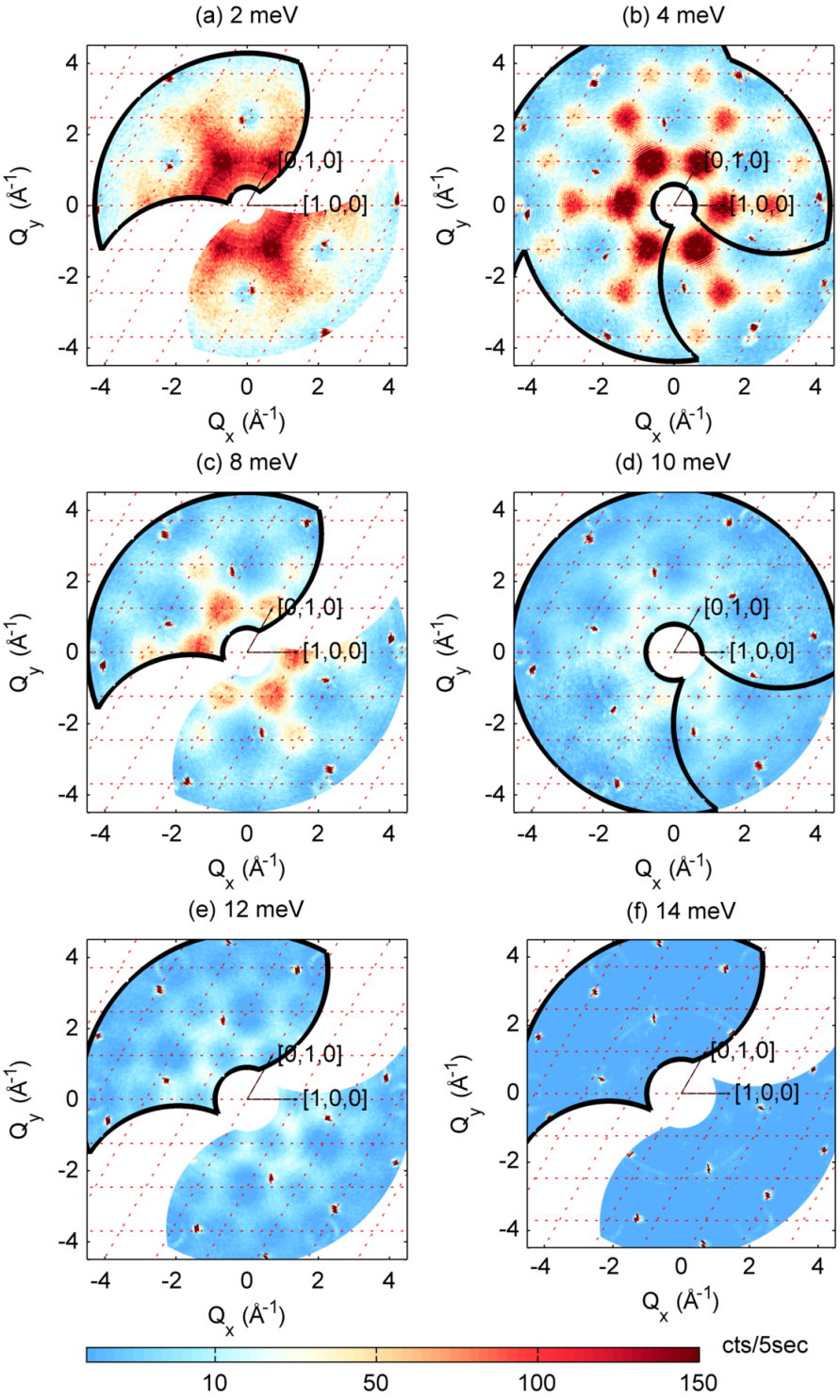

Figure 7.15.: Intensity mapping of magnetic excitations in $Ni_xMn_{1-x}TiO_3$ in the $[H, K, 0]$ plane in $Ni_xMn_{1-x}TiO_3$ at 2 K at IN8. The scattered neutron intensity was collected at constant energies from 2 to 14 meV. The same linear color scale was used for all maps. Black lines surround the measured data, the maps were completed by symmetrization.

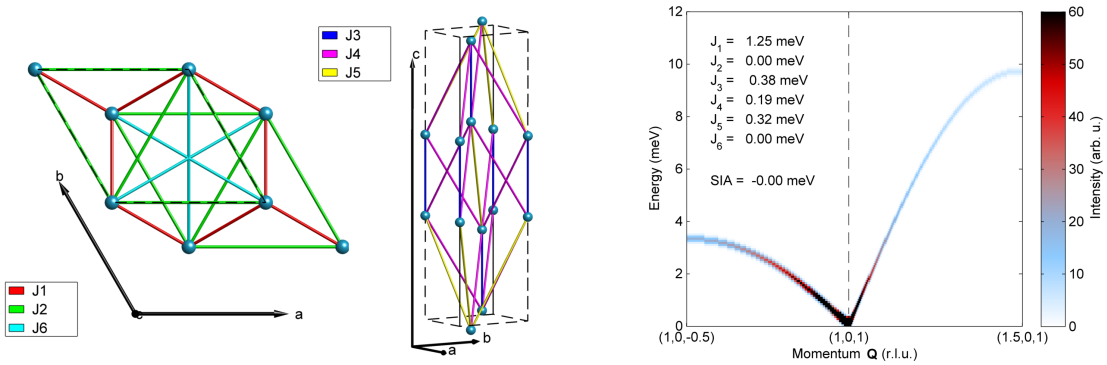

Figure 7.16.: Spin wave calculation in $MnTiO_3$ using *SpinW* [94]. (left) Exchange interaction paths in $MnTiO_3$ in the hexagonal *ab*-plane and between the planes along $\vec{c}$. The positions of the M^{2+} ions and the six shortest distances are shown. (right) Calculation of magnetic excitations along $[0, 0, L]$ and $[H, 0, 0]$ in $MnTiO_3$. The parameters used for the calculation are given in the inset.

7.4.3. Spin wave model

The comprehensive dataset of the excitation spectrum in the spin-glass phase of $Ni_{0.42}Mn_{0.58}TiO_3$ obtained on IN8 leads to the assumption that the dispersion is dominated by the AF-$Mn_{\parallel}$-type order. Todate *et al.* reported the magnon dispersion in $MnTiO_3$ at 4.2 K, obtained by inelastic neutron scattering [247]. Their model describing the Q-dependence of modes consists of three in-plane and three out-of-plane interaction paths, which have been discussed before theoretically by Goodenough *et al.* [234]. The interactions between the M^{2+} sites are shown in Figure 7.16(a). The index J_i denotes the order of paths in terms of moments distance. Consistent with theoretical aspects of the superexchange and super-superexchange paths, Todate *et al.* find all exchanges to be antiferromagnetic [234, 247].

The magnon dispersion of $MnTiO_3$ was modeled with *SpinW*, a *MATLAB* code for linear spin wave calculations (see Section 4.3 for details). The reported dispersion along $[0, 0, L]$ and $[H, 0, 0]$ could be reproduced using the following set of exchange interactions: $J_1 = 1.25\,\text{meV}$, $J_2 = 0.02\,\text{meV}$, $J_3 = 0.38\,\text{meV}$, $J_4 = 0.19\,\text{meV}$, $J_5 = 0.32\,\text{meV}$, $J_6 = 0.09\,\text{meV}$ and an easy axis anisotropy $SIA = 0.01\,\text{meV}$, confining the moments along $\vec{c}$.

The model for $MnTiO_3$ was slightly modified to describe spin-wave-dispersion observed in $Ni_{0.42}Mn_{0.58}TiO_3$. The energy scans at the magnetic zone centers did not show a gap, arising from an anisotropy. Accordingly, the anisotropy was set to zero. In addition, we will neglect the weak interactions J_2 and J_6. The calculated dispersion along $\vec{c}$ and $\vec{a}$ using the modified model is shown in Fig. 7.16(b).

The described model for $MnTiO_3$ was used to simulate scattering maps at constant

energy transfer, which can directly be compared to experimental data of the spin-glass phase in $Ni_{0.42}Mn_{0.58}TiO_3$. Intensity maps along $[H, 0, L]$ and $[H, K, 0]$ at specific energies are shown in Figure 7.17. The maps can be compared to the experimental data in Figure 7.14 and Figure 7.15. The calculation takes into account the magnetic form factor, the Bose factor at 2 K and an energy resolution of $\Delta E = 0.8$ meV.
The calculated intensity maps nicely reproduce the experimental data in the $[H, K, 0]$ plane, clearly showing the hexagonal symmetry. The distribution of weak and strong reflections in the$[H, 0, L]$ also fits the experiment rather well. One discrepancy between simulation and experiment lays in the correlation along $\vec{c}$, which is stronger in $MnTiO_3$.
The magnon dispersion of the $MnTiO_3$ model and the experimental data from $Ni_{0.42}Mn_{0.58}TiO_3$ can be compared directly by producing vertical cuts through the $(\vec{Q}, E)$ space. This has been done for both experimental orientations, $[H, 0, L]$ (Fig. 7.18) and $[H, K, 0]$ (Fig. 7.19). The organization of both figures is the same. The top image shows the three-dimensional experimental data set with the energy being on the vertical axis. Vertical planes indicate the 2D-cuts through the dataset. Below, the experimental data is shown on the left side and the calculation on the right. The experimental data was treated using the *MATLAB*-code *fcplot* [85].
The dispersion in the hexagonal plane can be described surprisingly well by the $MnTiO_3$ model. The deviation of simulation and experimental data at low energies arises from strong Bragg peak scattering, which is visible at higher energies due to the finite energy resolution. Scattering from static Bragg peaks has not been taken into account for the calculation. The range of the dispersion and the spectral weight is correctly reproduced. The cut along the c-axis is more difficult to interpret. If there would be only weak interaction along $\vec{c}$, one would expect at flat mode at low energies. Instead, the experimental data shows a broad mode up to 5 meV with only little Q_L-dependence. It seems plausible that interactions along $\vec{c}$ exist as proposed by the model, yet they are limited to small correlated regions. The regions are independent of each other and thus smear out the dispersion along the hexagonal axis.

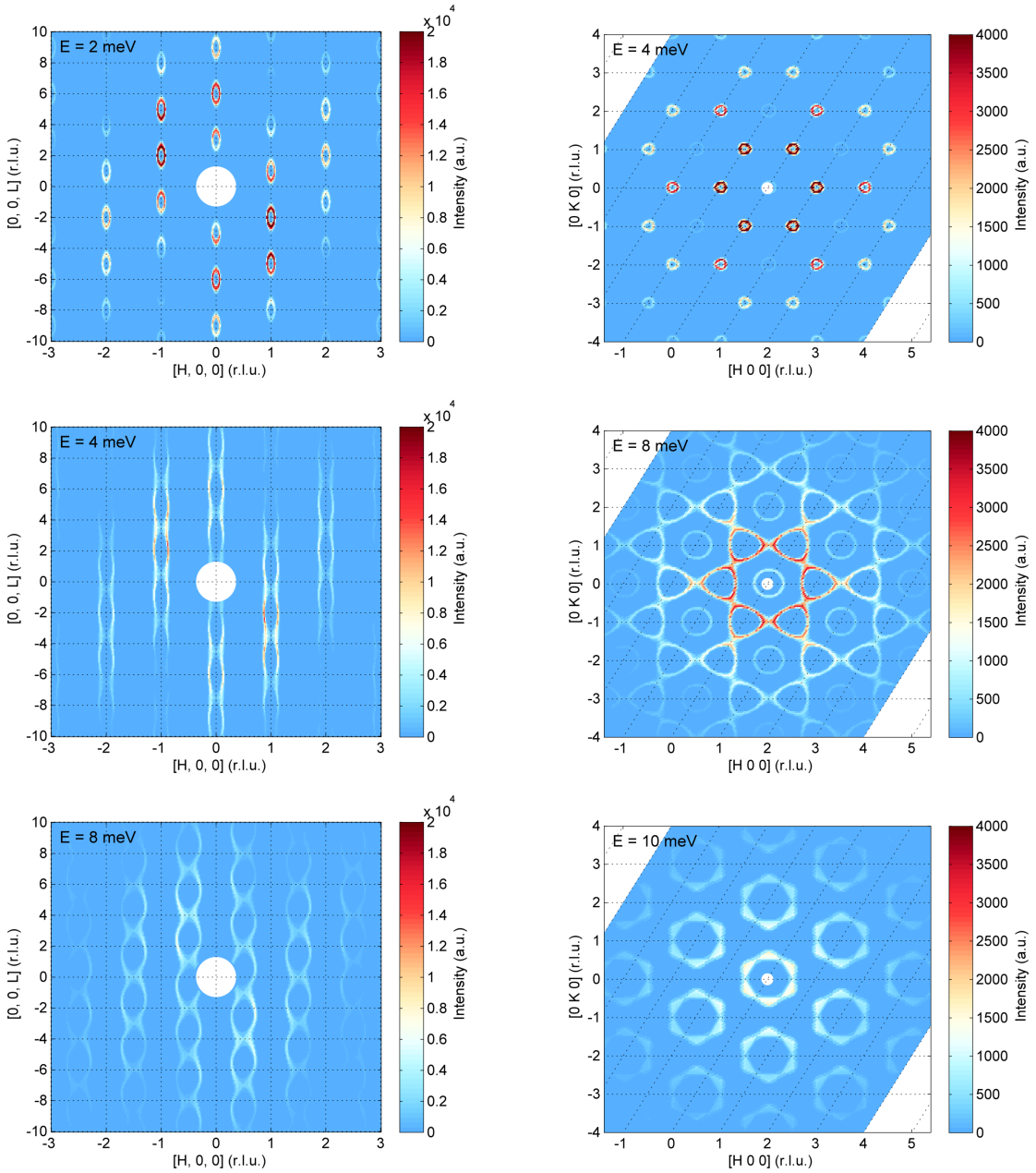

Figure 7.17.: Neutron scattering intensities of constant energy planes calculated for $MnTiO_3$ using *SpinW* [94]. Intensity mappings of scattering in the $[H, 0, L]$ plane (left) and in the $[H, K, 0]$ plane (right) are shown at different constant energies. The intensity is linearly color-coded. The calculation takes into account the magnetic form factor, the Bose factor at 2 K and an energy resolution of $\Delta E = 0.8\,\mathrm{meV}$.

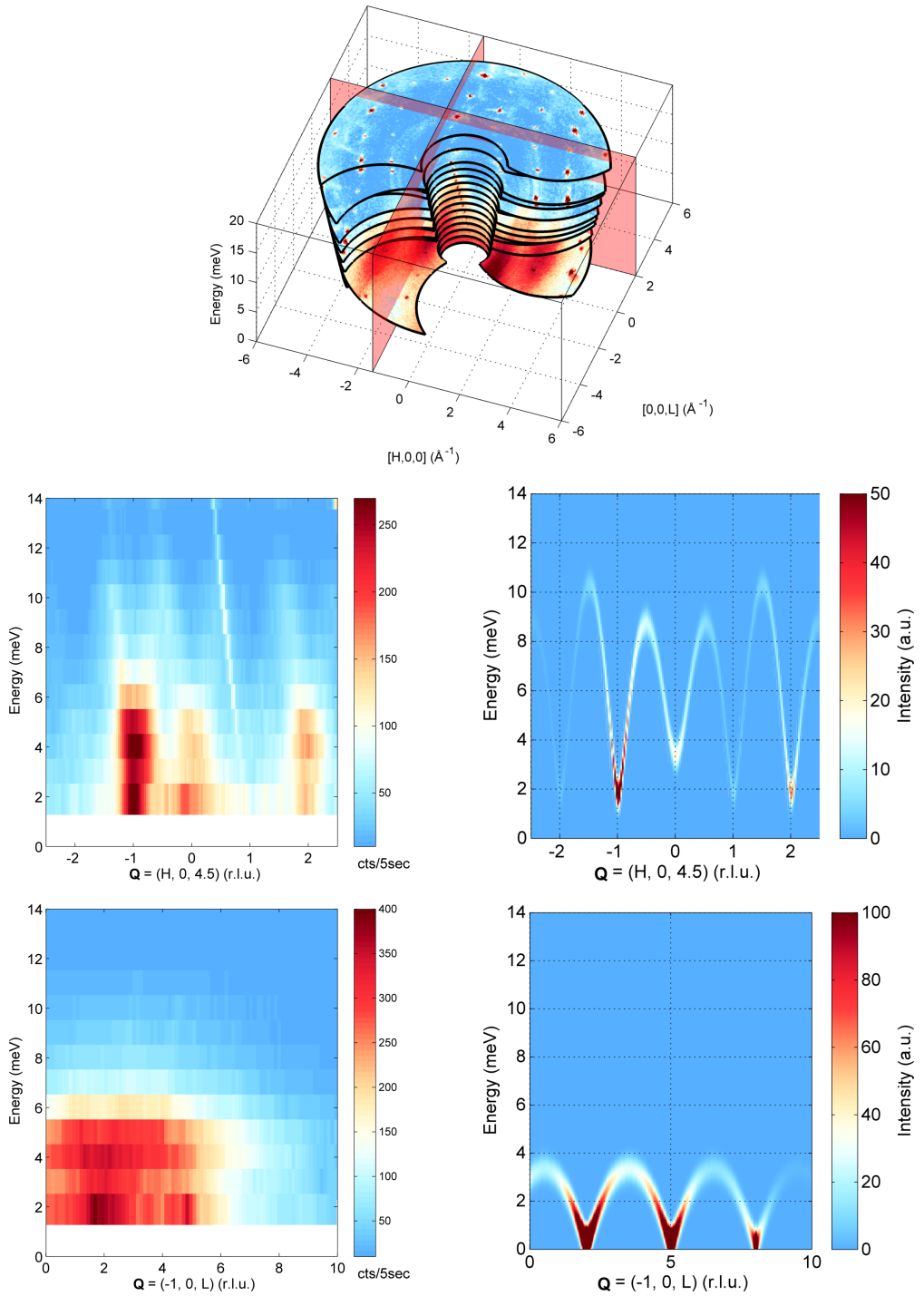

Figure 7.18.: Comparison of measured (IN8) and calculated neutron scattering intensities in $Ni_xMn_{1-x}TiO_3$ at 2 K in the $[H, 0, L]$ plane. Intensity mappings of scattering along $\vec{Q} = (H,\ 0,\ 4.5)$ and $\vec{Q} = (-1,\ 0,\ L)$ are shown. (right) Cuts from data determined on IN8. The corresponding planes are indicated on the top. (left) Intensities calculated using *SpinW* [94] for the AF-$Mn_{||}$ order in $MnTiO_3$, taking into account the magnetic form factor, the Bose factor and an energy resolution of $\Delta E = 0.8$ meV.

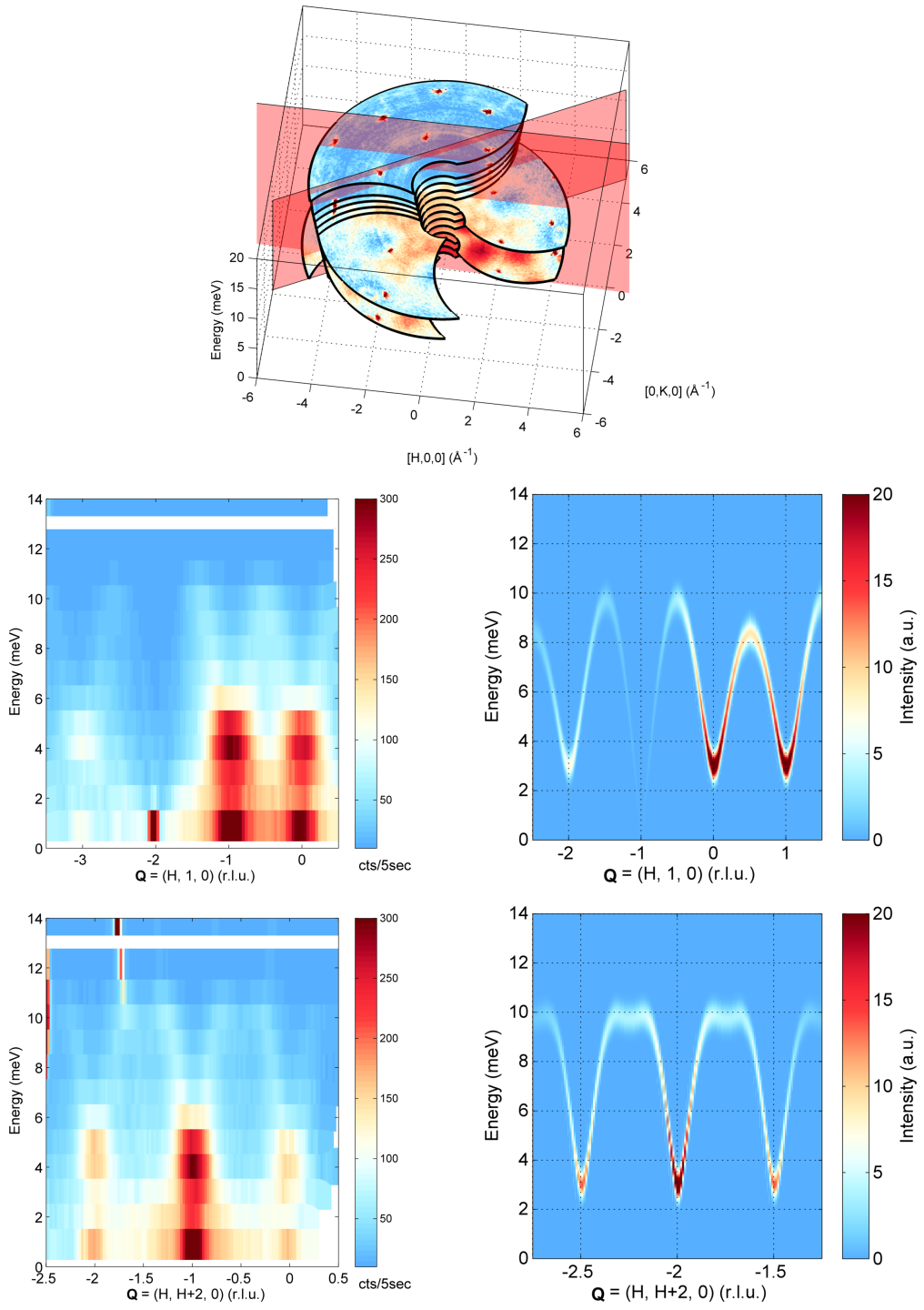

Figure 7.19.: Comparison of measured (IN8) and calculated neutron scattering intensities in $Ni_xMn_{1-x}TiO_3$ at 2 K in the $[H, K, 0]$ plane. Intensity mappings of scattering along $\vec{Q} = (H,\ 1,\ 0)$ and $\vec{Q} = (H,\ H+2,\ 0)$ are shown. (right) Cuts from data determined on IN8. The corresponding planes are indicated on the top. (left) Intensities calculated using *SpinW* [94] for the AF-$Mn_{\parallel}$ order in $MnTiO_3$, taking into account the magnetic form factor, the Bose factor and an energy resolution of $\Delta E = 0.8$ meV.

The comparison of experimental data and simulation showed that the dispersion in $Ni_{0.42}Mn_{0.58}TiO_3$ can be described by assuming an AF-$Mn_{\parallel}$-type model with Mn moments only. In the spin-glass phase, nevertheless, short-ranged regions of AF-$Mn_{\parallel}$ and AF-Ni order coexist, which are formed by Mn and Ni moments. The simulation hence implies that the excitation spectrum is not disturbed by the frustration introduced by Ni moments and that Ni moments contribute to the AF-$Mn_{\parallel}$ fluctuations.

7.5. Conclusion

In this chapter, the magnetic ordering of Mn and Ni moments in the spin-glass system $Ni_{0.42}Mn_{0.58}TiO_3$ was presented. The properties of the magnetic structure and the magnetic excitations were investigated using unpolarized and polarized neutron scattering. The compound arose interest due to its magnetoelectric effect that was observed inside the short-range magnetic phase [18].
The detailed analysis of the magnetic scattering in the spin-glass phase revealed a distinct contribution of Ni and Mn moments. Diffuse magnetic signal is present at the Bragg peak position of the magnetic order of the parent compounds $Ni_{0.42}Mn_{0.58}TiO_3$ and $MnTiO_3$. This shows that a short-range order of $Ni_{0.42}Mn_{0.58}TiO_3$-type and $MnTiO_3$-type coexist in the spin-glass phase. The moments of the Mn ions are tilted relative to the c-axis. It was possible to estimate a contribution of 25 % of Ni moments and 45 % of Mn moments to the total magnetic scattering.
The dependence of crossed magnetic and electric field on the magnetic order in the spin-glass phase was investigated using spherical neutron polarimetry. It could be shown that a magnetic field applied parallel to the hexagonal plane aligns the Mn-moments within the plane. The antiferromagnetic domains could be controlled by a reversal of the magnetic field.
Finally, we were able to measure the magnetic excitations in the spin-glass phase. A comprehensive dataset was obtained within the hexagonal plane and perpendicular to it. The excitations are found to be significantly broadened along the c-direction, indicating a weak coupling of the hexagonal planes along $\vec{c}$. The magnon dispersion in the hexagonal plane is comparable to the $MnTiO_3$ mother compound [247]. The magnetic excitation spectrum in the spin-glass phase could be well described by linear spin wave theory. The applied model could be derived by taking into account only a contribution of the Mn-moments.

Chapter 8

Summary

This work contains experimental studies on the magnetic properties of four different transition-metal oxides with the focus on multiferroic and magnetoelectric effects. These studies will be summarized in the following.

The multiferroic phase of $TbMnO_3$ was intensively studied since its observation in 2003 [5]. The magnetic frustration in the *ab*-plane and the coupling between Mn and the Tb-subsystem are the reason for the complexity of the system and its fascinating magnetoelectric effects. Within this work, it was possible to investigate the properties of the successive magnetic phase transitions and the dynamics in the multiferroic phase.
The detailed analysis of the magnetic fluctuations in the paramagnetic and the spin-density-wave phase of $TbMnO_3$ revealed significant diffuse scattering arising from the Tb and the Mn-subsystems. The contributions could be distinguished using neutron polarization analysis and it was shown that magnetic fluctuations of the *bc* spin-spiral are present throughout the ordered SDW phase. This indicates an almost continuous transition towards the spin-spiral phase.
The magnetic excitations in the multiferroic spiral phase were studied in the past by inelastic neutron scattering [12] and different models for the spin-wave dispersion were proposed [114, 143]. We presented a comprehensive dataset of the excitation spectrum in the multiferroic phase obtained by time-of-flight spectroscopy. We developed a model of the Mn-subsystem in order to describe the magnon dispersion using linear spin wave theory. The model takes into account the nearest-neighbor exchanges along $\vec{c}$ and in the *ab*-plane, as well as the next-nearest-neighbor exchange along $\vec{b}$. At the zone center, we find an in-plane mode and two out-of-plane modes of the spiral. The splitting of the out-of-plane mode was achieved by introducing a distorted easy-plane anisotropy. The model is able to quantitatively describe the full spin-wave dispersion in the multiferroic phase.
Multiferroic materials of spin origin are perfect candidates to study electromagnons,

which are coupled phonon-magnon excitations. The polarization of the zone center mode derived from the spin-wave model predicts one electrically active magnon mode. The energy of this mode agrees with observations from infrared spectroscopy [57] and inelastic neutron scattering [12]. This supports the assumption that the lowest of the electromagnetic excitations observed in $TbMnO_3$ can be attributed to the DM mechanism. Furthermore, the spin-wave model could describe the dispersion of the chiral component, which was observed by poling a single crystalline sample in an electric field.
The magnetic excitation spectrum was also studied in the multiferroic high-field phase in magnetic fields parallel $\vec{b}$. The analysis of the Q-dependence allowed for the separation of in-plane and out-of-plane modes at the magnetic zone center. The energy of the mode which is predicted to be electrically active by the DM mechanism is found at the same energy as a reported electric mode [60]. This finding supports again the existence of an electromagnon in $TbMnO_3$ of DM origin.

The tungstate $MnWO_4$ is another multiferroic material of spin origin. Upon cooling, the spins order first in a spin-density wave before a spiral order is realized, which induces the ferroelectric polarization [175]. We studied the diffuse quasi-elastic scattering in all magnetic phases. By the separation of contributions from the SDW and the spiral order, we could demonstrate the almost continuous nature of the PM→SDW→spiral transition. A comprehensive dataset of the magnetic fluctuations was obtained documenting a characteristic shape of the magnetic fluctuations, which is linked to the complex magnetic exchange interactions in $MnWO_4$.
The vector chirality of the spiral structure is directly correlated to the ferroelectric polarization of the multiferroic phase [13]. The chirality of the diffuse scattering could be poled by an electric field and observed using polarized neutron analysis. The poling was only possible in a small range above the transition, which could be explained by comparing the energy of the electric field with thermal fluctuations. The chiral character of the fluctuations can be compared to the critical slowing down of electric fluctuations observed by dielectric spectroscopy [203].
Furthermore, we report the magnetic excitations in the multiferroic phase. The magnon modes possess a strong chiral component, which could be poled by applying an electric field. As in the study of $TbMnO_3$, we find modes of both chiral states which coexist within one Brillouin zone.

The double tungstate $NaFe(WO_4)_2$ exhibits a complex magnetic phase diagram and shows strong hysteresis effects [213]. We investigated the magnetic structure in the zero-field phase and in the high field phases in magnetic fields applied along the monoclinic axis $\vec{b}$ using elastic neutron scattering.
It could be demonstrated that the Fe magnetic moments order directly in a spin

spiral with incommensurate propagation vector $\vec{k_{ic}} = (0.485,\ 0.5,\ 0.48)$ at 3.9 K. The rotation plane of the Fe moments is similar to the multiferroic phase of $MnWO_4$ [175]. This magnetic phase does not induce a ferroelectric polarization, as the DM effect is canceled out by the symmetry of the moments in the unit cell. The incommensurability of the structure is strongly temperature dependent and could be related to an anharmonic distortion of the spiral. The hysteresis effect of the propagation vector directly corresponds to features in thermal expansion data [213].
In magnetic fields applied along $\vec{b}$, the magnetic structure becomes commensurate with a propagation vector of $\vec{k_c} = (0.5,\ 0.5,\ 0.5)$. This commensurate phase should be the ground state of $NaFe(WO_4)_2$, since it persists even after the subsequent removal of an magnetic field at constant temperature. This phase is similar to the commensurate ground state of $MnWO_4$ [175].

The ilmenite $Ni_{0.42}Mn_{0.58}TiO_3$ develops a spin-glass phase due to a frustration of magnetic interactions and anisotropies [18]. We were able to investigate the magnetic properties of the Ni and Mn-subsystems and presented a comprehensive study of the dynamic correlations.
In the spin-glass phase, we find contributions at the magnetic Bragg peak position of $NiTiO_3$ and $MnTiO_3$-type. The elastic signal is significantly broadened, indicating an incomplete magnetic order. It was possible to estimate a contribution of 25 % of Ni moments and 45 % of Mn moments to the total scattering. The onset of the Ni-order can be attributed to a sharp feature in the magnetic susceptibility, while the Mn-order develops continuously. Spherical neutron polarimetry was applied in order to analyze the orientation of the moments. The Ni moments are aligned in the *ab*-plane while the Mn-moments can be described by a canting relative to the *c*-axis.
The antiferromagnetic domains could be controlled by crossed magnetic and electric fields, which were applied within the hexagonal plane. Our observations indicate that the $MnTiO_3$-type magnetic order can be accounted for the magnetoelectric effect which was observed in the spin-glass phase [18]. The G-type magnetic ordering breaks the inversion symmetry and allows for finite elements of the ME tensor.
The magnetic excitations in the spin-glass phase were studied intensively by unpolarized and polarized neutrons. We collected a comprehensive dataset which documents correlated hexagonal planes which are only weakly coupled along the *c*-axis. It was found that the inelastic scattering primarily arises from the Mn-subsystem. A model was developed which only slightly deviates from the spin-wave model of $MnTiO_3$ [247]. The calculated neutron intensity maps are able to reproduce the main features of the experimental data.

Appendix A

Unit conversion

The properties of the incident and final neutron beam are often given in different units, adapted to the specific experimental approach. Table A.1 lists the corresponding values for various neutron wavelengths.

Table A.1.: Conversion of units for neutron scattering. In general, neutrons are classified as hot ($0.4\,\text{Å} < \lambda < 1\,\text{Å}$), thermal ($1\,\text{Å} < \lambda < 3\,\text{Å}$) and cold ($3\,\text{Å} < \lambda < 20\,\text{Å}$).

λ (Å)	k (Å^{-1})	E (meV)	v (m s^{-1})	ν (THz)	T (K)	$\tilde{\nu}$ (cm^{-1})	t (ps)
0.50	12.57	327.24	7912.07	79.12	3797.58	2639.18	0.01
0.80	7.85	127.83	4945.04	30.91	1483.43	1030.93	0.03
1.00	6.28	81.81	3956.03	19.78	949.40	659.80	0.05
1.50	4.19	36.36	2637.36	8.79	421.95	293.24	0.11
2.00	3.14	20.45	1978.02	4.95	237.35	164.95	0.20
2.36	2.66	14.66	1674.80	3.55	170.16	118.25	0.28
3.00	2.09	9.09	1318.68	2.20	105.49	73.31	0.46
4.00	1.57	5.11	989.01	1.24	59.34	41.24	0.81
5.00	1.26	3.27	791.21	0.79	37.98	26.39	1.26
8.00	0.79	1.28	494.50	0.31	14.83	10.31	3.24
10.00	0.63	0.82	395.60	0.20	9.49	6.60	5.06
25.00	0.25	0.13	158.24	0.03	1.52	1.06	31.60
50.00	0.13	0.03	79.12	0.01	0.38	0.26	126.39

The following equations were applied to calculate the values in Table A.1 for the given neutron wavelengths λ [71]:

wave vector	$k = \frac{2\pi}{\lambda}$
energy	$E = \frac{h^2}{2m_n\lambda}$
velocity	$v = \sqrt{\frac{2 \cdot E}{m_n}}$
frequency	$\nu = \frac{E}{h}$
temperature	$T = \frac{E}{k_B}$
wave number	$\tilde{\nu} = E/c$
time	$t = \frac{1}{\nu}$

neutron mass	$m_n = 1.674\,954 \cdot 10^{-27}\,\mathrm{kg}$
speed of light	$c = 2.997\,924\,0 \cdot 10^{7}\,\mathrm{m\,s^{-1}}$
Planck constant	$h = 6.626\,18 \cdot 10^{-34}\,\mathrm{J\,s}$
electron volt	$1\,\mathrm{eV} = 1.6021 \cdot 10^{-19}\,\mathrm{J}$

Appendix B

SpinW code for $TbMnO_3$

In Chapter 4.4, a model was presented to simulate the magnon dispersion in the multiferroic phase of $TbMnO_3$ (model M-II). The underlying code is presented below. The calculation was done using *MATLAB* R2014a 64-bit [82] and the library *SpinW* (version 2.1 revision 238) [94].
In order to use the space group *Pbnm* to describe the crystal structure of $TbMnO_3$, the following line had to be added at the bottom of the *SpinW*-file *symmetry.dat*: *231 P b n m: -x,-y,z+1/2;-x+1/2,y+1/2,-z+1/2;-x,-y,-z* .

```
%%% CRYSTAL STRUCTURE %%%
%Definition of the Pbnm lattice.
tbmno = sw;
tbmno.genlattice('lat_const',[5.30 5.85 7.40],'sym','P b n m');

%Definition of the magnetic Mn3+ atom with S = 4 / 2.
tbmno.addatom('r',[1/2; 0; 0],...
              'S',4/2,'label','MMn3','color', [40; 178; 223]);

%Definition of the oxygen atoms.
r1O = [0.1083;  0.4694;  0.25];
r2O = [0.7085;  0.3267;  0.0523];
tbmno.addatom('r',[r1O r2O],'S',[0 0],...
              'label',{'O' 'O'},'color', [255 255; 0 0; 0 0]);

%Definition of the Tb atoms.
tbmno.addatom('r',[0.9836;  0.0810; 0.25],...
              'S',0,'label','Tb','color', [200; 200; 200]);

%%% MAGNETIC STRUCTURE %%%
%Definition of k and the magnetic unit cell 1x7x1.
kinc=2/7; kvec=[0 kinc 0]; mucell=7;
Mb=[0 1 0]; Mc=[0 0 0.72];
ucell=[0.5 0.5 0 0;0 0 0.5 0.5; 0 0.5 0.5 0];
```

```
%Generation of moments in unit cell.
longucell=[]; mom=[];
for i=0:(mucell-1)
    longucell=[longucell ucell+[0 0 0 0;i i i i;0 0 0 0]];
end
for i=1:numel(longucell(1,:))
mom=[mom (Mc'*cos(2*pi*kvec*longucell(:,i))...
     -Mb'*sin(2*pi*kvec*longucell(:,i) ))*(-1)^(2*longucell(3,i))];
end
tbmno.genmagstr('mode','direct','S',mom,'nExt',[1 mucell 1]);

%%% EXCHANGE INTERACTIONS %%%
%Definition of exchange parameters.
neta=-sin(2*pi*kinc*0.5)/sin(2*pi*kinc);
Jab=-0.3808; Jbb=neta*Jab; Jcc=+0.837;
tbmno.gencoupling
tbmno.addmatrix('label','Jab','value',Jab,'color','r');
tbmno.addmatrix('label','Jbb','value',Jbb,'color','g');
tbmno.addmatrix('label','Jcc','value',Jcc,'color','b');
tbmno.addcoupling('Jab',2);
tbmno.addcoupling('Jbb',6);
tbmno.addcoupling('Jcc',1)

%%% ANISOTROPY AND DM %%%
%Definiton of distorted easy plane.
D=-0.124*[0.0 sum(Mb) sum(Mc)];
tbmno.addmatrix('label','D','value',diag(D),'color',[1 1 1]*200)
tbmno.addaniso('D')

%%% DISPERSION IN AND OUT-OF-PLANE %%%
% polarization analysis in bc plane.
tbpol=tbmno.spinwave({[0 -1 1] [0 1 1] 100},...
                     'hermit',true,'formfact',true);
tbpol=sw_neutron(tbpol,'pol',true,'uv',{[0 1 0] [0 0 1]});
tbpol=sw_egrid(tbpol,'component','Sperp','Evect',linspace(0,10,100));
sw_plotspec(tbpol,'mode','color','dE',0.2,'axLim',[0 13]);
```

Appendix C

Supplemental data for $Ni_{0.42}Mn_{0.58}TiO_3$

C.1. Field dependence of magnetic scattering components

The dependence of magnetic scattering components on crossed magnetic and electric fields in the spin-glass phase of $Ni_{0.42}Mn_{0.58}TiO_3$ was discussed in Section 7.3.2 at the Bragg peak position $\vec{Q} = (-1,\ 0,\ 2)$. The comparison of experimental and simulated compounds was also determined at $\vec{Q} = (-1,\ 0, -1)$ and $\vec{Q} = (0,\ 0, -3)$ and is shown in Tables C.1 and C.2. The experimental values were determined following the component separation in spherical neutron polarimetry, cf. Tab. 3.1. The simulated components were determined by calculating the nuclear and magnetic structure factors for different antiferromagnetic domain settings. The details of the calculation are given in Section 7.3.2.

Table C.1.: Magnetic and electric-field dependency of magnetic scattering components in $Ni_{0.42}Mn_{0.58}TiO_3$, determined at $\vec{Q}_{AF-Mn} = (-1,\ 0, -1)$ at 2 K. The intensities were normalized to a monitor of 200 (cts/0.5 s). The electric field was applied along $[1, 1, 0]$ and the magnetic field applied along $[\bar{1}, 2, 0]$. Below, simulated intensities are shown for different domain constellations of the AF-$Mn_{\parallel}$ and AF-$Mn_{\perp}$ order. The simulated intensities were normalized to $M_yM_y^*$ of AF-$Mn_{\parallel}$.

B (T)	E (kV)	$M_yM_y^*$	$M_zM_z^*$	ReM_yN	ReM_z^*N	ImM_y^*N	ImM_z^*N
0	0	4.0(4)	1.6(4)	0.6(6)	-0.2(6)	3.3(6)	6.8(6)
+1	-1.5	5.3(7)	23.9(6)	1.2(6)	0.6(3)	4.9(6)	62.4(6)
+1	+0.9	5.4(5)	9.9(5)	0.5(6)	1.0(6)	3.1(5)	39.5(5)
-1	-1.2	-3.0(5)	22.0(4)	-0.2(5)	-1.4(5)	1.3(5)	-79.6(9)
-1	+0.5	0.0(6)	14.5(5)	0.5(6)	-0.8(6)	1.0(4)	-47.8(7)

Simulation	$M_yM_y^*$	$M_zM_z^*$	ReM_y^*N	ReM_z^*N	ImM_y^*N	ImM_z^*N
AF-$Mn_{\parallel}$	1.00	0.00	0.00	0.00	0.00	0.00
$[0, 0, 1]$	1.00	0.00	0.00	0.00	-1.13	0.00
$[0, 0, \bar{1}]$	1.00	0.00	0.00	0.00	1.13	0.00
AF-$Mn_{\perp}$	0.05	0.55	0.00	0.00	0.00	0.00
$[1, 0, 0]$	0.10	0.00	0.00	0.00	0.35	0.00
$[\bar{1}, 0, 0]$	0.02	0.82	0.00	0.00	-0.18	-1.03
$[0, \bar{1}, 0]$	0.02	0.82	0.00	0.00	-0.18	1.03
$[1, 0, \bar{1}]$	0.10	0.00	0.00	0.00	-0.35	-0.00
$[0, 1, 0]$	0.02	0.82	0.00	0.00	0.18	1.03
$[\bar{1}, 0, 1]$	0.02	0.82	0.00	0.00	0.18	-1.03

Table C.2.: Magnetic and electric field dependency of magnetic scattering components in $Ni_{0.42}Mn_{0.58}TiO_3$, determined at $\vec{Q}_{AF-Mn} = (0,\ 0, -3)$ at 2 K. The intensities were normalized to a monitor of 200 (cts/0.5 s). The electric field was applied along $[1, 1, 0]$ and the magnetic field applied along $[\bar{1}, 2, 0]$. Below, simulated intensities are shown for different domain constellations of the AF-$Mn_{\parallel}$ and AF-$Mn_{\perp}$ order. The simulated intensities were normalized to $M_yM_y^*$ of AF-$Mn_{\perp}$.

B (T)	E (kV)	$M_yM_y^*$	$M_zM_z^*$	ReM_yN	ReM_z^*N	ImM_y^*N	ImM_z^*N
0	0	0.9(6)	1.1(6)	1.6(9)	-1.6(4)	4.9(4)	16.5(9)
+1	-1.5	12.3(8)	44.6(7)	-0.4(9)	1.6(5)	17.3(9)	174.6(9)
+1	+0.9	6.8(7)	21.2(6)	1.2(9)	1.1(4)	12.2(9)	115.5(9)
-1	-1.2	-4.3(4)	15.3(4)	-1.0(9)	-0.5(9)	-1.5(7)	-90.2(9)
-1	+0.5	-7.3(8)	24.9(7)	-1.1(9)	-1.8(9)	0.5(3)	-151.4(9)

Simulation	$M_yM_y^*$	$M_zM_z^*$	ReM_y^*N	ReM_z^*N	ImM_y^*N	ImM_z^*N
AF-$Mn_{\parallel}$	0.00	0.00	0.00	0.00	0.00	0.00
$[0, 0, 1]$	0.00	0.00	0.00	0.00	0.00	0.00
$[0, 0, \bar{1}]$	0.00	0.00	0.00	0.00	0.00	0.00
AF-$Mn_{\perp}$	1.00	1.00	0.00	0.00	0.00	0.00
$[1, 0, 0]$	2.01	0.00	0.00	0.00	6.31	0.00
$[\bar{1}, 0, 0]$	0.50	1.51	0.00	0.00	-3.16	-5.47
$[0, \bar{1}, 0]$	0.50	1.51	0.00	0.00	-3.16	5.47
$[1, 0, \bar{1}]$	2.01	0.00	0.00	0.00	-6.31	-0.00
$[0, 1, 0]$	0.50	1.51	0.00	0.00	3.16	5.47
$[\bar{1}, 0, 1]$	0.50	1.51	0.00	0.00	3.16	-5.47

C.2. Magnetic excitations

In Section 7.4.2, inelastic neutron scattering data was presented in the spin-glass phase of $Ni_{0.42}Mn_{0.58}TiO_3$. Supplemental data obtained at the thermal neutron TAS instrument IN8 at the ILL will be presented in the following. The single crystal sample was mounted in the [100]/[010] scattering plane, the final neutron energy was $E_f = 18.6\,\text{meV}$ ($k_f = 3.0\,\text{Å}^{-1}$) and the energy resolution can be estimated to be $\Delta E \approx 0.8\,\text{meV}$.
The instrument was equipped with the *FlatCone* multi-detector, which covers a large area in Q-space. It allows for a vertical tilting of the detector plane of -10 to 20°. This enables to access a momentum transfer which is vertical to the horizontal scattering plane [84]. The scattering plane $[H, K, -1]$ could be accessed by a combined tilting of detector and a cryostat.
The elastic scattering map in the $[H, K, -1]$ plane is shown in Figure C.1. The intensity is logarithmically color coded. The intensity map significantly differs from the $[H, K, 0]$ elastic map, cf. Fig. 7.9. The strongest reflections can be attributed to the nuclear structure, while the weak signal arises from diffuse magnetic and nuclear scattering.
Figure C.2 shows intensity maps at an energy transfer of 4 meV and 8 meV at 2 K. The inelastic intensity is similar to the data obtained in the $[H, K, 0]$ map, cf. Figure 7.15. This demonstrates the weak coupling along the hexagonal axis $\vec{c}$.
Finally, the temperature dependence of the inelastic signal in the $[H, K, 0]$ plane is shown in Figure C.3. The same color scale was used for all temperatures. The inelastic signal significantly weakens upon heating, but is present up to 300 K. The sharp features arising at higher temperatures can be attributed to phonon scattering, whose intensity is enhanced by the Bose factor.

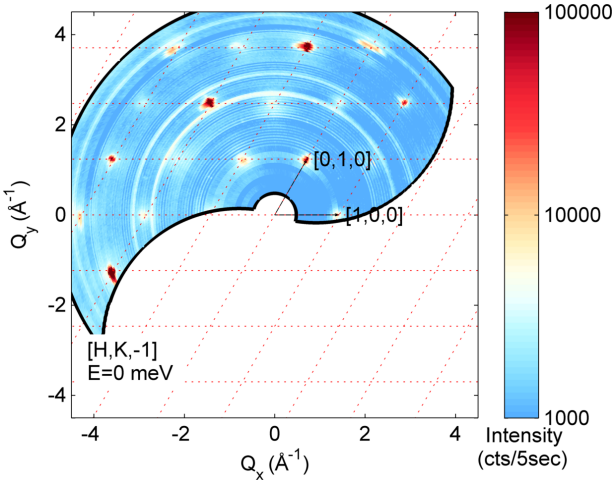

Figure C.1: Elastic neutron scattering map of $Ni_xMn_{1-x}TiO_3$ at 2 K in the $[H, K, 1]$ plane at IN8. Dotted lines indicate the reciprocal directions $[1, 0, 0]$ and $[0, 1, 0]$. The intensity is logarithmically color coded.

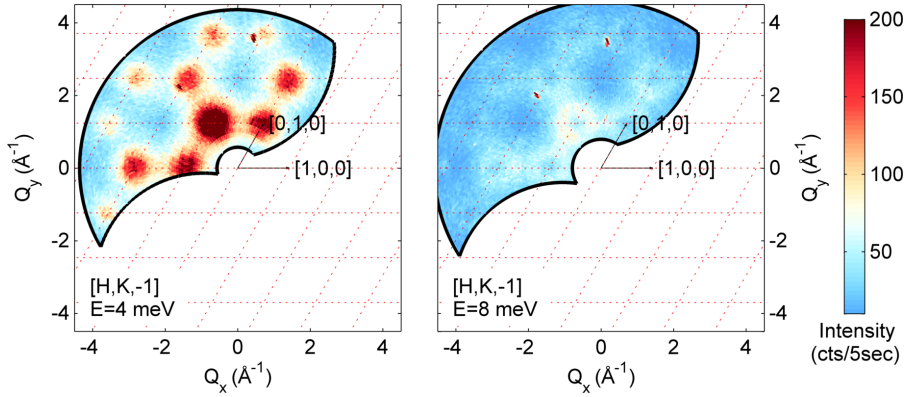

Figure C.2.: Intensity mapping of magnetic excitations in $Ni_xMn_{1-x}TiO_3$ in the $[H, K, 1]$ plane in $Ni_xMn_{1-x}TiO_3$ at 2 K at IN8. The scattered neutron intensity was collected at constant energies (a) 4 meV and (b) 8 meV. The same linear color scale was used for both maps.

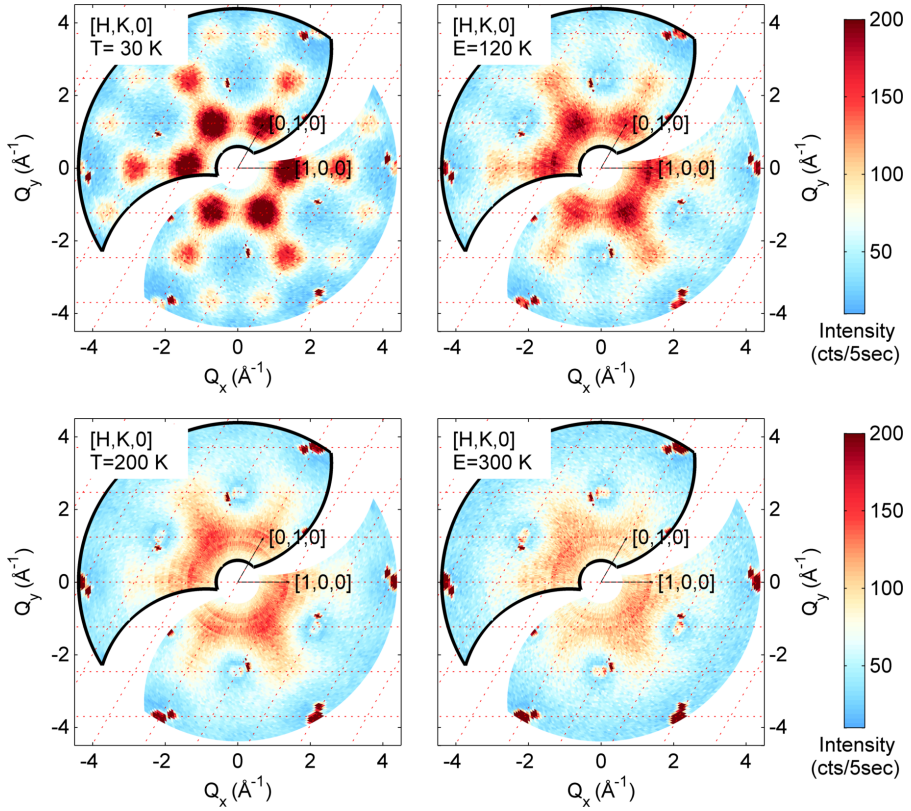

Figure C.3.: Temperature dependence of magnetic excitations in $Ni_xMn_{1-x}TiO_3$ in the $[H, K, 0]$ plane in $Ni_xMn_{1-x}TiO_3$ at IN8. The scattered neutron intensity was collected at constant energy of 4 meV. The same linear color scale was used for both maps. The black frame indicate the experimental data, the maps were completed by symmetrization.

Bibliography

[1] F. Vargas, *Coule La Seine* (J'Ai Lu, 2005). [p. 3]

[2] P. Curie, *Sur la symétrie dans les phénomènes physiques, symétrie d'un champ électrique et d'un champ magnétique*, J. Phys. Théor. Appl. **3**, 393 (1894). [p. 9], [p. 12]

[3] K. Dörr and A. Herklotz, *Materials science: Two steps for a magnetoelectric switch*, Nature **516**, 337 (2014). [p. 9]

[4] N. A. Hill, *Why Are There so Few Magnetic Ferroelectrics?*, J. Phys. Chem. B **104**, 6694 (2000). [p. 9], [p. 14]

[5] T. Kimura, T. Goto, H. Shintani, K. Ishizaka, T. Arima and Y. Tokura, *Magnetic control of ferroelectric polarization*, Nature **426**, 55 (2003). [p. 9], [p. 10], [p. 12], [p. 15], [p. 17], [p. 37], [p. 40], [p. 41], [p. 89], [p. 149], [p. 187]

[6] D. Khomskii, *Transition Metal Compounds* (Cambridge University Press, 2014). [p. 9], [p. 14], [p. 15], [p. 16], [p. 63], [p. 140]

[7] M. Fiebig, *Revival of the magnetoelectric effect*, J. Phys. D. Appl. Phys. **38**, R123 (2005). [p. 9], [p. 12]

[8] T. Kimura, G. Lawes, T. Goto, Y. Tokura and a. Ramirez, *Magnetoelectric phase diagrams of orthorhombic $RMnO_3$ (R=Gd, Tb, and Dy)*, Phys. Rev. B **71**, 1 (2005). [p. 9], [p. 17], [p. 40], [p. 41], [p. 42], [p. 67], [p. 81], [p. 82]

[9] T. Goto, T. Kimura, G. Lawes, a. P. Ramirez and Y. Tokura, *Ferroelectricity and Giant Magnetocapacitance in Perovskite Rare-Earth Manganites*, Phys. Rev. Lett. **92**, 1 (2004). [p. 9], [p. 37], [p. 40], [p. 41]

[10] S.-W. Cheong and M. Mostovoy, *Multiferroics: a magnetic twist for ferroelectricity*, Nat. Mater. **6**, 13 (2007). [p. 9], [p. 14]

[11] M. Kenzelmann, a. Harris, S. Jonas, C. Broholm, J. Schefer, S. Kim, C. Zhang, S.-W. Cheong, O. Vajk and J. Lynn, *Magnetic Inversion Symmetry*

Breaking and Ferroelectricity in $TbMnO_3$, Phys. Rev. Lett. **95**, 27 (2005). [p. 9], [p. 37], [p. 39], [p. 40], [p. 51], [p. 58], [p. 60], [p. 66], [p. 78], [p. 93], [p. 147]

[12] D. Senff, P. Link, K. Hradil, a. Hiess, L. P. Regnault, Y. Sidis, N. Aliouane, D. N. Argyriou and M. Braden, *Magnetic Excitations in Multiferroic $TbMnO_3$: Evidence for a Hybridized Soft Mode*, Phys. Rev. Lett. **98**, 28 (2007). [p. 9], [p. 18], [p. 19], [p. 37], [p. 44], [p. 45], [p. 57], [p. 64], [p. 65], [p. 66], [p. 73], [p. 74], [p. 83], [p. 84], [p. 89], [p. 97], [p. 187], [p. 188]

[13] H. Sagayama, K. Taniguchi, N. Abe, T.-h. Arima, M. Soda, M. Matsuura and K. Hirota, *Correlation between ferroelectric polarization and sense of helical spin order in multiferroic $MnWO_4$*, Phys. Rev. B **77**, 220407 (2008). [p. 9], [p. 91], [p. 95], [p. 112], [p. 124], [p. 188]

[14] Y. Tokura, S. Seki and N. Nagaosa, *Multiferroics of spin origin*, Reports on Progress in Physics **77**, 076501 (2014). [p. 9], [p. 15], [p. 19]

[15] H. Katsura, N. Nagaosa and A. Balatsky, *Spin Current and Magnetoelectric Effect in Noncollinear Magnets*, Phys. Rev. Lett. **95**, 57205 (2005). [p. 10], [p. 16], [p. 40], [p. 94], [p. 97], [p. 114], [p. 149], [p. 154]

[16] I. Sergienko and E. Dagotto, *Role of the Dzyaloshinskii-Moriya interaction in multiferroic perovskites*, Phys. Rev. B **73**, 094434 (2006). [p. 10], [p. 16], [p. 17], [p. 40], [p. 154]

[17] K. Taniguchi, N. Abe, T. Takenobu, Y. Iwasa and T. Arima, *Ferroelectric Polarization Flop in a Frustrated Magnet $MnWO_4$ Induced by a Magnetic Field*, Phys. Rev. Lett. **97**, 97203 (2006). [p. 10], [p. 17], [p. 91], [p. 93], [p. 94], [p. 95], [p. 115], [p. 124], [p. 125]

[18] Y. Yamaguchi, T. Nakano, Y. Nozue and T. Kimura, *Magnetoelectric Effect in an XY-like Spin Glass System $Ni_xMn_{1-x}TiO_3$*, Phys. Rev. Lett. **108**, 057203 (2012). [p. 10], [p. 149], [p. 154], [p. 155], [p. 157], [p. 170], [p. 171], [p. 186], [p. 189]

[19] W. Eerenstein, N. D. Mathur and J. F. Scott, *Multiferroic and magnetoelectric materials.*, Nature **442**, 759 (2006). [p. 11]

[20] J. C. Maxwell, *A Dynamical Theory of the Electromagnetic Field*, Philosophical Transactions of the Royal Society of London **155**, 459 (1865). [p. 11]

[21] Y. Wang, J. Li and D. Viehland, *Magnetoelectrics for magnetic sensor applications: status, challenges and perspectives*, Materials Today **17**, 269 (2014). [p. 12]

[22] D. Astrov, *The magnetoelectric effects*, Sov. Phys. JETP **11**, 708 (1960). [p. 12]

[23] I. E. Dzyaloshinskii, *On the Magneto-Electrical Effect In Antiferromagnets*, Sov. Phys. JETP **4**, 241 (1959). [p. 12], [p. 16]

[24] L. D. Landau, L. P. Pitaevskii and E. Lifshitz, *Electrodynamics of Continuous Media, Second Edition: Volume 8 (Course of Theoretical Physics S)* (Butterworth-Heinemann, 1984). [p. 12]

[25] *International Tables for Crystallography, Volume D: Physical Properties of Crystals*, 1st ed., edited by A. Authier (Kluwer Academic Publishers, 2003). [p. 13]

[26] G. A. Gehring, *On the microscopic theory of the magnetoelectric effect*, Ferroelectrics **161**, 275 (1994). [p. 13]

[27] W. F. Brown, R. M. Hornreich and S. Shtrikman, *Upper Bound on the Magnetoelectric Susceptibility*, Phys. Rev. **168**, 574 (1968). [p. 13]

[28] H. Schmid, *Multi-ferroic magnetoelectrics*, Ferroelectrics **162**, 317 (1994). [p. 13]

[29] G. A. Smolenskii and C. I. E., *Ferroelectromagnets*, Soviet Physics Uspekhi **25**, 475 (1982). [p. 13], [p. 43]

[30] E. Ascher, H. Rieder, H. Schmid and H. Stössel, *Some Properties of Ferromagnetoelectric Nickel-Iodine Boracite, $Ni_3B_7O_{13}I$*, J. Appl. Phys. **37**, 1404 (1966). [p. 14]

[31] H. Schmid, *Some symmetry aspects of ferroics and single phase multiferroics*, J. Phys.: Condens. Matter **20**, 434201 (2008). [p. 14], [p. 146], [p. 155]

[32] D. Khomskii, *Multiferroics: Different ways to combine magnetism and ferroelectricity*, J. Magn. Magn. Mater. **306**, 1 (2006). [p. 14]

[33] K. Wang, J.-M. Liu and Z. Ren, *Multiferroicity: the coupling between magnetic and polarization orders*, Adv. Phys. **58**, 321 (2009). [p. 14]

[34] D. Khomskii, *Classifying multiferroics: Mechanisms and effects*, Physics **2**, (2009). [p. 15], [p. 17], [p. 91]

[35] L. W. Martin, S. P. Crane, Y.-H. Chu, M. B. Holcomb, M. Gajek, M. Huijben, C.-H. Yang, N. Balke and R. Ramesh, *Multiferroics and magnetoelectrics: thin films and nanostructures*, J. Phys.: Condens. Matter **20**, 434220 (2008). [p. 15]

[36] T. Zhao, A. Scholl, F. Zavaliche, K. Lee, M. Barry, A. Doran, M. Cruz, Y. Chu, C. Ederer, N. Spaldin, R. Das, D. Kim, S. Baek, C. Eom and R. Ramesh, *Electrical control of antiferromagnetic domains in multiferroic BiFeO3 films at room temperature*, Nat. Mater. **5**, 823 (2006). [p. 15]

[37] H. Béa, M. Gajek, M. Bibes and A. Barthélémy, *Spintronics with multiferroics*, J. Phys.: Condens. Matter **20**, 434221 (2008). [p. 15]

[38] T. Kimura, *Spiral Magnets as Magnetoelectrics*, Annu. Rev. Mater. Res. **37**, 387 (2007). [p. 15], [p. 42]

[39] Y. J. Choi, H. T. Yi, S. Lee, Q. Huang, V. Kiryukhin and S.-W. Cheong, *Ferroelectricity in an Ising Chain Magnet*, Phys. Rev. Lett. **100**, 047601 (2008). [p. 15]

[40] I. A. Sergienko, S. Cengiz and E. Dagotto, *Ferroelectricity in the Magnetic E-Phase of Orthorhombic Perovskites*, Phys. Rev. Lett. **97**, 227204 (2006). [p. 16]

[41] T.-h. Arima, *Ferroelectricity Induced by Proper-Screw Type Magnetic Order*, J. Phys. Soc. Jpn. **76**, 073702 (2007). [p. 16]

[42] H. Murakawa, Y. Onose, S. Miyahara, N. Furukawa and Y. Tokura, *Ferroelectricity Induced by Spin-Dependent Metal-Ligand Hybridization in* $Ba_2CoGe_2O_7$, Phys. Rev. Lett. **105**, 137202 (2010). [p. 16]

[43] M. Mostovoy, *Ferroelectricity in Spiral Magnets*, Phys. Rev. Lett. **96**, 67601 (2006). [p. 16], [p. 40], [p. 42], [p. 64], [p. 95], [p. 149]

[44] T. Moriya, *Anisotropic Superexchange Interaction and Weak Ferromagnetism*, Phys. Rev. **120**, 91 (1960). [p. 16]

[45] G. Lawes, A. B. Harris, T. Kimura, N. Rogado, R. J. Cava, A. Aharony, O. Entin-Wohlman, T. Yildirim, M. Kenzelmann, C. Broholm and et al., *Magnetically Driven Ferroelectric Order in* $Ni_2V_3O_8$, Phys. Rev. Lett. **95**, 087205 (2005). [p. 17]

[46] O. Heyer, N. Hollmann, I. Klassen, S. Jodlauk, L. Bohatý, P. Becker, J. Mydosh, T. Lorenz and D. Khomskii, *A new multiferroic material:* $MnWO_4$, J. Phys.: Condens. Matter. **18**, L471 (2006). [p. 17], [p. 91], [p. 93], [p. 94], [p. 125]

[47] A. Arkenbout, T. Palstra, T. Siegrist and T. Kimura, *Ferroelectricity in the cycloidal spiral magnetic phase of* $MnWO_4$, Phys. Rev. B **74**, 184431 (2006). [p. 17], [p. 91], [p. 93], [p. 94], [p. 95], [p. 96], [p. 125]

[48] N. Aliouane, K. Schmalzl, D. Senff, a. Maljuk, K. Prokeš, M. Braden and D. Argyriou, *Flop of Electric Polarization Driven by the Flop of the Mn Spin Cycloid in Multiferroic $TbMnO_3$*, Phys. Rev. Lett. **102**, 207205 (2009). [p. 17], [p. 40], [p. 42], [p. 81], [p. 83], [p. 90]

[49] Y. Yamasaki, H. Sagayama, T. Goto, M. Matsuura, K. Hirota, T. Arima and Y. Tokura, *Electric Control of Spin Helicity in a Magnetic Ferroelectric*, Phys. Rev. Lett. **98**, 1 (2007). [p. 17], [p. 32], [p. 41], [p. 73], [p. 75]

[50] T. Finger, D. Senff, K. Schmalzl, W. Schmidt, L. P. Regnault, P. Becker, L. Bohatý and M. Braden, *Electric-field control of the chiral magnetism of multiferroic $MnWO_4$ as seen via polarized neutron diffraction*, Phys. Rev. B **81**, 1 (2010). [p. 17], [p. 91], [p. 95], [p. 112], [p. 173]

[51] M. Baum, J. Leist, T. Finger, K. Schmalzl, A. Hiess, L. Regnault, P. Becker, L. Bohatý, G. Eckold and M. Braden, *Kinetics of the multiferroic switching in $MnWO_4$*, Phys. Rev. B **89**, 144406 (2014). [p. 17], [p. 91], [p. 95]

[52] J. Stein, M. Baum, S. Holbein, V. Hutanu, A. C. Komarek and M. Braden, *Control of multiferroic domains by external electric fields in $TbMnO_3$*, J. Phys.: Condens. matter **27**, 446001 (2015). [p. 17], [p. 42]

[53] S. Blundell, *Magnetism in Condensed Matter (Oxford Master Series in Physics)*, 1 ed. (Oxford University Press, USA, 2001). [p. 17], [p. 63], [p. 93], [p. 95], [p. 127]

[54] H. Katsura, A. V. Balatsky and N. Nagaosa, *Dynamical Magnetoelectric Coupling in Helical Magnets*, Phys. Rev. Lett. **98**, 027203 (2007). [p. 18], [p. 19], [p. 37], [p. 43], [p. 44], [p. 86], [p. 87]

[55] T. Finger, K. Binder, Y. Sidis, A. Maljuk, D. N. Argyriou and M. Braden, *Magnetic order and electromagnon excitations in $DyMnO_3$ studied by neutron scattering experiments*, Phys. Rev. B **90**, 224418 (2014). [p. 18], [p. 19], [p. 44], [p. 61], [p. 67], [p. 87]

[56] D. Senff, P. Link, N. Aliouane, D. Argyriou and M. Braden, *Field dependence of magnetic correlations through the polarization flop transition in multiferroic $TbMnO_3$: Evidence for a magnetic memory effect*, Phys. Rev. B **77**, 174419 (2008). [p. 19], [p. 44], [p. 81], [p. 86], [p. 88]

[57] A. Pimenov, A. A. Mukhin, V. Y. Ivanov, V. D. Travkin, a. M. Balbashov and A. Loidl, *Possible evidence for electromagnons in multiferroic manganites*, Nat. Phys. **2**, 97 (2006). [p. 19], [p. 37], [p. 44], [p. 67], [p. 89], [p. 97], [p. 188]

[58] Y. Takahashi, N. Kida, Y. Yamasaki, J. Fujioka, T. Arima, R. Shimano, S. Miyahara, M. Mochizuki, N. Furukawa and Y. Tokura, *Evidence for an*

Electric-Dipole Active Continuum Band of Spin Excitations in Multiferroic $TbMnO_3$, Phys. Rev. Lett. **101**, 187201 (2008). [p. 19]

[59] A. Pimenov, A. Shuvaev, A. Loidl, F. Schrettle, A. Mukhin, V. Travkin, V. Ivanov and A. Balbashov, *Magnetic and Magnetoelectric Excitations in $TbMnO_3$*, Phys. Rev. Lett. **102**, 107203 (2009). [p. 19], [p. 44], [p. 67], [p. 79], [p. 81]

[60] A. M. Shuvaev, V. D. Travkin, V. Y. Ivanov, A. A. Mukhin and A. Pimenov, *Evidence for Electroactive Excitation of the Spin Cycloid in $TbMnO_3$*, Phys. Rev. Lett. **104**, 097202 (2010). [p. 19], [p. 44], [p. 81], [p. 86], [p. 87], [p. 90], [p. 188]

[61] S. Holbein, P. Steffens, T. Finger, A. C. Komarek, Y. Sidis, P. Link and M. Braden, *Field and temperature dependence of electromagnon scattering in$TbMnO_3$ studied by inelastic neutron scattering*, Phys. Rev. B **91**, 014432 (2015). [p. 19], [p. 44]

[62] Y. Takahashi, R. Shimano, Y. Kaneko, H. Murakawa and Y. Tokura, *Magnetoelectric resonance with electromagnons in a perovskite helimagnet*, Nature Physics **8**, 121 (2011). [p. 19]

[63] R. Valdés Aguilar, A. B. Sushkov, C. L. Zhang, Y. J. Choi, S.-W. Cheong and H. D. Drew, *Colossal magnon-phonon coupling in multiferroic $Eu_{0.75}Y_{0.25}MnO_3$*, Phys. Rev. B **76**, 060404(R) (2007). [p. 19]

[64] A. B. Sushkov, R. V. Aguilar, S. Park, S.-W. Cheong and H. D. Drew, *Electromagnons in Multiferroic YMn_2O_5 and $TbMn_2O_5$*, Phys. Rev. Lett. **98**, 027202 (2007). [p. 19]

[65] N. Kida, Y. Ikebe, Y. Takahashi, J. P. He, Y. Kaneko, Y. Yamasaki, R. Shimano, T. Arima, N. Nagaosa and Y. Tokura, *Electrically driven spin excitation in the ferroelectric magnet $DyMnO_3$*, Phys. Rev. B **78**, 104414 (2008). [p. 19], [p. 67]

[66] R. Valdés Aguilar, M. Mostovoy, A. Sushkov, C. Zhang, Y. Choi, S.-W. Cheong and H. Drew, *Origin of Electromagnon Excitations in Multiferroic $RMnO_3$*, Phys. Rev. Lett. **102**, 047203 (2009). [p. 19], [p. 37], [p. 44]

[67] S. Seki, N. Kida, S. Kumakura, R. Shimano and Y. Tokura, *Electromagnons in the Spin Collinear State of a Triangular Lattice Antiferromagnet*, Phys. Rev. Lett. **105**, 097207 (2010). [p. 19]

[68] M. Kenzelmann, *Retrospective - Electromagnons offer the best of two worlds*, Physics (College. Park. Md). **4**, 88 (2011). [p. 19]

[69] W. Chen and M. Sigrist, *Dissipationless Multiferroic Magnonics*, Phys. Rev. Lett. **114**, 157203 (2015). [p. 19]

[70] M. Matsubara, S. Manz, M. Mochizuki, T. Kubacka, A. Iyama, N. Aliouane, T. Kimura, S. L. Johnson, D. Meier and M. Fiebig, *Magnetoelectric domain control in multiferroic $TbMnO_3$*, Science **348**, 1112 (2015). [p. 19]

[71] B. T. M. Willis and C. J. Carlile, *Experimental Neutron Scattering* (Oxford University Press, 2009). [p. 21], [p. 34], [p. 192]

[72] A. Furrer, J. Mesot and T. Strässle, *Neutron Scattering in Condensed Matter Physics (Neutron Techniques and Applications) (Series on Neutron Techniques and Applications)* (World Scientific Publishing Company, 2009). [p. 21], [p. 26]

[73] C. G. Shull and J. S. Smart, *Detection of Antiferromagnetism by Neutron Diffraction*, Phys. Rev. **76**, 1256 (1949). [p. 22]

[74] J. Chadwick, *Possible existence of a neutron*, Nature **129**, 312 (1932). [p. 22]

[75] F. Bloch, *On the Magnetic Scattering of Neutrons*, Phys. Rev. **50**, 259 (1936). [p. 22]

[76] B. N. Brockhouse and A. T. Stewart, *Scattering of Neutrons by Phonons in an Aluminum Single Crystal*, Phys. Rev. **100**, 756 (1955). [p. 22]

[77] G. L. Squires, *Introduction to the Theory of Thermal Neutron Scattering* (Dover Publications, 1997). [p. 22], [p. 30]

[78] T. Chatterji, in *Neutron Scattering from Magnetic Materials*, edited by T. Chatterji (Elsevier B. V., 2006), Chap. 1 - Magnetic Neutron Scattering, p. 215-244. [p. 22], [p. 23]

[79] *The yellow book - Guide to neutron research facilities*, Institut Laue-Langevin (2008), E-book, available online at `http://www.ill.eu/instruments-support/`; visited on October 6th 2015. [p. 24], [p. 117]

[80] W. Massa, *Kristallstrukturbestimmung* (Vieweg+Teubner Verlag, 2007). [p. 24]

[81] Fullprof by J. Rodriguez-Carvajal, available online at `www.ill.eu/sites/fullprof/`; visited on October 6th 2015. [p. 24], [p. 26], [p. 136], [p. 137], [p. 139]

[82] MATLAB, *version 8.3.0.532 (R2014a 64-bit)* (The MathWorks Inc., 2014). [p. 24], [p. 193]

[83] G. Shirane, S. M. Shapiro and J. M. Tranquada, *Neutron Scattering with a Triple-Axis Spectrometer: Basic Techniques* (Cambridge University Press, 2006). [p. 27]

[84] M. Kempa, B. Janousova, J. Saroun, P. Flores, M. Boehm, F. Demmel and J. Kulda, *The FlatCone multianalyzer setup for ILL's three-axis spectrometers*, Physica B: Condensed Matter **385-386**, 1080 (2006). [p. 27], [p. 160], [p. 198]

[85] *MATLAB* library for treatment of Flatcone and TAS Data by P. Steffens, available online at `https://www.ill.eu/instruments-support/instruments-groups/instruments/in20/more/software/`; visited on October 6th 2015. [p. 27], [p. 103], [p. 182]

[86] J. Ollivier and H. Mutka, *IN5 Cold Neutron Time-of-Flight Spectrometer, Prepared to Tackle Single Crystal Spectroscopy*, J. Phys. Soc. Jpn. **80**, SB003 (2011). [p. 27], [p. 68]

[87] Horace suite for *MATLAB*, available online at `horace.isis.rl.ac.uk`; visited on October 6th 2015. [p. 27], [p. 68]

[88] F. Bloch, *Zur Theorie des Ferromagnetismus*, Z. Physik **61**, 206 (1930). [p. 28]

[89] J. C. Slater, *Cohesion in Monovalent Metals*, Phys. Rev. **35**, 509 (1930). [p. 28]

[90] A. W. Sáenz, *Spin Waves in Exchange-Coupled Complex Magnetic Structures and Neutron Scattering*, Phys. Rev. **125**, 1940 (1962). [p. 28], [p. 57]

[91] S. Toth and B. Lake, *Linear spin wave theory for single-Q incommensurate magnetic structures*, J. Phys.: Condens. Matter **27**, 166002 (2015). [p. 28], [p. 57]

[92] J. T. Haraldsen and R. S. Fishman, *Spin rotation technique for non-collinear magnetic systems: application to the generalized Villain model*, J. Phys.: Condens. Matter **21**, 216001 (2009). [p. 28]

[93] S. Petit, *Numerical simulations and magnetism*, Collection SFN **12**, 105 (2011). [p. 28]

[94] spinW, version 2.1 revision 238, by S. Toth, available online at `www.psi.ch/spinw`; visited on October 6th 2015. [p. 28], [p. 29], [p. 57], [p. 64], [p. 122], [p. 181], [p. 183], [p. 184], [p. 185], [p. 193]

[95] T. Holstein and H. Primakoff, *Field Dependence of the Intrinsic Domain Magnetization of a Ferromagnet*, Phys. Rev. **58**, 1098 (1940). [p. 28]

[96] J. Colpa, *Diagonalization of the quadratic boson hamiltonian*, Physica A: Statistical Mechanics and its Applications **93**, 327 (1978). [p. 28]

[97] F. Moussa, M. Hennion, J. Rodriguez-Carvajal, H. Moudden, L. Pinsard and a. Revcolevschi, *Spin waves in the antiferromagnet perovskite LaMnO3: A neutron-scattering study.*, Phys. Rev. B. Condens. Matter **54**, 15149 (1996). [p. 29], [p. 57]

[98] *Neutron Scattering from Magnetic Materials*, edited by T. Chatterji (Elsevier Science, 2006). [p. 30]

[99] R. M. Moon, T. Riste and W. C. Koehler, *Polarization Analysis of Thermal-Neutron Scattering*, Phys. Rev. **181**, 920 (1969). [p. 30], [p. 31], [p. 34], [p. 105]

[100] M. Blume, *Polarization Effects in the Magnetic Elastic Scattering of Slow Neutrons*, Phys. Rev. **130**, 1670 (1963). [p. 31]

[101] S. Maleev, V. Bar'yakhtar and R. Suris, *The scattering of slow neutrons by complex magnetic structures*, Sov. Phys. Solid State **4**, 2533 (1963). [p. 31]

[102] P. J. Brown, in *Neutron Scattering from Magnetic Materials*, edited by T. Chatterji (Elsevier B. V., 2006), Chap. 5 - Spherical Neutron Polarimetry, p. 215-244. [p. 32], [p. 165], [p. 170]

[103] P. Steffens, privat communication. [p. 33]

[104] L. P. Regnault, in *Neutron Scattering from Magnetic Materials*, edited by T. Chatterji (Elsevier B. V., 2006), Chap. 8 - Inelastic Neutron Polarization Analysis, p. 215-244. [p. 34]

[105] J. R. Stewart, P. P. Deen, K. H. Andersen, H. Schober, J.-F. Barthélémy, J. M. Hillier, A. P. Murani, T. Hayes and B. Lindenau, *Disordered materials studied using neutron polarization analysis on the multi-detector spectrometer, D7*, Journal of Applied Crystallography **42**, 69 (2008). [p. 34], [p. 102], [p. 105]

[106] *The spin of the neutron as a measuring probe*by O. Schärpf (2010), E-book, available online at `http://host-82-135-31-182.customer.m-online.net/neutronpol.pdf`; visited on October 6th 2015. [p. 34], [p. 102]

[107] F. Givord, J. Schweizer and F. Tasset, *On the magnetic structure of CeAl2: a 3-d neutron polarization analysis investigation*, Physica B: Condensed Matter **234-236**, 685 (1997). [p. 35]

[108] F. Tasset, *Neutron beams at the spin revolution*, Physica B: Condens. Matter **297**, 1 (2001). [p. 35], [p. 170]

[109] E. Leliévre-Berna, E. Bourgeat-Lami, P. Fouilloux, B. Geffray, Y. Gibert, K. Kakurai, N. Kernavanois, B. Longuet, F. Mantegezza, M. Nakamura and et al., *Advances in spherical neutron polarimetry with Cryopad*, Physica B: Condensed Matter **356**, 131 (2005). [p. 35], [p. 165]

[110] *Neutron Spin Echo Spectroscopy: Basics, Trends and Applications (Lecture Notes in Physics)*, edited by F. Mezei, C. Pappas and T. Gutberlet (Springer, 2003). [p. 35]

[111] B. Farago, *Recent neutron spin-echo developments at the ILL (IN11 and IN15)*, Physica B: Cond. Matter **267-268**, 270 (1999). [p. 35]

[112] J. Blasco, C. Ritter, J. García, J. de Teresa, J. Pérez-Cacho and M. Ibarra, *Structural and magnetic study of $Tb_{1-x}Ca_xMnO_3$ perovskites*, Phys. Rev. B **62**, 5609 (2000). [p. 37], [p. 47], [p. 58], [p. 66]

[113] Web of science search for *TbMnO3*, available online at `http://apps.webofknowledge.com`; visited on October 6th 2015. [p. 37]

[114] M. Mochizuki, N. Furukawa and N. Nagaosa, *Theory of Electromagnons in the Multiferroic Mn Perovskites: The Vital Role of Higher Harmonic Components of the Spiral Spin Order*, Phys. Rev. Lett. **104**, 177206 (2010). [p. 37], [p. 61], [p. 64], [p. 65], [p. 67], [p. 76], [p. 187]

[115] J. Jensen and A. R. Mackintosh, in *Rare Earth Magnetism: Structures and Excitations (The International Series of Monographs on Physics)*, edited by J. Birman, S. F. Edwards, C. H. L. Smith and M. Rees (Clarendon Press, 1991). [p. 38]

[116] D. Senff, Dissertation, *Neutron Scattering Studies on Magnetic Excitations in Complex Ordered Manganites*, Universität zu Köln, (2007). [p. 38], [p. 61], [p. 64], [p. 68]

[117] D. Meier, Diplomarbeit, *Thermische Ausdehnung und Magnetostriktion multiferroischer Seltenerdmanganate*, Universtität zu Köln, (2006). [p. 38]

[118] R. D. Shannon, *Revised effective ionic radii and systematic studies of interatomic distances in halides and chalcogenides*, Acta Cryst. **32**, 751 (1976). [p. 38], [p. 93], [p. 126]

[119] T. Kimura, S. Ishihara, H. Shintani, T. Arima, K. Takahashi, K. Ishizaka and Y. Tokura, *Distorted perovskite with e_g^1 configuration as a frustrated spin system*, Phys. Rev. B **68**, 060403 (2003). [p. 38], [p. 39]

[120] J. Rodríguez-Carvajal, M. Hennion, F. Moussa, A. H. Moudden, L. Pinsard and A. Revcolevschi, *Neutron-diffraction study of the Jahn-Teller transition in stoichiometric $LaMnO_3$*, Phys. Rev. B **57**, R3189 (1998). [p. 38]

[121] M. W. Kim, S. J. Moon, J. H. Jung, J. Yu, S. Parashar, P. Murugavel, J. H. Lee and T. W. Noh, *Effect of Orbital Rotation and Mixing on the Optical Properties of Orthorhombic $RMnO_3$ (R = La, Pr, Nd, Gd, and Tb)*, Phys. Rev. Le **96**, 247205 (2006). [p. 39]

[122] J.-S. Zhou and J. Goodenough, *Unusual Evolution of the Magnetic Interactions versus Structural Distortions in $RMnO_3$ Perovskites*, Phys. Rev. Lett. **96**, 247202 (2006). [p. 39]

[123] R. Kajimoto, H. Mochizuki, H. Yoshizawa, H. Shintani, T. Kimura and Y. Tokura, *R -Dependence of Spin Exchange Interactions in $RMnO_3$ (R = Rare-Earth Ions)*, J. Phys. Soc. Japan **74**, 2430 (2005). [p. 39], [p. 78]

[124] J. B. Goodenough, *Theory of the Role of Covalence in the Perovskite-Type Manganites [La, M(II)]MnO_3*, Phys. Rev. **100**, 564 (1955). [p. 39]

[125] S. Quezel, F. Tcheou, J. Rossat-Mignod, G. Quezel and E. Roudaut, *Magnetic structure of the perovskite-like compound $TbMnO_3$*, Physica **86**, 916 (1977). [p. 39], [p. 40], [p. 46]

[126] E. F. Bertaut, *Representation analysis of magnetic structures*, Acta Cryst. **A24**, 217 (1968). [p. 39], [p. 92], [p. 136]

[127] N. Aliouane, O. Prokhnenko, R. Feyerherm, M. Mostovoy, J. Strempfer, K. Habicht, K. C. Rule, E. Dudzik, a. U. B. Wolter, A. Maljuk and D. N. Argyriou, *Magnetic order and ferroelectricity in $RMnO_3$ multiferroic manganites: coupling between R- and Mn-spins*, J. Phys.: Condens. Matter **20**, 434215 (2008). [p. 39], [p. 40]

[128] M. Baum, Dissertation, *Neutron-Scattering Studies on Chiral Multiferroics*, Universität zu Köln, (2013). [p. 39], [p. 42], [p. 54], [p. 73]

[129] D. Meier, N. Aliouane, D. N. Argyriou, J. a. Mydosh and T. Lorenz, *New features in the phase diagram of $TbMnO_3$*, New J. Phys. **9**, 100 (2007). [p. 40]

[130] R. Kajimoto, H. Yoshizawa, H. Shintani, T. Kimura and Y. Tokura, *Magnetic structure of $TbMnO_3$ by neutron diffraction*, Phys. Rev. B **70**, 012401 (2004). [p. 40], [p. 46], [p. 54]

[131] O. Prokhnenko, R. Feyerherm, M. Mostovoy, N. Aliouane, E. Dudzik, A. U. B. Wolter, A. Maljuk and D. N. Argyriou, *Coupling of Frustrated Ising Spins to the Magnetic Cycloid in Multiferroic $TbMnO_3$*, Phys. Rev. Lett. **99**, 177206 (2007). [p. 40], [p. 46], [p. 65], [p. 78]

[132] J. Voigt, J. Persson, J. W. Kim, G. Bihlmayer and T. Brückel, *Strong coupling between the spin polarization of Mn and Tb in multiferroic $TbMnO_3$*

determined by x-ray resonance exchange scattering, Phys. Rev. B **76**, 104431 (2007). [p. 40], [p. 78]

[133] K. Noda, M. Akaki, T. Kikuchi, D. Akahoshi and H. Kuwahara, *Magnetic-field-induced switching between ferroelectric phases in orthorhombic-distortion-controlled $RMnO_3$*, Journal of Applied Physics **99**, 08S905 (2006). [p. 41]

[134] T. Arima, A. Tokunaga, T. Goto, H. Kimura, Y. Noda and Y. Tokura, *Collinear to Spiral Spin Transformation without Changing the Modulation Wavelength upon Ferroelectric Transition in $Tb_{1-x}Dy_xMnO_3$*, Phys. Rev. Lett. **96**, 097202 (2006). [p. 41]

[135] H. Kuwahara, M. Akaki, J. Tozawa, M. Hitomi, K. Noda and D. Akahoshi, *Persistent and reversible phase control in $GdMnO_3$ near the phase boundary*, Journal of Physics: Conference Series **150**, 042106 (2009). [p. 41]

[136] W. J. Merz, *Double Hysteresis Loop of $BaTiO_3$ at the Curie Point*, Phys. Rev. **91**, 513 (1953). [p. 41]

[137] T. Finger, Dissertation, *Analyse magnetischer Korrelationen in geschichteten oder multiferroischen Übergangsmetalloxiden durch Neutronenstreuung*, Universität zu Köln, (2013). [p. 42], [p. 45], [p. 55], [p. 73], [p. 75], [p. 94], [p. 97], [p. 114], [p. 119], [p. 121], [p. 123]

[138] T. Arima, T. Goto, Y. Yamasaki, S. Miyasaka, K. Ishii, M. Tsubota, T. Inami, Y. Murakami and Y. Tokura, *Magnetic-field-induced transition in the lattice modulation of colossal magnetoelectric $GdMnO_3$ and $TbMnO_3$ compounds*, Phys. Rev. B **72**, 100102 (2005). [p. 42]

[139] N. Aliouane, D. Argyriou, J. Strempfer, I. Zegkinoglou, S. Landsgesell and M. Zimmermann, *Field-induced linear magnetoelastic coupling in multiferroic $TbMnO_3$*, Phys. Rev. B **73**, 020102 (2006). [p. 42], [p. 81]

[140] P. Tolédano, *Pseudo-proper ferroelectricity and magnetoelectric effects in $TbMnO_3$*, Phys. Rev. B **79**, 094416 (2009). [p. 42]

[141] M. Mochizuki and N. Furukawa, *Theory of Magnetic Switching of Ferroelectricity in Spiral Magnets*, Phys. Rev. Lett. **105**, 187601 (2010). [p. 42], [p. 61]

[142] D. Senff, N. Aliouane, D. N. Argyriou, A. Hiess, L. P. Regnault, P. Link, K. Hradil, Y. Sidis and M. Braden, *Magnetic excitations in a cycloidal magnet: the magnon spectrum of multiferroic $TbMnO_3$*, J. Phys.: Condens. Matter **20**, 434212 (2008). [p. 44], [p. 51], [p. 56], [p. 57], [p. 61], [p. 64], [p. 67], [p. 78], [p. 82], [p. 88]

[143] A. I. Milstein and O. P. Sushkov, *Magnetic excitations in the spin-spiral state of $TbMnO_3$ and $DyMnO_3$*, Phys. Rev. B **91**, 094417 (2015). [p. 44], [p. 60], [p. 64], [p. 65], [p. 187]

[144] A. M. Shuvaev, A. A. Mukhin and A. Pimenov, *Magnetic and magnetoelectric excitations in multiferroic manganites.*, J. Phys.: Condens. Matter **23**, 113201 (2011). [p. 44], [p. 79]

[145] M. Mochizuki, N. Furukawa and N. Nagaosa, *Theory of spin-phonon coupling in multiferroic manganese perovskites $RMnO_3$*, Phys. Rev. B **84**, 144409 (2011). [p. 44], [p. 49]

[146] P. Rovillain, M. Cazayous, Y. Gallais, M.-a. Measson, a. Sacuto, H. Sakata and M. Mochizuki, *Magnetic Field Induced Dehybridization of the Electromagnons in Multiferroic $TbMnO_3$*, Phys. Rev. Lett. **107**, 027202 (2011). [p. 44]

[147] A. C. Komarek, Dissertation, *Complex ordering phenomena in transition metal oxides and oxyhalides*, Universität zu Köln, (2009). [p. 45]

[148] D. O'Flynn, M. R. Lees and G. Balakrishnan, *Magnetic susceptibility and heat capacity measurements of single crystal $TbMnO_3$*, J. Phys.: Condens. Matter **26**, 256002 (2014). [p. 47], [p. 66]

[149] M. F. Collins, in *Magnetic Critical Scattering (Oxford Series on Neutron Scattering in Condensed Matter)*, edited by S. W. Lovesey and E. W. J. Mitchell (Oxford University Press, 1989). [p. 49], [p. 51], [p. 118]

[150] A. B. Harris, A. Aharony and O. Entin-Wohlman, *Order parameters and phase diagrams of multiferroics*, J. Phys.: Condens. Matter **20**, 434202 (2008). [p. 49], [p. 118]

[151] A. Oleaga, A. Salazar, D. Prabhakaran, J.-G. Cheng and J.-S. Zhou, *Critical behavior of the paramagnetic to antiferromagnetic transition in orthorhombic and hexagonal phases of $RMnO_3$ (R=Sm, Tb, Dy, Ho, Er, Tm, Yb, Lu, Y)*, Phys. Rev. B **85**, 184425 (2012). [p. 49]

[152] D. Hohlwein, J.-U. Hoffmann and R. Schneider, *Magnetic interaction parameters from paramagnetic diffuse neutron scattering in MnO*, Phys. Rev. B **68**, 140408R (2003). [p. 49]

[153] R. M. White, *Quantum Theory of Magnetism* (McGraw-Hill Book Company, 1970). [p. 49], [p. 51]

[154] T. Nagamiya, *Helical Spin Ordering - 1 Theory of Helical Spin Configurations*, Solid State Physics 305 (1968). [p. 51]

[155] K. Habicht, T. Keller and R. Golub, *The resolution function in neutron spin-echo spectroscopy with three-axis spectrometers*, Journal of Applied Crystallography **36**, 1307 (2003). [p. 52]

[156] K. Hirota, N. Kaneko, A. Nishizawa and Y. Endoh, *Two-Dimensional Planar Ferromagnetic Coupling in $LaMnO_3$*, J. Phys. Soc. Jpn. **65**, 3736 (1996). [p. 57]

[157] H. J. Xiang, S.-H. Wei, M. H. Whangbo and J. L. F. Da Silva, *Spin-Orbit Coupling and Ion Displacements in Multiferroic $TbMnO_3$*, Phys. Rev. Lett. **101**, 037209 (2008). [p. 61]

[158] A. Malashevich and D. Vanderbilt, *First Principles Study of Improper Ferroelectricity in $TbMnO_3$*, Phys. Rev. Lett. **101**, 037210 (2008). [p. 61]

[159] H. C. Walker, F. Fabrizi, L. Paolasini, F. de Bergevin, J. Herrero-Martin, a. T. Boothroyd, D. Prabhakaran and D. F. McMorrow, *Femtoscale magnetically induced lattice distortions in multiferroic $TbMnO_3$*, Science **333**, 1273 (2011). [p. 61]

[160] I. Solovyev, N. Hamada and K. Terakura, *Crucial Role of the Lattice Distortion in the Magnetism of $LaMnO_3$*, Phys. Rev. Lett. **76**, 4825 (1996). [p. 61]

[161] J. Deisenhofer, M. V. Eremin, D. V. Zakharov, V. A. Ivanshin, R. M. Eremina, H.-A. Krug von Nidda, A. A. Mukhin, A. M. Balbashov and A. Loidl, *Crystal field, Dzyaloshinsky-Moriya interaction, and orbital order in $La_{0.95}Sr_{0.05}MnO_3$ probed by ESR*, Phys. Rev. B **65**, 104440 (2002). [p. 61], [p. 62], [p. 63]

[162] M. Tovar, G. Alejandro, A. Butera, A. Caneiro, M. T. Causa, F. Prado and R. D. Sánchez, *ESR and magnetization in Jahn-Teller-distorted $LaMnO_{3+\delta}$: Correlation with crystal structure*, Phys. Rev. B **60**, 10199 (1999). [p. 61], [p. 66]

[163] M. Mochizuki and N. Furukawa, *Mechanism of Lattice-Distortion-Induced Electric-Polarization Flop in the Multiferroic Perovskite Manganites*, J. Phys. Soc. Japan **78**, 053704 (2009). [p. 61], [p. 65]

[164] M. Mochizuki and N. Furukawa, *Microscopic model and phase diagrams of the multiferroic perovskite manganites*, Phys. Rev. B **80**, 134416 (2009). [p. 61], [p. 63]

[165] T. A. Kaplan, *Frustrated classical Heisenberg model in one dimension with nearest-neighbor biquadratic exchange: Exact solution for the ground-state phase diagram*, Phys. Rev. B **80**, 012407 (2009). [p. 61]

[166] A. Malashevich and D. Vanderbilt, *First-principles theory of magnetically induced ferroelectricity in $TbMnO_3$*, Eur. Phys. J. B **71**, 345 (2009). [p. 65]

[167] N. S. Fedorova, C. Ederer, N. A. Spaldin and A. Scaramucci, *Biquadratic and ring exchange interactions in orthorhombic perovskite manganites*, Phys. Rev. B **91**, 165122 (2015). [p. 65]

[168] M. Baum, unpublished data, see ILL experimental report 4-01-1002. [p. 76], [p. 77]

[169] J. Jensen, *Chiral spin-wave excitations of the spin-$\frac{5}{2}$ trimers in the langasite compound $Ba_3NbFe_3Si_2O_{14}$*, Phys. Rev. B **84**, 104405 (2011). [p. 77]

[170] M. Loire, V. Simonet, S. Petit, K. Marty, P. Bordet, P. Lejay, J. Ollivier, M. Enderle, P. Steffens, E. Ressouche, A. Zorko and R. Ballou, *Parity-Broken Chiral Spin Dynamics in $Ba_3NbFe_3Si_2O_{14}$*, Phys. Rev. Lett. **106**, 207201 (2011). [p. 77]

[171] T. Goto, Y. Yamasaki, H. Watanabe, T. Kimura and Y. Tokura, *Anticorrelation between ferromagnetism and ferroelectricity in perovskite manganites*, Phys. Rev. B **72**, 220403(R) (2005). [p. 78]

[172] N. Reynolds, master thesis, *Investigation through Neutron Experimentation and Crystal Field Calculation into the Connectivity of Multiferroic $DyMnO_3$ and Antiferromagnetic RVO_3, R = [Dy, Tb, Nd, Ce]*, University of New South Wales (2013). [p. 83]

[173] P. Rovillain, J. Liu, M. Cazayous, Y. Gallais, M.-a. Measson, H. Sakata and a. Sacuto, *Electromagnon and phonon excitations in multiferroic $TbMnO_3$*, Phys. Rev. B **86**, 014437 (2012). [p. 87]

[174] H. Weitzel, *Kristallstrukturverfeinerung von Wolframiten und Columbiten*, Z. Kristallogr. **144**, 238 (1976). [p. 91], [p. 92], [p. 93], [p. 96], [p. 125], [p. 126]

[175] G. Lautenschläger, H. Weitzel, T. Vogt, R. Hock, A. Böhm, M. Bonnet and H. Fuess, *Magnetic phase transitions of $MnWO_4$ studied by the use of neutron diffraction*, Phys. Rev. B **48**, 6087 (1993). [p. 91], [p. 92], [p. 93], [p. 98], [p. 147], [p. 188], [p. 189]

[176] A. Poole, P. J. Brown and A. S. Wills, *Spherical neutron polarimetry (SNP) study of magneto-electric coupling in the multiferroic $MnWO_4$*, J. Phys. Conf. Ser. **145**, 012074 (2009). [p. 91], [p. 95]

[177] H. Dachs, *Zur Deutung der magnetischen Struktur des Hübnerits, $MnWO4$*, Solid State Commun. **7**, 1015 (1969). [p. 92], [p. 93]

[178] P. Tolédano, B. Mettout, W. Schranz and G. Krexner, *Directional magneto-electric effects in MnWO4: magnetic sources of the electric polarization.*, J. Phys.: Condens. Matter **22**, 065901 (2010). [p. 92], [p. 93], [p. 113]

[179] M. Kenzelmann, A. B. Harris, A. Aharony, O. Entin-Wohlman, T. Yildirim, Q. Huang, S. Park, G. Lawes, C. Broholm, N. Rogado and et al., *Field dependence of magnetic ordering in Kagomé-staircase compound $Ni_3V_2O_3$*, Phys. Rev. B **74**, 014429 (2006). [p. 93]

[180] H. Cid-Dresdner and C. Escobar, *The crystal structure of ferberite, $FeWO_4$*, Z. Kristallogr. **127**, 61 (1968). [p. 93], [p. 125], [p. 126]

[181] H. Weitzel, *Magnetische Struktur von $CoWO_4$, $NiWO_4$ und $CuWO_4$*, Solid State Communications **8**, 2071 (1970). [p. 93]

[182] H. Ehrenberg, H. Weitzel, H. Fuess and B. Hennion, *Magnon dispersion in $MnWO_4$*, J. Phys.: Condens. Matter **11**, 2649 (1999). [p. 94], [p. 95], [p. 119], [p. 122], [p. 123]

[183] C. Tian, C. Lee, H. Xiang, Y. Zhang, C. Payen, S. Jobic and M.-H. Whangbo, *Magnetic structure and ferroelectric polarization of $MnWO_4$ investigated by density functional calculations and classical spin analysis*, Phys. Rev. B **80**, 104426 (2009). [p. 94], [p. 96]

[184] F. Ye, R. S. Fishman, J. A. Fernandez-Baca, A. A. Podlesnyak, G. Ehlers, H. A. Mook, Y. Wang, B. Lorenz and C. W. Chu, *Long-range magnetic interactions in the multiferroic antiferromagnet $MnWO_4$*, Phys. Rev. B **83**, 140401 (2011). [p. 94], [p. 96], [p. 105], [p. 119], [p. 122]

[185] T. Finger, D. Senff, K. Schmalzl, W. Schmidt, L. P. Regnault, P. Becker, L. Bohatý and M. Braden, *Polarized-neutron-scattering studies on the chiral magnetism in multiferroic $MnWO_4$*, J. Phys. Conf. Ser. **211**, 012001 (2010). [p. 95], [p. 104]

[186] D. Meier, N. Leo, G. Yuan, T. Lottermoser, M. Fiebig, P. Becker and L. Bohatý, *Second harmonic generation on incommensurate structures: The case of multiferroic $MnWO_4$*, Phys. Rev. B **82**, 1 (2010). [p. 95]

[187] S. Holbein, Diplomarbeit, *Microscopic and macroscopic investigations of multiferroics*, Universtität zu Köln, (2011). [p. 95], [p. 125], [p. 130], [p. 136], [p. 142], [p. 143]

[188] D. Niermann, C. P. Grams, M. Schalenbach, P. Becker, L. Bohatý, J. Stein, M. Braden and J. Hemberger, *Domain dynamics in the multiferroic phase of $MnWO_4$*, Phys. Rev. B **89**, 134412 (2014). [p. 95]

[189] H. Ehrenberg, H. Weitzel, C. Heid, H. Fuess, G. Wltschek, T. Kroener, J. van Tol and M. Bonnet, *Magnetic phase diagrams of $MnWO_4$*, J. Phys.: Condens. Matter **9**, 3189 (1997). [p. 95]

[190] I. Urcelay-Olabarria, E. Ressouche, A. A. Mukhin, V. Y. Ivanov, A. M. Kadomtseva, Y. F. Popov, G. P. Vorob'ev, A. M. Balbashov, J. L. García-Munoz and V. Skumryev, *X phase of $MnWO_4$*, Phys. Rev. B **90**, 024408 (2014). [p. 95]

[191] R. P. Chaudhury, B. Lorenz, Y. Q. Wang, Y. Y. Sun and C. W. Chu, *Suppression and recovery of the ferroelectric phase in multiferroic $MnWO_4$*, Phys. Rev. B **77**, 104406 (2008). [p. 95]

[192] F. Ye, Y. Ren, J. A. Fernandez-Baca, H. A. Mook, J. W. Lynn, R. P. Chaudhury, Y.-Q. Wang, B. Lorenz and C. W. Chu, *Magnetic switching and phase competition in the multiferroic antiferromagnet $Mn_{1-x}Fe_xWO_4$*, Phys. Rev. B **78**, 193101 (2008). [p. 95]

[193] C. M. N. Kumar, Y. Xiao, P. Lunkenheimer, A. Loidl and M. Ohl, *Crystal structure, incommensurate magnetic order, and ferroelectricity in $Mn_{1-x}Cu_xWO_4$ ($0 < x < 0.19$)*, Phys. Rev. B **91**, 235149 (2015). [p. 95]

[194] F. Ye, S. Chi, J. A. Fernandez-Baca, H. Cao, K.-C. Liang, Y. Wang, B. Lorenz and C. W. Chu, *Magnetic order and spin-flop transitions in the cobalt-doped multiferroic $Mn_{1-x}Co_xWO_4$*, Phys. Rev. B **86**, 094429 (2012). [p. 95]

[195] R. P. Chaudhury, F. Ye, J. A. Fernandez-Baca, B. Lorenz, Y. Q. Wang, Y. Y. Sun, H. A. Mook and C. W. Chu, *Robust ferroelectric state in multiferroic $Mn_{1-x}Zn_xWO_4$*, Phys. Rev. B **83**, 014401 (2011). [p. 95]

[196] H. Ehrenberg, H. Weitzel and H. Fuess, *Magnon dispersion and magnetic phase diagram of $MnWO_4$*, Phys. B Condens. Matter **234-236**, 560 (1997). [p. 95], [p. 96], [p. 105]

[197] I. Solovyev, *Origin of multiferroicity in $MnWO_4$*, Phys. Rev. B **87**, 144403 (2013). [p. 96], [p. 141]

[198] S. Matityahu, A. Aharony and O. Entin-Wohlman, *Landau theory for the phase diagram of multiferroic $Mn_{1-x}(Fe, Zn, Mg)_xWO_4$*, Phys. Rev. B **85**, 174408 (2012). [p. 96], [p. 118]

[199] N. Hollmann, Z. Hu, T. Willers, L. Bohatý, P. Becker, A. Tanaka, H. H. Hsieh, H.-J. Lin, C. T. Chen and L. H. Tjeng, *Local symmetry and magnetic anisotropy in multiferroic $MnWO_4$ and antiferromagnetic $CoWO_4$ studied by soft x-ray absorption spectroscopy*, Phys. Rev. B **82**, 184429 (2010). [p. 96]

[200] T. Möller, P. Becker, L. Bohatý, J. Hemberger and M. Grüninger, *Infrared-active phonon modes in monoclinic multiferroic $MnWO_4$*, Phys. Rev. B **90**, 155105 (2014). [p. 97]

[201] W. S. Choi, K. Taniguchi, S. J. Moon, S. S. A. Seo, T. Arima, H. Hoang, I.-S. Yang, T. W. Noh and Y. S. Lee, *Electronic structure and anomalous band-edge absorption feature in multiferroic $MnWO_4$: An optical spectroscopic study*, Phys. Rev. B **81**, 205111 (2010). [p. 97]

[202] A. Shuvaev, privat communication. [p. 97]

[203] D. Niermann, C. P. Grams, P. Becker, L. Bohatý, H. Schenck and J. Hemberger, *Critical Slowing Down near the Multiferroic Phase Transition in $MnWO_4$*, Phys. Rev. Lett. **114**, 037204 (2015). [p. 97], [p. 113], [p. 114], [p. 119], [p. 124], [p. 188]

[204] C. Tölzer, Diplomarbeit, *Strukturbestimmung von Übergangsmetallen mit nicht ganz gefüllter d-Schale*, Universtität zu Köln, (2012). [p. 98], [p. 107], [p. 120]

[205] J. Stein, Diplomarbeit, *Makroskopische und mikroskopische Untersuchungen an Multiferroika*, Universtität zu Köln, (2012). [p. 98]

[206] LAMP, the Large Array Manipulation Program by D. Richard, M. Ferrand, G. J. Kearley, available online at `http://www.ill.eu/data_treat/lamp/`; visited on October 6th 2015. [p. 103]

[207] R. Didier, K. Andersen and R. Stewart, *D7 LAMP* (2003), E-book, available online at `https://www.ill.eu/instruments-support/instruments-groups/instruments/d7/more/data-analysis/d7-lamp-manual/`; visited on September 25th 2015. [p. 103]

[208] A. R. Wildes, *Scientific Reviews: Neutron Polarization Analysis Corrections Made Easy*, Neutron News **17**, 17 (2006). [p. 103]

[209] Experimental report 4-02-400, available online at `userclub.ill.eu`. [p. 116]

[210] Experimental report 4-02-422, available online at `userclub.ill.eu`. [p. 116]

[211] L. Nyam-Ochir, H. Ehrenberg, A. Buchsteiner, A. Senyshyn, H. Fuess and D. Sangaa, *The magnetic structures of double tungstates, $NaM(WO_4)_2$, M=Fe, Cr: Examples for superexchange couplings mediated by $[NaO_6]$-octahedra*, J. Magn. Magn. Mater. **320**, 3251 (2008). [p. 125], [p. 126], [p. 127], [p. 136], [p. 138], [p. 139], [p. 141], [p. 142]

[212] S. Jodlauk, Dissertation, *Neue Magnetoelektrika und magnetoelektrische Multiferroika*, Universität zu Köln, (2010). [p. 125], [p. 129], [p. 130]

[213] M. Ackermann, Dissertation, *Thermodynamic properties of new multiferroic and linear magnetoelectric crystals*, Universität zu Köln, (2014). [p. 125], [p. 127], [p. 128], [p. 129], [p. 130], [p. 140], [p. 147], [p. 188], [p. 189]

[214] P. Klevtsov and R. Klevtsova, *Single-crystal synthesis and investigation of the double tungstates $NaR^{3+}(WO_4)_2$, where R^{3+} = Fe, Sc, Ga, and In*, J. Solid State Chem. **2**, 278 (1970). [p. 126], [p. 134], [p. 141]

[215] A. P. Ramirez, *Strongly Geometrically Frustrated Magnets*, Annu. Rev. Mater. Sci. **24**, 453 (1994). [p. 127]

[216] measurements perfored by O. Breunig (unpublished). [p. 127]

[217] J. Rossat-Mignod, *Magnetic structures of rare earth intermetallics*, J. Phys. Colloques **40**, 95 (1979). [p. 132]

[218] K. Binder, *Spin glasses: Experimental facts, theoretical concepts, and open questions*, Rev. Mod. Phys. **58**, 801 (1986). [p. 133], [p. 157]

[219] K. G. Dergachev, *Magnetic resonance studies of the low-dimensional magnet $NaFe(WO_4)_2$*, Low Temp. Phys. **31**, 402 (2005). [p. 134]

[220] *International Tables for Crystallography, Volume A: Space-Group Symmetry*, 5th ed., edited by T. Hahn (Springer, 2002). [p. 136], [p. 162]

[221] R. Ballou and B. Ouladdiaf, *Representation Analysis of Magnetic Structures*, chap. 3, neutron scattering from magnetic materials. ed. (Elsevier, 2006). [p. 136]

[222] L. Chapon, *An introduction to the use of representation analysis for studying magnetoelectrics and multiferroics*, EPJ Web of Conferences **22**, 00013 (2012). [p. 136], [p. 146]

[223] D. Schmitt and B. Ouladdiaf, *Absorption Correction for Annular Cylindrical Samples in Powder Neutron Diffraction*, J Appl Cryst **31**, 620 (1998). [p. 138]

[224] N. Qureshi, E. Ressouche, A. A. Mukhin, V. Y. Ivanov, S. N. Barilo, S. V. Shiryaev and V. Skumryev, *Stabilization of multiferroic spin cycloid in $Ni_3V_2O_8$ by light Co doping*, Phys. Rev. B **88**, 174412 (2013). [p. 141]

[225] I. Urcelay-Olabarria, J. Perez-Mato, J. Ribeiro, J. Garcia-Munoz, E. Ressouche, V. Skumryev and A. Mukhin, *Incommensurate magnetic structures of multiferroic $MnWO_4$ studied within the superspace formalism*, Phys. Rev. B **87**, 014419 (2013). [p. 141]

[226] F. Neumann, in *Vorlesungen über die Theorie der Elastizität der festen Körper und des Lichtäthers*, edited by O. E. Meyer (B. G. Teubner-Verlag, 1885). [p. 146]

[227] A. S. Borovik-Ramanov and H. Grimmer, in *International Tables for Crystallography*, 1st ed., edited by A. Authier (Kluwer Academic Publishers, 2003), Vol. D: Physical Properties of Crystals, Chap. 1.5: Magnetic properties, p. 115-149. [p. 146], [p. 155]

[228] S. Goshen, D. Mukamel, H. Shaked and S. Shtrikman, *Mechanism Leading to Ferroelectricity Induced in Centrosymmetric Crystals by Antiferromagnetic Transitions*, Phys. Rev. B **2**, 4679 (1970). [p. 146]

[229] T. Lorenz, privat communication. [p. 147]

[230] A. Ito, H. Kawano, H. Yoshizawa and K. Motoya, *Magnetic properties and phase diagram of* $Ni_xMn_{1-x}TiO_3$, J. Magn. Magn. Mater. **104-107**, 1637 (1992). [p. 149], [p. 150], [p. 152], [p. 153], [p. 156]

[231] H. Kawano, H. Yoshizawa, A. Ito and K. Motoya, *Two Successive Spin Glass transitions in Nondiluted Heisenberg-Like Spin Glass* $Ni_{0.42}Mn_{0.58}TiO_3$, J. Phys. Soc. Japan **62**, 2575 (1993). [p. 149], [p. 150], [p. 154], [p. 156], [p. 158], [p. 167]

[232] Y. Yamaguchi and T. Kimura, *Magnetoelectric control of frozen state in a toroidal glass.*, Nat. Commun. **4**, 2063 (2013). [p. 149], [p. 154]

[233] G. Shirane, S. J. Pickart and Y. Ishikawa, *Neutron Diffraction Study of Antiferromagnetic* $MnTiO_3$ *and* $NiTiO_3$, J. Phys. Soc. Japan **14**, 1352 (1959). [p. 150], [p. 151], [p. 152], [p. 158], [p. 159], [p. 160], [p. 162], [p. 177]

[234] J. B. Goodenough and J. J. Stickler, *Theory of the Magnetic Properties of the Ilmenites* $MTiO_3$, Phys. Rev. **164**, 768 (1967). [p. 150], [p. 151], [p. 152], [p. 154], [p. 181]

[235] R. P. Liferovich and R. H. Mitchell, *Rhombohedral ilmenite group nickel titanates with Zn, Mg, and Mn: synthesis and crystal structures*, Phys. Chem. Miner. **32**, 442 (2005). [p. 150], [p. 151]

[236] H. Yoshizawa, H. Kawano, H. Mori, S. Mitsuda and A. Ito, *Phase diagram of a Heisenberg-like spin glass* $Ni_xMn_{1-x}TiO_3$, Phys. B **181**, 94 (1992). [p. 150], [p. 153], [p. 156]

[237] G. S. Heller, J. J. Stickler, S. Kern and A. Wold, *Antiferromagnetism in* $NiTiO_3$, J. Appl. Phys. **34**, 1033 (1963). [p. 151]

[238] H. Watanabe, H. Yamauchi and H. Takei, *Magnetic Anisotropies in* $MTiO_3$ *(M = Co, Ni)*, J. Magn. Magn. Mater. **15-18**, 549 (1980). [p. 151]

[239] J. Ko and C. T. Prewitt, *High-pressure phase transition in $MnTiO_3$ from the ilmenite to the $LiNbO_3$ structure*, Phys. Chem. Miner. **15**, 355 (1988). [p. 151]

[240] C. J. Fennie, *Ferroelectrically Induced Weak Ferromagnetism by Design*, Phys. Rev. Lett. **100**, 167203 (2008). [p. 151]

[241] C. Xin, Y. Wang, Y. Sui, Y. Wang, X. Wang, K. Zhao, Z. Liu, B. Li and X. Liu, *Electronic, magnetic and multiferroic properties of magnetoelectric $NiTiO_3$*, J. Alloys Compd. **613**, 401 (2014). [p. 151]

[242] T. Acharya and R. N. P. Choudhary, *Structural, Ferroelectric, and Electrical Properties of $NiTiO_3$ Ceramic*, J. Electron. Mater. **44**, 271 (2015). [p. 151]

[243] M. Ohgaki, K. Tanaka, F. Marumo and H. Takei, *Electron-density distribution in ilmenite-type crystals. III. Nickel(II) titanium(IV) trioxide, $NiTiO_3$.*, Mineralogical Journal **14**, 133 (1988). [p. 151]

[244] Y. Ishikawa and S.-i. Akimoto, *Magnetic Property and Crystal Chemistry of Ilmenite ($MeTiO_3$) and Hematite (αFe_2O_3) System II. Magnetic Property*, J. Phys. Soc. Jpn. **13**, 1298 (1958). [p. 151]

[245] H. Yamauchi, H. Hiroyoshi, M. Yamada, H. Watanabe and H. Takei, *Spin flopping in $MnTiO_3$*, J. Magn. Magn. Mater. **31-34**, 1071 (1983). [p. 151], [p. 152]

[246] J. Akimitsu and Y. Ishikawa, *Magnetic Critical Behavior of a Quasi Two-Dimensional Antiferromagnet $MnTiO_3$*, J. Phys. Soc. Jpn. **42**, 462 (1977). [p. 152]

[247] Y. Todate, Y. Ishikawa, K. Tajima, S. Tomizoshi and H. Takei, *Spin Dynamics in a Quasi-Two Dimensional Antiferromagnet $MnTiO_3$*, J. Phys. Soc. Japan **55**, 4464 (1986). [p. 152], [p. 181], [p. 186], [p. 189]

[248] W. P. Osmond, *Magnetic exchange interactions in 'ilmenites' $MeTiO_3$ (Me = Mn, Fe, Co and Ni)*, Brit. J. Appl. Phys. **15**, 1377 (1964). [p. 152]

[249] N. Mufti, G. R. Blake, M. Mostovoy, S. Riyadi, A. A. Nugroho and T. T. M. Palstra, *Magnetoelectric coupling in $MnTiO_3$*, Phys. Rev. B **83**, 104416 (2011). [p. 152], [p. 154], [p. 173]

[250] S. W. Chen, P. A. Lin, H. T. Jeng, S. W. Fu, J. M. Lee, J. F. Lee, C. W. Pao, H. Ishii, K. D. Tsuei, N. Hiraoka and et al., *Exchange interaction mediated ferroelectricity in multiferroic $MnTiO_3$ with anisotropic orbital hybridization and hole delocalization*, Appl. Phys. Lett. **104**, 082104 (2014). [p. 152]

[251] D. Cragg and D. Sherrington, *Spin-Glass with Local Uniaxial Anisotropy*, Phys. Rev. Lett. **49**, 1190 (1982). [p. 154]

[252] H. Kawamura, *The ordering of XY spin glasses.*, J. Phys.: Condens. Matter **23**, 164210 (2011). [p. 154]

[253] H. Yoshizawa, S. Mitsuda, H. Aruga and A. Ito, *Mixed phase of spin-glass ordering and antiferromagnetism in an Ising system,* $Fe_xMn_{1-x}TiO_3$, Phys. Rev. Lett. **59**, 2364 (1987). [p. 154]

[254] T. Kurihara, T. Komai, A. Ito and T. Goto, *Magnetic Properties and Phase Diagram of* $Co_xMn_{1-x}TiO_3$ *with Exchange Frustration*, J. Phys. Soc. Jpn. **60**, 2057 (1991). [p. 154]

[255] V. V. Shvartsman, S. Bedanta, P. Borisov, W. Kleemann, A. Tkach and P. M. Vilarinho, *(Sr,Mn)*TiO_3*: A Magnetoelectric Multiglass*, Phys. Rev. Lett. **101**, 165704 (2008). [p. 154]

[256] N. A. Spaldin, M. Fiebig and M. Mostovoy, *The toroidal moment in condensed-matter physics and its relation to the magnetoelectric effect*, J. Phys.: Condens. Matter **20**, 434203 (2008). [p. 155]

[257] S. Chi, F. Ye, H. D. Zhou, E. S. Choi, J. Hwang, H. Cao and J. A. Fernandez-Baca, *Magnetoelectric coupling tuned by competing anisotropies in* $Mn_{1-x}Ni_xTiO_3$, Phys. Rev. B **90**, 144429 (2014). [p. 155], [p. 162], [p. 170], [p. 173]

[258] T. Fröhlich, privat communication. [p. 162]

[259] P. J. Brown, J. B. Forsyth and F. Tasset, *Studies of magneto-electric crystals using spherical neutron polarimetry*, Solid State Sciences **7**, 682 (2005). [p. 170]

[260] M. Baum, K. Schmalzl, P. Steffens, A. Hiess, L. P. Regnault, M. Meven, P. Becker, L. Bohatý and M. Braden, *Controlling toroidal moments by crossed electric and magnetic fields*, Phys. Rev. B **88**, 024414 (2013). [p. 170]

Glossary

Commonly used terms

AFM	Antiferromagnetic
EM	Electromagnon
DM	Dzyaloshinskii-Moriya
FE	Ferroelectric
FM	Ferromagnetic
INS	Inelastic neutron scattering
IR	Infrared
ME	Magnetoelectric
NRSE	Neutron resonance spin echo
NSE	Neutron spin echo
PG	Polycrystalline graphite
SIA	Single ion anisotropy
SOI	Spin-orbit interaction
SDW	Spin-density wave
TAS	Triple-axis spectrometer
TOF	Time of flight
$f^M(Q)$	Magnetic form factor
$\vec{k}$	Magnetic propagation vector
$\vec{Q}$	Scattering vector $\vec{Q} = \vec{k}_f - \vec{k}_i$
ω	Angle of sample rotation
2θ	Scattering angle
iSF	Spin-flip cross section $\sigma_{\bar{i}i}$ along i
iNSF	Non-spin-flip cross section σ_{ii} along i

Instruments and institutes

ILL	Institut Laue-Langevin, Grenoble (France)
IN3	Thermal neutron triple-axis spectrometer
IN5	Disk chopper time-of-flight spectrometer
IN8	Thermal neutron triple-axis spectrometer
IN11	Neutron Spin-Echo Spectrometer
IN14/Thales	Cold neutron triple-axis spectrometer with polarization analysis
D7	Diffuse Scattering Spectrometer
D10	Thermal neutron single-crystal four-circle diffractometer with three-axis energy analysis
LLB	Laboratoire Leon Brillouin, Saclay (France)
4F1	Cold neutron triple-axis spectrometer with polarization analysis
6T2	Thermal neutron two-axis diffractometer with lifting detector arm
FRM II	Forschungsreaktor München II, Garching (Germany)
TRISP	Thermal neutron resonance spin echo and triple-axis spectrometer
PANDA	Cold neutron triple-axis spectrometer

Chapter 4

J_{AFM}	Nearest-neighbor exchange along $\vec{c}$
J_{FM}	Nearest-neighbor exchange in the ab-plane
J_{NN}	Next-nearest-neighbor exchange along $\vec{b}$
T_N	Antiferromagnetic transition temperature
T_{FE}	Ferroelectric transition temperature
T_{TB}	Transition temperature of Tb-subsystem
$\vec{k}_{ic} = (0,\ q_k,\ 0)$	Propagation vector of Mn-order

Chapter 5

AFM3, T_{N3}	Incommensurate spin-density-wave phase
AFM2, T_{N2}	Incommensurate spin-spiral and ferroelectric phase
AFM1, T_{N1}	Commensurate collinear phase
$\vec{e}_{ac}$	Easy axis in the ab-plane
$\vec{k}_{ic} = (-0.214,\ 0.5,\ 0.457)$	Incommensurate propagation vector
$\vec{k}_{c} = (-0.25,\ 0.5,\ 0.5)$	Commensurate propagation vector
Schärpf-angle	Angle between direct beam and x-polarization axis at D7

Chapter 6

MS	Magnetostriction
TE	Thermal expansion
$\vec{e}_{ac}$	Easy axis in the ab-plane
$\vec{k}_{ic} = (0.485,\ 0.5,\ 0.48)$	Incommensurate propagation vector
$\vec{k}_{c} = (0.5,\ 0.5,\ 0.5)$	Commensurate propagation vector

Chapter 7

AF-$Mn_{\parallel}$	G-type structure, $\vec{M} \parallel \vec{c}$
AF-$Mn_{\perp}$	G-type structure, $\vec{M}$ in ab-plane
AF-Ni	A-type structure, $\vec{M}$ in ab-plane
SG	Spin glass
$T_{SG}^{\parallel}$	Freeze-in of moments parallel to the easy-plane anisotropy
$T_{SG}^{\perp}$	Freeze-in of moments perpendicular to the easy-plane anisotropy

Abstract

In this thesis, the magnetic properties of four transition-metal oxides are presented. Their multiferroic and magnetoelectric phases have been investigated by means of different neutron scattering techniques.

The materials $TbMnO_3$ and $MnWO_4$ belong to the group of spin-induced multiferroics. Their ferroelectric polarization can be explained by the inverse Dzyaloshinskii-Moriya interaction. Another common feature of both materials is the presence of subsequent magnetic transitions from a spin-density wave to a spin spiral. The features of the phase transitions have been studied in both materials and it could be shown that diffuse magnetic scattering from the spin spiral is present even in the ordered spin-density wave phase.
The excitation spectrum in the multiferroic phase of $TbMnO_3$ was investigated in detail and a comprehensive dataset was obtained using time-of-flight spectroscopy. A spin-wave model could be obtained which can quantitatively describe the full dispersion. Furthermore, the polarization of the zone-center excitations could be derived which fit well to data from inelastic neutron spectroscopy and infrared spectroscopy.
With the combination of spherical neutron polarimetry and a poling of the sample by an electric field, it was possible to observe the chiral magnetic component of the magnetic excitations in $TbMnO_3$ and $MnWO_4$. The spin-wave model for $TbMnO_3$ obtained in this thesis is able to correctly describe the dispersion of this component.

The double tungstate $NaFe(WO_4)_2$ is isostructural to the multiferroic $MnWO_4$ and develops a complex magnetic phase diagram. By the use of neutron diffraction techniques, the zero-field structure and high-field structures in magnetic field applied along the *b*-axis could be determined. The data reveal a direct transition into an incommensurate spin-spiral structure. The value of the incommensurability is driven by anharmonic modulations and shows strong hysteresis effects.

The static and dynamic properties in the magnetoelectric spin-glass phase of $Ni_{0.42}Mn_{0.58}TiO_3$ were studied in detail. The spin-glass phase is composed of short-ranged $MnTiO_3$ and $NiTiO_3$-type order. The antiferromagnetic domains

could be controlled by crossed magnetic and electric fields, which was visualized using spherical neutron polarimetry.
A comprehensive dataset of the magnetic excitations in the spin-glass phase was collected. The dataset revealed correlations in the hexagonal plane which are only weakly coupled along the c-axis. The excitation spectra could be simulated by taking into account the $MnTiO_3$-type order.

Kurzzusammenfassung

Die vorliegende Arbeit beschäftigt sich mit dem Magnetismus in vier Übergangsmetalloxiden. Die magnetischen und magnetoelektrischen Phasen dieser Materialien wurden mittels verschiedener Methoden der Neutronenstreuung experimentell untersucht.

Die Verbindungen $TbMnO_3$ und $MnWO_4$ gehören zu der Gruppe der Spin-induzierten Multiferroika. Die ferroelektrische Polarisation in diesen Materialien kann mithilfe des inversen Dzyaloshinskii-Moriya Mechanismus erklärt werden. Beide Materialien zeigen eine Abfolge von magnetischen Phasen, von einer sinus-modulierten Phase zu einer spiralen Phase. Die Eigenschaften der Phasenübergänge wurden in beiden Materialien untersucht und es konnte gezeigt werden, dass diffuse magnetische Streuung der spiralen Phase bereits in der geordneten sinus-modulierten Phase existiert.
Das Anregungsspektrum in der mulitferroischen Phase von $TbMnO_3$ wurde detailliert untersucht und ein umfangreicher Datensatz wurde mittels Neutronen-Flugzeitspektroskopie gemessen. Im Rahmen dieser Arbeit konnte ein Spinwellenmodel entwickelt werden, welches die komplette Dispersion qualitativ beschreiben kann. Die Polarisation der Magnonen des Models im Zonenzentrum stimmen sehr gut mit vorherigen Ergebnissen von inelastischer Neutronenstreuung und Infrarot-Spektroskopie überein.
Die gleichzeitige Nutzung von sphärischer Neutronen-Polarimetrie und einem angelegten elektrischen Feld haben es ermöglicht den chiralen magnetischen Beitrag der magnetischen Anregungen in $TbMnO_3$ und $MnWO_4$ zu messen. Das in dieser Arbeit entwickelte Spinwellenmodel beschreibt die Dispersion dieser Beiträge korrekt in $TbMnO_3$.

Die Verbindung $NaFe(WO_4)_2$ ist strukturgleich mit dem Multiferroika $MnWO_4$ und sie zeigt ein komplexes magnetisches Phasendiagramm. Die Strukturen der Nullfeld- und der Hochfeldphasen konnten mithilfe von Neutronendiffraktion in magnetischen Felder entlang der *b*-Achse ermittelt werden. Dabei wurde ein direkter Übergang in eine spirale Phase entdeckt. Die Periodizität ist inkommensurabel zu der Kristallstruktur. Diese ist mit einer anharmonischen Störung der Spirale verknüpft und zeigt starke Hysterese-Effekte.

Die statischen und dynamischen Eigenschaften der magnetoelektrischen Spin-Glass Phase von $Ni_{0.42}Mn_{0.58}TiO_3$ wurden detailliert untersucht. Die Spin-Glass Phase zeigt Beiträge von kurzreichweitigen Ordnungen des $MnTiO_3$ und des $NiTiO_3$-Types. Es konnte gezeigt werden, dass die antiferromagnetischen Domänen in gekreuzten magnetischen und elektrischen Feldern ausgerichtet werden können, wozu sphärische Neutronen-Polarimetrie verwendet wurde.
Ein umfangreicher Datensatz der magnetischen Anregungen in der Spin-Glas wurde ermittelt. Dieser dokumentiert magnetische Korrelationen in der hexagonalen Ebene und nur eine schwache Kopplung entlang der *c*-Achse. Die Anregungen konnten mittels eines Modelles simuliert werden, welches auf der $MnTiO_3$-Ordnung basiert.

Danksagung

Ein so umfangreiches Projekt wie eine Promotion ist ohne Hilfestellung nicht zu bewältigen. Ich möchte diese Gelegenheit nutzen den Leuten zu danken, die mich auf meinem Weg unterstützt haben.

Zuerst möchte ich mich herzlich bei meinem Doktorvater Prof. Markus Braden bedanken. Er hat es mir ermöglicht mich nach der Diplomarbeit in die Forschung der Multiferroika und der Neutronenstreuung zu vertiefen. Ich danke ihm für sein Vertrauen, für die vielen interessanten Aufgabenstellungen und dafür, mir einen Aufenthalt in Frankreich ermöglicht zu haben.

Bei Prof. Joachim Hemberger möchte ich mich für die Begutachtung der Arbeit bedanken und der freundlichen Zusammenarbeit seit der Diplomarbeit. Prof. Simon Trebst danke ich den Vorsitz der Prüfungskomission übernommen zu haben.

Dem Institut Laue-Langevin danke ich dafür, mich über den Zeitraum von zwei Jahren in ihr PhD-Programm aufgenommen zu haben. Dadurch wurde mir ermöglicht an der weltbesten Neutronenquelle zu arbeiten und zahlreiche Experimente an den verschiedensten Instrumenten durchzuführen. Darüber hinaus werden mir die kulturellen Erfahrungen in Grenoble in sehr guter Erinnerung bleiben.

Ein besonderer Dank gebührt Paul Steffens, der bereitwillig die Betreuung am ILL übernommen hat. Von ihm habe ich die vielen Details gelernt, die für ein erfolgreiches Neutronenexperiment wichtig sind. Ich konnte sehr von seiner Unterstützung profitieren und auch seine Matlab-Bibliothek *nplot* war mir bis zum Ende ein treuer Begleiter beim Auswerten der Datenmengen. Trotz der vielen Messungen blieb dennoch Zeit die Vorzüge des Lebens in den französischen Alpen gemeinsam zu genießen.

Je veux également remercier Laurent Chapon qui a aussi accepté d'encadrer le projet à l'ILL. Il m'a aidé à résoudre la structure magnétique de $NaFe(WO_4)_2$ et a toujours été de très bon conseil.

Die vielen erfolgreichen Streuexperimente wären nicht möglich gewesen ohne die hochwertigen Einkristalle, die mir zur Verfügung gestellt wurden. Ich bedanke

mich dabei herzlich bei Prof. Petra Becker, Prof. Ladislav Bohatý, Christine Tölzer, Chul-Ho Lee, Agung Nugroho und Alexander Komarek.

Throughout this thesis, many experiments have been performed at the neutron sources ILL, LLB and FRM II. I would like to thank the instrument scientists Peter Fouquet, Jacques Ollivier, Gøran Nilsen, Yvan Sidis, Alain Cousson, Astrid Schneidewind and Thomas Keller for their excellent support. Special thanks belong to Martin Böhm and Bachir Ouladdiaf for the internal usage of OrientExpress and IN3.

Prof. Catherine Pappas danke ich für den interessanten Einblick in die Spin-Echo Technik.

Je veux remercier tous les membres du groupe TAS à l'ILL de m'avoir si bien intégré et aidé pendant les deux ans passés à Grenoble. J'ai beaucoup apprécié l'ambiance chaleureuse de toutes les sorties de groupe auxquelles j'ai pu participer.

Ich möchte auch den aktuellen und ehemaligen Mitgliedern der AG Braden für die freundliche und produktive Zusammenarbeit danken. Im Besonderen sind hierbei Max Baum und Navid Qureshi zu nennen, die mir ihr Wissen über Multiferroika und Neutronenstreuung anvertraut haben, sowie Jonas Stein, der die DiMoS übernommen und weiterentwickelt hat und immer einen guten Rat wusste. Allen Dreien danke ich auch für das aufmerksame Korrekturlesen.

Den Mitarbeitern des II. Physikalischen Instituts danke ich für die entspannte Arbeitsatmosphäre und die gute Kooperation. Das hat dazu geführt, dass ich die ganzen Jahre über gern hier hin gekommen bin. Dabei danke ich besonders Prof. Thomas Lorenz für die hilfreichen Diskussionen über $NaFe(WO_4)_2$, sowie Oliver Breunig und Daniel Brünig für die Durchführung der makroskopischen Messungen.

Meinem Studienkollegen Christian, mit dem ich den Großteil der Studienzeit in Köln, Liverpool und später auch in Frankreich geteilt habe, danke ich für die jahrelange Freundschaft. Sein Ehrgeiz und seine beruflichen Erfolge waren mir stets ein Ansporn.

Meinen Eltern Leona und Thomas danke ich sehr für den bedingungslosen Rückhalt, den sie mir über die gesamte Studienzeit entgegengebracht haben. Mit eurer Unterstützung ist alles möglich!

Zuletzt möchte ich der Person danken, die am meisten unter der vorliegenden Arbeit hat leiden müssen. Ich danke dir, Héloïse, mit mir nach Frankreich gegangen zu sein, mich stets unterstützt und motiviert zu haben und nicht zuletzt für das mühsehlige Korrekturlesen. Je suis au comble du bonheur de t'avoir dans ma vie! Merci pour tout!

List of Publications

Publications including results of this thesis

- *Field and temperature dependence of electromagnon scattering in $TbMnO_3$ studied by inelastic neutron scattering*
  S. Holbein, P. Steffens, T. Finger, A. C. Komarek, Y. Sidis, P. Link, and M. Braden
  Phys. Rev. B **91**, 014432 (2015)

Further publications

- *Control of multiferroic domains by external electric fields in $TbMnO_3$*
  J. Stein, M. Baum, S. Holbein, H. Vladimir, A. C. Komarek, and M. Braden
  J. Phys.: Condens. matter **27**, 446001 (2015)
- *Magnetic structure and multiferroic coupling in pyroxene $NaFeSi_2O_6$*
  M. Baum, A. C. Komarek, S. Holbein, M. Fernandez-Diaz, G. Andre, A. Hiess, Y. Sidis, P. Steffens, P. Becker, L. Bohatý, and M. Braden
  Phys. Rev. B **91**, 214415 (2015)

Conference contributions

- *ILL PhD days 2014* in Grenoble, France (oral and poster)
- *JDN22 2014* conference in Saint-Pierre-d'Oléron, France (oral and poster)
- *SNI 2014* conference in Bonn, Germany (oral)
- *SCES 2014* conference in Grenoble, France (poster)
- *Flipper 2013* workshop in Grenoble, France (poster)
- *Tokyo-Cologne Workshop on Strongly Correlated Transition-Metal Compounds 2011* in Cologne, Germany (poster)
- *DPG Spring Meeting of the Condensed Matter Section 2011* in Dresden, Germany (poster)

Offizielle Erklärung

Ich versichere, dass ich die von mir vorgelegte Dissertation selbständig angefertigt, die benutzten Quellen und Hilfsmittel vollständig angegeben und die Stellen der Arbeit – einschließlich Tabellen, Karten und Abbildungen –, die anderen Werken im Wortlaut oder dem Sinn nach entnommen sind, in jedem Einzelfall als Entlehnung kenntlich gemacht habe; dass diese Dissertation noch keiner anderen Fakultät oder Universität zur Prüfung vorgelegen hat; dass sie – abgesehen von unten angegebenen Teilpublikationen – noch nicht veröffentlicht worden ist sowie, dass ich eine solche Veröffentlichung vor Abschluss des Promotionsverfahrens nicht vornehmen werde. Die Bestimmungen der Promotionsordnung sind mir bekannt. Die von mir vorgelegte Dissertation ist von Prof. Dr. M. Braden betreut worden.

Köln, den 20.11.2015 gez. Simon Holbein

Teilpublikationen der vorliegenden Arbeit

- *Field and temperature dependence of electromagnon scattering in $TbMnO_3$ studied by inelastic neutron scattering*
  S. Holbein, P. Steffens, T. Finger, A. C. Komarek, Y. Sidis, P. Link, and M. Braden
  Phys. Rev. B **91**, 014432 (2015)